A WAVELET BASED SPEED CONTROLLER FOR INTERIOR PERMANENT MAGNET MOTOR DRIVES

MD. ABDESH SHAFIEL KAFIEY KHAN

A Wavelet Based Speed Controller for Interior Permanent Magnet Motor Drives

by

© Md. Abdesh Shafiel Kafiey Khan

A thesis submitted in partial fulfillment
of the requirements for the degree of
Doctor of Philosophy

Faculty of Engineering and Applied Science
Memorial University of Newfoundland

St. John's Newfoundland Canada

January 2010

Abstract

The use of permanent magnet synchronous motors in high performance ac motor drives has increased recently due to advances in manufacturing and commercializing permanent magnet (PM) materials, power electronics, digital signal processors, and intelligent control algorithms. Among several designs of permanent magnet motors, the interior permanent magnet (IPM) synchronous motor, which has magnets buried in the rotor core, shows excellent properties such as robustness, rotor physical non saliency, and small effective air gap. Fast speed tracking, quick recovery of speed from disturbances, and insensitivity to parameter variations are some of the main criteria of the high performance drive (HPD) systems for applications such as automotive, aerospace, air conditioners, robotics, rolling mills, machine tools, etc. The IPM motor with a suitable speed controller can meet the required specifications of HPD systems.

This work presents the development and implementation of a novel wavelet neural network (WNN) based self-tuning multiresolution proportional integral derivative (MRPID) controller for accurate speed control of the interior permanent magnet synchronous motor (IPMSM) drive systems under system uncertainties. In the proposed self-tuning MRPID controller, the discrete wavelet transform is used to decompose the speed error, which is the difference between the command speed and the motor measured speed, into localized sub-band frequencies established by the discrete wavelet transform (DWT). Such localized decomposition of the speed error signal produce sets of independent coefficients, which also contain information about the system dynamics, effects of external disturbances, measurement errors, noise, etc. Moreover, these wavelet transformed coefficients are scaled by their respective gains, and then are added to generate the control signal for the drive system. Initially, the analogy between the

proportional integral derivative (PID) decomposition and the multiresolution decomposition of speed error is used in order to set the initial gains of the MRPID controller. Next the wavelet neural network (WNN) is used for self-tuning of the proposed MRPID controller to ensure optimal drive performances in real time under system disturbances and uncertainties. The learning rates of the WNN are derived on the basis of the discrete Lyapunov function in order to confirm the stability of the proposed self-tuning MRPID controller based IPMSM drive system.

The minimum description length (MDL) data criterion and the entropy based criterion are successfully used to select an optimum mother wavelet function and to find the optimal levels of decomposition of the speed error signal, respectively of the proposed self-tuning MRPID controller. The comparative performances of the IPMSM drive system using the fixed gain proportional integral (PI) controller, proportional integral derivative (PID) controller, adaptive artificial neural network (NN) controller, and the proposed self-tuning MRPID controller are presented. The proposed self-tuning MRPID controller is found better than the conventional fixed gain and adaptive speed controllers.

The performances of the proposed self-tuning MRPID controller are investigated in both simulation and experiments at different dynamic operating conditions of the IPMSM drive system. The flux weakening control scheme of the proposed self-tuning MRPID based IPMSM drive system is successfully implemented in real time using the dSPACE ds1102 digital signal processor board on the laboratory 1-hp IPM motor. The performances of the proposed drive system are also compared with the fixed gain PI controller based drive system in real time in order to verify the superiority of the proposed self-tuning MRPID controller over the conventional controllers. The simulation results and laboratory test results confirm the effectiveness of the proposed self-tuning MRPID controller as a robust controller for high performance industrial motor drive systems.

Acknowledgements

I would like to express my most sincere gratitude and thanks to my supervisor Dr. Md Azizur Rahman for his guidance, advice, and encouragements throughout the PhD program. I would like to thank him again for the financial support he provided me during the program. I would also like to thank the Natural Science and Engineering Resource Council of Canada for the financial support during the PhD and Master's program. I wish to thank the School of Graduate Studies of Memorial University of Newfoundland for providing me with the teaching assistantship and research fellowship to pursue my Doctoral study at the Faculty of Engineering and Applied Science of Memorial University of Newfoundland. I also wish to thank my supervisor and the Faculty of Engineering of Memorial University of Newfoundland for providing me with the necessary laboratory spaces, equipments, and technical assistances to complete the PhD research smoothly.

I wish to thank Dr. Glyn George and Dr. Michael Hinchey, members of my supervisory committee, for their useful suggestions and discussions during the PhD program. I would like to thank Dr. Ron Harley, external member of the examination committee of the Ph. D. thesis, for the substantive comments and discussions on the thesis. I would also like to thank Dr. Saleh A. Saleh for his useful discussions and comments on the Ph. D. thesis. I would also like to acknowledge the assistance from the Faculty, staff members, and graduate students of the Faculty of Engineering and Applied Science of Memorial University of Newfoundland during the PhD program.

I express my sincere appreciation to my wife, Umme Masikin, my parents, Dr. Md. Abdul Kuddus Khan and Mrs. Samsun Nahar Khan, my sister, Mehjabin Tusqin Khan, uncle, Dr. Golam Mostafa, as well as other family members, relatives, and friends for their encouragements and supports throughout the program.

DEDICATED TO:

My parents, ***Dr. Md. Abdul Kuddus Khan*** and ***Mrs. Samsun Nahar Khan***

&

My wife, ***Umme Masikin***

Contents

Abstract ii

List of Figures x

List of Tables xxvi

List of Symbols xxvii

List of Acronyms xxxi

1 Introduction 1

1.1 Electric Motor Drives..... 1

1.1.1 Permanent magnet synchronous motors..... 5

1.2 Literature Review of the PMSM Drives..... 9

1.2.1 PMSM drives using conventional and adaptive controllers 15

1.2.2 PMSM drives using artificial intelligent controllers..... 22

1.2.3 PMSM drives using wavelet based intelligent controllers..... 27

1.3 Problem Identification and Research Objectives..... 32

1.4 Outline of the Thesis..... 35

2 Vector Control of the Interior Permanent Magnet Synchronous Motor (IPMSM) Drive **37**

2.1 Modeling of Interior Permanent Magnet Synchronous Motor 38

2.2 Vector Control Scheme 44

2.3 Implementation of Vector Control Technique 46

2.3.1 Design of speed controllers 48

2.3.2 Vector rotator and PWM voltage source inverter..... 52

2.3.3 Design of current controller..... 56

2.4 Simulation of the Conventional Speed Controllers Based IPMSM Drive System..... 59

2.4.1 Results and discussions..... 59

2.5 Concluding Remarks..... 67

3 High Speed Control of the IPMSM **68**

3.1 Flux Weakening Control Principle..... 69

3.2 Implementation of the Flux Weakening Control..... 75

3.3 Results and Discussions..... 77

3.4 Concluding Remarks..... 84

4 Wavelet Transform Based Multiresolution Speed Controller **85**

4.1 Wavelets and Scaling Functions 86

4.1.1 Orthogonal wavelets..... 90

4.1.2 Non-orthogonal wavelets..... 94

4.2 Wavelet Transforms 94

4.2.1 Continuous wavelet transform..... 94

4.2.2 Discrete wavelet transform..... 98

4.2.3 Wavelet packet transform..... 100

4.3 Multiresolution Analysis..... 102

4.3.1 Quadrature mirror filter banks..... 104
4.4 Selection of Wavelet..... 105
4.5 Number of Levels of Decomposition..... 114
4.6 Wavelet Based Multiresolution PID Controller..... 115
4.7 Concluding Remarks..... 121

5 **Implementation of Wavelet Based Control of the IPMSM Drive** **123**
5.1 Modeling of the IPMSM for the MRPID Controller 124
5.2 MRPID Controller Based IPMSM Drive System..... 127
5.3 Implementation of the MRPID Controller Based IPMSM Drive System 128
5.4 Concluding Remarks..... 151

6 **Self-Tuning MRPID Control of the IPMSM Drive** **152**
6.1 Wavelet Neural Network..... 153
6.1.1 Adaptive on-line training of the wavelet neural network..... 156
6.1.2 Stability analysis..... 159
6.2 Software Implementation of the WNN based Self-Tuning MRPID Controller..... 171
6.3 Concluding Remarks..... 194

7 **Real Time Implementation of the Wavelet Based Self-Tuning MRPID Controller** **195**
7.1 Laboratory Setup for the Real Time Implementation of the IPMSM Drive..... 196
7.2 Hardware Components for the Real Time Implementation of the IPMSM Drive 198

7.3 Software Development for the Real Time Implementation of the IPMSM Drive..... 201
7.3.1 Peripheral initialization..... 202
7.3.2 Interrupt service routine..... 204
7.4 Experimental Results and Discussions..... 204
7.5 Concluding Remarks..... 233

8 Summary and Conclusions **234**
8.1 Major Contributions of the Thesis..... 238
8.2 Future Scope of Work..... 240
8.3 Conclusions..... 242

Bibliography **244**
Appendix A **259**
Appendix B **260**
Appendix C **262**
Appendix D **266**

List of Figures

1.1	Classification of the PM synchronous motors.....	7
1.2	Cross section of the interior type PM synchronous motor.....	8
1.3	Cross section of the surface mounted type PM synchronous motor.....	8
1.4	Cross section of the inset type PM synchronous motor.....	9
1.5	Schematic of the vector control scheme of the permanent magnet synchronous motor (PMSM) drive.....	11
2.1	Relative positions of stationary d-q axis and rotating d^r-q^r axis.....	40
2.2	Equivalent circuit model of the IPMSM: (a) d^r-axis and (b) q^r-axis.....	43
2.3	Basic vector diagram of the IPMSM: (a) general and (b) modified with $i_d^r = 0$.....	47
2.4	Block diagram of a vector controlled voltage source inverter (VSI) fed IPMSM drive system with $i_d^r = 0$.....	48
2.5	Three-layer structure of the neural network controller.....	51
2.6	Flow chart of the adaptive learning of the NN controller.....	51
2.7	Schematic of a current controlled voltage source inverter of the IPMSM drive.....	52
2.8	Inverter voltage vectors	55
2.9	Block diagram of a three-phase hysteresis current controller.....	55
2.10	Current and PWM voltage waveforms: (a) fixed band hysteresis control, (b) sinusoidal band hysteresis control, and (c) mixed band hysteresis control	58
2.11	Simulated starting speed responses of the IPMSM drive system under no load and rated command speed (188.6 rad/sec.) conditions: (a) PI controller, (b) PID controller, and (c) adaptive NN controller.....	61

2.12 Simulated starting current responses of the IPMSM drive system under no load and rated command speed (188.6 rad/sec.) conditions: (*a*) PI controller, (*b*) PID controller, and (*c*) adaptive NN controller..... 62

2.13 Simulated speed responses of the IPMSM drive system for step increase (from 130 rad/sec. to 188.6 rad/sec.) and step decrease (from 188.6 rad/sec. to 150 rad/sec.) of command speeds under rated load condition: (*a*) PI controller, (*b*) PID controller, and (*c*) adaptive NN controller..... 63

2.14 Simulated current responses of the IPMSM drive system for step increase (from 130 rad/sec. to 188.6 rad/sec.) and step decrease (from 188.6 rad/sec. to 150 rad/sec.) of command speeds under rated load condition: (*a*) PI controller, (*b*) PID controller, and (*c*) adaptive NN controller..... 64

2.15 Simulated speed responses of the IPMSM drive system when load is changed at $t = 1$ sec. from no load to rated load under rated command speed (188.6 rad/sec.) condition: (*a*) PI controller, (*b*) PID controller, and (*c*) adaptive NN controller..... 65

2.16 Simulated current responses of the IPMSM drive system when load is changed at $t = 1$ sec. from no load to rated load under rated command speed (188.6 rad/sec.) condition: (*a*) PI controller, (*b*) PID controller, and (*c*) adaptive NN controller..... 66

3.1 Typical torque-speed and power-speed characteristic curves of an IPM motor over a wide range of operating speed..... 74

3.2 Block diagram of the complete IPMSM drive system incorporating the flux weakening operation..... 75

3.3 Flow chart for the real time implementation of the proposed MTPA and FW control algorithms of the IPMSM drive system..... 76

3.4 Variation of the steady state developed torque with phase-*a* current of the IPMSM drive for the command speeds of 110 rad/sec. and 250 rad/sec. incorporating the $i_d^r = 0$ control technique and the flux weakening (FW) control techniques with $i_d^r \neq 0$..... 77

3.5 Simulated responses of the IPMSM drive system using the flux weakening control technique with $i_d^r \neq 0$ for step changes of command speeds (from 0 to 188.6 rad/sec. and from 188.6 rad/sec. to 300 rad/sec.) at no load condition: (*a*) speed, (*b*) *q*-axis command torque current (i_q^{r*}), and (*c*) *d*-axis command magnetizing current (i_d^{r*})..... 80

3.6 Experimental speed and *q*-axis command torque current responses of the IPMSM drive system for step changes of command speeds (from 130 rad/sec. to 150 rad/sec., from 150 rad/sec. to 188.6 rad/sec., from 188.6 rad/sec. to 175 rad/sec., from 175 rad/sec. to 188.6 rad/sec.) at rated load condition: (*a*) $i_d^r = 0$ control technique and (*b*) flux weakening control technique with $i_d^r \neq 0$. (Y1: 1 V/div., 1V = 20 rad/sec.; Y2: 1 V/div., 1V = 1.6 A; time: 2 sec./div.)..... 81

3.7 Experimental speed and *q*-axis command torque current responses of the IPMSM drive system for a step change in load at the rated speed of 188.6 rad/sec.: (*a*) $i_d^r = 0$ control technique and (*b*) flux weakening control technique with $i_d^r \neq 0$. (Y1: 1 V/div., 1V = 20 rad/sec.; Y2: 1 V/div., 1V = 1.6 A; time: 2 sec./div.)..... 82

3.8 Experimental starting responses of the IPMSM drive system using the flux weakening control technique with $i_d^r \neq 0$ for the command speed of 250 rad/sec. at rated load condition: (*a*) speed and (*b*) current (Y1: 2 V/div., 1V = 25 rad/sec.; Y2: 5 V/div., 1V = 0.933 A; time: 2 sec./div.)..... 83

4.1 The *Daubechies* ('*db*3') wavelet: (*a*) mother wavelet function and (*b*) scaling function 92

4.2 The *Spline* bi-orthogonal ('*bior*2.6') wavelet: (*a*) scaling function during the decomposition, (*b*) mother wavelet function during the decomposition, (*c*) scaling function during the reconstruction, and (*d*) mother wavelet function during the reconstruction..... 93

4.3 The non-orthogonal wavelet functions: (*a*) *Morlet* ('*morl*') wavelet function and (*b*) *Mexican Hat* ('*mexh*') wavelet function..... 95

4.4 Stretching ($a = 0.5$) and squeezing ($a = 2$) of the Mexican Hat wavelet function..... 97

4.5 Translation (b_1 via b_2 to b_3) of the Mexican Hat wavelet function 97

4.6 Two-level decomposition of a discrete signal of the discrete wavelet transform (DWT)..... 103

4.7 Two-level decomposition of a discrete signal of the wavelet packet transform (WPT)..... 103

4.8 The frequency responses of the *Daubechies* '*db*3' high pass filter: (*a*) amplitude response and (*b*) phase response..... 106

4.9 The frequency responses of the *Daubechies* '*db*3' low pass filter: (*a*) amplitude response and (*b*) phase response..... 107

4.10 Experimental data acquisition setup of the IPMSM drive system..... 108

4.11 Entropy values (*H*) of the speed error at different level of resolution of the discrete wavelet transform (DWT) for the command speed of 188.6 rad/sec..... 117

4.12 Entropy values (*H*) of the speed error at different level of resolution of the discrete wavelet transform (DWT) for the command speed of 50 rad/sec..... 117

4.13 Entropy values (*H*) of the speed error at different level of resolution of the discrete wavelet transform (DWT) for the command speed of 250 rad/sec..... 118

4.14 Comparison of PID control and multiresolution decomposition of error signal: (*a*) proportional error and (*b*) low frequency components of error..... 120
4.15 Comparison of PID control and multiresolution decomposition of error signal: (*a*) integral of error and (*b*) medium frequency components of error..... 120
4.16 Comparison of PID control and multiresolution decomposition of error signal: (*a*) derivative of error and (*b*) high frequency components of error..... 120
4.17 Specific schematic of the wavelet based MRPID controller for the IPMSM drive systems 121
5.1 Schematic of the new IPMSM control system using the proposed wavelet based MRPID controller..... 128
5.2 Simulated starting responses of the proposed MRPID controller based IPMSM drive system under no load and rated speed (188.6 rad/sec.) conditions: (*a*) speed, (*b*) phase current (i_a), (*c*) *q*-axis command current (i_q^*), and (*d*) *d*-axis command current (i_d^*)..... 133
5.3 Simulated starting responses of the proposed MRPID controller based IPMSM drive system under rated load and rated speed (188.6 rad/sec.) conditions: (*a*) speed, (*b*) phase current (i_a), (*c*) *q*-axis command current (i_q^*), and (*d*) *d*-axis command current (i_d^*)..... 134
5.4 Simulated starting responses of the proposed MRPID controller based IPMSM drive system under no load and low speed (50 rad/sec.) conditions: (*a*) speed, (*b*) phase current (i_a), (*c*) *q*-axis command current (i_q^*), and (*d*) *d*-axis command current (i_d^*)..... 135

5.5 Simulated starting responses of the proposed MRPID controller based IPMSM drive system under rated load and low speed (50 rad/sec.) conditions: (*a*) speed, (*b*) phase current (i_a), (*c*) *q*-axis command current (i_q^*), and (*d*) *d*-axis command current (i_d^*)..... 136

5.6 Simulated starting responses of the proposed MRPID controller based IPMSM drive system under no load and high speed (250 rad/sec.) conditions: (*a*) speed, (*b*) phase current (i_a), (*c*) *q*-axis command current (i_q^*), and (*d*) *d*-axis command current (i_d^*)..... 137

5.7 Simulated starting responses of the proposed MRPID controller based IPMSM drive system under rated load and high speed (250 rad/sec.) conditions: (*a*) speed, (*b*) phase current (i_a), (*c*) *q*-axis command current (i_q^*), and (*d*) *d*-axis command current (i_d^*)..... 138

5.8 Simulated responses of the proposed MRPID controller based IPMSM drive system for step increase (from 150 rad/sec. to 250 rad/sec.) and step decrease (from 250 rad/sec. to 188.6 rad/sec.) of command speeds under no load condition: (*a*) speed, (*b*) phase current (i_a), (*c*) *q*-axis command current (i_q^*), and (*d*) *d*-axis command current (i_d^*)..... 139

5.9 Simulated responses of the proposed MRPID controller based IPMSM drive system for step increase (from 150 rad/sec. to 250 rad/sec.) and step decrease (from 250 rad/sec. to 188.6 rad/sec.) of command speeds under rated load condition: (*a*) speed, (*b*) phase current (i_a), (*c*) *q*-axis command current (i_q^*), and (*d*) *d*-axis command current (i_d^*)..... 140

5.10 Simulated responses of the proposed MRPID controller based IPMSM drive system when load is changed at $t = 0.5$ second from no load to rated load under rated command speed (188.6 rad/sec.) condition: (a) speed, (b) phase current (i_a), (c) q-axis command current (i_q^*), and (d) d-axis command current (i_d^*)..... 141

5.11 Simulated starting responses of the proposed MRPID controller based IPMSM drive system for change in stator resistance ($R_1 = 2*R$) under rated load and rated command speed (188.6 rad/sec.) conditions: (a) speed, (b) phase current (i_a), (c) q-axis command current (i_q^*), and (d) d-axis command current (i_d^*)..... 142

5.12 Simulated starting responses of the proposed MRPID controller based IPMSM drive system for change in rotor inertia ($J_1 = 2*J$) under rated load and rated command speed (188.6 rad/sec.) conditions: (a) speed, (b) phase current (i_a), (c) q-axis command current (i_q^*), and (d) d-axis command current (i_d^*)..... 143

5.13 Simulated starting responses of the proposed MRPID controller based IPMSM drive system when L_q is reduced by 25% under rated load and rated command speed (188.6 rad/sec.) conditions: (a) speed, (b) phase current (i_a), (c) q-axis command current (i_q^*), and (d) d-axis command current (i_d^*)..... 144

5.14 Experimental starting responses of the proposed MRPID controller based IPMSM drive system under rated load and rated speed (188.6 rad/sec.) conditions: (a) speed response (Y1: 2 V/div., 1V = 20 rad/sec., time: 2 sec./div.) and (b) current response (Y2: 2 V/div., 1V = 0.933 A, time: 2 sec./div.)..... 145

5.15 Experimental starting responses of the proposed MRPID controller based IPMSM drive system under rated load and low speed (50 rad/sec.) conditions: (*a*) speed response (Y1: 1 V/div., 1V = 20 rad/sec., time: 2 sec./div.) and (*b*) current response (Y2: 2 V/div., 1V = 0.933 A, time: 2 sec./div.)..... 146

5.16 Experimental responses of the proposed MRPID controller based IPMSM drive system for step changes in command speeds (130 rad/sec. to 150 rad/sec., 150 rad/sec. to 188.6 rad/sec., 188.6 rad/sec. to 175 rad/sec., 175 rad/sec. to 188.6 rad/sec.) at rated load condition: (*a*) speed and *q*-axis command current responses (Y1: 1 V/div., 1V = 20 rad/sec., Y2: 1 V/div., 1V = 1.6 A, time: 2 sec./div.) and (*b*) phase current response (Y3: 2 V/div., 1V = 0.933 A, time: 2 sec./div.) 147

5.17 Experimental responses of the proposed MRPID controller based IPMSM drive system for a step change in load under command speed of 150 rad/sec.: (*a*) speed and *q*-axis command current responses (Y1: 2 V/div., 1V = 20 rad/sec., Y2: 1 V/div., 1V = 1.6 A, time: 2 sec./div.) and (*b*) phase current response (Y3: 2 V/div., 1V = 0.933 A, time: 2 sec./div.)..... 148

5.18 Experimental starting responses of the proposed MRPID controller based IPMSM drive system for change in inertia under rated load and rated speed (188.6 rad/sec.) conditions: (*a*) speed response (Y1: 2 V/div., 1V = 20 rad/sec., time: 2 sec./div.) and (*b*) current response (Y2: 5 V/div., 1V = 0.933 A, time: 2 sec./div.) 149

5.19 Experimental starting responses of the proposed MRPID controller based IPMSM drive system for change in resistance under rated load and rated speed (188.6 rad/sec.) conditions: (*a*) speed response (Y1: 2 V/div., 1V = 20 rad/sec., time: 2 sec./div.) and (*b*) current response (Y2: 2 V/div., 1V = 0.933 A, time: 2 sec./div.) 150

6.1 Proposed structure of a four-layer wavelet neural network of the self-tuning MRPID controller of the IPMSM drive system..... 154

6.2 Schematic of the IPMSM drive system incorporating the WNN based self-tuning MRPID controller..... 171

6.3 Flow chart for the on-line training of the WNN for the self-tuning of the proposed MRPID controller of the IPM motor drive system..... 173

6.4 Simulated starting responses of the proposed self-tuning MRPID controller based IPMSM drive system under no load and rated speed (188.6 rad/sec.) conditions: (*a*) speed, (*b*) phase current (i_a), (*c*) *q*-axis command current (i_q^*), and (*d*) *d*-axis command current (i_d^*)..... 179

6.5 Simulated starting responses of the proposed self-tuning MRPID controller based IPMSM drive system under rated load and rated speed (188.6 rad/sec.) conditions: (*a*) speed, (*b*) phase current (i_a), (*c*) *q*-axis command current (i_q^*), and (*d*) *d*-axis command current (i_d^*)..... 180

6.6 Simulated starting responses of the proposed self-tuning MRPID controller based IPMSM drive system under no load and low speed (50 rad/sec.) conditions: (*a*) speed, (*b*) phase current (i_a), (*c*) *q*-axis command current (i_q^*), and (*d*) *d*-axis command current (i_d^*)..... 181

6.7 Simulated starting responses of the proposed self-tuning MRPID controller based IPMSM drive system under rated load and low speed (50 rad/sec.) conditions: (*a*) speed, (*b*) phase current (i_a), (*c*) *q*-axis command current (i_q^*), and (*d*) *d*-axis command current (i_d^*)..... 182

6.8 Simulated starting responses of the proposed self-tuning MRPID controller based IPMSM drive system under no load and high speed (250 rad/sec.) conditions: (*a*) speed, (*b*) phase current (i_a), (*c*) *q*-axis command current (i_q^*), and (*d*) *d*-axis command current (i_d^*)..... 183

6.9 Simulated starting responses of the proposed self-tuning MRPID controller based IPMSM drive system under rated load and high speed (250 rad/sec.) conditions: (*a*) speed, (*b*) phase current (i_a), (*c*) *q*-axis command current (i_q^*), and (*d*) *d*-axis command current (i_d^*)..... 184

6.10 Simulated starting responses of the proposed self-tuning MRPID controller based IPMSM drive system for step increase in command speeds (from 188.6 rad/sec. to 350 rad/sec.) under no load condition: (*a*) speed, (*b*) phase current (i_a), (*c*) *q*-axis command current (i_q^*), and (*d*) *d*-axis command current (i_d^*)..... 185

6.11 Simulated starting responses of the proposed self-tuning MRPID controller based IPMSM drive system for step increase in command speeds (from 188.6 rad/sec. to 350 rad/sec.) under rated load condition: (*a*) speed, (*b*) phase current (i_a), (*c*) *q*-axis command current (i_q^*), and (*d*) *d*-axis command current (i_d^*)..... 186

6.12 Simulated responses of the proposed self-tuning MRPID controller based IPMSM drive system when load is changed at $t = 0.5$ second from no load to rated load under rated speed (188.6 rad/sec.) condition: (*a*) speed, (*b*) phase current (i_a), (*c*) *q*-axis command current (i_q^*), and (*d*) *d*-axis command current (i_d^*)..... 187

6.13 Simulated starting responses of the proposed self-tuning MRPID controller based IPMSM drive system for change in stator resistance ($R_l = 2*R$) under no load and rated speed (188.6 rad/sec.) conditions: (*a*) speed, (*b*) phase current (i_a), (*c*) *q*-axis command current (i_q^*),and (*d*) *d*-axis command current (i_d^*)..... 188

6.14 Simulated starting responses of the proposed self-tuning MRPID controller based IPMSM drive system for change in stator resistance ($R_l = 2*R$) under rated load and rated speed (188.6 rad/sec.) conditions: (*a*) speed, (*b*) phase current (i_a), (*c*) *q*-axis command current (i_q^*), and (*d*) *d*-axis command current (i_d^*)..... 189

6.15 Simulated starting responses of the proposed self-tuning MRPID controller based IPMSM drive system for change in rotor inertia ($J_1 = 2*J$) under no load and rated speed (188.6 rad/sec.) conditions: (a) speed, (b) phase current (i_a), (c) q-axis command current (i_q*), and (d) d-axis command current (i_d*)..... 190

6.16 Simulated starting responses of the proposed self-tuning MRPID controller based IPMSM drive system for change in rotor inertia ($J_1 = 2*J$) under rated load and rated speed (188.6 rad/sec.) conditions: (a) speed, (b) phase current (i_a), (c) q-axis command current (i_q*), and (d) d-axis command current (i_d*)..... 191

6.17 Simulated starting responses of the proposed self-tuning MRPID controller based IPMSM drive system when L_q is reduced by 25% under no load and rated speed (188.6 rad/sec.) conditions: (a) speed, (b) phase current (i_a), (c) q-axis command current (i_q*), and (d) d-axis command current (i_d*)..... 192

6.18 Simulated starting responses of the proposed self-tuning MRPID controller based IPMSM drive system when L_q is reduced by 25% under rated load and rated speed (188.6 rad/sec.) conditions: (a) speed, (b) phase current (i_a), (c) q-axis command current (i_q*), and (d) d-axis command current (i_d*)..... 193

7.1 Laboratory setup for the real time implementation of the IPMSM drive system 197

7.2 Hardware schematic for the real time implementation of the IPMSM drive system using the dSPACE ds1102 DSP controller board 199

7.3 Block diagram of the dSPACE ds1102 DSP controller board 200

7.4 Flow chart for the real time implementation of the proposed self-tuning MRPID controller based IPMSM drive system using the dSPACE ds1102 DSP controller board 203

7.5 Experimental starting responses of the fixed gain PI controller based IPMSM drive system under no load and rated speed (188.6 rad/sec.) conditions: (*a*) speed response (Y1: 2 V/div., 1V = 20 rad/sec., time: 2 sec./div.) and (*b*) current response (Y2: 5 V/div., 1V = 0.933 A, time: 2 sec./div.)..... 214

7.6 Experimental starting responses of the proposed self-tuning MRPID controller based IPMSM drive system under no load and rated speed (188.6 rad/sec.) conditions: (*a*) speed response (Y1: 2 V/div., 1V = 20 rad/s, time: 2 sec./div.) and (*b*) current response (Y2: 5 V/div., 1V = 0.933 A, time: 2 sec./div.)..... 215

7.7 Experimental starting responses of the fixed gain PI controller based IPMSM drive system under rated load and rated speed (188.6 rad/sec.) conditions: (*a*) speed response (Y1: 2 V/div., 1V = 20 rad/sec., time: 2 sec./div.) and (*b*) current response (Y2: 5 V/div., 1V = 0.933 A, time: 2 sec./div.)..... 216

7.8 Experimental starting responses of the proposed self-tuning MRPID controller based IPMSM drive system under rated load and rated speed (188.6 rad/sec.) conditions: (*a*) speed response (Y1: 2 V/div., 1V = 20 rad/sec., time: 2 sec./div.) and (*b*) current response (Y2: 5 V/div., 1V = 0.933 A, time: 2 sec./div.)..... 217

7.9 Experimental starting responses of the fixed gain PI controller based IPMSM drive system under no load and high speed (250 rad/sec.) conditions: (*a*) speed response (Y1: 2 V/div., 1V = 25 rad/sec., time: 2 sec./div.) and (*b*) current response (Y2: 5 V/div., 1V = 0.933 A, time: 2 sec./div.)..... 218

7.10 Experimental starting responses of the proposed self tuning MRPID controller based IPMSM drive system under no load and high speed (250 rad/sec.) conditions: (*a*) speed response (Y1: 2 V/div., 1V = 25 rad/sec., time: 2 sec./div.) and (*b*) current response (Y2: 5 V/div., 1V ≡ 0.933 A, time: 2 sec./div.)..... 219

7.11 Experimental starting responses of the fixed gain PI controller based IPMSM drive system under rated load and high speed (250 rad/sec.) conditions: (*a*) speed response (Y1: 2 V/div., 1V = 25 rad/sec., time: 2 sec./div.) and (*b*) current response (Y2: 5 V/div., 1V = 0.933 A, time: 2 sec./div.)..... 220

7.12 Experimental starting responses of the proposed self tuning MRPID controller based IPMSM drive system under rated load and high speed (250 rad/sec.) conditions: (*a*) speed response (Y1: 2 V/div., 1V = 25 rad/s, time: 2 sec./div.) and (*b*) current response (Y2: 5 V/div., 1V = 0.933 A, time: 2 sec./div.)..... 221

7.13 Experimental responses of the fixed-gain PI controller based IPMSM drive system for step changes in command speeds (from 130 rad/sec. to 150 rad/sec., from 150 rad/sec. to 188.6 rad/sec., from 188.6 rad/sec. to 175 rad/sec., from 175 rad/sec. to 188.6 rad/sec.) at no load condition: (*a*) speed and *q*-axis command current responses (Y1: 1 V/div., 1V = 20 rad/sec., Y2: 1 V/div., 1V = 1.6 A, time: 2 sec./div.) and (*b*) phase current response (Y3: 2 V/div., 1V = 0.933 A, time: 2 sec./div.)..... 222

7.14 Experimental responses of the proposed self-tuning MRPID controller based IPMSM drive system for step changes in command speeds (from 130 rad/sec. to 150 rad/sec., from 150 rad/sec. to 188.6 rad/sec., from 188.6 rad/sec. to 175 rad/sec., from 175 rad/sec. to 188.6 rad/sec.) at no load condition: (*a*) speed and *q*-axis command current responses (Y1: 1 V/div., 1V = 20 rad/s, Y2: 1 V/div., 1V = 1.6 A, time: 2 sec/div.) and (*b*) phase current response (Y3: 2 V/div., 1V = 0.933 A, time: 2 sec./div.)..... 223

7.15 Experimental responses of the fixed-gain PI controller based IPMSM drive system for step changes in command speeds (from 130 rad/sec. to 150 rad/sec., from 150 rad/sec. to 188.6 rad/sec., from 188.6 rad/sec. to 175 rad/sec., from 175 rad/sec. to 188.6 rad/sec.) at rated load condition: (*a*) speed and *q*-axis command current responses (Y1: 1 V/div., 1V = 20 rad/sec., Y2: 1 V/div., 1V = 1.6 A, time: 2 sec./div.) and (*b*) phase current response (Y3: 2 V/div., 1V = 0.933 A, time: 2 sec/div.)..... 224

7.16 Experimental responses of the proposed self-tuning MRPID controller based IPMSM drive system for step changes in command speeds (from 130 rad/sec. to 150 rad/sec., from 150 rad/sec. to 188.6 rad/sec., from 188.6 rad/sec. to 175 rad/sec., from 175 rad/sec. to 188.6 rad/sec.) at rated load condition: (*a*) speed and *q*-axis command current responses (Y1: 1 V/div., 1V = 20 rad/sec., Y2: 1 V/div., 1V = 1.6 A, time: 2 sec./div.) and (*b*) phase current response (Y3: 2 V/div., 1V = 0.933 A, time: 2 sec./div.)..... 225

7.17 Experimental responses of the fixed gain PI controller based IPMSM drive system for a change in load at rated speed (188.6 rad/sec.) condition: (*a*) speed and *q*-axis command current responses (Y1: 1 V/div., 1V = 20 rad/sec., Y2: 1 V/div., 1V = 1.6 A, time: 2 sec./div.) and (*b*) phase current response (Y3: 2 V/div., 1V = 0.933 A, time: 2 sec./div.)..... 226

7.18 Experimental responses of the proposed self-tuning MRPID controller based IPMSM drive system for a change in load at rated speed (188.6 rad/sec.) condition: (*a*) speed and *q*-axis command current responses (Y1: 1 V/div., 1V = 20 rad/sec., Y2: 1 V/div., 1V = 1.6 A, time: 2 sec./div.) and (*b*) phase current response (Y3: 2 V/div., 1V = 0.933 A, time: 2 sec./div.)..... 227

7.19 Experimental starting responses of the fixed gain PI controller based IPMSM drive system for change in rotor inertia under rated load and rated speed (188.6 rad/sec.) conditions: (*a*) speed response (Y1: 2 V/div., 1V = 20 rad/sec., time: 2 sec./div.) and (*b*) current response (Y2: 5 V/div., 1V = 0.933 A, time: 2 sec./div.)..... 228

7.20 Experimental starting responses of the proposed self-tuning MRPID controller based IPMSM drive system for change in rotor inertia under rated load and rated speed (188.6 rad/sec.) conditions: (*a*) speed response (Y1: 2 V/div., 1V = 20 rad/sec., time: 2 sec./div.) and (*b*) current response (Y2: 5 V/div., 1V = 0.933 A, time: 2 sec/div.)..... 229

7.21 Experimental starting responses of the fixed gain PI controller based IPMSM drive system for change in stator resistance under rated load and rated speed (188.6 rad/sec.) conditions: (*a*) speed response (Y1: 2 V/div., 1V = 20 rad/sec., time: 2 sec./div.) and (*b*) current response (Y2: 5 V/div., 1V = 0.933 A, time: 2 sec./div.)..... 230

7.22 Experimental starting responses of the proposed self-tuning MRPID controller based IPMSM drive system for change in stator resistance under rated load and rated speed (188.6 rad/sec.) conditions: (*a*) speed response (Y1: 2 V/div., 1V = 20 rad/sec., time: 2 sec./div.) and (*b*) current response (Y2: 5 V/div., 1V = 0.933 A, time: 2 sec./div.)..... 231

7.23 Harmonic spectra of the phase current response of the IPMSM drive system at the rated command speed and rated load conditions: (*a*) PI controller and (*b*) self-tuning MRPID controller..... 232

B.1 Basic circuit of a BJT inverter module..... 261

C.1 Pin diagram of the voltage level shifter chip SN7407N..... 263

C.2 Schematic of the isolated power supply for the optocoupler and the drive..... 264

C.3 Pin diagram of the optocoupler chip HP2531 and the driver chip IR213021..... 265

List of Tables

2.1 Logic operation of the voltage source inverter (VSI) under current control..... 54

4.1 The MDL Indices of Speed Error of the IPMSM Drive System for the Command Speed of 188.6 rad/sec. (60 Hz)..... 111

4.2 The MDL Indices of Speed Error of the IPMSM Drive System for the Command Speed of 50 rad/sec. (16 Hz)..... 112

4.3 The MDL Indices of Speed Error of the IPMSM Drive System for the Command Speed of 250 rad/sec. (80 Hz)..... 113

7.1 Starting Performance Comparisons of the IPMSM Drive System at the Rated Command Speed of 188.6 rad/sec..... 212

7.2 Starting Performance Comparisons of the IPMSM Drive System at the High Command Speed of 250 rad/sec..... 212

7.3 Performance Comparisons of the IPMSM Drive System for Step Change in Load at the Rated Command Speed of 188.6 rad/sec..... 213

7.4 Starting Performance Comparisons of the IPMSM Drive System for Change in Rotor Inertia at the Rated Command Speed of 188.6 rad/sec..... 213

List of Symbols

v_d^r, v_q^r	d^r-q^r axis voltages
i_d^r, i_q^r	d^r-q^r axis currents
$i_d^{r^*}, i_q^{r^*}$	d^r-q^r axis command currents
λ_d^r, λ_q^r	d^r-q^r axis flux linkages
L_d, L_q	d-q axis inductances
L_{md}, L_{mq}	d-q axis magnetizing inductances
L_l	Leakage inductance
v_o^r, i_o^r	Zero sequence voltage and current, respectively
i_a, i_b, i_c	Actual currents of phases a, b, and c, respectively
i_a^*, i_b^*, i_c^*	Command currents of phases a, b, and c, respectively
v_a, v_b, v_c	Actual voltages of phases a, b, and c, respectively
r_a, r_b, r_c	Stator resistances of phases a, b, and c, respectively
R	Stator resistance per phase
$\lambda_{af}, \lambda_{bf}, \lambda_{cf}$	Stator flux linkages of phases a, b, and c, respectively
$\lambda_a, \lambda_b, \lambda_c$	Air gap flux linkages of phases a, b, and c, respectively
λ_M	Permanent magnet flux linkage
L_{aa}, L_{bb}, L_{cc}	Self inductances of phases a, b, and c, respectively
M_{ab}, M_{bc}, M_{ca}	Mutual inductances between phases a and b, b and c, c and a
I_a	Armature current
I_m	Maximum amplitude of the stator current

V_a	Stator phase voltage
V_m	Maximum amplitude of the stator phase voltage
V_m'	Maximum amplitude of the stator phase voltage neglecting the stator resistance drop
I_f	Field current
ϕ_f	Field flux
$\overline{v}, \overline{i}$	Inverter voltage and current vectors, respectively
V_B	Inverter dc bus voltage
θ_r	Rotor position angle
ω_r	Rotor mechanical speed
ω_r^*	Command speed
$\Delta\omega_r$	Speed error
Δe	Change of speed error
p	Differential operator
P	Number of pole pair
T_e	Electromagnetic torque
T_e^*	Electromagnetic command torque
ΔT_e	Change in electromagnetic torque
T_L	Load torque
B_m	Damping coefficient
J_m	Rotor inertia
P_{mech}	Total mechanical power
K_t, K_1, K_2	Torque constants
A, B, C	Load torque constants
T_s	Sampling period

N_A, N_B, N_C	Logic variables for three-phase voltage source inverter
H	Band limit of the hysteresis current controller
$\psi(t)$	Wavelet function
$\hat{\psi}(t)$	Dual of wavelet function
$\psi^*(t)$	Complex conjugate of wavelet function
$\hat{\psi}(f)$	Fourier transform of the wavelet function
$\phi(t)$	Scaling function
$\hat{\phi}(t)$	Dual of scaling function
$\mathbb{N}$	Set of positive integers
m_v	Number of vanishing moments of a wavelet function
j	Number of levels of resolution
n	Discrete integer
N	Length of a signal
M	Total number of wavelet filters
$x[n]$	Discrete signal
$g[n]$	Discrete low pass filter
$h[n]$	Discrete high pass filter
$a^1[n]$	Approximations of a discrete signal at first level of resolution
$d^1[n]$	Details of a discrete signal at first level of resolution
$aa^2[n]$	Low frequency approximations of a discrete signal at second level of resolution
$da^2[n]$	High frequency approximations of a discrete signal at second level of resolution
$ad^2[n]$	Low frequency details of a discrete signal at second level of resolution

$dd^2[n]$	High frequency details of a discrete signal at second level of resolution
m_{ij}	Translation parameter for the input (i) at mother wavelet layer (j) of wavelet neural network
σ_{ij}	Dilation parameter for the input (i) at mother wavelet layer (j) of wavelet neural network
δ_o^4	Error propagation in the output layer (o) of wavelet neural network
δ_k^3	Error propagation in the wavelet layer (k) of wavelet neural network
δ_j^2	Error propagation in the mother wavelet layer (j) of wavelet neural network
R_u	Number of nodes in the wavelet layer (k) of wavelet neural network
w_{ko}^4	Connection weights between the output layer (o) and the wavelet layer (k) of wavelet neural network
w_{jk}^3	Connection weights between the wavelet layer (k) and the mother wavelet layer (j) of wavelet neural network
η_w	Learning rate for the output weights of wavelet neural network
η_m, η_σ	Learning rates for the translation and dilation parameters of wavelet neural network
u_{pid}	PID control signal
u_{mrpid}	MRPID control signal
k_p, k_i, k_d	Gains for proportional, integral, and derivative of speed error
$k_{a^2}, k_{d^2}, k_{d^1}$	Gains for low, medium, and high frequency components of speed error
k_ω	Stator winding factor
$H(x)$	Entropy of a signal $x(t)$

List of Acronyms

ADALINE	Adaptive linear neuron
A/D	Analog to digital
ac	alternating current
BLDC	Brushless dc
BJT	Bipolar junction transistor
CSI	Current source inverter
CWT	Continuous wavelet transform
DSP	Digital signal processor
DSPM	Doubly salient permanent magnet motor
DTC	Direct torque control
DRFWN	Dynamic recurrent fuzzy wavelet network
DWT	Discrete wavelet transform
D/A	Digital to analog
dc	direct current
EMF	Electromotive force
FEA	Finite element analysis
FBFN	Fuzzy basis function network
FW	Flux weakening
FPGA	Field programmable gate array
FLC	Fuzzy logic controller
FFT	Fast Fourier transform
GE	General Electric
GA	Genetic algorithm
GFLC	Genetic fuzzy logic controller

HPD	High performance drive
IM	Induction motor
IPM	Interior permanent magnet
IPMSM	Interior permanent magnet synchronous motor
ILC	Iterative learning control
IP	Intellectual property
IC	Integrated circuit
ISR	Interrupted service routine
I/O	Input/output
LPMSM	Linear permanent magnet synchronous motor
LQM	Linear quadratic method
MRA	Multiresolution analysis
MRPID	Multiresolution proportional integral derivative
MRAC	Model reference adaptive controller
MRAS	Model reference adaptive system
MDL	Minimum description length
MTPA	Maximum torque per ampere
MMF	Magneto motive force
NN	Neural network
NNC	Neural network controller
NFC	Neuro fuzzy controller
Nd-Fe-B	Neodymium iron boron
PM	Permanent magnets
PMSM	Permanent magnet synchronous motor
PWM	Pulse width modulation
PI	Proportional integral
PID	Proportional integral derivative
PD	Proportional derivative
PDF	Pseudo derivative feedback

QMF	Quadrature mirror filter
SCFNN	Self-constructing fuzzy neural network
STFT	Short time Fourier transform
SRM	Switched reluctance motor
STR	Self-tuning regulator
SPICE	Simulation program with integrated circuit emphasis
VSC	Variable structure controller
VLSI	Very large scale integrated
VSI	Voltage source inverter
WT	Wavelet transform
WC	Wavelet controller
WPT	Wavelet packet transform
WPD	Wavelet packet decomposition
WFC	Wavelet fuzzy controller
WNN	Wavelet neural network

Chapter 1

Introduction

1.1 Electric Motor Drives

Electric motors are electromagnetic energy conversion devices that translate an input electrical energy into an output mechanical motion. Electric motors have been playing important roles in the developments of modern technology for over a century. Better understanding of energy conversion principles coupled with evolution of new and improved materials has contributed to the developments of motor designs to meet increasing industrial demands. The applications of electric motors are increasing rapidly with increased technological advancements. The advents of modern digital computers and recent developments in power electronics and semiconductor devices have made revolutionary contributions on the design and control of electric motors. The direct current (dc), induction, and synchronous motors are the three basic electric motors that serve industrial and household needs. Recently, the theory of finite element analysis has helped in further developments and design optimization of electric motors. As a result, new electric motor designs such as brushless dc (BLDC) motor, switched reluctance motor, permanent magnet hysteresis motor, and permanent magnet synchronous motor have been successfully developed and implemented for household and industry applications [1]–[3].

The dc motors have been dominating the field of adjustable speed drives until the 1980s. The torque in a dc motor is developed by following the right hand screw BLI rule [1]. The orthogonal disposition of magnetic field (B) and armature magnetomotive force (LI) provides the rotation of dc motors. This type of electric machine has been traditionally favored in motion control and industrial drive applications. However, certain limitations are associated with dc motors such as narrow range of speed operations, lack of robustness, wear of brush gears, and low load capability. In addition, the commutators and brushes of the dc motor need periodic maintenance that makes the motor less reliable and unsuitable to operate in harsh environments. These shortcomings have encouraged researchers to find alternatives to the dc motors for high performance variable speed operations where high reliability and minimum maintenance are the prime requirements [4]–[5]. For these reasons, considerable attentions have been focused on the developments of ac motors. The ac motors such as the induction and synchronous motors have been favored for constant speed applications. However, recent developments of power electronics, very large scale integrated (VLSI) circuits, digital signal processor (DSP) boards, and microcomputer based controllers have expanded the use of ac motors in the modern variable speed drive systems. In addition, the vector control technique offers an excellent opportunity of using ac motors for variable speed high performance drive (HPD) systems [6].

Among the ac motors used for variable speed drives, the induction motor, particularly the squirrel cage type, has been the workhorse in industry because of its ruggedness, reliability, good efficiency, and low cost. The squirrel cage induction motors are cheap and available widely over the world in mass scale production. However, there are several limitations of induction motors, which discourage their use in high performance drive applications. An induction motor always operates at a lagging power factor because of the fact that the rotor field is singly excited from the stator side. Thus it operates with only slip speed. The cost and complexity of the control equipments for the induction motor drives are generally high. The performance of the induction motor drive system is not as efficient as expected due to the slip power loss. The inverter fed

induction motors are also subjected to non-sinusoidal voltage and current waveforms resulting in two major detrimental effects: additional power losses and torque pulsations. The dynamic control of an induction motor drive system and its real-time implementation depends on the sophisticated modeling of motor and the estimation of motor parameters in addition to complicated control circuitry [7]. The wound rotor type induction motors are used in large power industrial and utility motor applications.

The well known doubly fed wire-wound synchronous motors operate at constant speed irrespective of loads. The rotor field excitation of wire-wound synchronous motors is supplied through slip rings and brushes from dc sources including the static power semiconductors based dc exciter. Modern synchronous motors are brushless type with an ac exciter and imbedded rotating diode bridge rectifiers. Since synchronous motors always run at synchronous speed, the control of these motors is rather simple. The unity power factor mode operation of the motor renders small copper loss in the stator and permits reduction of inverter size with simple commutation and control circuits. However, the requirements of extra power supply, slip rings, and brushes discourage their applications for the high performance electric motor drive systems.

Recently special motors have been developed in order to overcome the limitations of the conventional ac induction and wire-wound synchronous motors. These motors can be categorized as the permanent magnet motor, stepping motor, switched reluctance motor, synchronous reluctance motor, hysteresis motor, hysteresis reluctance motor, hysteresis permanent magnet motor, and hybrid hysteresis reluctance permanent magnet motor. Among these motors, the permanent magnet (PM) motors are getting rapid industrial acceptance in the highly competitive motor application markets worldwide because of their advantageous features such as high torque to current ratio, high power to weight ratio, high efficiency, high power factor, low noise, and robustness. Unlike in the wire-wound synchronous motors, the rotor excitation of the PM motors is provided by permanent magnets. Thus, the PM motors do not need extra power supply or field windings in order to provide rotor excitation. So, the power losses related to the field windings are eliminated in the PM motors.

The first PM excitation system has been implemented for electric motors as early as the nineteenth century. However, the use of poor quality hard magnetic materials including the tungsten steel as the PM excitation systems soon have discouraged their use in favor of the dc electromagnetic excitation systems. The invention of aluminum-nickel-cobalt (Alnico) in 1932 revived PM excitation systems, and its application was limited to small and fractional horsepower dc commutator motors. Currently most of the PM dc commutator motors with slotted rotors use ferrite magnets. The rare earth PM have successfully replaced ferrite and Alnico magnets because of high power to mass ratio, better dynamic performance and high efficiency [8].

The PM motors are basically three types. These are PM dc commutator motors, PM brushless dc motors, and PM ac synchronous motors. The PM dc commutator motor is sometimes called PM dc motor. It is the separately excited dc motor where the conventional dc field winding is replaced by constant PM excitation. The PM brushless dc motor is commercially known as brushless dc motor. It is a three-phase electronically commutated sequentially excited PM synchronous motor. Its basic principle of operation is similar to PM switched reluctance motor. The PM brushless dc motor is fed with three-phase rectangular voltage waveforms, which are shifted by 120° electrical from each other. These waveforms are kept constant for 120° conduction angle of inverter switch in order to generate ripple free torque. The armature current and induced electromotive force (emf) are usually trapezoidal for the case of PM brushless dc motor. The PM brushless dc motor conducts armature current in two phases at a time. In the closed loop controlled PM brushless dc motor drive system, the discrete feedback of rotor position is used at every sixty degree mechanical angle of rotor position [8]. The PM ac synchronous motors, which are also known as PM synchronous motors (PMSM), are fed with sinusoidal voltage waveforms shifted by 120° electrical from each other. In the PMSM, the armature current and induced emf are ideally sinusoidal. The PMSM drive system uses continuous feedback of rotor position in order to determine the command torque current and the command flux current for the drive system. The PMSM provides less I^2R losses and therefore, the power density is increased as compared to conventional dc

motor, induction motor, and wire wound excited synchronous motor. Considerable improvements in the dynamics of the PM synchronous motors can be achieved because of high air gap magnetic flux density, low rotor inertia, and decoupling control characteristics of speed and flux. The first two types of PM motors are not covered in this thesis. The PM synchronous motor is further covered in the following subsection.

1.1.1 Permanent magnet synchronous motors

The basic classification of the PM synchronous motors is shown in Fig. 1.1. Broadly, the PM synchronous motors can be classified into stator line-fed and stator inverter-fed types. The stator line-fed PM synchronous motors with rotor conduction cage use the cage winding to provide the starting torque of the motor at line voltage and frequency. The stator inverter-fed PM synchronous motors with rotor conduction cage are similar in construction of the stator line-fed PM synchronous motors. The stator inverter-fed PM synchronous motors with rotor conduction cage can be operated in both open loop and closed loop conditions at variable voltage and/or variable frequency. The stator inverter-fed PM synchronous motors without rotor cage use the feedback of rotor position to start smoothly from standstill up to the steady state command speed. The rotor position can be sensed using an absolute encoder or an incremental encoder, or can be estimated using the position sensorless approaches. The PM synchronous motors have been implemented in a variety of application fields, which include automotive, air conditioner, aerospace, machine tools, servo drive, ship propulsion drive, etc. Recently, the PM synchronous motors of higher than 1 MW have been successfully designed. The PM synchronous motors of 3.7–5.5 kW ratings have been the industrial standard of Japanese air conditioner manufacturers such as Mitsubishi, Daiken, Toshiba, and Carrier [9]–[11].

Based on the use of rotor position sensor, the PMSM drives can be classified into two categories: (i) with sensor PMSM drives and (ii) sensorless PMSM drives. In the sensorless drive, the rotor position is estimated from motor currents, voltages, and motor parameters using an observer or using a computational technique. The implementation of the sensorless scheme for the PMSM drives can be difficult as it requires sophisticated

algorithms to estimate the rotor position. The estimated rotor position may not be accurate because of the variations of the parameter for different operating conditions of the PM synchronous motor.

Based on the orientation of magnets in the rotor, the PM synchronous motors can be broadly classified into three categories: (i) interior type, where the permanent magnets are buried within the rotor core, (ii) surface mounted type, where the permanent magnets are mounted on the surface of the rotor, and (iii) inset type, where the permanent magnets are fully or partially inset into the rotor core. The cross sections of the interior, surface mounted, and inset type PM synchronous motors are shown in Figs. 1.2, 1.3, and 1.4, respectively. The PM synchronous motors can be classified into three types based on the direction of magnetic field of the permanent magnets. These include radial type, circumferential type, and axial type.

The direction of magnetic field of the interior type PM synchronous motors and the inset type PM synchronous motors can be either radial or circumferential. The direction of magnetic field is radial for the case of surface mounted type PM synchronous motors [3]. The directions of magnetic field of the PM synchronous motors of Figs. 1.2–1.4 are radial. The majority of commercially available PM synchronous motors are constructed with permanent magnets buried inside the iron rotor core. These types of motors are known as the interior permanent magnet (IPM) synchronous motors. The geometry of IPM produces several significant effects on the operating characteristics of the motor. Burying the magnets inside the rotor of the IPM motor provides a mechanically robust rotor since the magnets are physically contained and protected. On the other hand, the magnets of the surface mounted type PM synchronous motors are held protected against centrifugal forces by means of adhesive or high strength bands during the high speed operation. Therefore, the rotor of the surface mounted type PMSM is less robust than the interior type PMSM for high speed applications. The IPM synchronous motor with radial magnetization is the most economical to manufacture. Moreover, as the permanent magnets are buried within the rotor core of the IPM motor, so it provides smooth rotor surface and reduced air gap. The IPM synchronous motor also shows higher

efficiency than the induction motor of simillar rating [12]. As a result, improved dynamic and steady state performances can be achieved with this type of PM synchronous motor. In order to utilize such advantages, the interior permanent magnet synchronous motor (IPMSM) is considered as the working model of the research in this thesis.

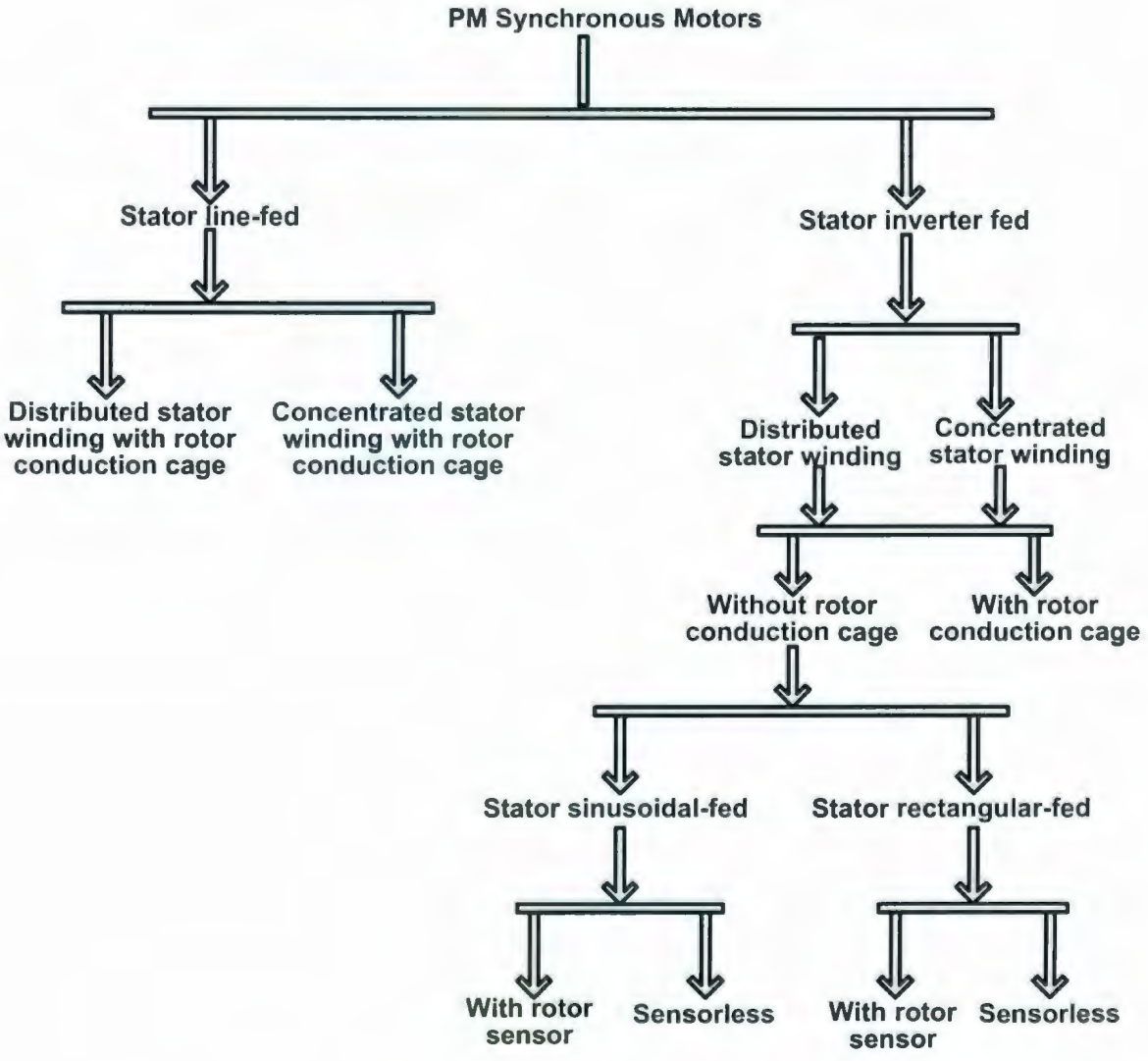

Figure 1.1: Classification of the PM synchronous motors.

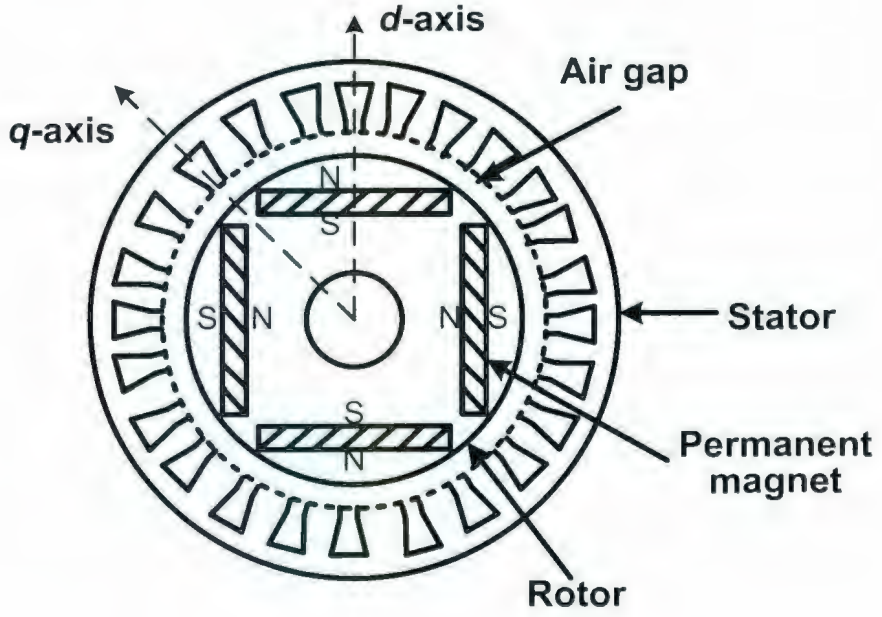

Figure 1.2: Cross section of the interior type PM synchronous motor.

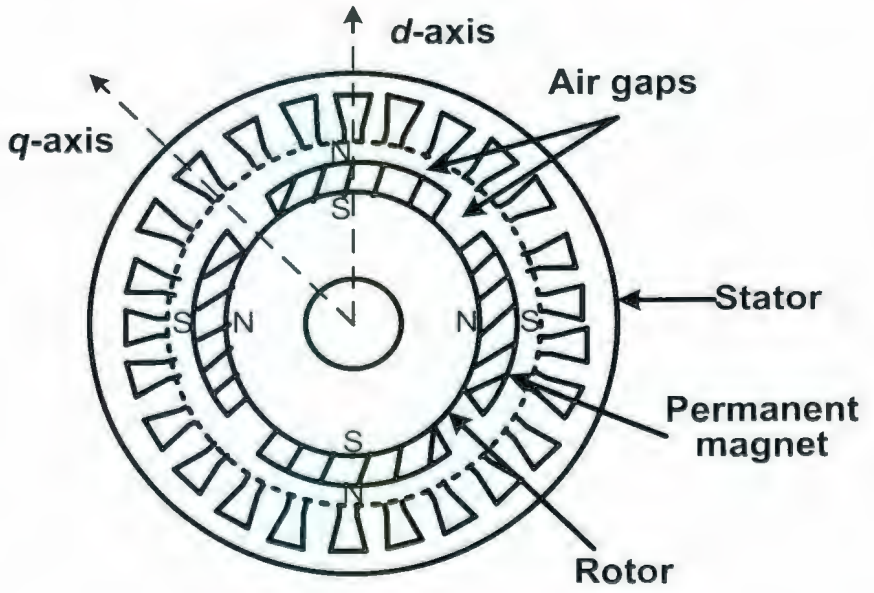

Figure 1.3: Cross section of the surface mounted type PM synchronous motor.

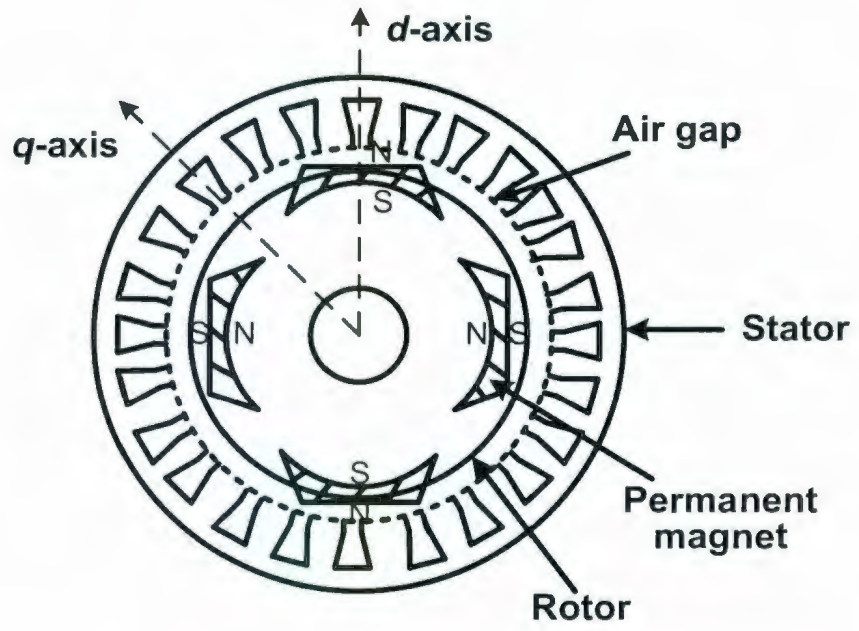

Figure 1.4: Cross section of the inset type PM synchronous motor.

In the following section, a brief review of the current state of high performance PMSM drives using the conventional, adaptive, and intelligent controllers for applications such as in automotive, aerospace, air conditioner, heating and ventilation, household, etc, is provided.

1.2 Literature Review of the PMSM Drives

Advances in electronics and PM quality have boosted the use of PM synchronous motors including the interior permanent magnet synchronous motor (IPMSM) in electric motor drives. Therefore, it is essential to develop a robust controller for the IPMSM to be used in the high performance drive (HPD) system in order to overcome various system uncertainties such as parameter variations, load disturbances, and sudden changes of command speeds. The speed controllers for electric motor drives can be broadly classified into three categories: (i) fixed gain types, (ii) adaptive types, and (iii) artificial intelligent types. The fixed gain speed controllers include the proportional integral (PI), proportional derivative (PD), proportional integral derivative (PID), and pseudo

derivative feedback (PDF) controllers. The adaptive types are the model reference adaptive controller (MRAC), variable structure controller (VSC), self-tuning regulator (STR), and sliding mode controller (SMC). The artificial intelligent controllers include the fuzzy logic controller (FLC), neural network controller (NNC), neuro fuzzy controller (NFC), wavelet controller (WC), and wavelet fuzzy controller (WFC).

The vector control technique is widely used in industry for high performance control of the PMSM drives. The indirect vector control technique is simply stated as the vector control technique. In ac motor, the stator currents i_a, i_b, and i_c are resolved into two current components: direct axis current (i_d) component and quadrature axis current (i_q) component. In the vector control technique, the motor variables are transformed into an orthogonal set of *d-q* axis variables such that flux and torque can be controlled separately. The phases of stator current are positioned orthogonal to the magnet flux with the help of a position sensor or using any sensorless algorithm. This technique allows the PMSM to achieve superior dynamic performance capabilities similar to the separately excited dc machine, while retaining the general advantages of the ac motors over dc motors. Figure 1.5 shows a typical closed loop vector control scheme of the PMSM drive. Researchers have continued their efforts on the development and implementation of the highly efficient PMSM drives. Major points of the earlier works on the modeling, control, and performance analysis of the vector controlled PMSM drives are briefly summarized below.

Researchers [13]–[22] have studied the performances of the voltage source inverter (VSI) or current source inverter (CSI) fed PMSM drives using the vector control technique. Himei *et al.* [13] have developed an analytical program to analyze the steady state behavior of a VSI fed PMSM drive using a controlled half bridge converter and an *LC* filter. The influence of harmonics of the inverter voltage on the performance of the motor drive system has been investigated using the analytical program.

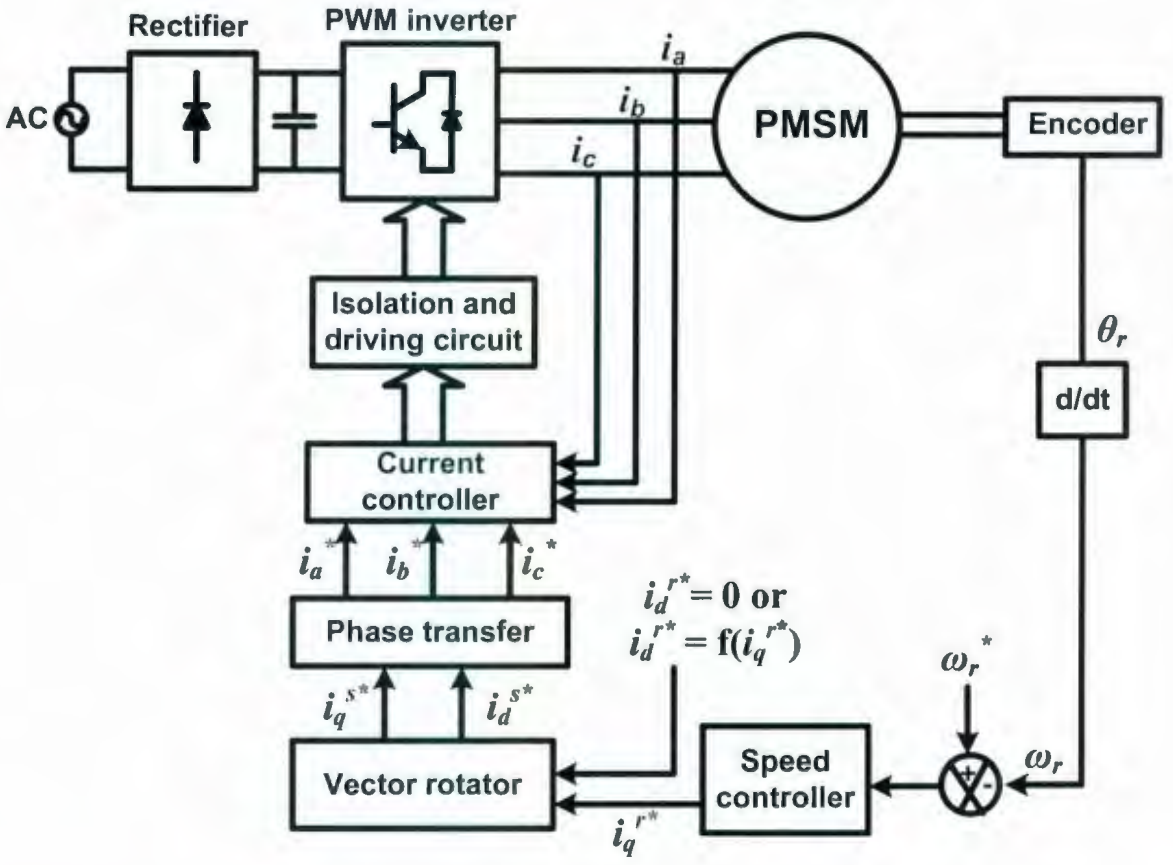

Figure 1.5: Schematic of the vector control scheme of the permanent magnet synchronous motor (PMSM) drive.

Dhaouadi *et al.* [14] have investigated different current controllers including the ramp, hysteresis, and space vector controllers for the VSI fed PMSM drive. They have used the vector control strategy where the rotor position is sensed using the position sensor. They have implemented the flux-weakening control algorithm for wide speed operation of the PMSM considering the effects of current saturation. However, the performances of the current controllers have not been investigated in detail over wide speed ranges of the PMSM. Uddin *et al.* [15] have presented a comparative analysis of various current controllers for the VSI fed IPMSM drive. The fixed, sinusoidal, and mixed-band hysteresis current controllers as well as the conventional and improved ramp

comparator controllers have been investigated for the drive system. It has been recommended that the hybrid controller, which includes the hysteresis controller for high speed operation and the ramp comparator controller for low speed operation, can be used for better performances. However, the performances of the drive system have not been predicted over the rated speed operation of the IPM synchronous motor.

Gumaste and Slemon [16] have investigated the steady state performances of the VSI fed PMSM drive system in constant torque and constant power modes of operation. The steady state performances of the CSI fed PMSM drive system have been presented in reference [17]. Optimal control strategies for two regions of the torque-speed profile of the PMSM drive have been presented. However, the dynamic stability of the drive system, which is quite important apart from the steady state performances, has not been investigated. Mohanty *et al.* [18] have investigated the root locus based dynamic stability of the CSI fed PMSM drive system. The subtransient reactances equation models of a salient pole synchronous motor in the *d-q* axis reference frame have been used in the analysis. The influences of machine and converter parameters on the dynamic stability of the drive system have been presented. Nedic *et al.* [19] have implemented a current source inverter with sinusoidal input current for the PMSM drive system. The proposed drive system used a three-phase PWM buck rectifier, a dc link inductor, and a load commutated thyristor inverter. However, the current source inverter fed PMSM drive system showed low power factor because of the large firing angle of the thyristor switches of the inverter.

For the majority of industrial applications, the conventional VSI fed PMSM drive facilitates the most economical system. However, smoothing of the DC link voltage of the VSI fed drive system requires large electrolytic capacitors. It has been shown in [20] that these capacitors can survive in underwater environments when enclosed in large air-filled chambers at atmospheric pressure. Snary *et al.* [20] have used an observer based state estimation technique for the sensorless control of the PM synchronous motors using the matrix converter. Experimental results of a matrix converter fed 1 hp PMSM drive for a subsea actuator pump have been presented. However, matrix converters require more

voltage sensors than those required for the voltage source inverter. The performances of a six-phase current-controlled VSI fed two-motor drive system are presented in [21]. The work analyzed series connected two-motor drive system, which includes a six-phase symmetrical induction motor and a three-phase PMSM. However, the PMSM drive system showed speed and current ripples because of the interaction of spatial harmonics of the induction motor with the torque and flux producing current components of the PMSM. Liu *et al.* [22] have investigated a microprocessor based speed controller for the VSI fed PM brushless dc motor drive system. The controller has been implemented in the high performance 16-bit microprocessor. The performances of the proposed controllers have been investigated through computer simulation and experiments.

Pillay *et al.* [23] have presented a modeling approach for a vector controlled PMSM drive system. The proposed model includes the nonlinear *d-q* model of the motor, the state space model of the speed controller, and the real time model of the inverter switches. The comparative performance of the PWM and the hysteresis current controlled based PMSM drives have been presented. The performances of the drive system have not been predicted over the wide speed ranges of the PM synchronous motors. In addition, the linear model of the PMSM is used for the development of the speed controller. Fardoun *et al.* [24] have presented a simulation program with integrated circuit emphasis (SPICE) model for an electronically commutated PM brushless dc motor drive system. The model estimates the drive components, which include inductances, resistances, and induced voltages of the motor. Slemon and Liu [25] have presented various models of the PMSM for the approximate analysis of winding losses, torque and power factor, and the thermal and electric properties of the permanent magnets. These models have been used in an optimization program, which uses sequential unconstrained minimization techniques in order to produce optimal designs for wide variety of PMSM applications. However, these models may need to be modified in order to meet the design requirements.

Kang *et al.* [26] have proposed an IPM motor model based on the finite element analysis (FEA). This method estimated the *d-q* axis inductances of the IPM motor for variations of current magnitude and phase angles with different loading conditions. The magnetic saturation in the field-weakening region has been considered. It has been reported that the *d-q* axis inductances of the IPMSM vary nonlinearly with current magnitude and phase angle. However, the speed and current responses of the drive system using the model have not been investigated at various operating conditions. Mohammed *et al.* [27] have developed a high frequency model of the PMSM drive using the measurements and the FEA. The high frequency models for the inverter and cable have been developed using the measurements while the high frequency model for the PMSM has been developed using the FEA. The models have been used to study over voltage and electromagnetic interference of the drive system. However, the effects of parameter variations due to noise and temperature changes on the drive performance have not been investigated. Roshen [28] has developed a model for the prediction of iron losses in the surface mounted type PMSM. The model estimated the eddy current loss component using the FEM analysis. It considered losses for both normal and circumferential components of flux density in the stator yoke. However, the tooth flux density has not been considered in the proposed model.

Consoli and Abela [29] have analyzed the transient performances of the VSI fed IPMSM using the modified *d-q* axis model of the motor. The proposed model has been derived from the conventional *d-q* axis model by modifying the flux equations to consider the effects of armature reaction and saturation on the air gap flux distribution of the motor. The magnetic flux has been modeled as the function of *d-q* axis currents. The performances of the drive system have been studied during the synchronization process only. Nakamura *et al.* [30] have presented a magnetic equivalent circuit model of the IPMSM for use in the SPICE software package. The model considered the reluctances and magneto motive forces (MMFs) due to permanent magnets. The magnetic model of the motor and the driving circuit have been coupled in the SPICE simulation. The dynamic performances of the IPMSM drive including the starting performances have

been investigated. However, the performances of the model have not been investigated for parameter variations or extreme load excursions.

Many researchers have reported their works on the development and implementation of high performance controllers for the IPMSM drive systems. The majority of reported works, which use the intelligent controllers for IPMSM drive systems are briefly discussed below [31]–[89].

1.2.1 PMSM drives using conventional and adaptive controllers

The conventional proportional integral (PI) and proportional integral derivative (PID) controllers based control techniques have been in existence for many years. These controllers are still widely used due to their simple control structure, ease of design, and low cost. In addition to their effectiveness as control means, the reasons for their longevity are due to the fact that these are easy to implement and easy to tune. The conventional PI and PID controllers have been used in the PMSM drive systems [31]–[45].

Liu and Cheng [31] have investigated the performances of the PI, H^2, and H^∞ controllers for the position sensorless control of the PMSM drive system. The H^2 controller is the equivalent frequency domain optimal solution for the standard linear quadratic Gaussian (LQG) problem. The H^∞ controller, which is the solution of an optimization problem, minimizes the H^∞ norm of a closed loop transfer function. The H^∞ norm of a transfer function equals the distance from the origin to the farthest point on the Nyquist plot of that particular transfer function. In reference [31], the H^2, and H^∞ controllers have been implemented using the multi-processor digital control system for the PMSM drive system. The frequency domain controllers outperformed the conventional PI controller for different command speeds and change in load. However, the H^2 controller based drive system showed steady state speed error. In addition, separate microprocessors have been used in order to implement the speed and vector control algorithms of the PMSM drive system. Birou *et al.* [32] have investigated the

performances of the PI, H^2, and H^∞ controllers based PMSM servo drive system using the MATLAB software package for change in load, moment of inertia, and friction. However, the performance of the drive system has been investigated in simulation only for a certain command speed. In addition, the controllers have been designed using the simplified model of the PMSM. As a result, the performances of the drive may not be accurate in real time using these linear controllers. Cheng *et al.* [33] have developed and implemented a discrete variable PI controller for the doubly salient permanent magnet (DSPM) motor drive. The drive system has been implemented and tested in the 16-bit microcomputer. The proposed DSPM motor drive system showed good performances below the rated command speed of the drive system. However, the performances of the drive system have not been predicted at high speeds in the flux-weakening region of operation. Cheng and Sun [34] have implemented the genetic algorithm in order to optimize the gains of the variable PI controller for the DSPM motor drive system. The drive system using the variable PI controller showed better dynamic performances than with the fixed gain PI controller. However, the effects of magnetic saturation and parameter variations on the performances of the drive system have not been considered in the work.

Haylock *et al.* [35] have investigated the performances of various current controllers for the PMSM drive at high speeds. The current controllers based on flux linkage model have been compared with the PI controller. The model based controllers showed better control performances than with the PI based controller. The model based current controllers showed stead state errors because the proposed controller did not consider voltage drops in phase winding and power converters. Xu *et al.* [36] have implemented a modular control strategy based on the iterative learning control (ILC) for the surface mounted PMSM drive system. The proposed ILC module generated the reference current for the PMSM drive system. It recorded the cyclic torque and reference current over one cycle, and then used these signals to update the reference current for the next cycle. The modular control approach accurately followed the command torque and

minimized the torque pulsations. However, the computational complexity of the proposed control technique limit its appeal for the high performance PMSM drive systems.

Panda *et al.* [37] have proposed a self-tuning scheme for the fixed gain PI controller of the PMSM drive system. In the tuning scheme, the proportional and integral gains have been varied within a predetermined range. The performances of the tuning scheme have been studied in the MATLAB software package. However, the determination of ranges for proportional and integral gains may be varied for various operating conditions of the drive system. Lourde *et al.* [38] have implemented optimal control theories for the on-line tuning of the fixed gain PI controller of the PMSM drive system. The eigenvalue assignment technique has been used in the design of optimal control laws for the multi input multi output vector controlled PMSM servo drive. The performances of the optimal controller have been evaluated for different command speeds, changes in motor parameters, and load torques. However, the model suffers from high computational burden for the real-time implementation.

Seok *et al.* [39] have presented a sensorless control strategy for the PMSM drive system. This approach is based on the PI regulation of output voltage of the *d*-axis current regulator. The proposed technique considers the effect of permanent magnet flux linkage. Experimental results have been presented to demonstrate the effectiveness of the proposed technique. However, comprehensive tests of the drive have not been conducted for different dynamic operating conditions. In addition, the responses of the drive showed significant steady state speed ripples for changes in load torque at low speed. Hemici *et al.* [40] have developed a PID based back stepping control technique for the PMSM drive system. The technique included both the nonlinear PID regulator and the back stepping control technique. A comparative study between the proposed technique and the feedback linearizing control has been made in both simulation and experiments. However, the performances of the drive system have not been investigated for different dynamic conditions including the effects of magnetic saturation and parameter variations.

Dan and Jun [41] have presented an adaptive single neuron based self-tuning PID speed controller for the four-switch three-phase fault tolerant PMSM drive system. The

supervisory Delta learning rule has been used with non-supervisory Hebbian learning rule to optimize the controller parameters online. The PID controller based PMSM drive system has been modeled and studied in the MATLAB software package. However, the performances of the drive have not been investigated in real time. Garcia *et al.* [42] have developed an iterative method based on the infinity-norm of sensitivity functions for the tuning of the PID controller of a double-axis linear permanent magnet synchronous motor (LPMSM) drive system. However, the performance of the drive system can be unsatisfactory at low and high frequencies because of the measurement noise and logarithmical representation of the sensitivity functions.

Tursini *et al.* [43] have developed a real time tuning strategy for the PI speed controller of the PMSM drive system. The technique has been developed from the analysis of step response of the PMSM drive system. The performances of the drive system have been investigated in real time. However, the performances of the technique have not been investigated for nonlinearities including the saturation of the controllers at high speeds. Xiao *et al.* [44] have presented a self-tuning PID controller based on the minimum variance method for the speed control of a surface mounted PMSM drive system. The stability of the drive system has been ensured using the pole assignment based stability algorithm. This technique used the discrete time dynamic model of the q-axis current control loop of the PMSM drive system. The complete vector control scheme including the self-tuning PID controller has been implemented in real time using the digital signal processor (DSP) board TMS320F2812. However, the performance of the drive has been investigated only for a fixed speed. In addition, the performances of the drive system have not been evaluated during the transition from the constant torque to constant power mode of operation.

Vaez-Zadeh *et al.* [45] have presented an adaptive loss minimization controller for the IPMSM drive system. The controller minimized the total input power of the drive system by continuous adjustment of the d-axis current component. The controller improved the overall efficiency of the drive system because of the minimum input power and the short search time required to find this minimum. However, the controller tracked

the change in input power continuously. Thus, more memory is needed for the on-line implementation of the controller. In addition, the PI controller has been used in the speed regulation of the drive system. Hence, parameter variations or extreme load excursions may influence the stability of the drive system.

The PI and PID controllers have been used as both speed and current regulators for the PMSM drives for many years due to their simplicity, ease of design, and inexpensive cost. However, these controllers are very sensitive to sudden changes of command speeds, parameter variations due to saturation and temperature, load disturbances, and other uncertainties. Hence, it is difficult to tune the parameters of these controllers for both off-line and on-line implementations. The performances of these controllers vary with operating conditions. As a result, the performances of the closed-loop controlled IPMSM drive using these controllers may deteriorate significantly. These conventional controllers, which are usually designed in the linear region ignoring saturation, can no longer satisfy the stringent requirements of the high performance drive applications. Therefore, there have been recent interests in applying modern control schemes including the adaptive control techniques for the PMSM drive systems. The availability of powerful and relatively inexpensive digital signal processor (DSP) board has inspired researchers to implement the adaptive controllers for the PMSM drives.

In recent years, researchers have focused their attention on the application of adaptive controllers [46]–[56] for the PMSM drive systems. Cerruto *et al.* [46] have developed adaptive speed and position regulators for the IPMSM drives in robotics. The proposed adaptive control scheme, which is based on the model reference adaptive control (MRAC), has been developed to compensate for the variation of system parameters such as inertia and load torque. A torque observer has been employed to balance the load torque and to reduce the complexity of the adaptive algorithm. Simulation and experimental test results of the robotic drive using the IPM synchronous motor have been presented and compared with the standard speed and position regulators. However, the performance of the control system has not been investigated for adoptions with noise or persistent speed error. Ebrahimirad *et al.* [47] have investigated a sliding

mode controller (SMC) for the speed control of the PMSM drive system. The controller used a hyperbolic tangent switching function in order to overcome the chattering problem. Computer simulation has been performed for excessive load disturbances, parameter uncertainty, and noisy feedback signals. However, the drive system has not been investigated in real-time where unknown and unavoidable parameter variations always exist.

Shyu *et al.* [48] have developed a robust optimal controller for the position control of the PMSM drive system. The control scheme includes the applications of the linear quadratic (LQ) method and the variable structure control (VSC) method. In the control scheme, the LQ method has been used to determine the feedback gain in order to shape the dynamics of the reaching phase response and to meet the requirements of the performance indices. The proposed control algorithm has been implemented in a Pentium PC. However, the performances of the drive have not been investigated over the wide range of speeds. Moreover, the drive system showed the chattering problems during the steady state speed response. Uddin *et al.* [49] have developed a self-tuning PI controller based on the genetic algorithm (GA) and the fuzzy basis function network (FBFN) for the IPMSM drive system. The PI controller parameters have been optimized offline using the GA in order to meet the performance indices of minimum settling time, minimum overshoot/undershoot, and zero steady state error. The closed loop vector control scheme of the IPMSM drive incorporating the FBFN controller has been successfully implemented in real time for a laboratory 1-hp IPMSM drive. However, the performance of the drive has not been investigated for the variation of the *d-q* axis inductances of the IPM motor due to magnetic saturation and load torque.

Ming *et al.* [50] have presented an on-line self-tuning PI speed controller for the PMSM servo drive system. The technique used the ILC scheme for the self-tuning of the PI controller. The input and output uncertainty have been considered in the technique. The controller has been implemented in real time using the DSP board TMS320LF2407A. However, the convergence condition of the controller has not been investigated. Fukomoto *et al.* [51] have analyzed the influences of motor parameters and

PWM dead time on the estimation of rotor position for the position sensorless vector control of the IPMSM drive system. The stator resistance, *d-q* axis inductances, and permanent magnet flux have been measured off-line, and these have been used in the on-line compensation of the adaptive observer. The on-line dead time compensation at low speed and no load conditions has been performed by determining the compensation pattern experimentally. However, the estimated speed showed high amount of fluctuation at high speeds for this sensorless operation of the IPMSM drive.

Mohamed [52] has proposed a direct instantaneous torque and flux controller for the PMSM drive system using an adaptive linear neuron (ADALINE) model of the motor. The controller used a linear VSC model to control the increment of torque angle and a dynamic internal model within the flux control loop to control the permanent magnet flux. However, an appropriate switching gain of the VSC model diverts the controller from the sliding surface, which in turn can cause control chattering and low efficiency. Shinnaka [53] has developed a sensorless vector control technique for the IPMSM drive systems. The method estimated the phase of rotor flux using a minimum order state observer in the stationary reference frame. The method has been examined and confirmed through experiments. However, the stability analysis of the drive system has not been performed, and its performances have not been investigated for variable and rated speed conditions. Shinnaka [54] has reported another work on the sensorless vector control for the IPMSM drive system. This method estimated the phase of rotor flux using a D-state observer. The D-state observer has been implemented for a 400 W salient pole IPM synchronous motor. However, the speed response of the proposed controller showed fluctuation near zero speed of the motor.

Kim [55] has presented a sequential parameter auto-tuning algorithm for the nonlinear speed control of the PMSM drive system. The influence of the simultaneous estimation of motor parameters using observers or model reference adaptive systems on the speed dynamics of the PMSM drive system have been investigated and validated. The sequential parameter auto-tuning algorithm has been used at startup where motor parameters are estimated one by one in a prescribed sequential routine. The control

scheme has been implemented using the DSP controller board TMS320C31, and the effectiveness has been verified through simulation and experiments. Hasegawa and Matsui [56] have presented a position sensorless control technique for the IPMSM drive system based on the adaptive flux observer with inductance identification. The adaptive full order observer used two adaptive schemes for identifying inductance during magnetic saturation. The first scheme has been modeled on a stationary reference frame, and the other has been developed on a rotating reference frame, which is aligned with the synchronously rotating rotor position. Experimental performances of the drive system including the on-line identification of inductance have been presented.

Several adaptive control algorithms have been theoretically developed and implemented in the last few years. Unfortunately, such powerful algorithms are weighted by the relevant complexity of the control actions in terms of computational efforts. So, more memory and large numbers of calculations are needed during the estimation and design phases of the adaptive algorithms. Since the control loop actions in electric drives must be performed within 1 ms, the practical implementation of these adaptive algorithms is not always feasible without high speed digital signal processors or microprocessors. Recently, adaptive linearization, nonlinear sliding mode control, and intelligent observer based techniques are reported to improve the control performance. However, these techniques are based on the assumption that the variation of an unknown disturbance is very small during each sampling interval. Although good performances can be achieved using these schemes, the performance may not be satisfactory under specific conditions such as large inertia variation, fast speed transients, large sampling time, etc.

1.2.2 PMSM drives using artificial intelligent controllers

Recently, researchers [57]–[70] have looked into the artificial intelligent controllers based PMSM drive system in order to handle the unpredictable and unknown dynamics. These include neural network (NN), fuzzy logic, and neuro fuzzy controllers. Robustness, adaptability, and adaptive learning are the main features of an artificial intelligent system. Advances in computer technology, modern control techniques, and

computational intelligence have expedited the developments of intelligent control theories and their application for the PMSM drive systems.

Ibrahim *et al.* [57] have conducted a detail comparison between the PI controller and the fuzzy logic controller (FLC) for the speed control of a vector controlled PMSM drive system. The FLC used the speed error and change of speed error as the inputs. The membership functions of triangular shape with equal width and overlap have been used for each input variable. The transient performances of the drive have been examined in simulation and experiments. The transient studies included speed response for large and small step changes in command speeds with nominal and increased inertia, and for step changes in load torque. The Fuzzy logic (FL) based speed control showed superior performances than the PI speed control for the case of load transient at all operating conditions. However, the PI controller demonstrated better responses for step changes in command speeds at one third of the rated speed, while the FLC offered better behavior for the remainder of the speed control range. Cheng *et al.* [58] have developed a self-tuning fuzzy PI controller with conditional integral action for the doubly salient PMSM drive. The fuzzy controller tuned the PI controller in order to speed up the transient process. The conditional integration acted to diminish the steady state speed error in order to satisfy both dynamic and steady state performance requirements of the drive system. Initially, the parameters of the PI controller have been optimized using the genetic algorithms. The proposed controller has been implemented in a single chip N87C196KD. Simulation and experimental results have been presented for wide speed ranges of the IPMSM with different operating conditions. However, the drive showed significant noise in the steady state speed responses because of the memory limitation of the chip N87C196KD.

Kadjoudj *et al.* [59] have developed a fuzzy logic algorithm for the speed control of the IPMSM drive system. The proposed algorithm included a classical fuzzy controller with IF-THEN rules, where the gradually varying symmetrical triangular membership functions have been used. The proposed adaptive Fuzzy logic controller (FLC) has been compared with the fixed gain PI controller in simulation. A comparative analysis of two-

level and three-level voltage source inverters fed IPMSM drive systems has been presented. However, the performances of the drive systems have been investigated in simulation only. Singh *et al.* [60] have analyzed the performances of a fuzzy logic controlled PMSM drive system. The PID control has been used for dc link voltage control, and the fuzzy PID controller has been used for speed control of the PMSM drive. The performances of the controllers have been investigated for different steady state and transient operating conditions under parameter variations. However, the drive system suffers from a high computation burden for the on-line implementation because of the fact that separate reference currents are needed for the dc link voltage control and for the closed-loop speed control of the PMSM drive.

Butt *et al.* [61] have developed a simplified fuzzy logic based speed controller for maximum torque per ampere (MTPA) vector control of the IPMSM drive system. The simplified FLC based IPMSM drive system have been tested in simulation and experiments at dynamic operating conditions. The complete vector control scheme has been implemented in real time using the 32-bit floating point DSP processor TMS320C31. However, the performances of the drive have been investigated for a very limited selection of motor dynamics. which include the starting speed response for a certain command speed and the steady state speed response for sudden application of load torque. Uddin *et al.* [62] have presented a genetic algorithm based fuzzy logic controller (GFLC) for the IPMSM drive system. The genetic algorithm (GA) is used to tune the controller parameters. The performances of the controller have been compared with a conventional PI controller in simulation and experiments at various operating conditions. However, the simplified model of the IPMSM with the *d*-axis command current equal to zero condition, have been used for the implementation of the drive system. Moreover, the performance of the drive system has not been investigated at low speeds.

A cost effective four-switch three-phase PWM inverter fed IPMSM drive system using the Fuzzy logic (FL) speed controller has been investigated in reference [63]. The four-switch three-phase IPMSM drive system has been compared with a conventional

six-switch three-phase IPMSM system based on the harmonic content of stator current. However, the performances of the drive system have not been investigated for parameter sensitivity and non-linearity of the load torque. Yu *et al.* [64] have proposed a fuzzy logic controller (FLC) for the surface mounted PMSM drive system in elevator drive applications. The control rules and membership functions of the FLC have been designed based on the system characteristics. The complete vector control scheme for the elevator drive system incorporating the FLC has been implemented in real time using the DSP controller board TMS320VC33. However, the performance of the drive system has been investigated only for the rated command speed of 188.6 rad/sec with the *d*-axis command current equal to zero condition. Kung and Tsai [65] have presented a digital integrated circuit (IC) based on the field programmable gate array (FPGA) technology for the speed control of the PMSM drive system. The motor control IC used two embedded processors with intellectual property (IP) applications. One of the processors has been adopted to implement the adaptive fuzzy control functions using software, and the other processor has been used to realize the vector controller with hardware.

Rahman and Hoque [66] have developed an on-line self-tuning neural network (NN) based speed controller for the IPMSM drive system. The NN speed controller has been developed based on motor dynamics and non-linear load characteristics. The controller has been integrated with the vector control scheme of the IPMSM drive system. The complete drive system has been implemented in real time using the DSP controller board ds1102 on a laboratory 1-hp IPMSM. However, the linearized model of the IPMSM has been used to develop the control algorithm. Elbuluk *et al.* [67] have presented a NN based model reference adaptive system (MRAS) to estimate the speed and position of the sensorless PMSM drive system. The adaptation technique has been used as an optimization tool for the comprehensive parameter estimation. The estimation strategy first estimated the stator resistance and torque constant with the use of the NN adaptation system. The speed estimation algorithm based on the back EMF has been used for the determination of motor position and speed. The sensorless drive system has been tested in simulation and experiments. However, the system suffers from excessive online

computations because of the nonlinear functions and divisions of the neural estimator. Moreover, the number of neurons of the adaptive system need to be optimized between the performance and computation time. Yi *et al.* [68] have presented an NN based real time adaptive controller for the accurate speed control of the IPMSM drive system under system uncertainties. The off-line training has been used for the initialization of the NN speed controller. A dynamic training technique based on the Levenburg–Marquardt algorithm has been used in the online training to update the network parameters under continuous mode of operation. The controller has been implemented in real time using a DSP based hardware environment. However, the significant drawbacks of this scheme are the complex system structure, sophisticated training procedure, and requirement of an additional network for system identification.

Lin *et al.* [69] have developed a self-constructing fuzzy neural network (SCFNN) for the speed control of the PMSM drive system. The structure and parameter learning of the SCFNN have been performed online. The structure learning algorithm partitioned the input space while the parameter learning algorithm updated the network parameters using the gradient descent technique including the delta adaptation law. Simulation and experimental results have been provided to demonstrate the effectiveness of the proposed SCFNN control strategy. However, the proposed structure and parameter learning algorithms are very complicated and suffer for high computational burden for practical implementation. Elmas *et al.* [70] have developed a neuro fuzzy controller (NFC) for the speed control of the PMSM drive system. The four-layer neural network has been used to adjust the membership functions of the controller. The back propagation learning algorithm has been implemented for the off-line training of the network. The performance of the controller has been verified in simulations and experiments. The controller has been implemented using the DSP board TMS320F240. However, the control technique is not very robust because of the off-line training of the network, and may not be suitable for dynamic conditions such as parameter sensitivity and system disturbances. Moreover, a fixed structure of neural network with large number of neurons in hidden layers has been used in the control technique. The structure of the network has

been determined in advance. As a result, the control performance using the network structure may not be satisfactory for different ratings of the PMSM drive system [66], [91].

Extensive research have been carried out on the development and implementation of fuzzy logic controller (FLC), neural network controller (NNC), and neuro fuzzy controller (NFC) for the high performance PMSM drive systems. The FLC is the simplest for the speed control of high performance PMSM drives. However, it is not guaranteed that a general FLC will not be chaotic. It has been reported in reference [57] that the FLC is not necessarily superior to the optimally tuned PI controller at all operating conditions of the PMSM drive system. The NN controllers are deliberately constructed to make use of the organizational principles of the human brain. However, it is extremely difficult to generate training data for the NN controller, which can handle all operating modes of the PMSM drive system. The NFC implements high level learning and low computational power of neural network to fuzzy control system. It also provides high level humanlike thinking and reasoning to neural networks. However, the problem of finding a well-defined procedure for determining optimum network topology of the neuro Fuzzy controller (NFC) for the nonlinear PMSM drive system still has been a challenge.

1.2.3 PMSM drives using wavelet based intelligent controllers

Recently, wavelet transforms have been used in the modeling, analysis, and control of electric motor drives for high performance applications. The wavelet transforms, which are different from the traditional fast Fourier transform (FFT) and short time Fourier transform (STFT), have been implemented in a number of techniques for high performance control and diagnostic of permanent magnet synchronous motor (PMSM) drive, brushless dc motor drive, and induction motor drive. In general, the wavelet transforms have the ability to decompose wide band signals into time localized and frequency localized sub bands, which have dyadic changing frequency bands. The wide band signals include the stationary, non-stationary, periodic, non-periodic, and

transient signals. As compared to the PI, PID, adaptive and intelligent controllers, a wavelet controller has the following advantages:

- it is based on the time localized filter bank structure of the orthogonal wavelet and scaling functions,
- it can accurately parameterize wide range of signals with complex time-frequency structure,
- it is independent of the exact model of the system.

Khan *et al.* [71] have developed and implemented a hybrid wavelet packet transform (WPT) and artificial neural network (ANN) based faults diagnostic and protection technique for both line-fed and inverter-fed IPM synchronous motors. The stator currents of different faulted and normal conditions of the IPMSM have been preprocessed by the WPT algorithm. The second level WPT coefficients of stator currents have been used as inputs of a three-layer feed forward neural network. Simulation and experimental performances of the 1-hp IPM synchronous motor drive system using the WPT and ANN diagnostic algorithms have been presented. In [72], the WPT algorithm has been used for faults diagnostic and protection of three-phase induction motors. The comparison of the WPT coefficients of stator currents during the faulted conditions with the healthy operations of the motor has been used to detect a fault in the proposed diagnostic algorithm. The algorithm has been implemented in real time using the Texas Instrument 32-bit DSP processor TMS320C31.

Chaplais *et al.* [73]–[74] have developed an on-line wavelet based de-noising algorithm for the three-phase PM brushless dc motor drive of a reaction wheel system. The wavelet based algorithm has been implemented to de-noise the feedback signal of the brushless dc motor drive. The average interpolation scheme has been used to develop a wavelet transform algorithm on the negative real axis in order to perform causal wavelet processing with a small delay. The algorithm has been implemented in SIMULINK [90] of the MATLAB software package. The real time workshop toolbox of the MATLAB has been used to generate and download the real time code from the complete SIMULINK diagram. Khorbotly *et al.* [75] have developed a wavelet based real time de-noising

technique for noisy signals. The technique has been implemented for the position sensorless control of the switched reluctance motor (SRM) drive system. The rotor position has been estimated using a computational subsystem. The three-level wavelet de-noising system with a moving filter has been used in the work. The filter moved the de-noising blocks to different locations within the system to analyze the resulting noise. However, the performances of the drive system have not been investigated for variable speed operations.

Song *et al.* [76] have presented a wavelet neural network (WNN) based speed estimation technique for the sensorless control of the PM brushless dc (BLDC) motor drives. The structure of the WNN has been determined from the BLDC motor dynamics. The network has been trained off-line using the Levenberg Marquardt algorithm. Simulation and experimental results have been presented to validate the performances. However, the drive system incorporating the WNN based speed estimator shows unsatisfactory performances during the high speed operation of the brushless dc motor because of the off-line training of the network. Yilmaz *et al.* [77] have presented a wavelet based speed prototype approach for the sensorless control of the BLDC motor drives. In the proposed approach, the phase currents of the test motor have been processed using the discrete wavelet transform. It has been shown that the wavelet transformed coefficients of stator current can be used in order to estimate the rotor position accurately. However, the performances of the sensorless drive system have not been investigated in detail.

Cao *et al.* [78] have presented a wavelet neural network (WNN) based on-line stator resistance identification technique for the direct torque control (DTC) of the induction motor (IM) drive system. The actual and change of winding temperatures have been used as the inputs of the proposed identifier. The low speed performance of the drive system has been investigated using the identifier. However, the performances of the drive system have not been investigated at high speeds. Wai *et al.* [79] have developed a WNN based back stepping control technique for the position control of an indirect field-oriented IM drive system. A model reference adaptive system (MRAS) has been used for

the estimation of rotor time-constant. The MRAS estimated the slip angular velocity and preserved the decoupling control of torque and flux. Simulation and experimental performances of the proposed control scheme have been presented and compared with the neural network based back stepping control.

Wai [80] has developed a WNN based robust control scheme for the permanent magnet synchronous servo motor drive. A position controller has been developed based on the principle of computed motor torque. The WNN uncertainty observer has been used to adapt the uncertainties of motor parameters online. The position controller with the WNN based uncertainty observer has been used as the main tracking controller. Simulation and experimental results have been provided to validate the effectiveness of the robust control scheme. However, the control scheme required a priori knowledge of the system. Moreover, the drive system suffers from high computation burden due to the system complexity. Jun *et al.* [81] have developed a dynamic recurrent fuzzy wavelet network (DRFWN) based speed controller for the PMSM drive system. The DRFWN controller with adaptive learning rates has been implemented to evaluate the uncertainty bounds of the PMSM drive. The performances of the drive have been investigated in simulation only. So, the controller may not be suitable for real time applications where performances are adversely affected by nonlinear load characteristics, parameter variations, and magnetic saturation.

Azadi *et al.* [82] have presented a wavelet neural network (WNN) based speed controller for the PMSM drive system. The WNN based speed controller has been trained with data extracted from PID controller based drive system in order to achieve reasonable performances in all operating regions. The proposed controller has been simulated for parameter variations. However, the stability of the drive system has not been investigated. Parvez *et al.* [83] have developed a wavelet based multiresolution speed controller for the brushless dc motor servo drive system. The wavelet transform has been used to decompose the speed error signal at different scales. These decomposed signals have been used to compensate for the system uncertainties. The performances of the controller have been evaluated through simulation and experimental results. Khan *et al.*

[84] have presented a novel wavelet based multiresolution PID controller for accurate speed control of the IPMSM drive under system uncertainties. The proposed controller is based on the multiresolution decomposition of the discrete wavelet transform (DWT) of the speed error between command and actual speeds. The wavelet transformed coefficients of the speed error of different frequency sub-bands of the DWT tree have been used to generate the control signal. The proposed wavelet based PID controller for the IPMSM drives has been successfully implemented in real time using the DSP board ds1102 on a laboratory 1-hp IPMSM. The performances of the controller have been evaluated through simulation and experimental results. In reference [85], the wavelet neural network (WNN) has been used for the self-tuning of the wavelet based multiresolution PID controller for the IPMSM drive system. Simulation and experimental performances of the proposed self-tuning multiresolution proportional integral derivative (PID) controller based IPMSM drive system have been presented. The WNN based self-tuning MRPID controller showed better performances than with the fixed-gain multiresolution MRPID controller.

Khan *et al.* [86] have developed and implemented a WNN based adaptive controller for the IPM motor drive system. The tracking speed error and change of speed error have been used as the inputs of the proposed controller. The output of the controller is the command torque current for the IPM motor drive system. The proposed WNN has been trained on line with adaptive learning rates using the back propagation training algorithm. The convergence of the speed tracking error has been ensured using the adaptive learning rates. The performances of the proposed controller have been evaluated by simulation and experimental results. A comparative performance analysis of the intelligent speed controllers for the IPM motor drive system has been presented in reference [87]. The performances of the fixed-gain PI, PID, and adaptive neural network (NN) controllers based IPMSM drive system have been compared with the proposed wavelet based multiresolution MRPID controller based drive system. The proposed wavelet based multiresolution MRPID controller showed better performances than with the fixed gain and adaptive controllers. Khan *et al.* [88]–[89] have presented the

performances of the wavelet based multiresolution PID controller for the induction motor drive system in both simulation and experiments. The proposed MRPID controller has been compared with the fixed gain PI, PID controllers, and adaptive switching mode controller (SMC).

Based on the above discussions it can be concluded that there exists a recent trend of research activities on the applications of wavelet transforms in ac motor drives. Earlier works on the application of wavelet based observers and controllers in motor drives are mainly theoretical and are based on the investigation of drive responses in either simulation or experiments for low and medium speed operating conditions. These works are largely limited to signal processing of controlled variables using wavelet transforms so that the performance of the existing control systems could be improved indirectly.

Research works on the implementation of wavelet transforms for the brushless dc motor drive, switched reluctance motor drive, induction motor drive, and permanent magnet synchronous motor drive have been reported in references [71]–[89]. However, a systematic research on the development and implementation of a wavelet based speed controller for the high performance IPMSM drive system has yet to be reported. Thus, there exists a need to develop and implement a new wavelet based speed controller in real time for the IPMSM drive system. The self-tuning wavelet based multiresolution proportional integral derivative (MRPID) controller is proposed as a speed controller for an IPMSM drive system.

1.3 Problem Identification and Research Objectives

The IPMSM has effective rotor geometry to ensure optimal use of the expensive rare earth permanent magnet materials while maintaining a high magnetic field in the air gap. However, the performances of the interior permanent magnet (IPM) motor drive system can be strongly affected by system uncertainties, demagnetization of permanent magnets, and magnetic saturation. The saturation of the rotor iron around the permanent magnets causes significant distortion of the air gap flux. The saturation of air gap flux affects the *d-q* axis reactance parameters of the IPMSM, and hence the performance of

the drive system. The IPMSM is constructed commonly with the Nd-Fe-B permanent magnets where the flux density is affected by temperature variation and corrosive environment. The stator winding resistance of the IPMSM also varies with winding temperature. Therefore, the precise control of an IPMSM drive system becomes a complex issue and needs special attention for the high performance drive (HPD) applications. The vector control technique enables an IPMSM to achieve superior dynamic performance capabilities to a separately excited dc motor. The speed and flux are controlled separately in the field-oriented vector control of an IPMSM drive system. The decoupling control provides easier control and faster speed response. The speed controller of a vector controlled IPMSM drive satisfies the major criteria of the HPD system. It enables a drive system to follow any command speed accurately considering the effects of parameter variations, system uncertainties, non-linear load, and magnetic saturation [91]–[92].

The conventional controllers such as fixed-gain proportional integral (PI) or proportional integral derivative (PID) controllers are widely used for speed controls of dc and ac motor drive systems. However, the performances of these controllers are affected by parameter variations, noise, temperature, and unknown load dynamics and system uncertainties. Moreover, these types of controllers are very difficult to design if an accurate model of the system is not available. Researchers have developed adaptive controllers to overcome the problems of conventional controllers. The adaptive controllers for the IPMSM drive include the model reference adaptive controller (MRAC), sliding mode controller (SMC), variable structure controller (VSC), self-tuning regulator (STR), and artificial intelligent controllers. The approximate model parameters are required in the design of these controllers. As a result, the performances of these controllers using approximate parameters are not satisfactory for the wide speed range of the drive system. Moreover, strict conditions and a prior knowledge of the controlled system are also required in these control techniques.

Recently, increased attention has been given on the use of wavelet transforms in the modeling, analysis, and control of electric motor drives. The wavelet transforms can

play a key role on the identification and control of the high performance IPMSM drive systems. Therefore, an effort is aimed to develop a practical and easy to implement IPMSM drive system in real time incorporating a wavelet based intelligent speed controller. The main objective of this work is to develop and implement a self-tuning wavelet based multiresolution proportional integral derivative (MRPID) controller in real time for precise speed control of an IPMSM drive system under system uncertainties. In the wavelet based MRPID controller, the discrete wavelet transform (DWT) is used to decompose the speed error between actual and command speeds into different frequency components at various scales. The wavelet transformed coefficients of speed error of different frequency sub-bands of the DWT are scaled by their respective gains, and then are added together to generate the control signal. Initially, the analogy between the PID decomposition and the multiresolution decomposition of speed error is used in order to set the gains of the fixed gain MRPID controller. Then the wavelet neural network (WNN) is used for the on-line tuning of the MRPID controller to ensure optimal drive performances in real time under system disturbances and uncertainties. The WNN utilizes the learning ability of neural networks and the localization property of wavelet decomposition in the self-tuning of the proposed wavelet based MRPID controller.

The proposed self-tuning MRPID control technique ensures excellent speed tracking performances for different command speeds. It also makes the drive system insensitive to parameter variations and unknown load dynamics. The proposed self-tuning wavelet based MRPID controller is trained on-line with adaptive learning rates for the closed loop speed control of the IPMSM drive system. The adaptive learning rates are derived using the discrete Lyapunov stability theorem. It guarantees the convergence of the speed tracking error in the closed-loop IPMSM drive system. The performances of this newly devised self-tuning wavelet controller are evaluated by simulation and experimental results. The complete control scheme incorporating the proposed self-tuning wavelet based MRPID controller is successfully implemented in real time using the DSP board ds1102 for the laboratory 1-hp interior permanent magnet (IPM) synchronous motor. The maximum torque per ampere (MTPA) and flux-weakening (FW) control

techniques are used in order to operate the drive system below and over the rated speed of the IPM motor.

1.4 Outline of the Thesis

In this section, the outline of the remaining chapters of the thesis is given. Chapter two presents the vector control scheme of a voltage source inverter (VSI) fed interior permanent magnet synchronous motor (IPMSM) drive system. The mathematical model of an IPMSM drive is presented and integrated with the vector control technique. The simulation performances of the fixed gain PI, PID controllers and the adaptive neural network (NN) controller based IPMSM drive systems incorporating the vector control technique are presented in the chapter. The hysteresis current controller is used for the vector control of the IPMSM drive system.

Chapter three presents the wide speed control of the IPMSM drive system. The control scheme includes the maximum torque per ampere (MTPA) control in the constant torque region and the flux-weakening (FW) control in the constant power region. The performances of the maximum torque per ampere (MTPA) control and flux-weakening (FW) control with $i_d \neq 0$ are compared with the vector control technique with $i_d = 0$. The comparative performance analysis is presented.

Chapter four presents the wavelet based multiresolution PID (MRPID) controller for the IPMSM drive system. The wavelet transforms and multiresolution analysis are briefly discussed at the beginning. The mathematical formulations of wavelet transforms are presented. The procedures for selections of optimum mother wavelet and optimal levels of resolution of the MRPID controller are described, and then these are implemented for the IPMSM drive system. The fundamental idea of the wavelet based MRPID controller for the IPMSM drive system is briefly presented at the end.

Chapter five presents a novel wavelet based vector control scheme for the IPMSM drive system. The specific wavelet based MRPID controller for the IPMSM drive system is developed considering motor dynamics and unknown load characteristics. The complete control scheme incorporating the MRPID controller is implemented in

simulation and real time in order to predict the performances of the proposed wavelet based MRPID controller. The simulation and experimental results are presented at the end of this chapter.

Chapter six presents the proposed wavelet neural network (WNN) based self-tuning MRPID controller for the interior permanent magnet (IPM) motor drive system. The structure and mathematical formulations of the proposed WNN are given at the beginning. Then, the outline of the training algorithm for the on-line updating of network parameters is presented. The stability analysis of the proposed self-tuning MRPID controller is also illustrated. In order to predict the performances of the proposed self-tuning wavelet based MRPID controller, extensive simulations are carried out before the real time implementation of the drive system. The simulated performances are presented at the end.

Chapter seven presents the real time implementation of the complete control scheme of the IPMSM drive system incorporating the proposed self-tuning wavelet based MRPID controller. The software and hardware implementation procedures of the proposed technique are presented in detail. The proposed drive system is successfully implemented in real time using the DSP board ds1102 on a laboratory 1-hp IPM synchronous motor. Experiments are carried out on the IPMSM drive system at different dynamic operating conditions. The performances of the new self-tuning wavelet based MRPID controller are compared with the fixed gain PI controller in experiments under the same operating conditions. The experimental results validate the simulation results presented in chapter six. The performances of the proposed self-tuning MRPID based IPMSM drive system are found more robust as compared to those of the conventional PI controller based IPMSM drive system. The summary and conclusions of this work are given in chapter eight. The pertinent references and appendices are listed after chapter eight.

Chapter 2

Vector Control of the Interior Permanent Magnet Synchronous Motor (IPMSM) Drive

This chapter presents the development and implementation of a complete current-controlled voltage source inverter (VSI) fed IPMSM drive system. The vector control technique is implemented for the high performance control of the IPMSM drive system. The underlying principle of vector control is to eliminate the coupling between armature and field mmf (magneto motive forces) by separating the direct (d) and quadrature (q) axes components of stator current. In order to decouple the d-q axis currents, the machine equations can be expressed in the synchronously rotating reference frame of the Park's transform [93], [120]. In this chapter, the d^r-q^r axis model of the IPMSM in the synchronously rotating reference frame is used to analyze the performances of the drive system incorporating the vector control technique. The speed and current controllers are the key components of the vector-controlled IPMSM drive system. These components play crucial roles for the drive to follow the command speed accurately at different operating conditions. Various speed and current controllers are developed in this chapter in order to investigate the performances of the vector-controlled IPMSM drive system. The fixed gain PI, PID speed controllers and an adaptive neural network (NN) speed controller are developed and implemented for the performance analysis of the drive system. The performances of the vector-controlled IPMSM drive system using the fixed-

band hysteresis type current controller and the conventional speed controllers are evaluated through simulation results.

2.1 Modeling of Interior Permanent Magnet Synchronous Motor

The excitation in the IPMSM is provided by the permanent magnets, while the excitation in the conventional synchronous motor is provided from a separate dc source in the wire-wound rotor field winding. The permanent magnets provide the constant flux linkage, and it is denoted as λ_M in equation (2.1). The flux linkages in the three-phase stator sinusoidal windings of the interior permanent magnet synchronous motor (IPMSM) due to the permanent magnet rotor can be expressed in the matrix form as [93]–[94]

$$[\lambda_F] = \begin{bmatrix} \lambda_{af} \\ \lambda_{bf} \\ \lambda_{cf} \end{bmatrix} = \begin{bmatrix} \lambda_M \sin\theta_r \\ \lambda_M \sin\left(\theta_r - \frac{2\pi}{3}\right) \\ \lambda_M \sin\left(\theta_r + \frac{2\pi}{3}\right) \end{bmatrix} \tag{2.1}$$

where λ_{af}, λ_{bf}, and λ_{cf} are the stator flux linkages of phases a, b, and c, respectively due to the permanent magnet alone, and θ_r is the rotor position angle. The three-phase air gap flux linkages can be stated in the matrix form as

$$[\lambda] = \begin{bmatrix} \lambda_a \\ \lambda_b \\ \lambda_c \end{bmatrix} = \begin{bmatrix} L_{aa} & M_{ab} & M_{ac} \\ M_{ba} & L_{bb} & M_{bc} \\ M_{ca} & M_{cb} & L_{cc} \end{bmatrix} \begin{bmatrix} i_a \\ i_b \\ i_c \end{bmatrix} + \begin{bmatrix} \lambda_M \sin\theta_r \\ \lambda_M \sin\left(\theta_r - \frac{2\pi}{3}\right) \\ \lambda_M \sin\left(\theta_r + \frac{2\pi}{3}\right) \end{bmatrix} \tag{2.2}$$

where λ_a, λ_b, λ_c are the air gap flux linkages of phases *a*, *b*, and *c*, respectively, L_{aa}, L_{bb}, L_{cc} are the self inductances, and M_{ab}, M_{bc}, M_{ca} are the mutual inductances. The three-phase voltage equations of the IPMSM can be written as

$$[v]=\begin{bmatrix} v_a \\ v_b \\ v_c \end{bmatrix}=\begin{bmatrix} r_a & 0 & 0 \\ 0 & r_b & 0 \\ 0 & 0 & r_c \end{bmatrix}\begin{bmatrix} i_a \\ i_b \\ i_c \end{bmatrix}+p\begin{bmatrix} \lambda_a \\ \lambda_b \\ \lambda_c \end{bmatrix} \tag{2.3}$$

where p is a differential operator defined as $p = \frac{d}{dt}$. It is to be noted from equations (2.2)–(2.3) that the coefficients of three-phase voltages and flux linkages of the IPMSM are functions of rotor position and speed. Therefore, the three-phase voltages are time varying except when the motor is stationary. To avoid the complexity of equations (2.2)–(2.3), the voltages equations are transformed to the synchronously rotating rotor reference frame where the machine equations are not dependent on the rotor position. These transformations are done in two steps using the Park's transformation technique [93], [120]. In the first step, the machine equations are transformed from the stationary *a-b-c* reference frame to the stationary *d-q* reference frame. In the second step, the machine equations are transformed from the stationary *d-q* frame to the synchronously rotating d^r-q^r frame. The co-efficient matrix (C) for the transformation from the *a-b-c* frame to the rotating d^r-q^r frame can be written in the matrix form as

$$[C]=\frac{2}{3}\begin{bmatrix} \cos\theta_r & \cos\left(\theta_r-\frac{2\pi}{3}\right) & \cos\left(\theta_r+\frac{2\pi}{3}\right) \\ \sin\theta_r & \sin\left(\theta_r-\frac{2\pi}{3}\right) & \sin\left(\theta_r+\frac{2\pi}{3}\right) \\ \frac{1}{2} & \frac{1}{2} & \frac{1}{2} \end{bmatrix}. \tag{2.4}$$

The inverse co-efficient matrix for the transformation from the rotating d^r-q^r frame to the *a-b-c* frame can be written in the matrix form as

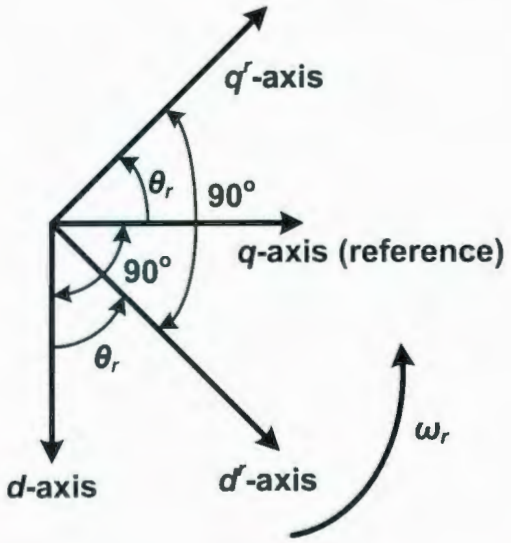

Figure 2.1: Relative positions of stationary d-q axis and rotating d^r-q^r axis.

$$\left[C^{-1}\right]=\begin{bmatrix} \cos\theta_r & \sin\theta_r & 1 \\ \cos\left(\theta_r-\frac{2\pi}{3}\right) & \sin\left(\theta_r-\frac{2\pi}{3}\right) & 1 \\ \cos\left(\theta_r+\frac{2\pi}{3}\right) & \sin\left(\theta_r+\frac{2\pi}{3}\right) & 1 \end{bmatrix}. \qquad (2.5)$$

Here, the rotor position angle θ_r is defined as

$$\theta_r = \int_0^t \omega_r(t)\,\mathrm{dt} + \theta_r(0) \qquad (2.6)$$

where ω_r is the mechanical speed in rad/sec. The rotor position angle θ_r in equations (2.4)–(2.5) is equal to $\theta_r(0)$ when these are defined in the stationary reference frame. The angle $\theta_r(0)$ is the difference of angle between the q-axis and phase-a axis. In the balanced three-phase operation, the $\theta_r(0)$ is set to zero so that the q-axis coincides with the phase-a axis. The relative positions of the stationary d-q axis and rotating d^r-q^r axis are shown in Fig. 2.1. The quantities in the stationary d-q frame are converted to the synchronously rotating d^r-q^r frame with the help of Fig. 2.1. The transformation is defined as [6]

$$\begin{bmatrix} x_q^r \\ x_d^r \end{bmatrix} = \begin{bmatrix} \cos\theta_r & -\sin\theta_r \\ \sin\theta_r & \cos\theta_r \end{bmatrix} \begin{bmatrix} x_q \\ x_d \end{bmatrix} \tag{2.7}$$

$$\begin{bmatrix} x_q \\ x_d \end{bmatrix} = \begin{bmatrix} \cos\theta_r & \sin\theta_r \\ -\sin\theta_r & \cos\theta_r \end{bmatrix} \begin{bmatrix} x_q^r \\ x_d^r \end{bmatrix} \tag{2.8}$$

where x_d, x_q are d-q axis stationary components, and x_d^r, x_q^r are d-q axis rotating components. The matrix element x represents either voltage or current. In order to derive the d^r-q^r model of the IPMSM drive, the following assumptions are made:

- hysteresis and eddy current losses are negligible,
- induced electro motive force (emf) is sinusoidal,
- saturation is negligible,
- stator resistances of three phases are balanced.

Now using equations (2.1)–(2.8) and above assumptions, the voltage equation (2.3) can be written as

$$\begin{bmatrix} v_q^r \\ v_d^r \\ v_0^r \end{bmatrix} = \begin{bmatrix} r_a & 0 & 0 \\ 0 & r_b & 0 \\ 0 & 0 & r_c \end{bmatrix} \begin{bmatrix} i_q^r \\ i_d^r \\ i_0^r \end{bmatrix} + P\omega_r \begin{bmatrix} \lambda_d^r \\ -\lambda_q^r \\ 0 \end{bmatrix} + p \begin{bmatrix} \lambda_q^r \\ \lambda_d^r \\ \lambda_0^r \end{bmatrix} \tag{2.9}$$

where v_d^r, v_q^r are d^r-q^r axis voltages, i_d^r, i_q^r are d^r-q^r axis currents, λ_d^r, λ_q^r are d^r-q^r axis flux linkages, r_a, r_b, r_c are three-phase stator resistances, v_o^r and i_o^r are zero sequence voltage and current, λ_o^r is the zero sequence flux linkage, and P is the number of pole pair. It is assumed that the stator resistance in each phase is equal, i.e.,

$$r_a = r_b = r_c = R \tag{2.10}$$

From equation (2.9) the quadrature axis voltage v_q^r can be represented as

$$v_q^r = R\, i_q^r + P\omega_r \lambda_d^r + p\lambda_q^r \tag{2.11}$$

and the direct axis voltage v_d^r as

$$v_d^r = R\, i_d^r - P\,\omega_r \lambda_q^r + p\lambda_d^r \tag{2.12}$$

and the zero sequence voltage v_o^r as

$$v_o^r = R\, i_o^r + p\lambda_o^r. \tag{2.13}$$

Now λ_d^r, λ_q^r, and λ_o^r can be determined as

$$\lambda_q^r = L_q\, i_q^r \tag{2.14}$$

$$\lambda_d^r = L_d\, i_d^r + \lambda_M \tag{2.15}$$

$$\lambda_o^r = L_l\, i_o^r \tag{2.16}$$

where

$$L_q = L_l + L_{mq} \tag{2.17}$$

$$L_d = L_l + L_{md} \tag{2.18}$$

Here, L_d, L_q are d-q axis inductances, L_{md}, L_{mq} are d-q axis magnetizing inductances, and L_l is the leakage inductance. Substituting equations (2.14) and (2.15) in equations (2.11) and (2.12) respectively, and ignoring the zero sequence terms for balanced three-phase system, the following expressions can be formulated as

$$v_q^r = \left(R + pL_q\right) i_q^r + P\,\omega_r L_d i_d^r + P\,\omega_r \lambda_M \tag{2.19}$$

$$v_d^r = \left(R + pL_d\right) i_d^r - P\,\omega_r L_q i_q^r. \tag{2.20}$$

Using equations (2.19) and (2.20), the interior permanent magnet synchronous motor is modeled by the equivalent d^r-axis and q^r-axis circuit diagrams of Figs. 2.2(a) and 2.2(b), respectively. The permanent magnet is represented as a current source I_M in the d^r-axis equivalent circuit model of the IPMSM of Fig. 2.2(a).

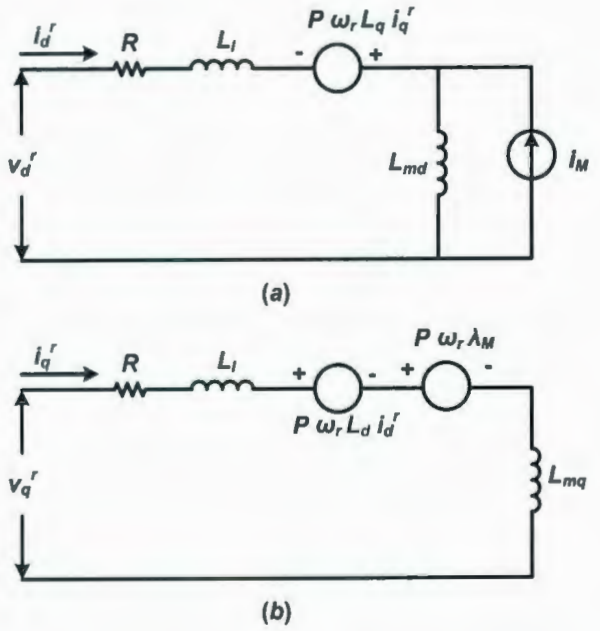

Figure 2.2: Equivalent circuit model of the IPMSM: (*a*) d^r-axis and (*b*) q^r-axis.

The IPMSM equivalent circuit model of Figs. 2.2(*a*)–2.2(*b*) is used to determine the electromagnetic torque of the IPMSM. The mechanical power per phase, which is the total average power of the voltage sources of the IPMSM model, is calculated as [94]–[95]

$$\begin{aligned} P_{phase} &= \frac{1}{2}\left(P\,\omega_r \lambda_M i_q^r + P\,\omega_r L_d i_d^r i_q^r - P\,\omega_r L_q i_q^r i_d^r\right) \\ &= \frac{1}{2} P\,\omega_r \left(\lambda_M i_q^r + i_d^r i_q^r \left(L_d - L_q\right)\right). \end{aligned} \tag{2.21}$$

From equation (2.21), the total mechanical power of the 3-phase IPMSM is calculated as

$$P_{mech} = \frac{3}{2} P\,\omega_r \left(\lambda_M\, i_q^r + i_d^r\, i_q^r \left(L_d - L_q\right)\right), \tag{2.22}$$

and the electromagnetic torque is calculated by dividing equation (2.22) by rotor speed and is obtained as

$$T_e = \frac{P_{mech}}{\omega_r} = \frac{3}{2} P\left(\lambda_M\, i_q^r + i_d^r\, i_q^r \left(L_d - L_q\right)\right). \tag{2.23}$$

Now, the motor dynamics are represented as

$$T_e = J_m \frac{d\omega_r}{dt} + B_m \omega_r + T_L \tag{2.24}$$

where T_L is the load torque in Nm, B_m is the damping coefficient in Nm/rad/sec., and J_m is the rotor inertia constant in kg-m^2.

2.2 Vector Control Scheme

In a separately excited dc motor, the electromagnetic torque is expressed as

$$T_e = K_1 I_a \phi_f = K_2 I_a I_f \tag{2.25}$$

where K_1, K_2 are the torque constants, I_a is the armature current, I_f is the field current, and ϕ_f is the magnetic flux linkage, which provide the dc excitation current in the field winding having N number of turns. The currents I_a and I_f are the orthogonal and decoupled vectors. Hence, the control task is simple for the separately excited dc motor. The electromagnetic torque of the permanent magnet synchronous motors is a function of d^r-q^r axis currents (i_d^r, i_q^r) and d-q axis inductances (L_d, L_q). The electromagnetic torque of equation (2.23) has two terms: the first term represents the magnetic torque produced by the permanent magnet flux λ_M and the torque producing current component i_q^r; the second term represents the reluctance torque produced by the complex interaction of d^r-q^r axis currents and inductances. In the surface mounted permanent magnet synchronous motor (PMSM), the reluctance torque is negligible since $L_d \cong L_q$. Therefore, the torque varies linearly with current, and hence the control task is easier for the surface mounted PMSM. However, L_q is usually designed larger than L_d for the IPMSM. In addition, the inductances (L_d, L_q) and excitation voltage due to permanent magnets vary significantly under steady state and dynamic operating conditions of the IPMSM [96]. So, the complexity of control for the IPMSM arises due to the nonlinear nature of the electromagnetic torque of equation (2.23). The vector control technique is one of the most effective techniques for decoupling d^r-q^r axis components of stator current in the

high performance PMSM drives. In the synchronously rotating rotor reference frame, the sinusoidal quantities appear as constant values at the steady state operating condition. In the vector control scheme for the IPMSM, the d^r-axis current, which is known as the magnetizing current component, is forced to zero. Thus, the magnet flux linkages are oriented in the d^r-axis, and the torque equation becomes linear. With this concept of control strategy, the torque equation (2.23) is written as

$$T_e = \frac{3}{2} P \lambda_M i_q^r \tag{2.26}$$

Now, the electromagnetic torque of equation (2.26) is a linear function of the torque current component i_q^r. So, a constant torque can be maintained by regulating the current i_q^r to the constant value. Using the $i_d^r = 0$ control technique, the dynamic equations (2.19)–(2.20) and (2.24) of the IPMSM can be rewritten as

$$p i_q^r = \frac{1}{L_q}\left(v_q^r - R i_q^r - P \lambda_M \omega_r\right) \tag{2.27}$$

$$v_d^r = - P \omega_r L_q i_q^r \tag{2.28}$$

$$p\omega_r = \frac{1}{J_m}\left[K_t i_q^r - T_l - B_m \omega_r\right] \tag{2.29}$$

where $K_t = \frac{3}{2} P \lambda_M$ and P is the number of pole pair.

The torque expressions of equations (2.25) and (2.26) are alike and decoupled. The steady state phase voltage V_a of the IPMSM is derived from the d^r-q^r axis voltages of equations (2.19)–(2.20) as

$$\begin{aligned} V_a &= v_d^r + j v_q^r \\ &= R i_d^r - \omega_s L_q i_q^r + j R i_q^r + j \omega_s L_d i_d^r + j \omega_s \lambda_M \\ &= R\left(i_d^r + j i_q^r\right) - \omega_s L_q i_q^r + j \omega_s L_d i_d^r + j \omega_s \lambda_M \\ &= R I_a - \omega_s L_q i_q^r + j \omega_s L_d i_d^r + j \omega_s \lambda_M \end{aligned} \tag{2.30}$$

where the steady state phase current $I_a = i_d^r + j i_q^r$ and $\omega_s = P\omega_r$. In the case of the IPMSM, the d^r-axis magnetizing current component i_d^r is negative. It demagnetizes the main flux provided by the permanent magnets. Using the negative polarity of i_d^r, the equation (2.30) can be re-written as

$$V_a = R I_a - \omega_s L_q i_q^r - j\omega_s L_d i_d^r + j\omega_s \lambda_M \qquad (2.31)$$

where the steady state phase current $I_a = -i_d^r + j i_q^r$. The basic vector diagram of the IPMSM is shown in Fig. 2.3. From the vector diagram it is obvious that the stator current can be regulated by controlling the d^r-q^r axis current components.

2.3 Implementation of Vector Control Technique

The practical configuration of a vector controlled voltage source inverter (VSI) fed interior permanent magnet synchronous motor (IPMSM) drive system is shown in Fig. 2.4. In the vector controlled IPMSM drive system, the motor is fed from a current controlled voltage source inverter. The current controller forces the actual motor current to follow the command currents as closely as possible in order to operate the motor at the command speeds. The feedback quantities in the vector control scheme are the rotor angular position and the actual motor currents. The command currents are synchronized to the rotor angular position in order to provide smooth starting of the drive system. The rotor position is measured by an optical incremental encoder mounted on the rotor shaft. The magnitude and frequencies of command currents are determined from the *d-q* axis command currents using the inverse Park transformation technique.

In Fig. 2.4, the command speed (ω_r*) is compared with the actual motor speed (ω_r). The speed error between the actual and command speeds is forwarded to the speed controller. The speed controller may include fixed gain or adaptive type controllers such as proportional integral (PI) controllers, proportional integral derivative (PID) controllers, adaptive neural network (NN) controllers, etc. The speed controller generates the command torque T_e* and hence the *q*-axis command current i_q^r* for the drive system. The

three-phase command and actual motor currents are processed in the current controller to generate the switching pulses for the inverter.

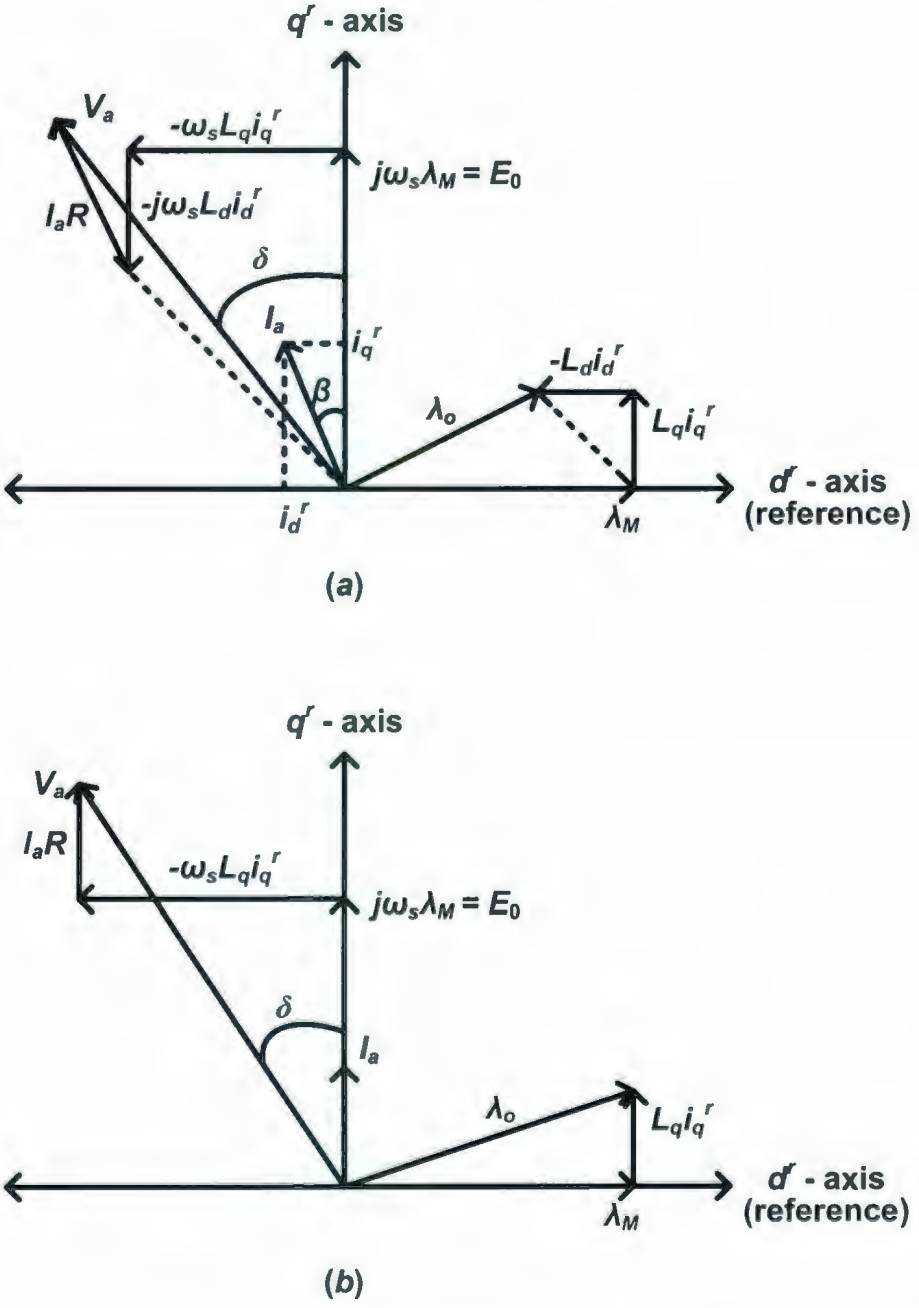

Figure 2.3: Basic vector diagram of the IPMSM: (*a*) general and (*b*) modified with $i_d^r = 0$.

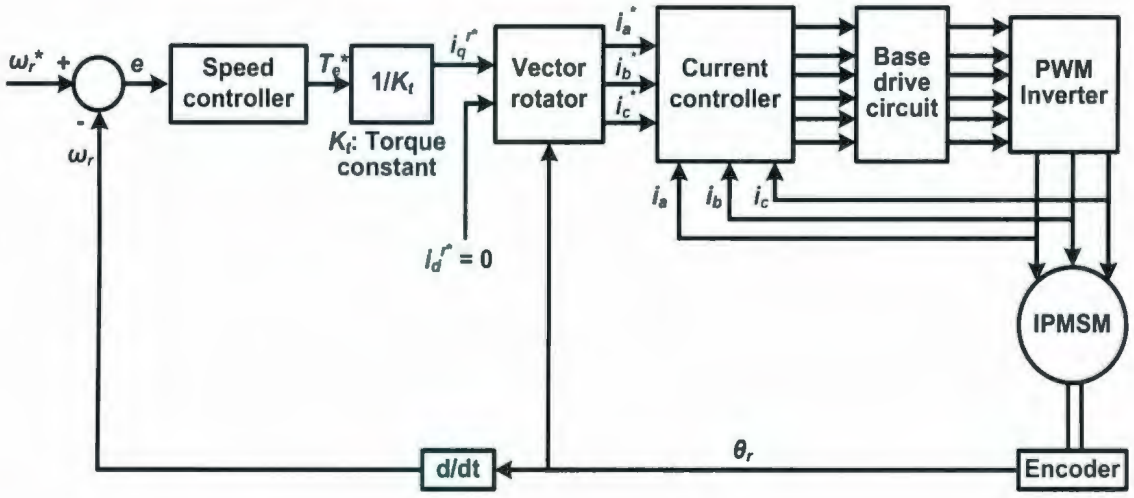

Figure 2.4: Block diagram of a vector controlled voltage source inverter (VSI) fed IPMSM drive system with $i_d^r = 0$.

In the following sub-sections, the mathematical models of the speed controller, the PWM voltage source inverter, and the current controller of a vector controlled VSI fed IPMSM drive system are presented.

2.3.1 Design of speed controllers

The conventional controllers such as the fixed gain PI, PID speed controllers and the adaptive controller such as neural network (NN) speed controller are implemented for standard and moderate performance IPMSM drive systems. The speed controller processes the speed error between command and actual speeds, and generates the command torque for the drive system. The change in speed ($\Delta\omega_r$) produces a corresponding change in torque (ΔT_e). Taking the load torque (T_L) as constant, the motor dynamic equation (2.24) can be rewritten as

$$\Delta T_e = J_m \frac{d(\Delta\omega_r)}{dt} + B_m \Delta\omega_r \tag{2.32}$$

The total change of torque is determined by integrating the equation (2.32) as

$$T_e = J_m \Delta\omega_r + B_m \int_0^t \Delta\omega_r(\tau)d\tau \tag{2.33}$$

The equation (2.33) represents the PI controller algorithm where the inertia constant (J_m) and damping coefficient (B_m) can be replaced by the proportional gain k_p and integral gain k_i, respectively. Thus the PI based speed controller can be defined as

$$T_e^* = K_p \Delta\omega_r + K_i \int_0^t \Delta\omega_r(\tau)d\tau \tag{2.34}$$

where $\Delta\omega_r = \omega_r^*$ - ω_r is the speed error between command speed (ω_r^*) and actual motor speed (ω_r) . In the Laplace domain, the PI controller algorithm can be written as

$$T_e^* = \left(K_p + \frac{K_i}{s}\right)\Delta\omega_r(s) \tag{2.35}$$

Now, after replacing the continuous terms of equation (2.34) by their finite differences, the discrete form of the PI controller algorithm can be written as

$$T^*(n) = T^*(n-1) + K_p\left[\Delta\omega_r(n) - \Delta\omega_r(n-1)\right] + K_i T_s \Delta\omega_r(n) \tag{2.36}$$

where $T^*(n)$ is the present sample of command torque, $T^*(n\text{-}1)$ is the past sample of command torque, $\Delta\omega_r(n)$ is the present sample of speed error, $\Delta\omega_r(n\text{-}1)$ is the past sample of speed error, and T_s is the sampling period. In the Laplace domain, the PID controller algorithm can be written as

$$T_e^* = \left(K_p + \frac{K_i}{s} + K_d\, s\right)\Delta\omega_r(s). \tag{2.37}$$

After replacing the continuous terms by their finite differences, the discrete form of the PID controller algorithm can be written as

$$T^*(n)=T^*(n-1)+K_p\left[\Delta\omega_r(n)-\Delta\omega_r(n-1)\right]+K_i T_s \Delta\omega_r(n) + \frac{K_d}{T_s}\left[\Delta\omega_r(n)-2\Delta\omega_r(n-1)+\Delta\omega_r(n-2)\right] \quad (2.38)$$

In this work, a neural network (NN) based adaptive speed controller has also been developed and implemented for the IPM motor drive system. The actual speed ($\omega_r(n)$), speed error ($\Delta\omega_r(n)$) between actual and command speeds, and change in speed error ($\Delta\omega_r(n)$- $\Delta\omega_r(n$-1)) of the IPM motor have been used as the inputs of the NN controller. The command torque ($T^*(n)$) for the drive system has been generated from the NN controller. The structure of the NN controller has been shown in Fig. 2.5. It has three layers which include input layer, hidden layer, and output layer. Three neurons have been used in the hidden layer of the NN controller. The number of hidden layers and number of neurons in the hidden layer have been chosen by trial and error. The '*tan-sigmoid*' type transfer function has been used in the hidden and output layers of the NN controller [97].

A combination of off-line and on-line trainings of the neural network controller has been used. The off-line training of the NN controller has been used in order to initialize the weights and biases of the hidden and output layers of the network. The off-line training data has been obtained experimentally from the closed loop IPMSM drive system. A PI type speed controller has been used in the speed control loop of the drive system during the experiment. The off-line training of the NN controller has been performed in the MATLAB software using the '*Neural Network*' toolbox [123]. The back propagation type training algorithm has been used for the continuous adaptation of the weights and biases of the NN controller during the on-line implementation. The gradient of cost function of speed error with respect to a parameter of the NN has been used to update the weights and biases of the NN controller. The learning rates for the weights and biases of the NN controller have also been updated on-line. This on-line updating of learning rate has been illustrated in the flow chart of Fig. 2.6. The time rate of change of speed error between actual and command speeds of the drive system have been used in the adaptation of learning rate of the NN speed controller.

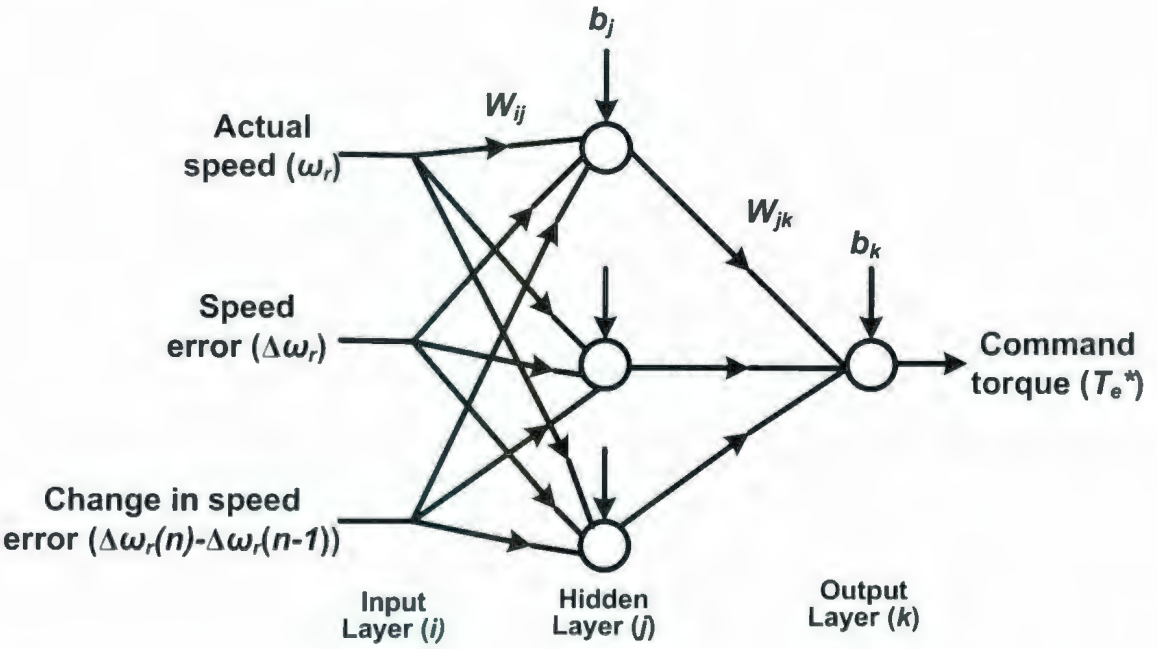

Figure 2.5: Three-layer structure of the neural network controller.

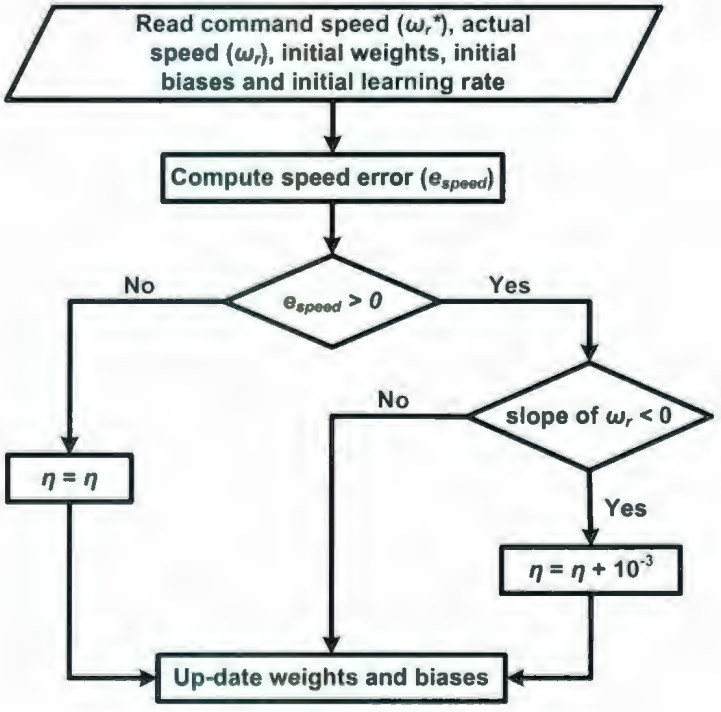

Figure 2.6: Flow chart of the adaptive learning of the NN controller.

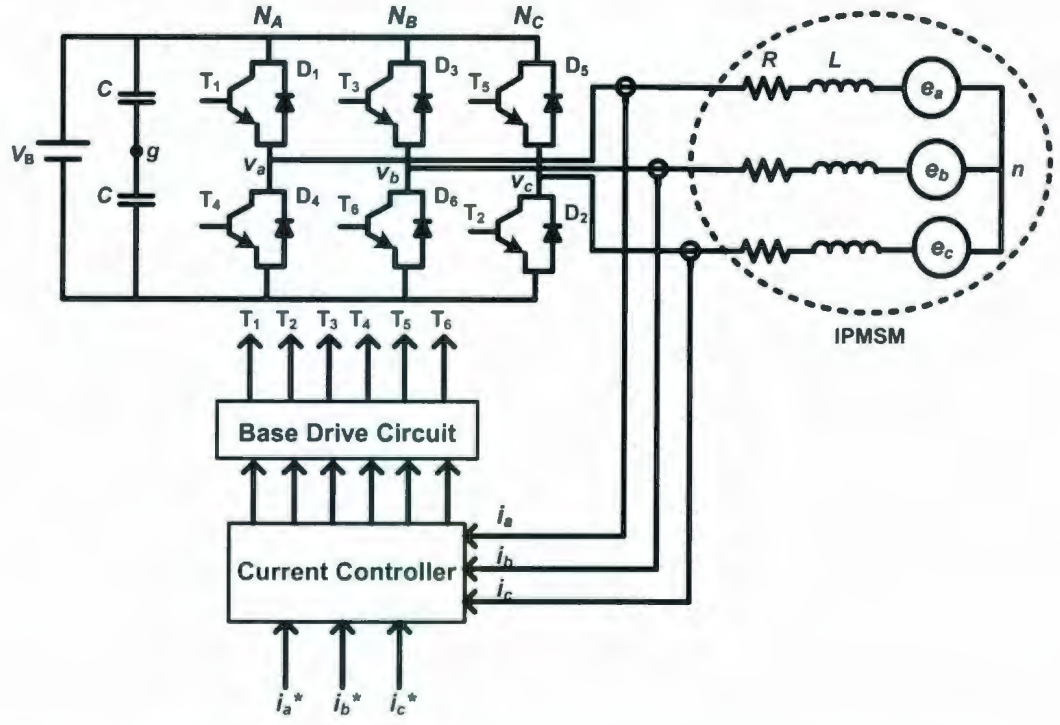

Figure 2.7: Schematic of a current controlled voltage source inverter of the IPMSM drive.

The IPMSM drive system has been simulated with the fixed gain PI, PID speed controllers and the adaptive NN based speed controller. The simulated results have been presented in section 2.4.

2.3.2 Vector rotator and PWM voltage source inverter

The vector rotator block of the IPMSM drive system of Fig. 2.4 transforms the quantities of the rotating rotor reference frame into the stator *a-b-c* reference frame. The inputs of this block are the d^r-q^r axis command currents (i_d^{r*}, i_q^{r*}) and the rotor position θ_r. The outputs are the three-phase command currents i_a^*, i_b^*, and i_c^* for the drive. In the transformation, the rotating d^r-q^r axis quantities are transformed into the stationary *d-q* axis quantities. Then, the stationary quantities are transformed into the stator *a-b-c* phase quantities. The operation of a current controlled voltage source inverter (VSI) for the IPMSM drive is analyzed using the circuit of Fig. 2.7. The stator phases of the IPMSM

are connected to three legs of the inverter. The neutral of the stator windings is uncoupled from the ground. The central point of two equal capacitors is taken as the ground. The error between the actual and command currents of the IPM motor is processed by the current controller to generate the control pulses for six switches $T_1,\ldots T_6$ of the inverter. In the figure, N_A, N_B, and N_C represent the three logic variables for three legs of the inverter.

The conduction states of the transistor switches for each leg of the inverter are determined using these logic variables. The transistor T_1 conducts when N_A is 1. The transistor T_4 conducts when N_A is 0. The voltage and current space vectors are considered for the analysis of current controller. The inverter voltage vector is defined as [98]

$$\bar{v} = \left(\frac{2}{3}\right)\left(v_a + \mathrm{a}v_b + \mathrm{a}^2 v_c\right) \tag{2.39}$$

where $\mathrm{a} = e^{j2\pi/3}$ and v_a, v_b, and v_c are phase voltages. Similarly, the inverter current vector is defined as

$$\bar{i} = \left(\frac{2}{3}\right)\left(i_a + \mathrm{a}i_b + \mathrm{a}^2 i_c\right). \tag{2.40}$$

Now if the logic variables are expressed as

$$[N] = \begin{bmatrix} N_A \\ N_B \\ N_C \end{bmatrix} V_B \tag{2.41}$$

then the phase voltages can be expressed in terms of the bus voltage (V_B) using the logic variables as

$$\begin{bmatrix} v_a \\ v_b \\ v_c \end{bmatrix} = \frac{1}{3}\begin{bmatrix} 2 & -1 & -1 \\ -1 & 2 & -1 \\ -1 & -1 & 2 \end{bmatrix}[N] = \frac{1}{3}\begin{bmatrix} 2 & -1 & -1 \\ -1 & 2 & -1 \\ -1 & -1 & 2 \end{bmatrix}\begin{bmatrix} N_A \\ N_B \\ N_C \end{bmatrix} V_B \tag{2.42}$$

There are eight switching combinations for six transistors of the inverter. So, the voltage vectors can be expressed as

$$\begin{aligned} \bar{v}_L &= \frac{2}{3} V_B e^{j(L-1)\frac{\pi}{3}} \quad \text{for } L=1,2,...,6 \\ &= 0 \qquad\qquad\qquad\quad \text{for } L=0,7 \end{aligned} \tag{2.43}$$

Table 2.1 summarizes the logic operation of the voltage source inverter under current control. Figure 2.8 shows the voltage vectors for eight switching states of the inverter. The magnitude of each voltage vector is $\frac{2}{3}V_B$ except v_0 and v_7. The voltage vectors v_0 and v_7 correspond to the freewheeling states of the inverter. The amplitudes of these vectors are equal to zero.

TABLE 2.1
LOGIC OPERATION OF THE VOLTAGE SOURCE INVERTER (VSI) UNDER CURRENT CONTROL

State (L)	Leg '*a*'		Leg '*b*'		Leg '*c*'		Operating modes	Voltage phasor
	T_1	T_4	T_3	T_6	T_5	T_2		
0	0	1	0	1	0	1	Freewheeling	v_0
1	1	0	0	1	0	1	Active	v_1
2	0	1	1	0	0	1	Active	v_2
3	1	0	1	0	0	1	Active	v_3
4	0	1	0	1	1	0	Active	v_4
5	1	0	0	1	1	0	Active	v_5
6	0	1	1	0	1	0	Active	v_6
7	1	0	1	0	1	0	Freewheeling	v_7

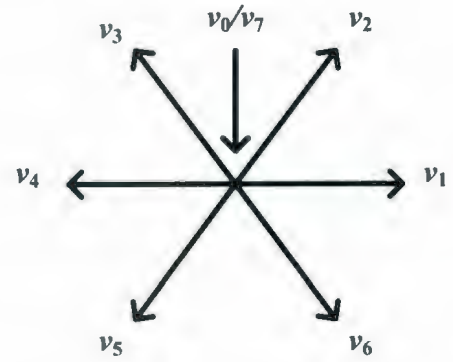

Figure 2.8: Inverter voltage vectors.

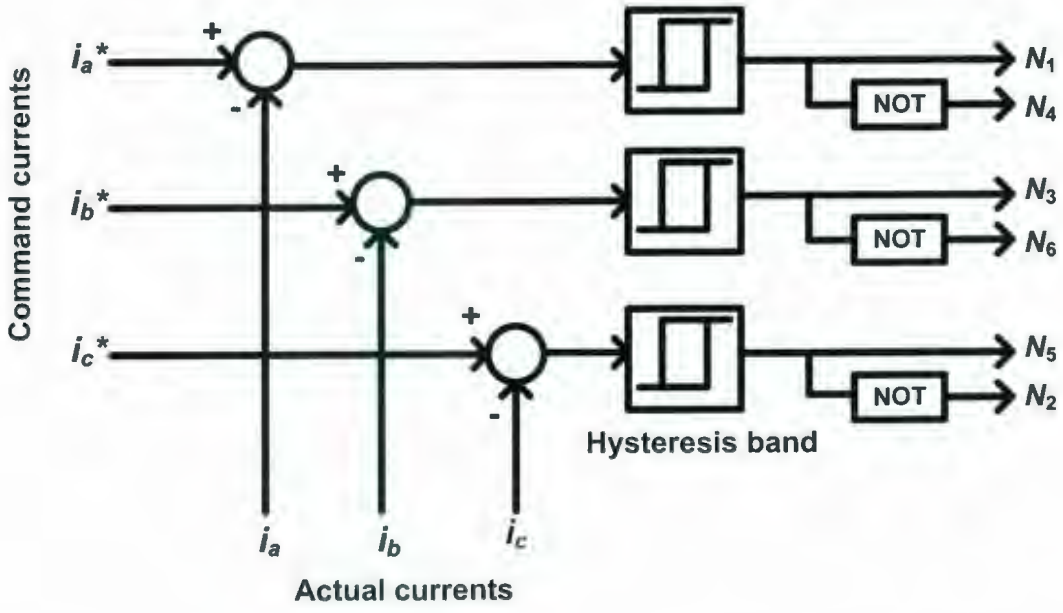

Figure 2.9: Block diagram of a three-phase hysteresis current controller.

2.3.3 Design of current controller

The current controller forces the motor currents to follow the command currents, which are generated from the command torque. The speed controller generates the command torque by processing the error between command and actual motor speed. Therefore, the current controller indirectly forces the motor to follow the command speed. The outputs of the current controller are the control pulses for the switches of the inverter. Among various current controller schemes, the hysteresis current controller is the most commonly used current controller for high performance drive applications. In addition, this type of controller is very simple to implement in real time. In the motor drive system, the hysteresis controller controls the motor current in such a way that it can follow the command current within a hysteresis band. The block diagram of a three-phase hysteresis current controller is shown in Fig. 2.10. Based on the type of hysteresis band, there are three types of hysteresis controllers. These are fixed band, sinusoidal band, and mixed band hysteresis controllers. These are shown in Figs. 2.10(*a*)–2.10(*c*), respectively. The logic signals N_1, N_3, and N_5 of Fig. 2.9 are considered for the switching of the upper leg transistors. The logic signals N_2, N_4, and N_6 of Fig. 2.7 are considered for the switching of the lower leg transistors. The transistor T_1 conducts when N_1 is 1. It is off when N_1 is 0. The operations of remaining logic signals are similar as the logic signal of N_1. In the hysteresis current controller, the upper and lower bands are defined by adding and subtracting a band limit H, respectively with the reference current (i_{ref}). These are defined as

$$i_{up} = i_{ref} + H \tag{2.44}$$

$$i_{low} = i_{ref} - H \tag{2.45}$$

If $i_a > i_{up}$, then the switching logic N_A equals 0. So, the inverter output voltage switches to negative in order to reduce the motor current. Similarly, if $i_a < i_{low}$, then the switching logic N_A equals 1. At this instant, the inverter output voltage switches to positive in order to increase the motor current. The band limit $H = c_1$ for the fixed band hysteresis controller, $H = d_1\sin(\omega_r t)$ for the sinusoidal band hysteresis controller, and $H =$

$c_2 + d_2\sin(\omega_r t)$ for the mixed band hysteresis controller. Here c_1, d_1, c_2, and d_2 are constants. The fixed band hysteresis controller of Fig. 2.10(a) shows low switching frequency. The harmonic content is also high at low command speeds. In the sinusoidal band hysteresis controller of Fig. 2.10(b), the switching frequency is very high near zero crossing. So, the operating frequency of the inverter increases. Another advantage of this scheme is that the harmonic content is low at both low and high command speeds. However, this controller follows the low command speed with a small steady state error. In the mixed band type hysteresis controller of Fig. 2.10(c), the hysteresis band varies sinusoidally plus a constant value around the reference. The performance of this controller compromises between maximum switching frequency and harmonic content of current [15]. However, the problems of sinusoidal band controller also remain in the mixed band controller. The performances of the mixed band controller are better than those of the fixed band controller but it increases the computational burden. Thus, the fixed band type hysteresis current controller with low computational complexity is used for the implementation of the vector control of the IPMSM drive system.

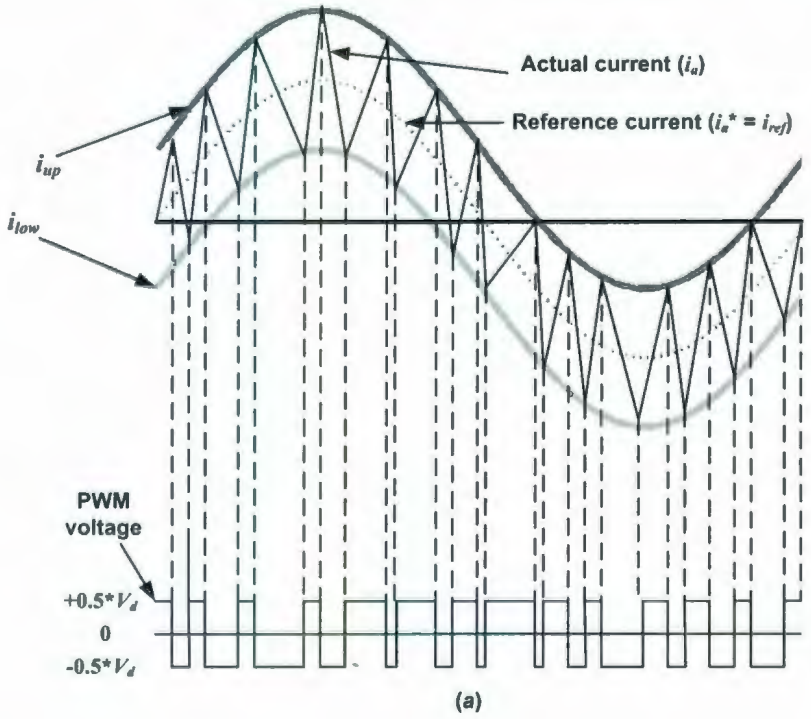

(a)

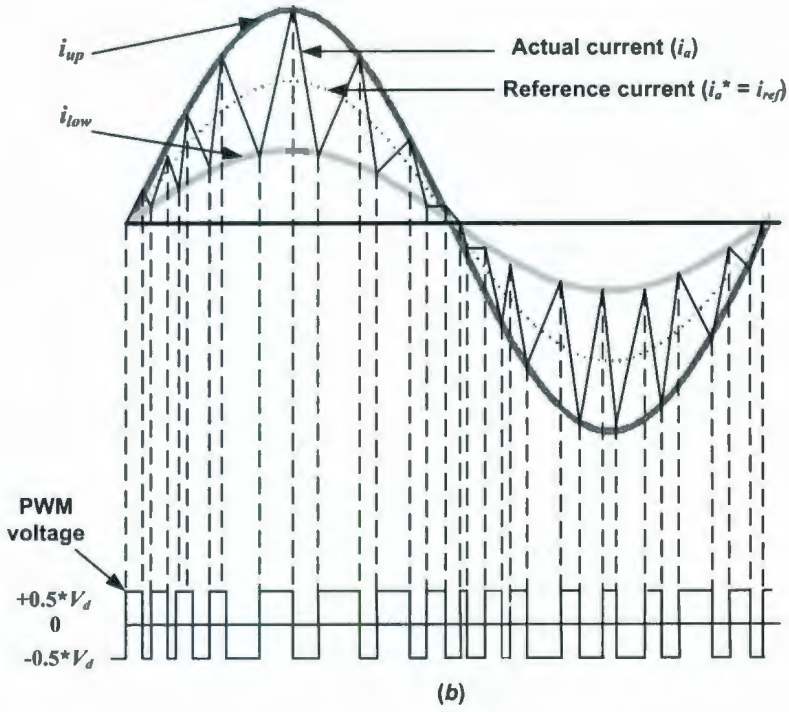

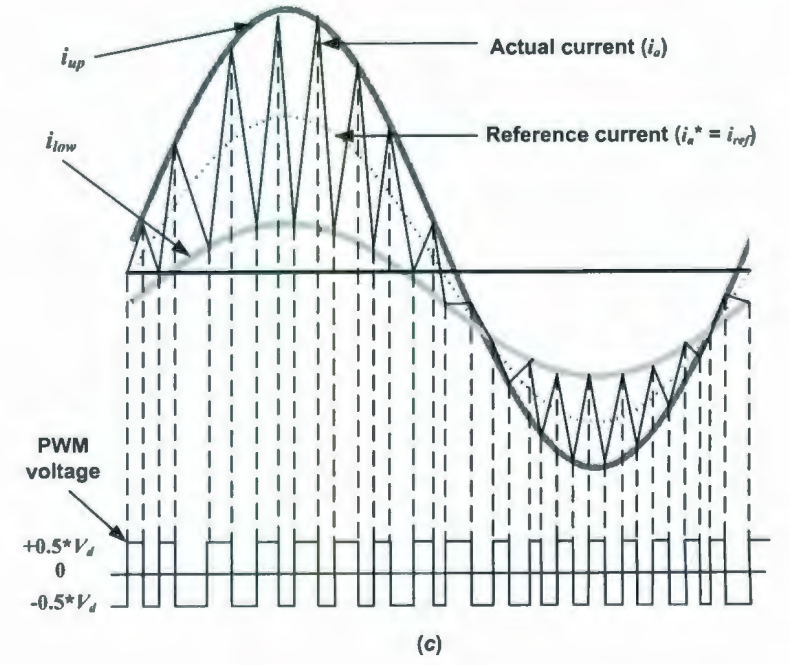

Figure 2.10: Current and PWM voltage waveforms: (*a*) fixed band hysteresis control, (*b*) sinusoidal band hysteresis control, and (*c*) mixed band hysteresis control.

2.4 Simulation of the Conventional Speed Controllers Based IPMSM Drive System

The computer simulation of the hysteresis current controlled voltage source inverter (VSI) fed IPMSM drive system incorporating the fixed gain and adaptive speed controllers has been carried out in the MATLAB software. The speed controllers such as the fixed gain PI, PID controllers and an adaptive neural network (NN) controller have been investigated. The schematic diagram of the complete drive system is shown in Fig. 2.4. The inverter transistors have been modeled as ideal switches with zero turn-on and zero turn-off times. The control algorithms have been developed using the m-file format of the MATLAB software. Both transient and steady state operating conditions of the drive system have been investigated. The IPMSM circuit parameters and the command speed (ω_r^*) have been used as the inputs for the MATLAB simulation models. The speed and current responses of the IPMSM simulation model have been investigated.

2.4.1 Results and discussions

Figures 2.11–2.16 show the simulated speed and current responses of the conventional and adaptive speed controllers based IPMSM drive system. The fixed gain PI, PID speed controllers and the adaptive neural network (NN) speed controller are used in the simulation. It is to be noted that the NN speed controller is trained appropriately for different operating conditions of the drive system. The weights and biases of the NN controller are updated continuously through the adaptive learning of the network during the simulation.

The simulated starting speed responses of the drive system using the PI, PID, and NN speed controllers are shown in Figs. 2.11(*a*), 2.11(*b*), and 2.11(*c*), respectively. In these cases, the drive system is started at no load for the command speed of 188.6 rad/sec. Figures 2.12(*a*), 2.12(*b*), and 2.12(*c*) show the corresponding current responses. The PI and PID speed controllers based starting speed responses of Figs. 2.11(*a*)–2.11(*b*) suffer from large overshoot/undershoot and take long settling time (0.5 sec) to reach the steady state command speed. The IPMSM drive system using the properly trained NN

controller for this particular condition follows the command speed after 0.25 sec with slight overshoot and undershoot in Fig. 2.11(*c*).

The simulated speed responses of the drive system using the PI, PID, and NN speed controllers for step increase and step decrease of command speeds are shown in Figs. 2.13(*a*), 2.13(*b*), and 2.13(*c*), respectively at the rated load condition. Figures 2.14(*a*), 2.14(*b*), and 2.14(*c*) show the corresponding current responses of the drive system for this condition. It is evident from Figs. 2.13(*a*)–2.13(*c*) that the performances of the PI, PID, and NN speed controllers based drive systems are affected for a step change in command speeds. Figures 2.15(*a*), 2.15(*b*), and 2.15(*c*) show the simulated speed responses of the IPMSM drive system incorporating the PI, PID, and NN controllers, respectively for a step change in load. Figures 2.16(*a*), 2.16(*b*), and 2.16(*c*) show the corresponding current responses of drive system for this condition. The speed responses of the drive system incorporating the PI and PID speed controllers of Figs. 2.15(*a*)–2.15(*b*) show large undershoot and overshoot at the instant of load impact. The speed response of the NN controller based drive system of Fig. 2.15(*c*) also shows slight undershoot and overshoot at the instant when the load is applied. Simulations are also carried out for the low command speed and for variations in parameter, which include changes in rotor inertia and stator resistance. The performances of the fixed gain speed controllers based drive systems are not satisfactory under these operating conditions.

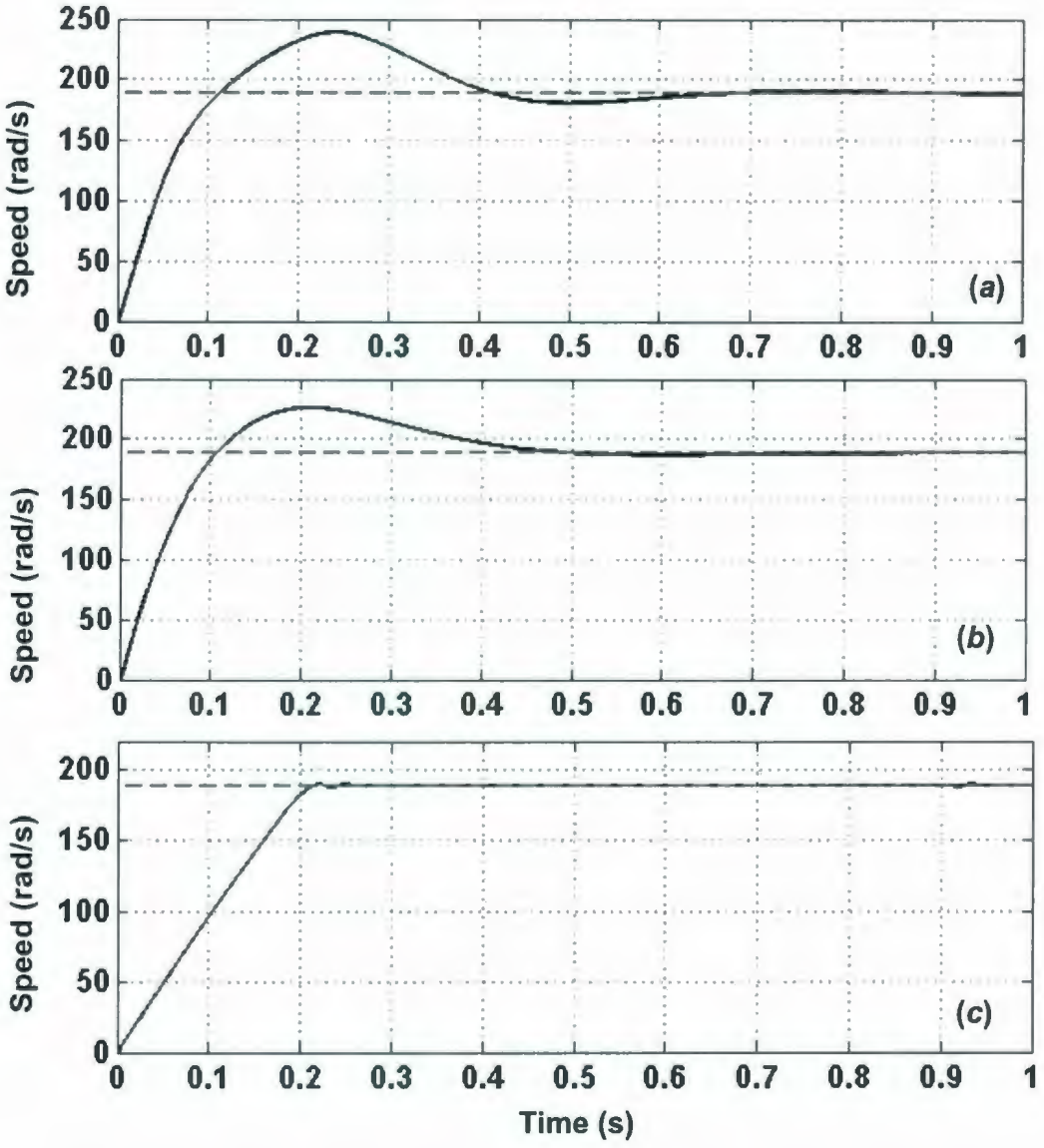

Figure 2.11: Simulated starting speed responses of the IPMSM drive system under no load and rated command speed (188.6 rad/sec.) conditions: (*a*) PI controller, (*b*) PID controller, and (*c*) adaptive NN controller.

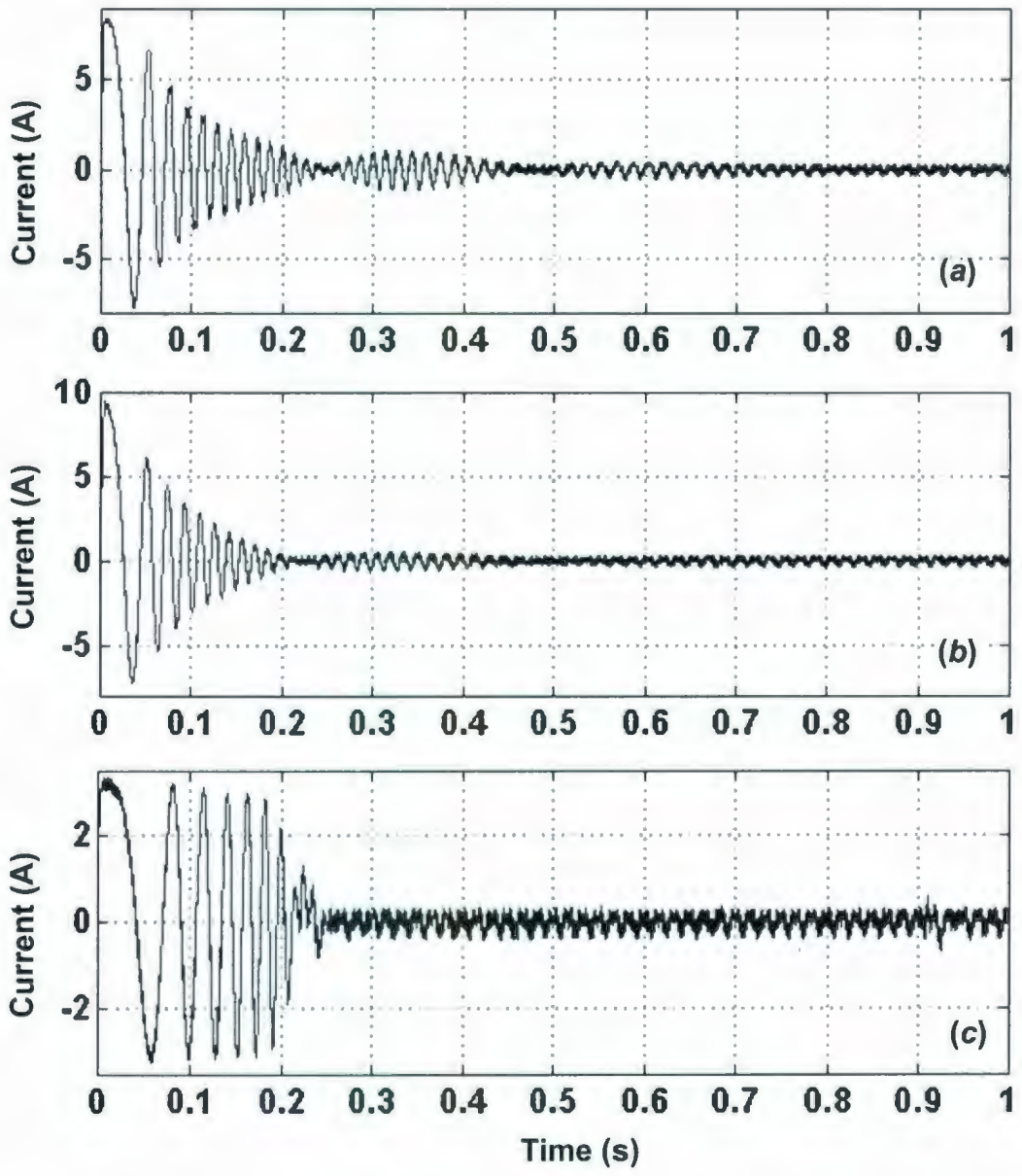

Figure 2.12: Simulated starting current responses of the IPMSM drive system under no load and rated command speed (188.6 rad/sec.) conditions: (*a*) PI controller, (*b*) PID controller, and (*c*) adaptive NN controller.

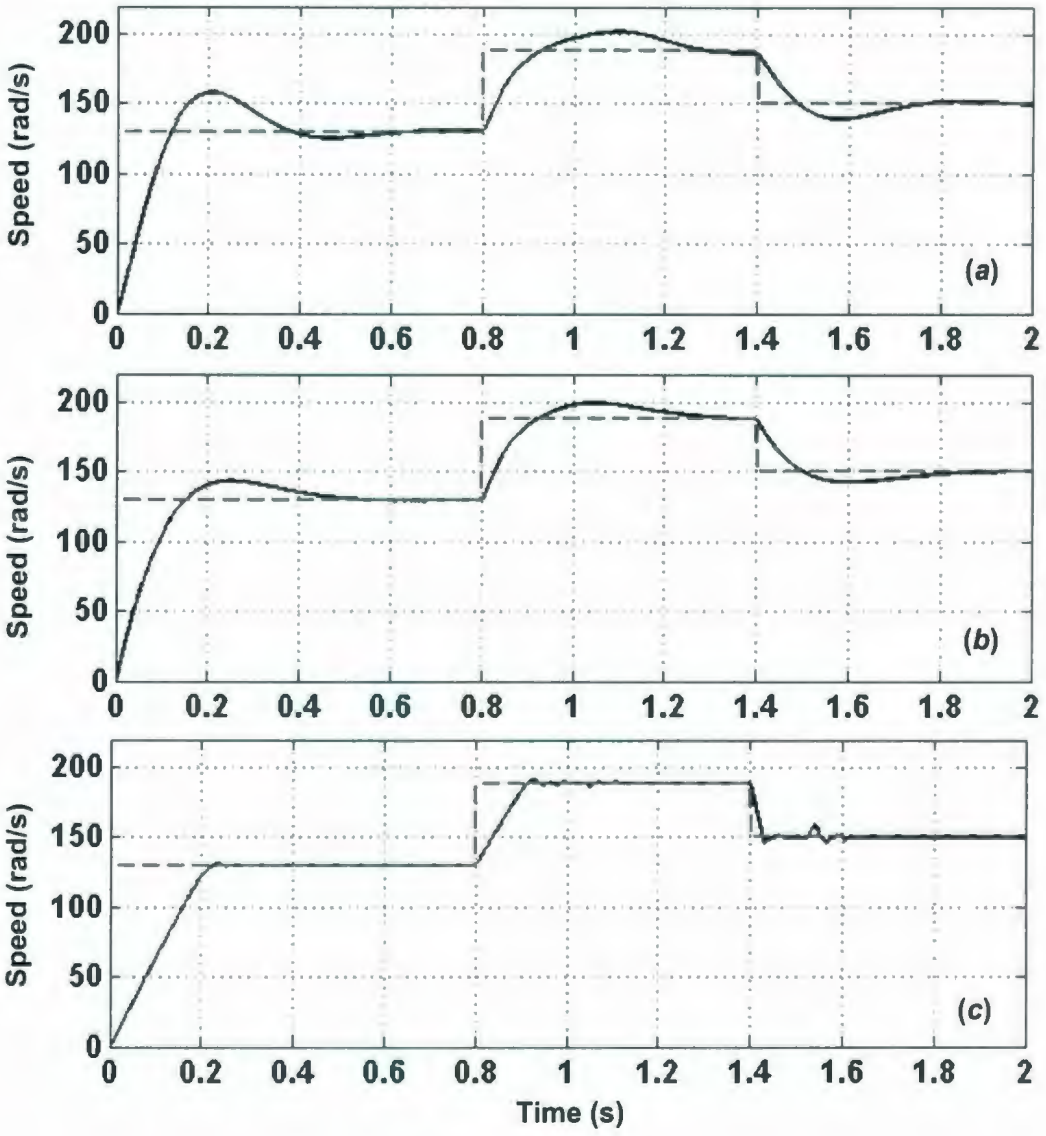

Figure 2.13: Simulated speed responses of the IPMSM drive system for step increase (from 130 rad/sec. to 188.6 rad/sec.) and step decrease (from 188.6 rad/sec. to 150 rad/sec.) of command speeds under rated load condition: (*a*) PI controller, (*b*) PID controller, and (*c*) adaptive NN controller.

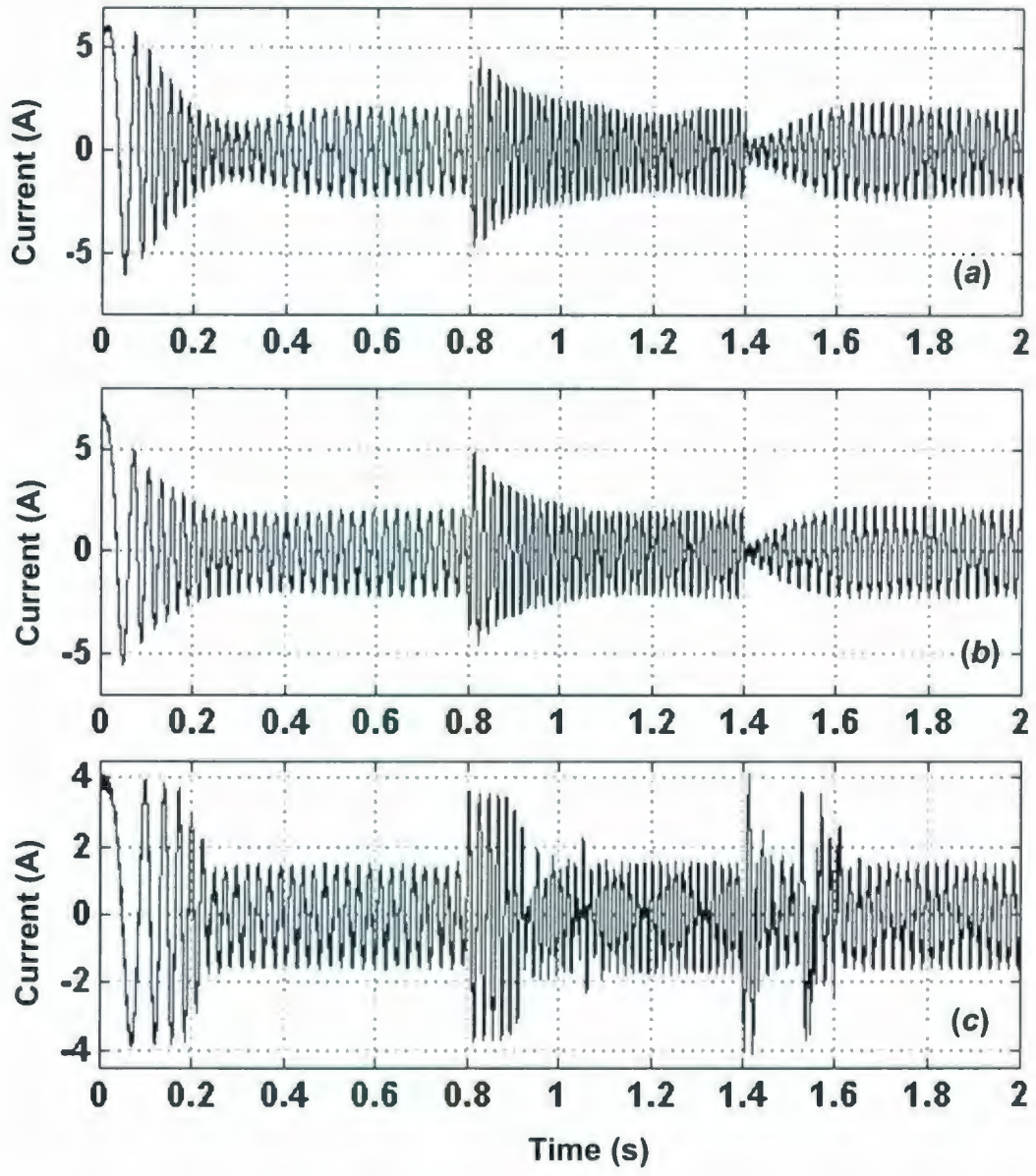

Figure 2.14: Simulated current responses of the IPMSM drive system for step increase (from 130 rad/sec. to 188.6 rad/sec.) and step decrease (from 188.6 rad/sec. to 150 rad/sec.) of command speeds under rated load condition: (*a*) PI controller, (*b*) PID controller, and (*c*) adaptive NN controller.

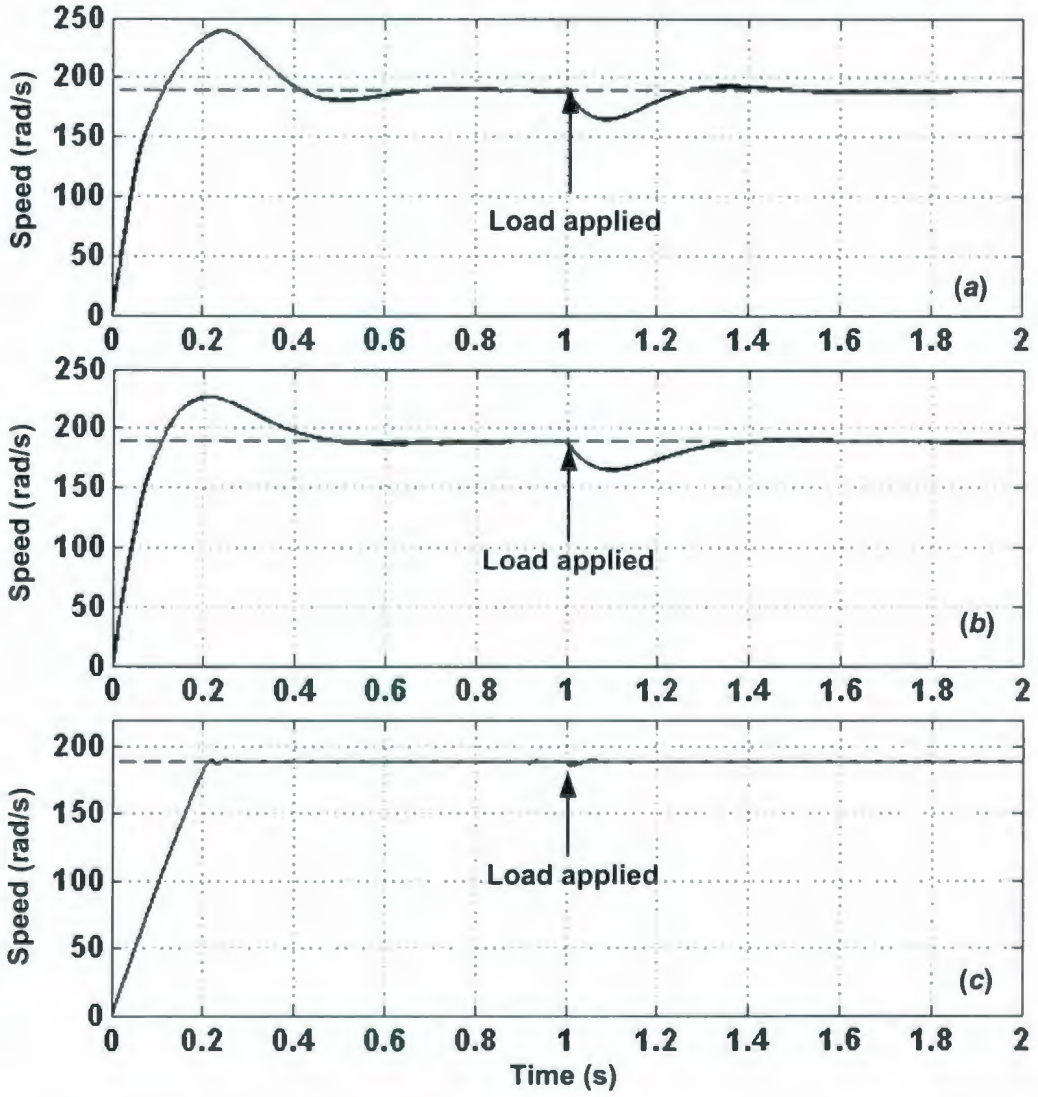

Figure 2.15: Simulated speed responses of the IPMSM drive system when load is changed at t = 1 sec. from no load to rated load under rated command speed (188.6 rad/sec.) condition: (*a*) PI controller, (*b*) PID controller, and (*c*) adaptive NN controller.

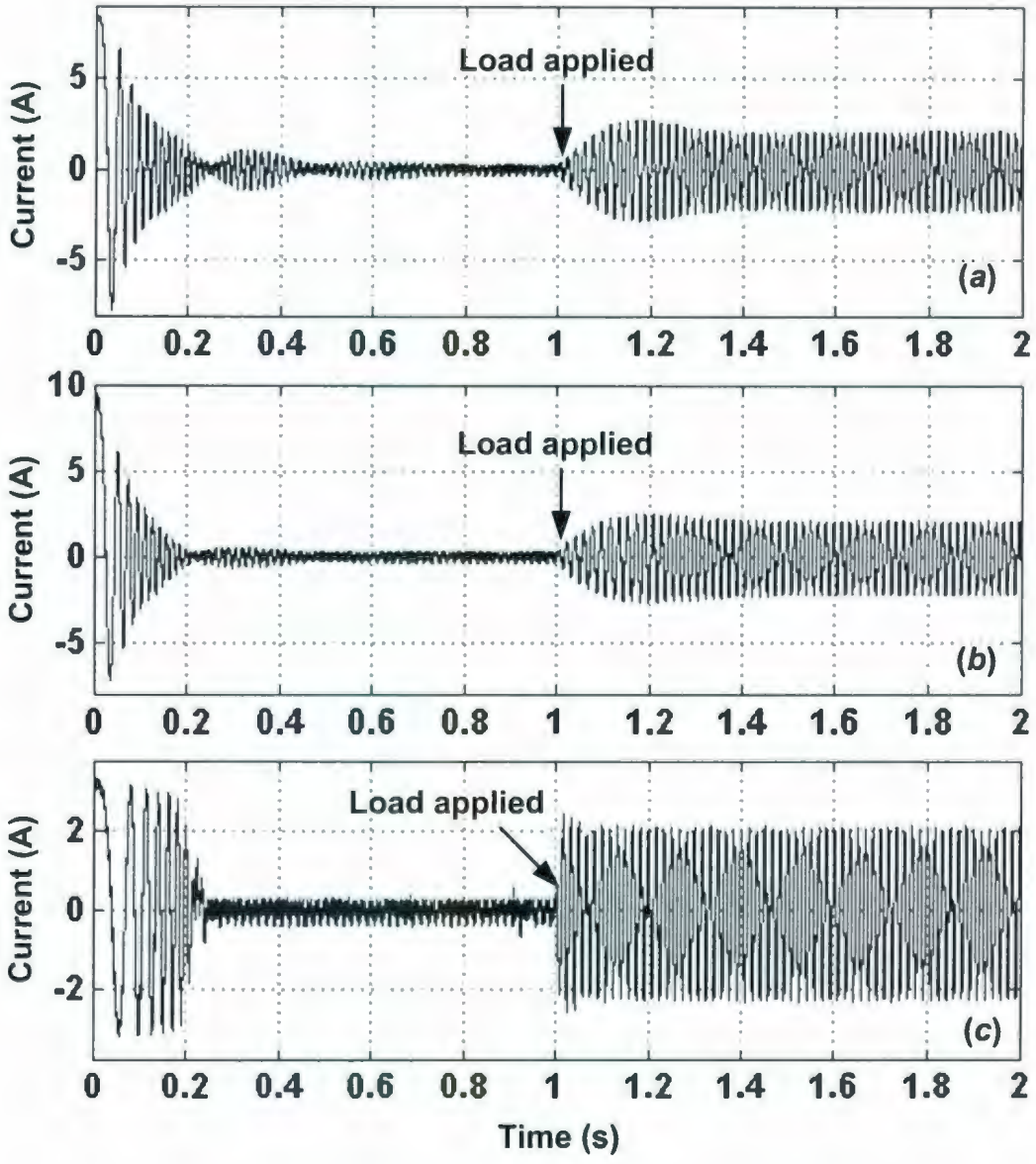

Figure 2.16: Simulated current responses of the IPMSM drive system when load is changed at t = 1 sec. from no load to rated load under rated command speed (188.6 rad/sec.) condition: (*a*) PI controller, (*b*) PID controller, and (*c*) adaptive NN controller.

2.5 Concluding Remarks

In this chapter, the vector control technique has been developed and implemented for the IPMSM drive system. The mathematical model of an IPMSM has been formulated and integrated with the vector control technique. The discrete models of the fixed gain PI and PID speed controllers have been presented and implemented for the drive system. An adaptive NN speed controller has also been developed and implemented for the IPMSM drive system. The hysteresis type current controller has been used to generate the control pulses for the inverter switches. The models of hysteresis current controllers have been presented and explained through figures 2.10(*a*)–2.10(*c*). The fixed band type hysteresis controller has been used for the implementation of the IPMSM drive system. The drive performances using the conventional speed controllers and the hysteresis current controller are investigated in simulation. From the simulated system performances, it can be concluded that the conventional speed controllers are not quite suitable for real time applications where the performances of the drive system are adversely affected by nonlinear load characteristics, parameter variations, and magnetic saturation. Thus, there exists a need to develop and implement an intelligent controller in real time for the IPMSM drive system. Since the wavelet transforms have the ability to better manage non-linear control problems like in IPM motors, and there are also other trends of research activities on the applications of wavelet transforms in ac motor drives, the performances of the IPMSM drive system using the wavelet based speed controller need to be explored in the next chapter.

Chapter 3

High Speed Control of the IPMSM

The interior permanent magnet synchronous motor (IPMSM), which has magnets securely embedded inside the rotor iron, offers wider speed control due to it's physical and operational features. For applications requiring a wide speed range of the IPMSM, the flux-weakening control can be applied. A substantially increased speed range of the IPMSM can be obtained by the flux-weakening control, which allows a constant power operation at speeds higher than the base speed. The field flux, which is proportional to the back emf and inversely proportional to the speed, needs to be decreased in order to operate the motor above the base speed within the rated voltage and current capacity of the motor and the inverter. However, the direct control of field flux is not available in the case of the IPMSM. The field flux can be weakened by the demagnetizing effect due to the *d*-axis armature reaction. In the flux-weakening control, the voltage and current remain fixed to their maximum value above the base speed. The operation above the base speed is called the constant power mode of operation [95], [99]–[100].

The performances of the IPMSM drive system up to the base speed are presented in chapter two. Here, the assumption of $i_d^r = 0$ is considered in the design of the controllers for the drive system. However, the drive system could not be operated above the base speed with the assumption of $i_d^r = 0$. In addition, the system suffered from

instability with this assumption even below the base speed. In this chapter, the performances of the IPMSM drive system over a wide speed range are presented. The scheme includes the maximum torque per ampere (MTPA) operation in the constant torque region below the base speed and the flux-weakening (FW) operation in the constant power region above the base speed. The power capacities of the motor and the inverter are considered in the design of the high speed control scheme. The performances of the IPMSM drive system over the wide speed range are evaluated by simulation and experimental results. Finally, the comparative performances between the $i_d^r = 0$ control technique and the proposed FW control technique where $i_d^r \neq 0$ are presented.

3.1 Flux Weakening Control Principle

The speed control above the rated speed of the inverter fed IPMSM can be achieved by means of flux-weakening control. The air gap induced emf in an ac machine is given by [121]

$$E = 4.44 k_\omega \phi_f f_s N_1 \tag{3.1}$$

where k_ω is the stator winding factor, ϕ_f is the peak air gap flux, f_s is the supply frequency, and N_1 is the number of stator turns per phase. Neglecting the stator impedance, the induced emf approximately equals the stator phase voltage V_a. Using $\omega_s = P\omega_r$, the equation (3.1) can be re-written as

$$\omega_r = \frac{V_a}{k_b \phi_f} \tag{3.2}$$

where k_b is the constant and ω_r is the rotor speed. In equation (3.2), the motor speed is inversely proportional to air gap flux for fixed supply voltage. In other words, speed increases with decrease of flux. In vector control scheme of the IPMSM, the flux producing current component is the d^r -axis current i_d^r. The air gap flux can be controlled by adjusting the d^r -axis current by artificially injecting negative value of i_d^r resulting lower value of air gap flux.

The mathematical model of an IPMSM for assumed sinusoidal stator excitation can be described by the following equations in a synchronously rotating rotor d^r-q^r axis reference frame as [92]–[93]

$$\begin{bmatrix} v_d^r \\ v_q^r \end{bmatrix} = \begin{bmatrix} R + pL_d & -P\omega_r L_q \\ P\omega_r L_d & R + pL_q \end{bmatrix} \begin{bmatrix} i_d^r \\ i_q^r \end{bmatrix} + \begin{bmatrix} 0 \\ P\omega_r \lambda_M \end{bmatrix}. \tag{3.3}$$

The electromagnetic developed torque can be calculated as

$$T_e = \frac{3P}{2}\left[\lambda_M i_q^r + (L_d - L_q) i_d^r i_q^r\right]. \tag{3.4}$$

The motor dynamics can be described by the following equation as

$$T_e = J_m \frac{d\omega_r}{dt} + B_m \omega_r + T_L. \tag{3.5}$$

The symbols of equations (3.3)–(3.5) are defined in chapter two. The first term of equation (3.4) represents the magnet torque due to the permanent magnet flux (λ_M) and the second term represents the reluctance torque due to the complex interaction of d-q axis currents and inductances of the IPMSM. The q-axis inductance (L_q) is higher than the d-axis inductance (L_d), and the d-axis current (i_d^r) is negative for the case of the IPMSM. So, the reluctance torque component of the IPMSM is a positive quantity and can be utilized for high performance applications. However, the complexity of the control arises due to the non-linear nature of the torque equation (3.4) for the IPMSM drive system. In order to make the torque equation linear and the control task easier, usually, i_d^r is set to zero. However, in an actual IPMSM drive, it is inappropriate to set $i_d^r = 0$. This assumption also leads to erroneous results [101]. The i_d^r is not set to zero in this research. The value of i_d^r is calculated from i_q^r maintaining the stator voltage and current within the ratings of the motor and the inverter. From the phasor diagram of the IPMSM of Fig. 2.3(a), the stator phase voltage and current can be related to the d–q axis voltages and currents as

$$\hat{V}_a = V_a \angle \delta = v_d^r + j v_q^r \tag{3.6}$$

$$\hat{I}_a = I_a \angle \beta = i_d^r + j i_q^r. \tag{3.7}$$

It is seen from equations (3.3) and (3.6) that in case of the $i_d^r = 0$ control, the magnitude of the terminal voltage V_a increases with an increase in motor speed ω_r or an increase in the q-axis current i_q^r. Therefore, the saturation of the current regulator occurs at high speeds for a given torque, which may cause instability of the drive. Below the base speed, the absolute value of the stator current (I_a) is kept constant at its maximum value (I_m) in order to calculate the i_d^r in terms of i_q^r for the MTPA control. Differentiating equation (3.4) with respect to i_q^r and setting it to zero, the i_d^r is obtained as

$$i_d^r = \frac{\lambda_M}{2\left(L_q - L_d\right)} - \sqrt{\frac{\lambda_M^2}{4\left(L_q - L_d\right)^2} + \left(i_q^r\right)^2}. \tag{3.8}$$

Substituting (3.8) in (3.4), a nonlinear relationship between i_q^r and T_e can be presented as

$$T_e = \frac{3P}{2}\left(\frac{\lambda_M i_q^r}{2} + \left(L_q - L_d\right)\sqrt{\frac{\left(\lambda_M i_q^r\right)^2}{4\left(L_q - L_d\right)^2} + \left(i_q^r\right)^4} \right). \tag{3.9}$$

The expressions (3.8) and (3.9) overburden the DSP implementation of the drive system. In order to solve this problem, a simpler relationship between i_d^r and i_q^r is obtained by expanding the square root term of equation (3.8) using the Maclaurin series expansion as

$$i_d^r \approx -0.11825 * \left(i_q^r\right)^2 + 0.00165 * \left(i_q^r\right)^4. \tag{3.10}$$

The numerical values of equation (3.10) are obtained using the IPMSM parameters. The parameters are given in Appendix A, and the detailed derivations of equation (3.10) are given in Appendix D. The multiplying factor with the subsequent i_q^r term of the square root expansion of equation (3.8) becomes very small with the increasing order of i_q^r. These terms are assumed negligible for the sake of brevity. The larger value of i_q^r also

causes saturation and non-linearity. Now, expanding the square root term of equation (3.9) using the Maclaurin series expansion and neglecting the third and higher order terms, a simpler relationship between i_q^r and T_e can be obtained as

$$i_q^r \approx 1.0616 * T_e. \tag{3.11}$$

The detailed derivation of equation (3.11) is given in Appendix D.

Above the base speed, the steady state current i_d^r can be calculated in terms of i_q^r in order to maintain the absolute value of stator phase voltage (V_a) constant at its maximum value of V_m. The i_d^r for this condition is obtained from equations (3.3) and (3.6) by neglecting the voltage drop across the stator resistance as

$$i_d^r = -\frac{\lambda_M}{L_d} + \frac{1}{L_d}\sqrt{\frac{(V_m')^2}{P^2\omega_r^2} - \left(L_q i_q^r\right)^2} \tag{3.12}$$

where V_m' is the maximum stator phase voltage neglecting the stator resistance voltage drop of equation (3.3), and it is defined as

$$V_m' = \sqrt{\left(v_{d0}^r\right)^2 + \left(v_{q0}^r\right)^2}, \tag{3.13}$$

$$\text{where,} \quad v_{d0}^r = -P\omega_r L_q i_q^r, \tag{3.14}$$

$$\text{and} \quad v_{q0}^r = P\omega_r L_d i_d^r + P\omega_r \lambda_M. \tag{3.15}$$

Here, the subscript 'o' refers to the reference. The maximum amplitude of the stator phase voltage (V_m), which can be sustained by the inverter without saturation of the current regulator, is modeled as a function of the dc bus voltage (V_B). It is defined as

$$V_m = \frac{2}{\pi} V_B. \tag{3.16}$$

Now, in order to overcome the burden for the DSP implementation of the flux-weakening control, the Maclaurin series expansion is applied again to the square root term of equation (3.12), and a simpler relationship between i_d^r and i_q^r can be obtained as

$$i_d^r = -7.398 + \frac{2249.06}{\omega_r}\left[1 - 0.000000347 \times \left(i_q^r \omega_r\right)^2\right]. \tag{3.17}$$

The detailed derivation of equation (3.17) is given in Appendix D. In the above expression of i_d^r, the stator resistance voltage drop is neglected, and the dc bus voltage (V_B) is set to 300 volt. Equation (3.12) represents an ellipse in the *d-q* plane, which indicates that an increase in rotor speed results in smaller ranges for the current vector. So, the amplitude of the terminal voltage can be adjusted to V_m by appropriately controlling the *d*-axis current i_d^r. The flux-weakening control not only extends the operating limits of IPMSM drive but also relieves the current regulator from saturation that occurs at high speed operation [102]. Figure 3.1 shows the typical torque-speed and power-speed characteristic curves of an IPM motor over a wide range of operating speed. Based on the above FW control algorithm, the block diagram of the complete IPMSM drive is shown in Fig. 3.2. The maximum attainable speed for a given set of stator voltages and currents can be obtained from equation (3.12). The torque producing current component will be zero at the maximum speed. Thus the maximum operating speed of the IPMSM for a set of maximum stator voltage and current can be calculated as [102]

$$\omega_{r\max} = \frac{V_m'}{P\left(L_d I_a + \lambda_M\right)} = \frac{\sqrt{V_m^2 - \left(I_a R\right)^2}}{P\left(L_d I_a + \lambda_M\right)}. \tag{3.18}$$

Here, P is the number of pole pair. The maximum attainable speed of the IPMSM can also be expressed as [102]

$$\omega_{r\max} = \frac{V_m}{P\lambda_M} \tag{3.19}$$

At the critical speed operating region, the rotational speed of the IPM motor is equal to the numerical value of the natural vibration of the rotor shaft. The critical speed has been labeled in Fig. 3.1. The magnet flux is demagnetized further in order to operate the motor above the critical speed. As a result, the electromagnetic torque reduces above the critical speed of Fig. 3.1. However, the power also reduces because of the vibration of the motor and the limitation of the power ratings of the inverter.

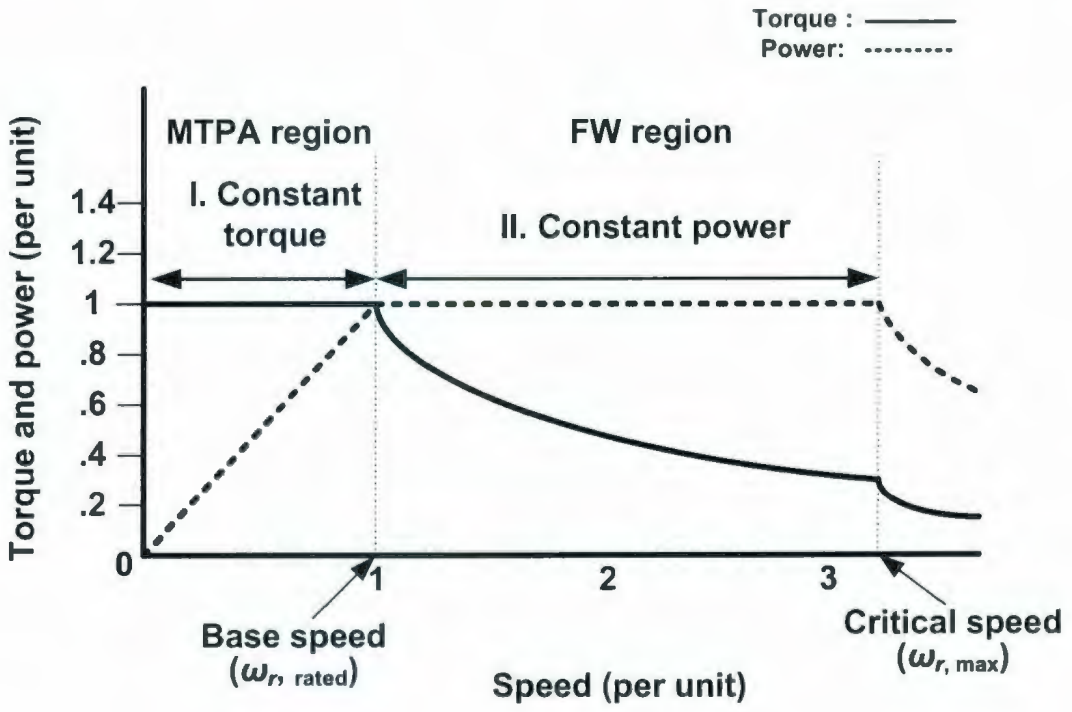

Figure 3.1: Typical torque-speed and power-speed characteristic curves of an IPM motor over a wide range of operating speed.

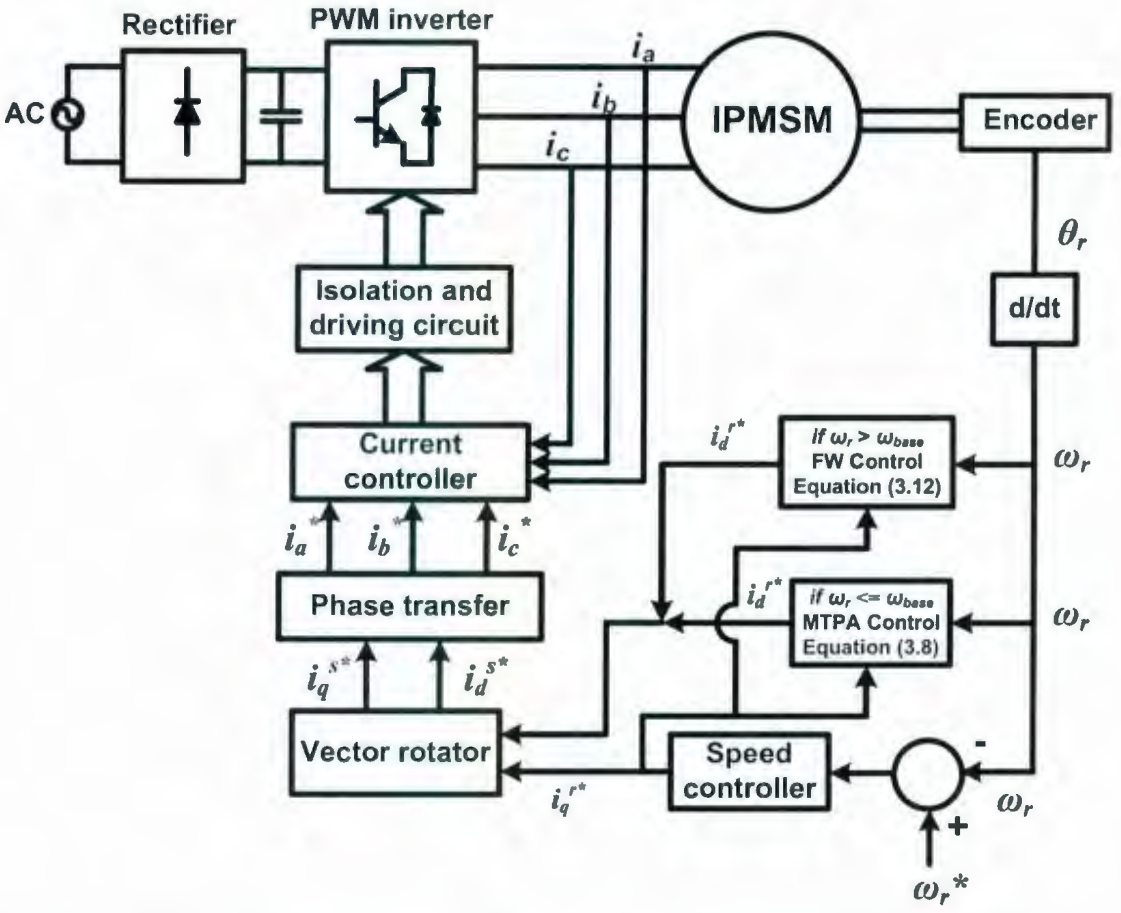

Figure 3.2: Block diagram of the complete IPMSM drive system incorporating the flux-weakening operation.

3.2 Implementation of the Flux Weakening Control

The complete IPMSM drive system incorporating the maximum torque per ampere (MTPA) and flux-weakening (FW) control techniques has been implemented in both simulation and real time. The drive system has been simulated using the MATLAB software package [90]. The dSPACE ds1102 digital signal processor (DSP) controller board [103] has been used for the real time implementation of the drive system. The control algorithm has been developed using the high level C programming language, and has been downloaded to the dSPACE control module using the DSP loader program for the real time implementation. The flow chart for the real time implementation of the

MTPA and FW control algorithms of the IPMSM drive system using a DSP board has been shown in Fig. 3.3.

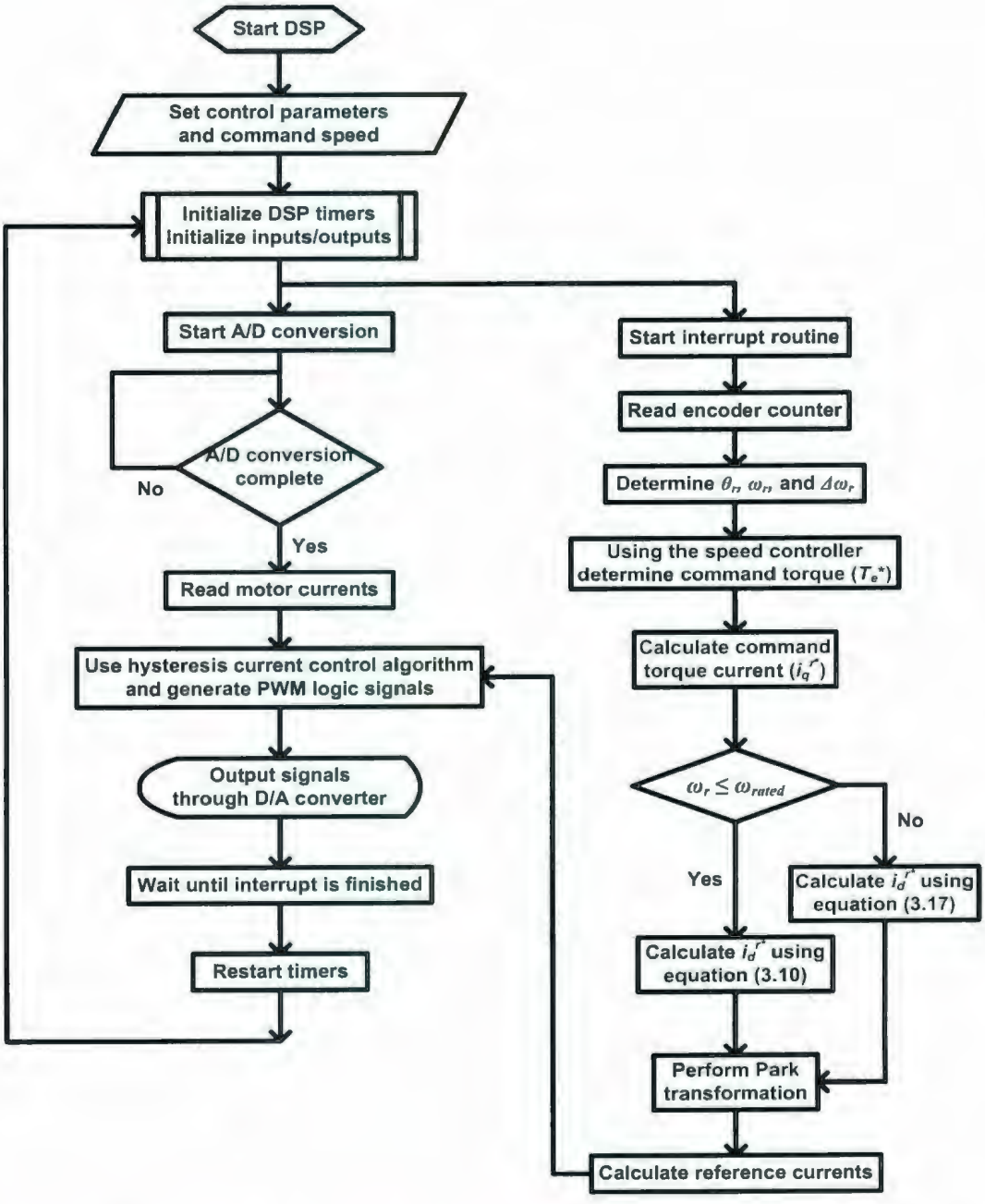

Figure 3.3: Flow chart for the real time implementation of the proposed MTPA and FW control algorithms of the IPMSM drive system.

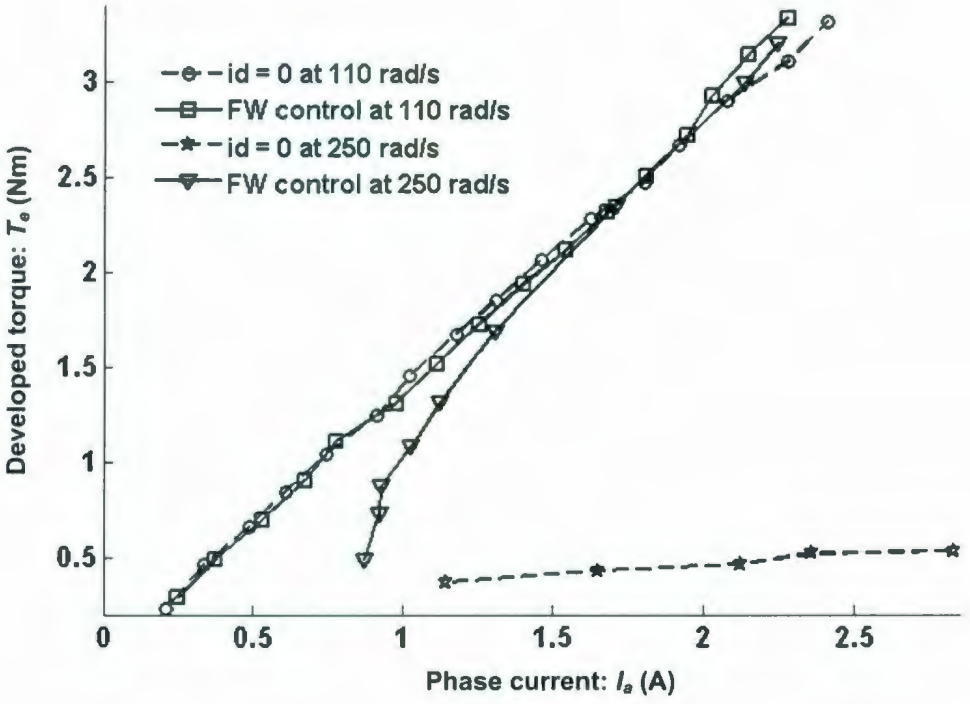

Figure 3.4: Variation of the steady state developed torque with phase-*a* current of the IPMSM drive for the command speeds of 110 rad/sec. and 250 rad/sec. incorporating the $i_d^r = 0$ control technique and the flux weakening (FW) control technique with $i_d^r \neq 0$.

3.3 Results and Discussions

The performances of the IPMSM drive system have been investigated in both simulation and experiments. The variations of steady state developed torque with the phase-*a* current of the IPMSM using the $i_d^r = 0$ control technique and using the flux-weakening (FW) control technique with $i_d^r \neq 0$ have been shown in Fig. 3.4. The variation of developed torque has been investigated both at the low command speed of

110 rad/sec. and at the high command speed of 250 rad/sec. In Fig. 3.4, the drive system with the FW control has developed more torque than with the $i_d^r = 0$ control for the same stator current of the drive system at both low and high command speeds of 110 rad/sec and 250 rad/sec., respectively. So, the drive system with the FW control can carry higher load while maintaining stability. The transient and steady state simulated responses of the drive system using the MTPA and FW control techniques have been shown in Fig. 3.5 for step changes of command speeds at no load operating condition. The drive system has followed the command speeds smoothly in both the constant torque and constant power modes of operation of the IPMSM. In the constant torque region of the IPMSM, the steady state command torque current (i_q^{r*}) has been settled to constant value while the steady state command flux current (i_d^{r*}) has become zero. However, the command flux current (i_d^{r*}) has become more negative at the starting with the increase of operating speed in the constant power region of the IPMSM. The negative command flux current has demagnetized the air gap flux in order to extend the operating speed of the IPMSM.

The experimental speed responses of the drive system for step changes of command speeds at the rated load condition have been shown in Figs 3.6(a) and 3.6(b) using the $i_d^r = 0$ control technique and the FW control technique, respectively. The drive system speed response using the $i_d^r = 0$ control technique of Fig. 3.6(a) has shown significant overshoots/undershoots and steady state oscillations. But the FW control based system response of Fig. 3.6(b) has shown less overshoots/undershoots, and the drive system has also reached the command speeds quickly than using the $i_d^r = 0$ control technique. However, some oscillations have been spotted in the steady state speed response of the IPMSM drive system using the FW control. The experimental speed responses of the drive system for a step change of load at the rated command speed of 188.6 rad/sec. have been presented in Figs. 3.7(a) and 3.7(b) using the $i_d^r = 0$ control technique and the FW control technique, respectively. The drive system response of Fig. 3.7(a) using the $i_d^r = 0$ control has shown significant speed dropping at the instant of load impact, and the system has also taken long time to settle to the steady state command speed of 188.6 rad/sec. However, the speed response has dropped slightly at the instant of

load in Fig. 3.7(*b*) for the case of FW control. In addition, there have been negligible steady state speed ripples using the FW control. It is to be noted that the *q*-axis command torque current (i_q^{r*}) responses of the IPM motor drive system using the MTPA and FW control technique of Figs. 3.6(*b*) and 3.7(*b*) have shown smaller spike than using the $i_d^r = 0$ control technique at the instants of step changes of command speeds and at the step change of load. In Fig. 3.6(*b*), the MTPA and FW control technique has provided smaller i_q^{r*} due to small speed undershoots and overshoots for step changes in speed of the IPM drive system. It is to be noted that the MTPA and FW control techniques have been designed to provide smaller current with increase in speed. The command torque current (i_q^{r*}) response of Fig. 3.7(*b*) using the MTPA and FW control techniques has also shown smaller change in amplitude because of the negligible speed dropping at the instant of load application.

It is to be noted that in Figs. 3.6–3.7, the variables Y1 and Y2 have been used to represent the speed response and the *q*-axis command torque current response of the IPMSM drive system, respectively. However, it is also to be noted that in Fig. 3.8, the variables Y1 and Y2 have been used to represent the speed response and the phase-*a* current response of the IPMSM drive system, respectively. The performances of the drive system have also been investigated in the constant power region of the IPMSM. The experimental starting speed and current responses of the drive system using the FW control technique have been shown in Figs. 3.8(*a*) and 3.8(*b*), respectively for the high command speed of 250 rad/sec. The drive system has followed the high command speed without overshoots/undershoots and steady state speed error. Therefore, the drive system using the FW control technique has been found more robust than using the conventional $i_d^r = 0$ control technique over a wide range of operating speed of the IPMSM.

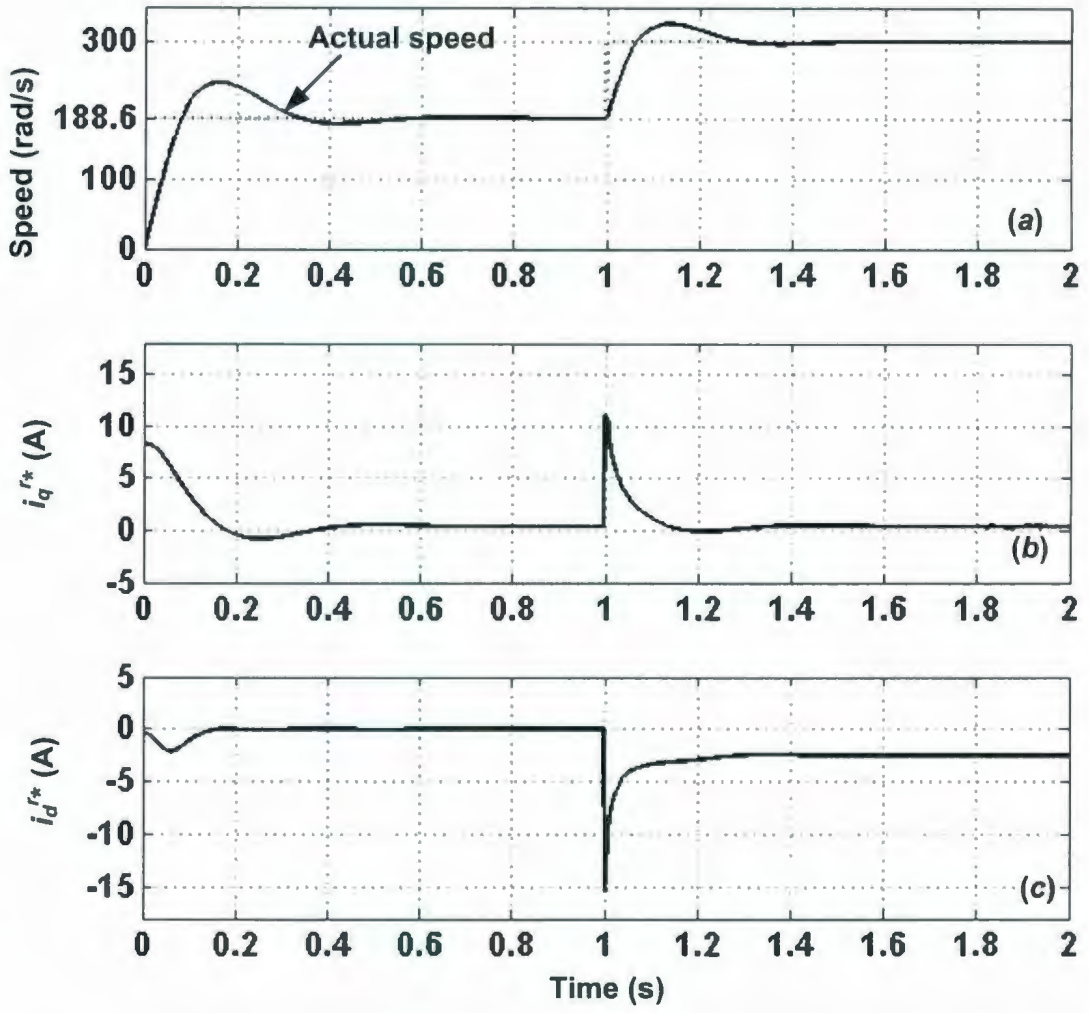

Figure 3.5: Simulated responses of the IPMSM drive system using the flux weakening control technique with $i_d^r \neq 0$ for step changes of command speeds (from 0 to 188.6 rad/sec. and from 188.6 rad/sec. to 300 rad/sec.) at no load condition: (*a*) speed, (*b*) *q*-axis command torque current (i_q^{r*}), and (*c*) *d*-axis command magnetizing current (i_d^{r*}).

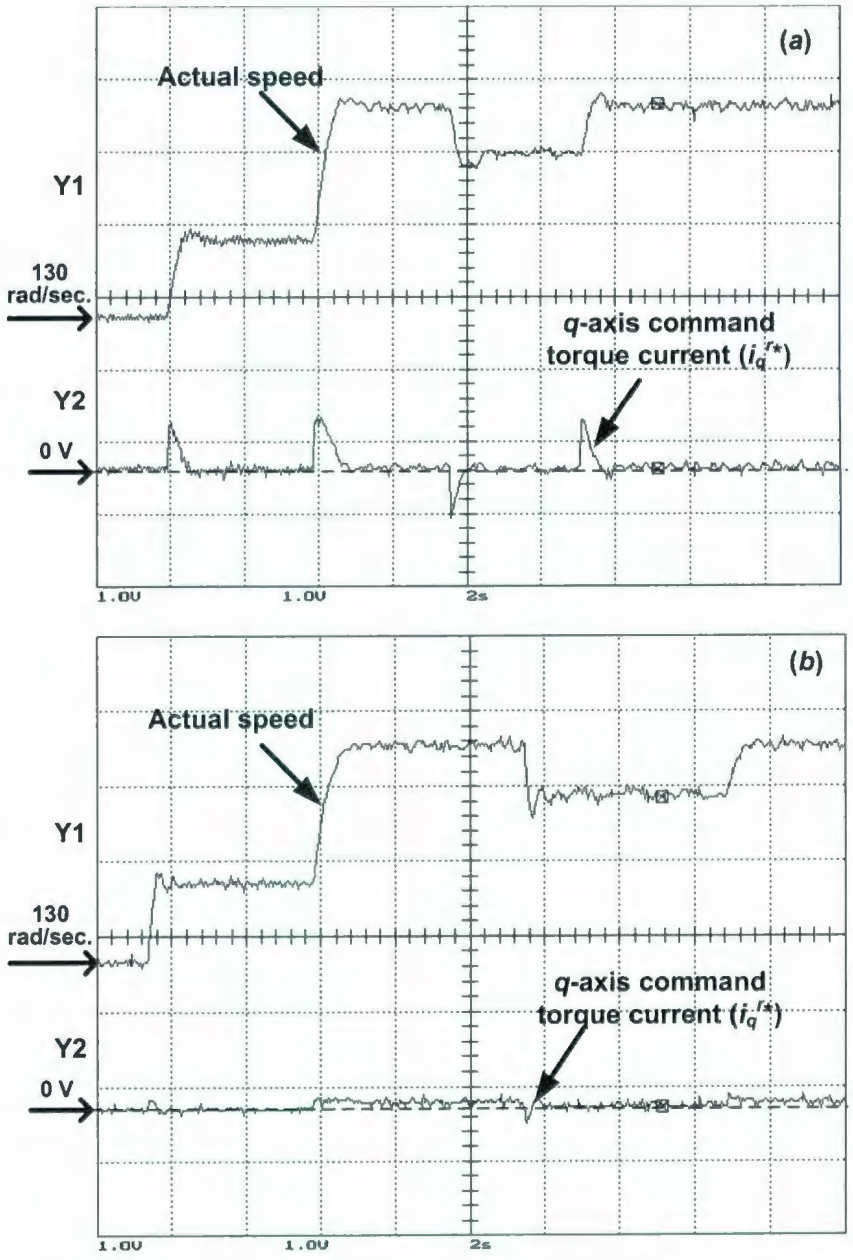

Figure 3.6: Experimental speed and q-axis command torque current responses of the IPMSM drive system for step changes of command speeds (from 130 rad/sec. to 150 rad/sec., from 150 rad/sec. to 188.6 rad/sec., from 188.6 rad/sec. to 175 rad/sec., from 175 rad/sec. to 188.6 rad/sec.) at rated load condition: (*a*) $i_d^r = 0$ control technique and (*b*) flux weakening control technique with $i_d^r \neq 0$. (Y1: 1 V/div., 1V = 20 rad/sec.; Y2: 1 V/div., 1V = 1.6 A; time: 2 sec./div.)

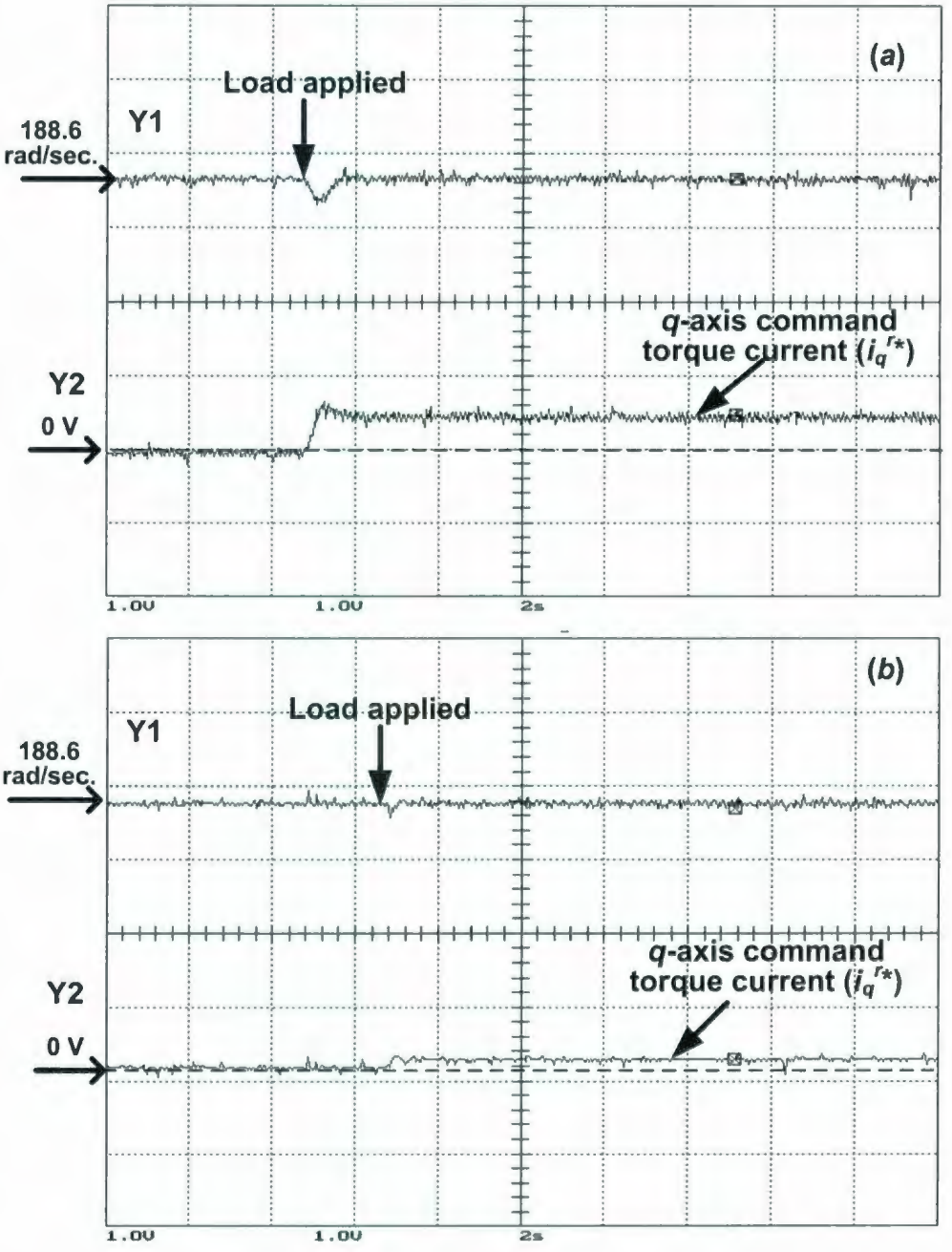

Figure 3.7: Experimental speed and q-axis command torque current responses of the IPMSM drive system for a step change in load at the rated speed of 188.6 rad/sec.: (*a*) $i_d^r = 0$ control technique and (*b*) flux weakening control technique with $i_d^r \neq 0$. (Y1: 1 V/div., 1V = 20 rad/sec.; Y2: 1 V/div., 1V = 1.6 A; time: 2 sec./div.)

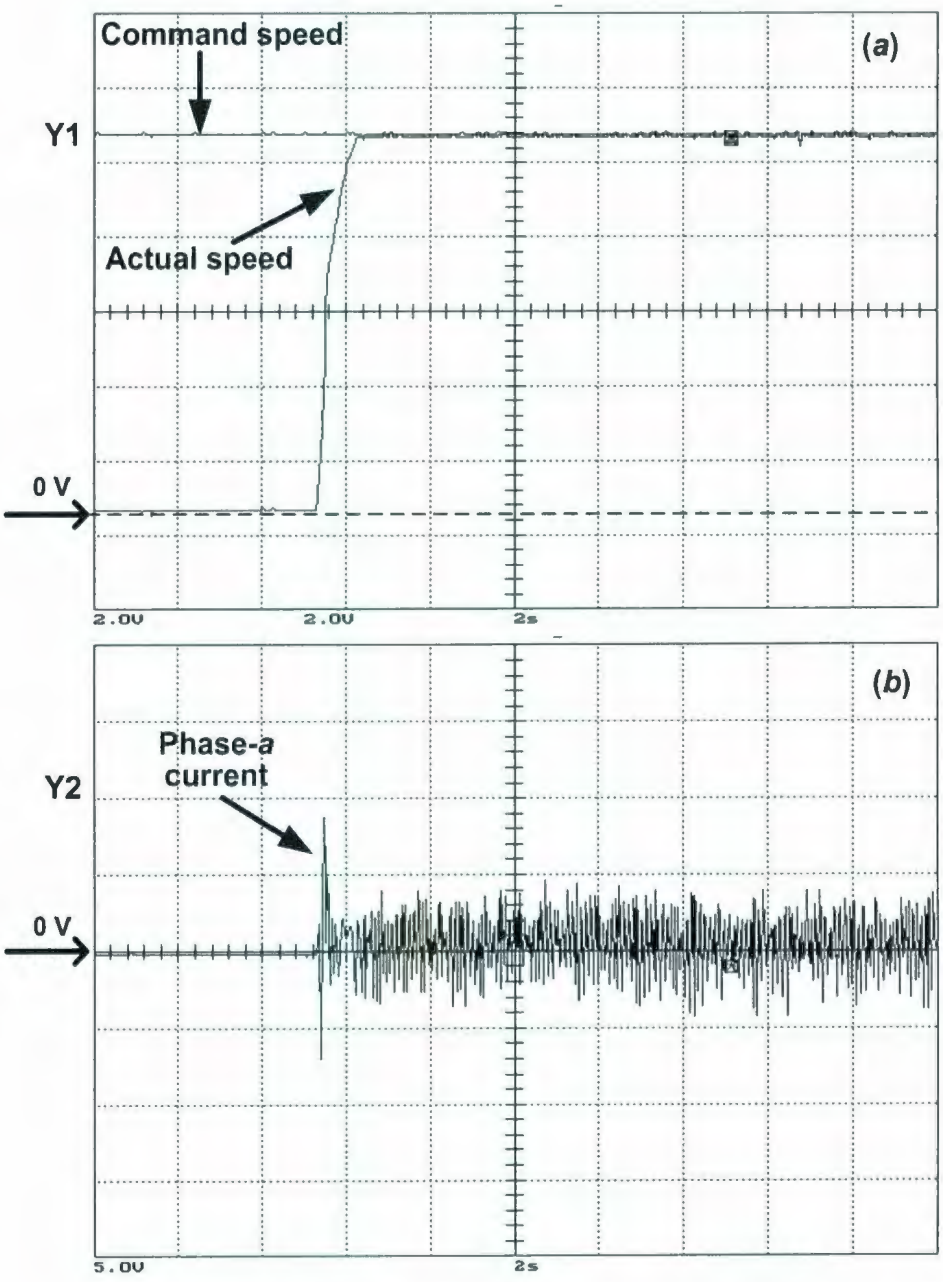

Figure 3.8: Experimental starting responses of the IPMSM drive system using the flux weakening control technique with $i_d^r \neq 0$ for the command speed of 250 rad/sec. at rated load condition: (*a*) speed and (*b*) current. (Y1: 2 V/div., 1V = 25 rad/sec.; Y2: 5 V/div., 1V = 0.933 A; time: 2 sec./div.)

3.4 Concluding Remarks

The performances of the IPMSM drive system using the $i_d^r = 0$ control technique and the flux-weakening (FW) control technique with $i_d^r \neq 0$ have been investigated in both simulation and experiments. The drive system has been simulated using the MATLAB software package. The DSP board ds1102 has been used for the real time implementation of the laboratory 1hp IPMSM drive system. The simulated and experimental performances of the IPMSM drive system using the $i_d^r = 0$ control technique and the FW control technique with $i_d^r \neq 0$ have been presented. These performances have revealed that the drive system using the FW control technique is more robust than using the conventional $i_d^r = 0$ control technique for step changes of command speeds or for a step change of load over a wide range of speed. The experimental performances of the FW control based drive system have also been investigated above the base speed in the constant power region. The FW control based drive system follows the high command speed smoothly. But the drive system using the $i_d^r = 0$ control technique may not be operated above the base speed of the IPMSM.

The performances of the IPMSM drive system using the conventional and adaptive controllers have been presented in chapter 2. The conventional fixed gain PI, PID speed controllers and the adaptive neural network (NN) speed controller have been used in the performance evaluation. These conventional and adaptive controllers have shown sensitive performances for drive system variations such as step change in command speeds, step change in load, change in rotor inertia, etc. Moreover, mathematical model of the drive system has been used in the development of the conventional controllers. In addition, complex mathematics have been implemented in the design of adaptive controller. A wavelet based speed controller has been developed in chapter 4 in order to tackle these drive system uncertainties and the limitations of the conventional controllers. It is to be noted that MTPA and FW control technique with $i_d^r \neq 0$ has been used for the implementation of wavelet controller based IPMSM drive system.

Chapter 4

Wavelet Transform Based Multiresolution Speed Controller

In this chapter, a wavelet based multiresolution speed controller has been developed to overcome the limitations of the conventional and adaptive controllers for the interior permanent magnet (IPM) motor drive system. A brief discussion of wavelet transforms and their properties including the multiresolution analysis and the filter back analysis has been presented at the beginning of this chapter. The brief discussion on wavelet transforms has been presented in order to illustrate the properties of wavelet transform to use as the speed controller for the IPM motor drive system.

The wavelet transforms have become a popular tool for processing signals with complex time frequency structures. Such popularity of wavelet transforms has been mainly due to their ability to concentrate the energy of processed signal into finite number of coefficients. This effective ability has been accompanied with time and frequency localization of the representing coefficients. In general, wavelet transform has been realized through successive stages of half-band filters separated by the down sampling operation. The wavelet transforms have been widely used for the analysis of non-stationary, non-periodic, intermittent, and transient signals. Therefore, a number of wavelet based techniques have been developed and implemented for signal manipulation and interrogation. The wavelet transforms have been applied in the investigation of

diverse physical phenomena such as climate change, financial market analysis, heart monitoring, condition monitoring of rotating machines, de noising of seismic signal and astronomical images, characterization of crack surface and turbulent intermittency, compression of video image and medical signal records, etc. Initially, the detail descriptions of the properties of wavelet transforms including the discrete wavelet transform and the wavelet packet transform have been presented in this chapter. Then, the criteria for selecting the mother wavelet function and for determining the levels of resolution of the proposed wavelet controller have been presented and implemented for the IPM motor drive system. Finally, the novel wavelet based multiresolution proportional integral derivative (MRPID) speed controller for the IPM motor drive has been presented. The mathematical formulations and the structure of the proposed MRPID controller for the IPM motor drive system have also been presented.

4.1 Wavelets and Scaling Functions

The wavelets are little waves of short duration. These have finite energy and decay quickly in time. The wavelets also have oscillating feature, which comes along with the location in time and frequency. These basic features make wavelets highly adequate for signal representation. The oscillating feature of wavelets is useful to extract the low and high frequency component of non-stationary and transient signals. Because of the finite nature of wavelets, the wavelet transforms provide negligible redundant information of a signal in time and frequency domains. The wavelet functions satisfy certain properties, which are described as [104]–[106]

(a) a wavelet function must have finite energy. This can be expressed as

$$E = \int_{-\infty}^{\infty} |\psi(t)|^2 \, dt < \infty \tag{4.1}$$

where E is the energy of the wavelet function $\psi(t)$. The energy is equal to the integral of the squared magnitude of the wavelet function. The vertical brackets $|\ |$ represent the modulus operator that gives the absolute value of

the wavelet function $\psi(t)$. If $\psi(t)$ is a complex function, then its magnitude is determined from the real and complex values of the function;

(b) if $\hat{\psi}(f)$ is the Fourier transform of $\psi(t)$, then

$$C_g = \int_0^\infty \frac{|\hat{\psi}(f)|^2}{f} df < \infty. \tag{4.2}$$

The above condition implies that the wavelet function should not have zero frequency component or it must have a zero mean. Equation (4.2) is known as the admissibility condition, and C_g is called the admissibility constant;

(c) the Fourier transform of the wavelet function must be real and must vanish for negative frequencies.

The wavelet functions of orthogonal type have a companion function, which is known as the scaling function $\phi(t)$. It is responsible for generating basis functions, which are required during the decomposition or reconstruction phases of a signal. The scaling function has certain properties, which are described as [107]

(a) compactness, which ensures the value of the scaling function will be zero outside the interval of support of the mother wavelet;

(b) averaging, which guarantees the average value of the scaling function will be one over the interval of support $[t_0, t_s]$ of the function. This property can be expressed as

$$\frac{1}{t_s - t_0} \int_{t_0}^{t_s} \phi(t)\, dt = 1. \tag{4.3}$$

(c) orthogonality, which ensures the orthogonal property in the translations of the scaling function. So, $\phi(t - m_1)$ is orthogonal to $\phi(t - m_2)$, where $m_1, m_2 \in \mathbb{N}$. Here $\mathbb{N}$ is the set of positive integers;

(d) regularity, which guarantees that constant and linear functions can be regenerated by the scaling function and its translations.

The term 'Mother' of the mother wavelet function implies that the wavelet functions with different region of support are derived from the one main function during the transformation process. The interval of support is defined as an interval of the smallest length outside of which the mother wavelet $\psi(t)$ vanishes. So, the wavelet function decays to zero quickly outside its interval of support. The scaling function (if it exists) of the mother wavelet have the capability of generating polynomials of degree p such that $p \leq m_v$ where m_v is the number of vanishing moments of the wavelet function. The level of resolution refers to the translations of the mother wavelet frequency bands. The translations produce another wavelet, which is the shifted scaled copy of the mother wavelet of the previous level of resolution. The new generated wavelet is known as the daughter wavelet. At each level of resolution, when a daughter wavelet is generated, the scaling function generates the basis functions. This can be expressed as

$$\phi_{j,k}(t) = 2^{-j/2}\phi(2^{-j}t - k); \quad j,k \in \mathbb{Z} \tag{4.4}$$

where j is the number of levels of resolution, and k is the dimension of the function space at level j.

The dilations and translations of the mother wavelet function $\psi(x)$ produce the orthogonal wavelet basis. This operation can be expressed as

$$\psi_{s,l}(x) = 2^{\frac{-s}{2}}\psi\left(2^{-s}x - l\right) \tag{4.5}$$

where the variables s and l are the integers, which scale and translate the mother function $\psi(x)$ to generate wavelets. The scale index s indicates the wavelet's width, and the location index l gives its position. In order to span the wavelet function over the data domain at different resolutions, the analyzing wavelet is used in a dilation equation. This equation is defined as [107]

$$W(x) = \sum_{k=-1}^{N-2}(-1)^k c_{k+1}\psi(2x + k) \tag{4.6}$$

where *W(x)* is the dilation function for the mother function $\psi(x)$, and c_k are the *wavelet coefficients*. The wavelet coefficients must satisfy linear and quadratic constraints of the form, which can be defined as [107]

$$\sum_{k=o}^{N-1} c_k = 2 \tag{4.7}$$

$$\sum_{k=o}^{N-1} c_k c_{k+2l} = 2\delta_l \tag{4.8}$$

where δ is the delta function and l is the location index. The coefficients $\{c_o\, c_1 ... c_k\}$ can be interpreted as a filter. The filter or coefficients are placed in a transformation matrix, which is applied to a raw data vector. The coefficients are ordered using two dominant patterns. One pattern works as a smoothing filter to bring out the "approximate" information of the data. Another pattern works to bring out the "detail" information of the data. These two orderings of the coefficients are called quadrature mirror filters (QMF) in the signal processing parlance. The features of the wavelet associated QMF banks are described later in section 4.3.1 of the chapter.

Almost all practically useful wavelet transforms use discrete time filter banks with QMF coefficients. These filter banks are called the wavelet and scaling filters in wavelets nomenclature. The scaling filter is a low-pass finite impulse response (FIR) filter of length *2N* and sum 1. The wavelet filter is a high pass filter, which is calculated as the quadrature mirror filter of the low pass filter. These filter banks may contain either finite impulse response (FIR) or infinite impulse response (IIR) filters. The filter banks can also be realized using the continuous time analog filter other than the wavelet associated filters. The continuous time analog filter include the Butterworth filter, Chebyshev filter, Elliptic filter, etc. The analog filter is normally realized electronically in an integrated circuit (IC) chip. However, the analog filters suffer from amplitude ripples in the pass band and stop band frequency responses. In addition, higher order analog filters are needed in order to get sharp cut-off frequency response. The filter design becomes complicated with the increase in the order of the filter.

Wavelets are classified into two main types: orthogonal and non-orthogonal. The following subsections give brief explanations of the main properties of each type.

4.1.1 Orthogonal wavelets

A mother wavelet with the scaling function, which is capable of generating orthogonal basis function at each level of resolution, is known as the orthogonal wavelet. In orthogonal wavelets, the wavelet functions are orthogonal to the basis functions. These basis functions are created through translations and dilations or expansions of the mother wavelet functions in time and frequency domains. There are several orthogonal wavelet families, which are the *Daubechies* family (*'dbN'*), *Coiflets* family (*'coifN'*), *Symlets* family (*'symN'*), *Meyer* family (*'meyr'*), and bi-orthogonal *spline* (*'biorN.M'*) family [108]. Here N and M denotes the order of a wavelet family during the decomposition and reconstruction of a discrete signal, respectively. The orthogonal wavelets meet the orthogonality or orthonormality condition, which is defined as

$$\begin{aligned} \int_{-\infty}^{\infty} \psi_{m,n}(t)\,\psi_{m',n'}(t)\,dt &= 1 \quad \text{if } m = m' \text{ and } n = n' \\ &= 0 \quad \text{otherwise.} \end{aligned} \tag{4.9}$$

The orthogonality condition implies that the product of each wavelet function with other functions, which are translated and/or dilated versions of the mother wavelet, in the same dyadic system is zero. Therefore, the information stored in the wavelet transformed coefficients of a discrete signal is not repeated, which allows complete regeneration of the original signal without redundancy. The most common properties of the orthogonal wavelets are [108]:

(a) compactness;

(b) number of vanishing moments is large for a support width;

(c) symmetric and perfect reconstruction;

(d) wavelet and scaling filters can be modeled using finite impulse response (FIR) approximations;

(e) use fast algorithm to determine wavelet coefficients.

The *Daubechies* family of the orthogonal wavelets is used extensively for control and diagnostic of the electric machines and drives, for detection and classification of the disturbances in power systems, and for processing and de-noising of the blurred image [104]. The phase responses of the *Daubechies* wavelets and their scaling filters are non linear. These filters show truncation problems at the edges of a signal including the starting and the end points. The edge problem can be solved by padding zeros at the edges of a signal or by wrapping around of the wavelet transformed coefficients of a signal. Figures 4.1(*a*) and 4.1(*b*) show the *Daubechies* ('*db*3') wavelet function and its scaling function, respectively. In certain application, it is necessary to use the real and symmetric wavelets. One way to get the symmetric wavelets is to construct two sets of the bi-orthogonal wavelets, which include the wavelet function $\psi_{m,n}(t)$ and its dual function $\hat{\psi}_{m,n}(t)$. The first set is used during the decomposition phase, and the second set is used during the reconstruction phase. The bi-orthogonal wavelets satisfy the bi-orthogonality condition, which is defined as

$$\begin{aligned} \int_{-\infty}^{\infty} \psi_{m,n}(t)\,\hat{\psi}_{m',n'}(t)\,dt &= 1 \quad \text{if } m = m' \text{ and } n = n' \\ &= 0 \qquad \text{otherwise} \end{aligned} \tag{4.10}$$

The bi-orthogonal wavelets allow one to get the symmetric and asymmetric wavelets. They also allow certain properties to be incorporated separately within the wavelet functions for both decomposition and reconstruction of a signal. The vanishing moments of the wavelet function $\psi_{m,n}(t)$ and its dual $\hat{\psi}_{m,n}(t)$ are different. If $\psi_{m,n}(t)$ has more vanishing moments than $\hat{\psi}_{m,n}(t)$, then decomposition using the wavelet function $\psi_{m,n}(t)$ will suppress higher order polynomials and will aid in the data compression. Reconstruction using the dual wavelet $\hat{\psi}_{m,n}(t)$ with fewer vanishing moments will lead to smoother reconstruction of the original signal [104]. Figures 4.2(*a*)–4.2(*d*) show the

spline bi-orthogonal ('*bior*2.6') wavelet functions and their scaling functions during the decomposition and reconstruction of a signal.

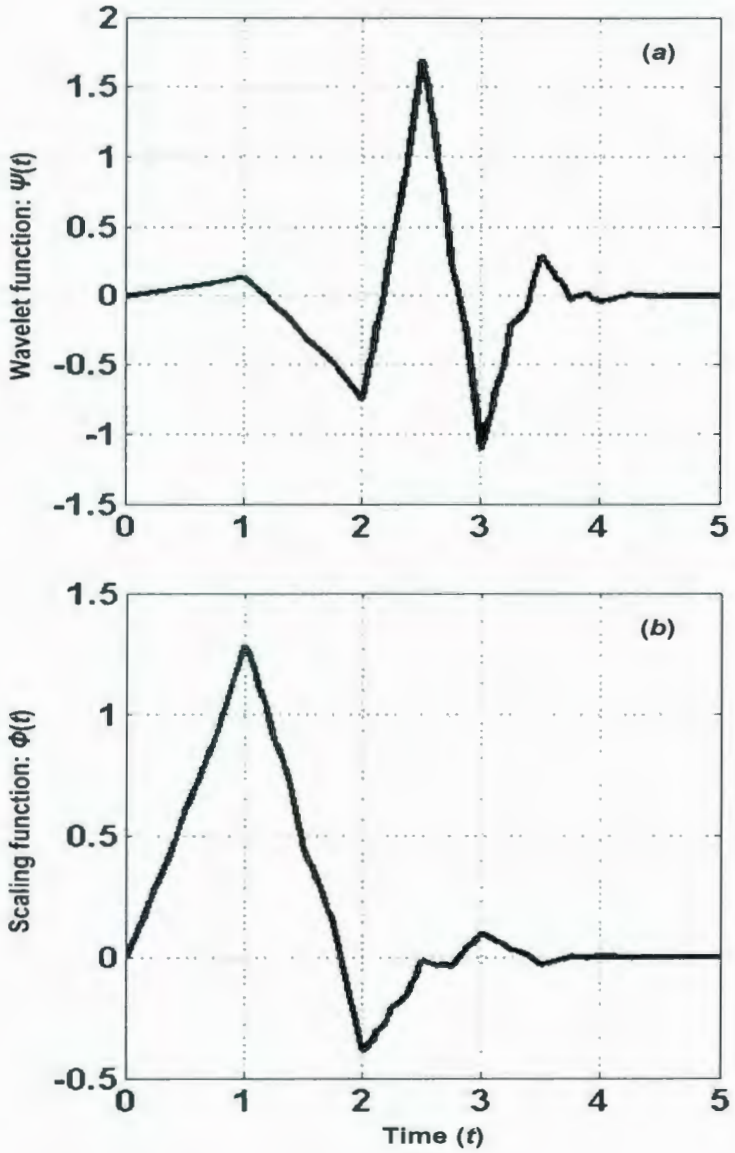

Figure 4.1: The *Daubechies* ('*db*3') wavelet: (*a*) mother wavelet function and (*b*) scaling function.

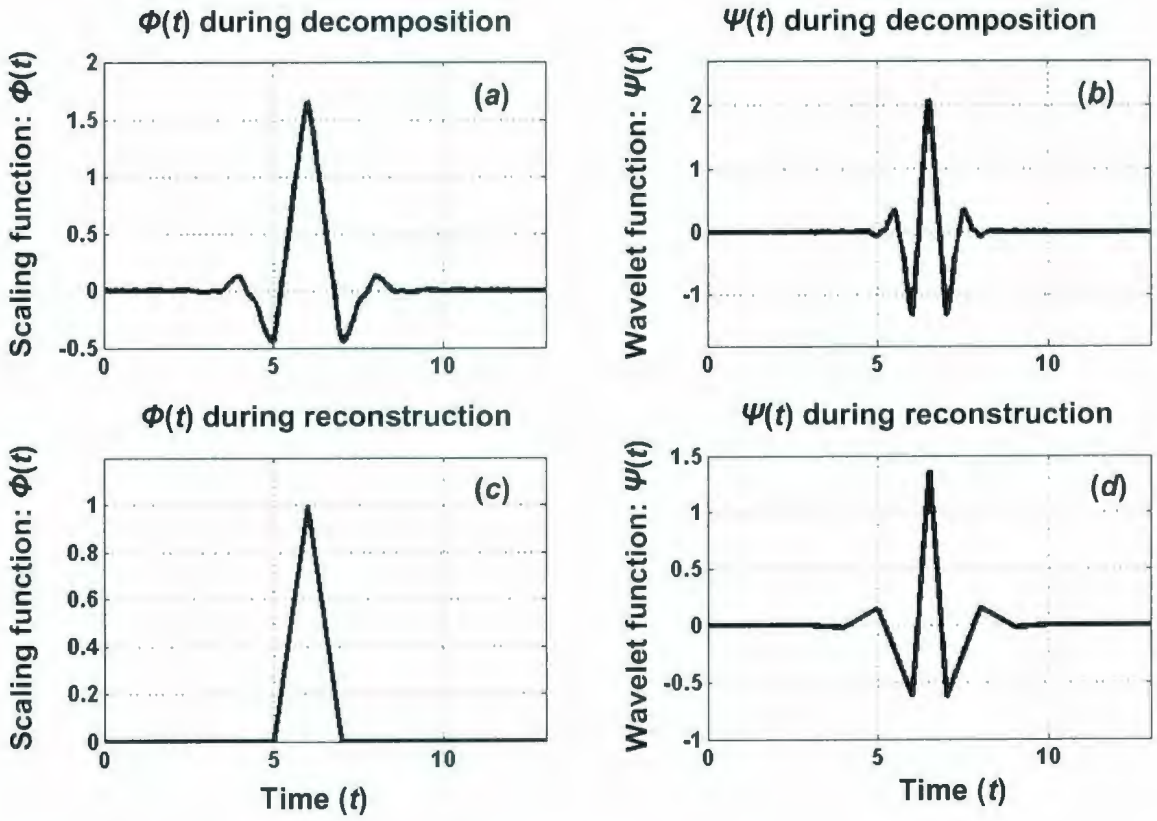

Figure 4.2: The *Spline* bi-orthogonal ('*bior*2.6') wavelet: (*a*) scaling function during the decomposition, (*b*) mother wavelet function during the decomposition, (*c*) scaling function during the reconstruction, and (*d*) mother wavelet function during the reconstruction.

4.1.2 Non-orthogonal wavelets

In non-orthogonal wavelets, mother wavelets either have scaling functions or do not have scaling functions. There are several types of non-orthogonal wavelets, which are *Morlet* ('*morl*') wavelet, *Mexican Hat* ('*mexihat*') wavelet, *Gaussian* ('*gaus*') wavelets, *complex Gaussian* wavelets, *complex Morlet* wavelet, *complex Shannon* wavelets, and *complex frequency B-spline* wavelets [108]. The problems with the non-orthogonal wavelets are that the mother wavelet and its bases are not compactly supported and perfect reconstruction is not possible without scaling functions. Figures 4.3(*a*) and 4.3(*b*) show the non-orthogonal *Morlet* and *Mexican Hat* wavelet functions, respectively.

4.2 Wavelet Transforms

The wavelet transforms use little wavelike functions, which are known as wavelets. Figures 4.1–4.3 show few examples of wavelets and their scaling functions. Wavelets are used to transform a signal under investigation into another representation of a more useful form. From the mathematical point of view, the wavelet transform is a convolution of the wavelet function with the signal. The wavelet function is manipulated in two ways: it is moved to various locations on the signal, and it is stretched or squeezed. If a wavelet function matches the shape of a signal well at a specific scale and location, then a large transformation value will be generated. On the other hand, if the wavelet function and signal do not correlate well, then a low value of transformation will be generated [104]. In the following subsections, different forms of wavelet transforms and their mathematical formulations are briefly presented.

4.2.1 Continuous wavelet transform

The wavelet transform of a continuous signal $x(t)$ with respect to the wavelet function $\psi(t)$ can be defined as

$$CWT_{a,b}x(t) = w(a)\int_{-\infty}^{\infty} x(t)\psi^*\left(\frac{t-b}{a}\right)dt \qquad (4.11)$$

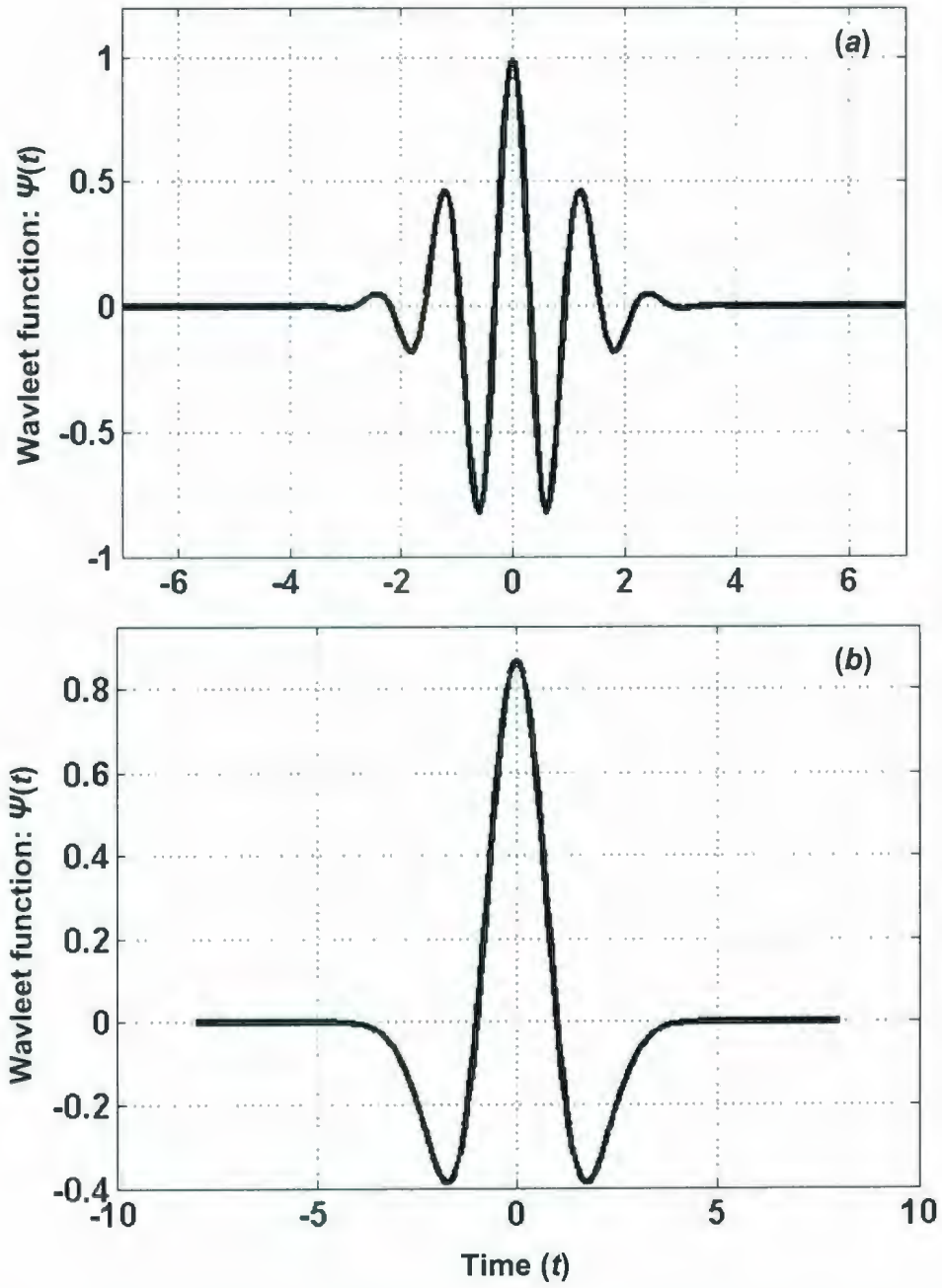

Figure 4.3: The non-orthogonal wavelet functions: (*a*) *Morlet* ('*morl*') wavelet function and (*b*) *Mexican Hat* ('*mexh*') wavelet function.

where $w(a)$ is the weighting function, a and b are the dilation and translation parameters, respectively. The asterisk indicates that the complex conjugate of the wavelet function is used in the transformation. The wavelet transform can be thought of as the cross correlation of a signal with a set of wavelets of various widths. Typically, $w(a)$ is set to $1/\sqrt{a}$ for the reason of energy conservation, which ensures identical energy of the wavelet transformed coefficients at each scale. If $w(a)$ is set to $1/\sqrt{a}$, then the wavelet transform of the continuous signal $x(t)$ can be rewritten as

$$CWT_{a,b}x(t) = \frac{1}{\sqrt{a}} \int_{-\infty}^{\infty} x(t)\psi^* \left(\frac{t-b}{a} \right) dt. \tag{4.12}$$

The equation (4.9) is known as the continuous wavelet transform (CWT) of the signal $x(t)$. It contains both the dilated and translated wavelets $\psi((t-b)/a)$, and the continuous signal $x(t)$. The signal $x(t)$ may be a beating heart, an audio signal, a financial index, the gearbox vibration signal, a spatial signal such as crack profile or land surface heights. The normalized wavelet function can be written more compactly as

$$\psi_{a,b}(t) = \frac{1}{\sqrt{a}} \psi \left(\frac{t-b}{a} \right) \tag{4.13}$$

where the normalization is in the sense of wavelet energy. Now the transform integral of equation (4.12) can be rewritten as

$$CWT_{a,b}x(t) = \int_{-\infty}^{\infty} x(t)\psi_{a,b}^*(t)\, dt \tag{4.14}$$

The dilation and contraction of the mother wavelet function is governed by the dilation parameter a, which is the distance between center of the wavelet function and its crossing on the time axis. The movement of the wavelet function along the time axis is governed by the translation parameter b. Figure 4.4 shows the stretching (double) and squeezing (half) of the Mexican Hat wavelet function on the time axis. Figure 4.5 shows the translation of the Mexican Hat wavelet function on the time axis from b_1 via b_2 to b_3.

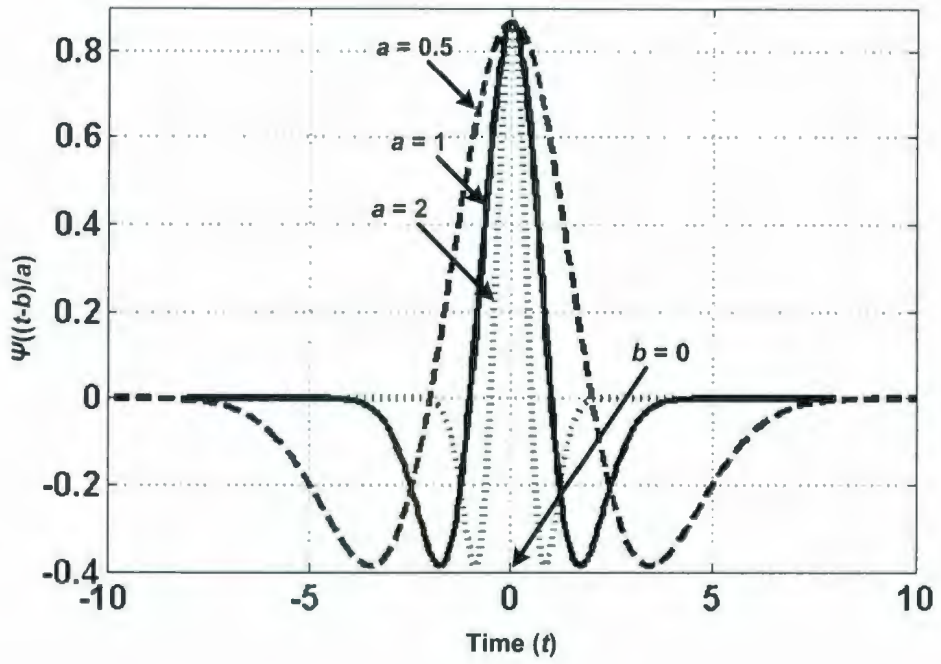

Figure 4.4: Stretching (a = 0.5) and squeezing (a = 2) of the Mexican Hat wavelet function.

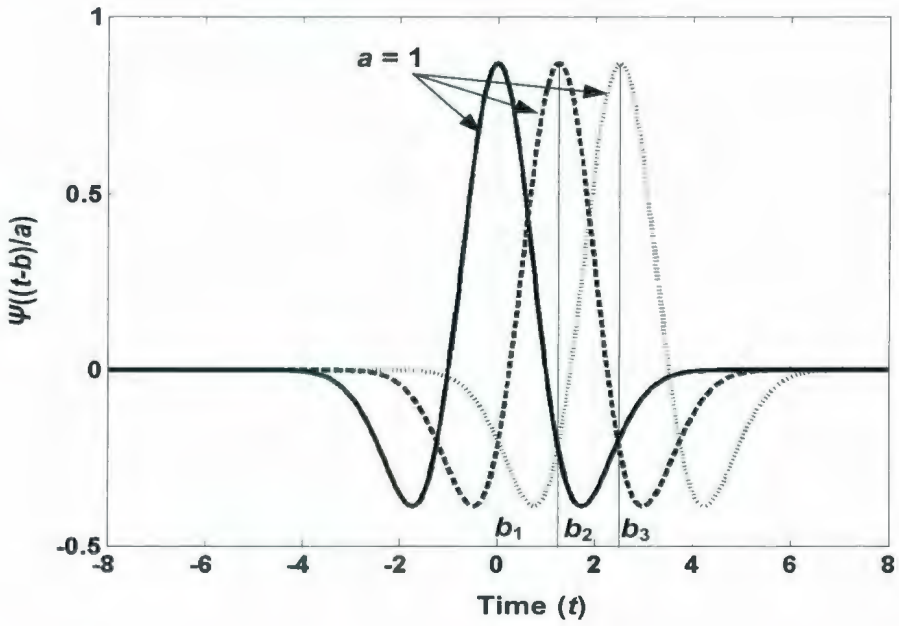

Figure 4.5: Translation (b_1 via b_2 to b_3) of the Mexican Hat wavelet function.

4.2.2 Discrete wavelet transform

In the continuous wavelet transform (CWT), the mother wavelet is dilated and translated continuously over a real continuous number system$(\mathbb{R})$. Therefore, it can generate substantial redundant information. The mother wavelet can be dilated and translated discretely by replacing $a = a_0^m$ and $b = nb_0a_0^m$, where a_0 and b_0 are the fixed constants with $a_0 > 1$, $b_0 > 0$, and $m, n \in \mathbb{N}$. Here $\mathbb{N}$ is the set of positive integers. Then, the discretized mother wavelet function can be expressed as [109]–[110]

$$\psi_{m,n}(t) = a_0^{-m/2}\,\psi\left(\frac{t - n\,b_0\,a_0^m}{a_0^m}\right) \tag{4.15}$$

and the corresponding discrete wavelet transform (DWT) can be expressed as

$$DWT_{m,n}x(t) = \int_{-\infty}^{\infty} x(t)\psi_{m,n}^{*}(t)\,dt \tag{4.16}$$

In the DWT, the family of dilated wavelets constitutes an orthonormal basis by careful selections of a_0 and b_0. There are several implications of the orthonormal basis. The orthonormality property ensures low information redundancy among the decomposed signals. With optimal choices of a_0 and b_0, there exists an elegant algorithm known as the multiresolution signal decomposition. It decomposes a signal into various scales with different time and frequency resolutions. The multiresolution analysis is illustrated later in section 4.3 of this chapter. The DWT analyzes a signal at different frequency bands with different resolutions by decomposing the signal into a coarse approximation and detail information. The DWT employs two sets of functions, which are called scaling functions and wavelet functions. The scaling and wavelet functions are associated with low pass and high pass filters, respectively. The time-scale representation of a digital signal is obtained using digital filtering techniques.

The filter bank realization of the discrete wavelet transform (DWT) is the same as implementing the wavelet decomposition in the continuous wavelet transform (CWT). It

is to be mentioned that the CWT is a correlation between a wavelet of different scales and the signal with the scale being used as a measure of similarity. The CWT is computed by changing the scale of the analysis window of the wavelet function. The analysis window is shifted in time and multiplied by the signal, and then integrated over all times. In the DWT using the filter banks, filters of different cutoff frequencies are used to analyze the signal at different scales. The signal is passed through a series of high pass filters to analyze the high frequencies, and it is passed through a series of low pass filters to analyze the low frequencies. The resolution of the signal, which is a measure of the amount of detail information in the signal, is changed by the filtering operations, and the scale is changed by up sampling and down sampling operations. Down sampling a signal corresponds to reducing the sampling rate or removing some of the samples of the signal. Up sampling a signal corresponds to increasing the sampling rate of a signal by adding new samples to the signal [104].

In the DWT, the procedure starts with passing the discrete signal $x[n]$ of length N through a digital low pass filter with impulse response $g[n]$ and a digital high pass filter with impulse response $h[n]$. The low pass and high pass filters are determined from scaling and wavelet filters, respectively. The outputs from the low pass filter are approximation coefficients ("a") of the discrete signal at first level of resolution of the DWT. The outputs from the high pass filter are detail coefficients ("d") of the discrete signal at first level of resolution of the DWT. The output of these filters consists of N wavelet coefficients. This constitutes first level of decomposition of the discrete signal and can be mathematically expressed as

$$a^1[n] = \sum_{k=0}^{N-1} g[k]\, x[n-k] \tag{4.17}$$

$$d^1[n] = \sum_{k=0}^{N-1} h[k]\, x[n-k]. \tag{4.18}$$

The approximation coefficients (a^1) at first level of resolution are used as inputs for another pair of wavelet filters (identical with the first pair) after being down sampled by two. The filters at second level of resolution generate sets of approximations and details coefficients of length *N/2*. This constitutes second level of decomposition of the discrete signal and can be mathematically expressed as

$$a^2[n] = \sum_{k=0}^{N/2-1} g[k]\, a^1[2n-k] \tag{4.19}$$

$$d^2[n] = \sum_{k=0}^{N/2-1} h[k]\, a^1[2n-k]. \tag{4.20}$$

The superscripts of "*a*" and "*d*" of equations (4.17)–(4.20) refer to the level of resolution of the discrete wavelet transform (DWT). Figure 4.6 shows the two-level decomposition tree of a discrete signal of the DWT. It uses the high pass filters (h) and the low pass filters (g) in the decomposition process.

4.2.3 Wavelet packet transform

The wavelet packets are alternative bases, which can be formed from the linear combinations of usual wavelet functions. These bases inherit properties such as orthonormality and time-frequency localization from their corresponding wavelet functions. A wavelet packet function is a function of three indices j, k and n, and is defined as [111]

$$W_{j,k}^n(t) = 2^{j/2} W^n(2^j t - k) \tag{4.21}$$

where the integers j and k are the indices for scale and translation operations, respectively. The index n is defined as the modulation or oscillation parameter. The first two wavelet packet functions are the scaling function and mother wavelet function, and these are defined as

$$W_{0,0}^0(t) = \phi(t) \tag{4.22}$$

$$W_{0,0}^{1}(t) = \psi(t). \tag{4.23}$$

The wavelet packet functions for $n = 2,3,\ldots$ can be computed as

$$W_{0,0}^{2n}(t) = \sqrt{2}\sum_{k} g(k)\, W_{1,k}^{n}(2t-k) \tag{4.24}$$

$$W_{0,0}^{2n+1}(t) = \sqrt{2}\sum_{k} h(k)\, W_{1,k}^{n}(2t-k) \tag{4.25}$$

where $g(k)$ and $h(k)$ are the quadrature mirror filters associated with the predefined scaling and mother wavelet functions. To measure specific time-frequency information of a signal, one simply takes the inner product of the signal with a particular basis function. The wavelet packet decomposition (WPD) involves applying both high pass and low pass filters to a discrete signal, and then recursively to each intermediate signal. The procedure is illustrated in Fig. 4.7 up to the second level of resolution.

The first level of decomposition of the discrete signal $x[n]$ of length N in the wavelet packet transform (WPT) generates two-frequency sub-bands, which are the approximation coefficients $a_n^1 = \left[a_0^1\ a_1^1\ a_2^1 \ldots a_{N-1}^1\right]$ and the detail coefficients $d_n^1 = \left[d_0^1\ d_1^1\ d_2^1 \ldots d_{N-1}^1\right]$. The second level of decomposition generates four-frequency sub-bands using same set of filters of the first level of resolution. These are defined as [110]

$$aa^2[n] = \sum_{k=0}^{N/2-1} g[k]\, a^1[2n-k] \tag{4.26}$$

$$ad^2[n] = \sum_{k=0}^{N/2-1} h[k]\, a^1[2n-k] \tag{4.27}$$

$$da^2[n] = \sum_{k=0}^{N/2-1} g[k]\, d^1[2n-k] \tag{4.28}$$

$$dd^2[n] = \sum_{k=0}^{N/2-1} h[k]\, d^1[2n-k] \tag{4.29}$$

The frequency sub-band aa^2 is defined as second level low frequency approximations of original signal. The frequency sub-band ad^2 is defined as second level low frequency details of original signal. The frequency sub-band da^2 is defined as second level high frequency approximations of original signal. The frequency sub-band dd^2 is defined as second level high frequency details of original signal.

4.3 Multiresolution Analysis

The multiresolution analysis (MRA) is a convenient framework for hierarchical representation of functions or signals at different scales. The idea of multiresolution analysis is to represent a function as a limit of successive approximations. Each of these successive approximations has the smoother version and the finer details of the original function. The multiresolution analysis (MRA) maps a one dimensional signal of time into a two-dimensional (2D) signal of time and frequency. The goal of MRA is to develop representation of a function $f(t)$ in terms of its orthonormal bases, which are the scaling and the wavelet functions. A mixed form N-level discrete wavelet series representation of a signal $f(t)$ can be defined as [112]

$$f(t)=\sum_{k} c_{N,k}\ \phi_{N,k}(t)+\sum_{m=1}^{N}\sum_{k} d_{m,k}\ \psi_{m,k}(t) \tag{4.30}$$

where

$$c_{m,k}=\sum_{k} f(t)\,\bar{\phi}_{m,k}(t) \tag{4.31}$$

$$d_{m,k}=\sum_{k} f(t)\,\bar{\psi}_{m,k}(t) \tag{4.32}$$

where $\bar{\phi}(t)$ and $\bar{\psi}(t)$ are the conjugate functions of $\phi(t)$ and $\psi(t)$, respectively. The properties of the multiresolution analysis are described as [104], [107]

(a) the multiresolution analysis decomposes a function space into the sequence of subspaces. Each subspace is contained in the higher subspaces. Therefore, a new level of resolution can be created by dilating the mother wavelet function without loss of information in the decomposed signal;

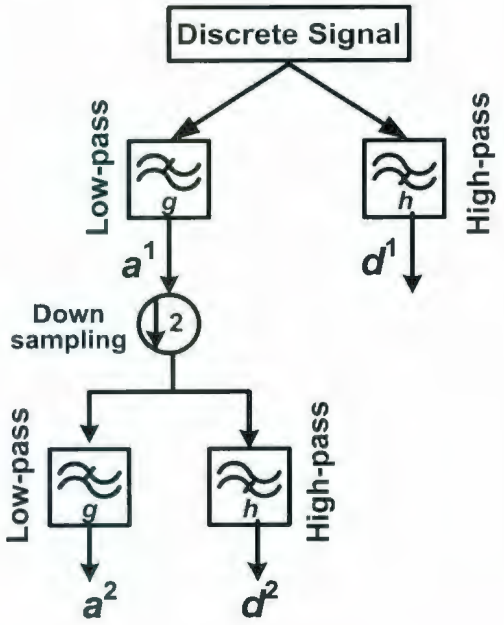

Figure 4.6: Two-level decomposition of a discrete signal of the discrete wavelet transform (DWT).

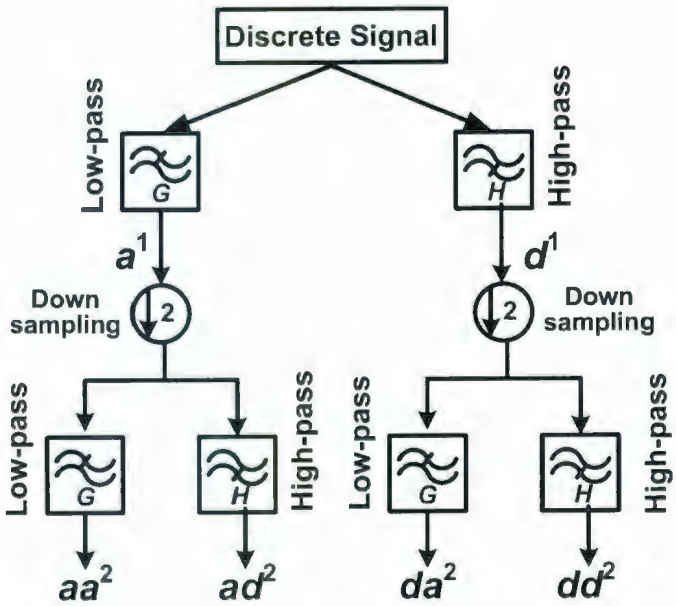

Figure 4.7: Two-level decomposition of a discrete signal of the wavelet packet transform (WPT).

(b) as the resolution gets coarser and coarser, more and more details are removed in such a way that when $j \to \infty$, then only a constant frequency component remains. Here j is the level of resolution;

(c) if a signal $x(t)$ does not have any fluctuation (transient components) at scales smaller than $1/2^j$, then $x(2t)$ will not contain any fluctuation at scales smaller than $1/2^{j+1}$.

4.3.1 Quadrature mirror filter banks

The MRA can be constructed using the quadrature mirror filter (QMF) banks. The selected wavelet function is used to generate the QMF coefficients. The filter coefficients of the QMF banks are derived using the conventional two-scale dilation equation. The dilation equation for the determination of filter coefficients is defined as

$$\phi(t) = \sqrt{2} \sum_k g(k)\, \phi(2t - k) \tag{4.33}$$

In general, QMF banks have stages of filters, where each stage has low pass filters (g) and high pass filters (h). The filters g and h of the quadrature mirror filter (QMF) bank satisfy the property of energy conservation, which is defined as [107]

$$\|y_0\|^2 + \|y_1\|^2 = \|x\|^2 \tag{4.34}$$

where y_0 is a decimated version of the finite energy signal x filtered through g. So, y_0 can be defined by $x_0 = g(x)$ and $y_0 = x_0(2n)$. Similarly, y_1 can be defined by $x_1 = h(x)$ and $y_1 = x_1(2n)$. This property ensures a perfect reconstruction of the associated two-channel filter banks scheme. The transfer functions $G(z)$ and $H(z)$ of the filters g and h satisfy the orthogonal condition, which is defined as [107]

$$\|G\|^2 + \|H\|^2 = 1 \tag{4.35}$$

The filter coefficients of the low pass filters (g) and the high pass filters (h) of the QMF backs are dependent on each other by the following expression [107]

$$h(k) = (-1)^k \, g(L-k); \; k = 0, 1, 2, ..., L-1 \qquad (4.36)$$

where $h(k)$ and $g(k)$ represent the coefficients of the high pass filter and the low pass filter, respectively. The filter bank, which satisfies the conditions of equations (4.34)–(4.36), is known as the quadrature mirror filter (QMF) bank. The frequency responses of the QMF filter banks have minimum attenuation in the pass band and maximum attenuation in the stop band. The filters have real coefficients with almost linear phase response for both symmetric and asymmetric mother wavelet functions. They allow perfect reconstruction of a signal due to the elimination of non-ideal transition from the pass band to the stop band frequencies. Each filter in the QMF banks can be described using a minimal set of parameters, which are directly related to zeros of the filter function [110]. The filters of the *Daubechies* wavelet family satisfy the properties of the QMF banks. The amplitude and phase responses of the '*db*3' filters of the *Daubechies* family have been shown in Figs. 4.8–4.9. Figure 4.8 shows the amplitude and phase responses of the '*db*3' high pass filter. Figure 4.9 shows the amplitude and phase responses of the '*db*3' low pass filter.

4.4 Selection of Wavelet

The choice of a wavelet function, which can accurately parameterize and expand a signal, depends on the signal as well as the type of information to be extracted from the signal. An optimum wavelet function can decompose and reconstruct a signal using shifted and dilated version of the wavelet function. It also preserves the energy of a signal under transformation. If an asymmetric wavelet function is selected, then the drifting of information during the transformation can be avoided. The problem of selecting an optimum wavelet function can be defined as selecting orthonormal basis function. The compact property of wavelet functions provide the means to detect frequency components present in a process signal. Such property can be useful in designing motor

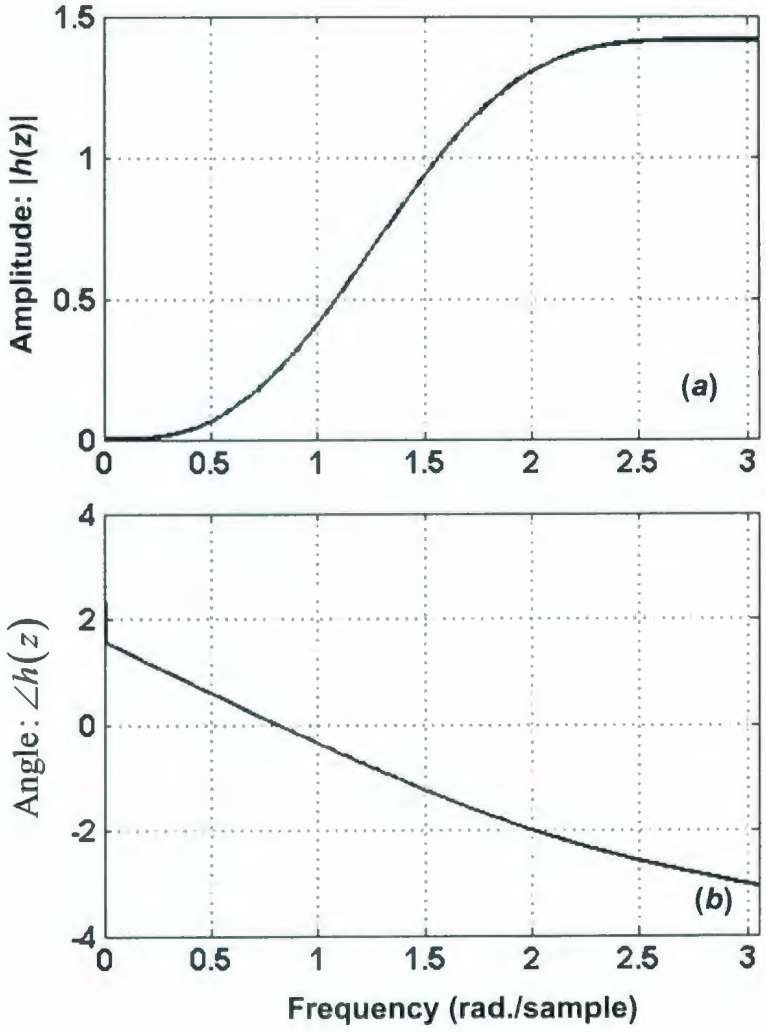

Figure 4.8: The frequency responses of the *Daubechies* '*db*3' high pass filter: (*a*) amplitude response and (*b*) phase response.

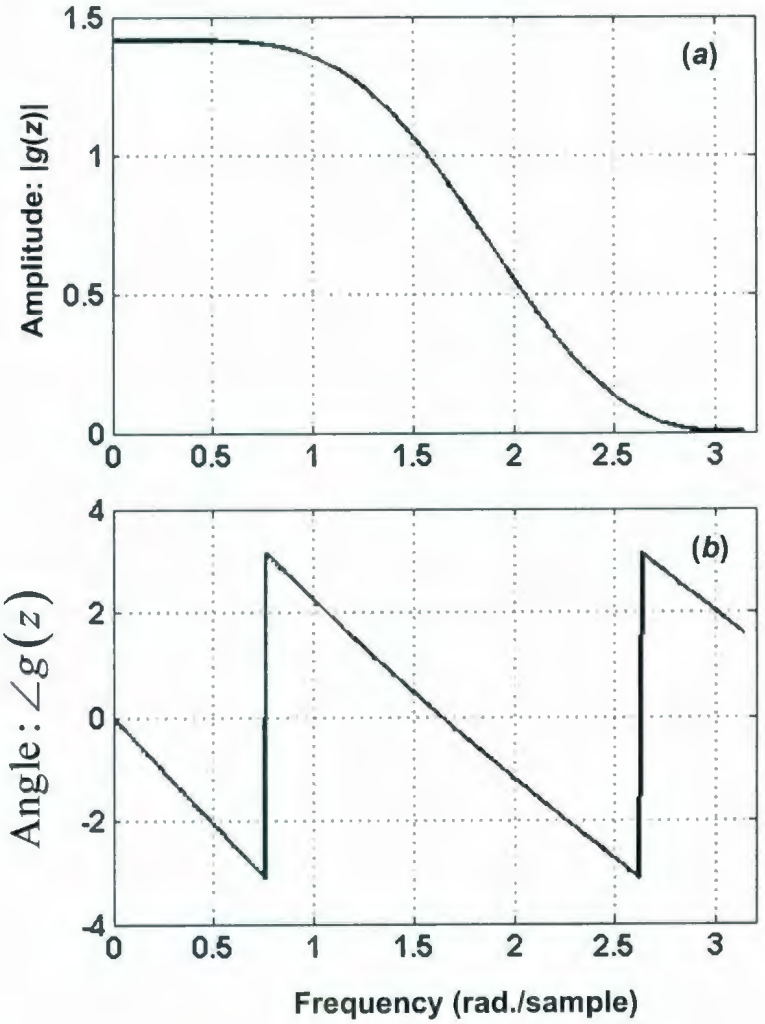

Figure 4.9: The frequency responses of the *Daubechies* '*db*3' low pass filter: (*a*) amplitude response and (*b*) phase response.

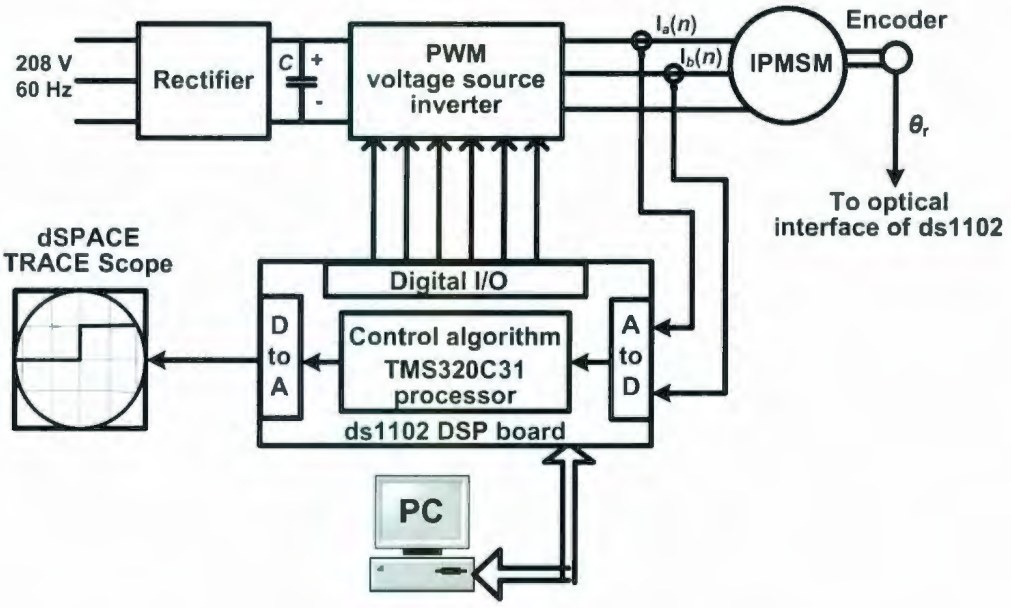

Figure 4.10: Experimental data acquisition setup of the IPMSM drive system.

controller such that the speed error changes of the drive system can be detected quickly, and then the control signal can be applied immediately. The compactness property has another advantage of small computational efforts for real time implementation.

In the proposed interior permanent magnet synchronous motor (IPMSM) drive applications, the objective is to apply wavelet analysis to the speed error signal. The actual responses of the IPMSM drive system are considered for accurate selection of mother wavelet function and number of levels of decomposition of the error signal. The experimental setup for the data acquisition for selections of wavelet function and number of levels of resolution is shown in Fig. 4.10. The data acquisition instrument consists of a dSPACE ds1102 DSP controller board that includes the 32-bit floating point processor TMS320C31. The three-phase motor currents are acquired through three-channel analog-to-digital (A/D) converters of the controller board. The control program, which is written in turbo C language, used a set of initialization and input/output (I/O) functions for initializing TMS320C31's on-chip timers and for accessing ds1102's on board A/D and D/A converters. The IPMSM drive system is operated for the command speeds of 50 rad/sec., 188.6 rad/sec. and 250 rad/sec. The proportional integral (PI) controller is used

in the speed control loop. The fixed band hysteresis controller is used in the current control loop.

The actual and command speed responses of the IPMSM drive system are collected and stored in a PC through the dSPACE TRACE module. These data are then converted to the ASCII format for selection of wavelet function. The minimum description length (MDL) data criterion is applied on the collected data to select an optimum wavelet function in the proposed wavelet based multiresolution proportional integral derivative (MRPID) controller for the IPMSM drive systems. Once a mother wavelet is selected, the Shannon non-normalized entropy criterion is used to determine optimal levels of decomposition of the speed error signal using the optimum mother wavelet. The MDL data criterion is used to select the optimum wavelet filter of the proposed MRPID controller. The MDL principle states that the best model within group of models has the shortest description of data and the model itself. The MDL data criterion of indexes p and q is defined as [113]

$$MDL(p,q) = \min\left\{\frac{3}{2}\, p\, log N + \frac{N}{2}\, log\left\|\alpha_q - \alpha_q^{(p)}\right\|^2\right\} \tag{4.37}$$

where

$$0 \le p < N \tag{4.38}$$

$$1 \le q \le M. \tag{4.39}$$

The indexes p and q denote the number of coefficients to be retained and the number of wavelet filters, respectively. The integers N and M denote the length of the signal and the total number of wavelet filters, respectively. The α_q is a vector of the wavelet transformed coefficients of the speed error signal. The $\alpha_q^{(p)} = \Theta^p \alpha_q$ is a vector of p number of nonzero coefficients. The threshold parameter Θ^p keeps p number of largest elements and sets all other elements to zero.

The value of the MDL function using a wavelet filter determines optimal number of coefficients to be retained. In this work, the available orthogonal and non-orthogonal

wavelets of the MATLAB wavelet toolbox are tested by the MDL data criterion in order to select an optimum wavelet function. The orthogonal mother wavelets that are tested for this work are *Daubechies* wavelets (*db*1, *db*3, *db*4, *db*6, *db*8), *Coiflet* wavelets (*coif*1, *coif*3, *coif*5, *coif*8), *Meyer* wavelet (*dmey*), *Symlet* wavelets (*sym*1, *sym*2, *sym*3, *sym*4), and bi-orthogonal wavelets (*bior*1.3, *bior*3.5). The non-orthogonal mother wavelets that are tested for this work are *Morlet* wavelet (*morl*), *Gaussian* wavelets (*gaus*1, *gasu*4, *gaus*8), and *Mexican Hat* wavelet (*mexh*). The MDL criterion is applied on the collected data of the IPMSM drive system for each candidate mother wavelet function. The collected discrete data are decomposed up to the second level of resolution of the DWT by each candidate mother wavelet function. Table 4.1 shows the evaluation of the MDL indices of each candidate mother wavelet when the drive system is operated at the command speed of 188.6 rad/sec. Table 4.2 shows the evaluation of the MDL indices of each candidate mother wavelet when the drive system is operated at the command speed of 50 rad/sec. Table 4.3 shows the evaluation of the MDL indices of each candidate mother wavelet when the drive system is operated at the command speed of 250 rad/sec.

The evaluation of the MDL indices of Tables 4.1–4.3 show that the wavelet function '*gaus*8' of the non-orthogonal *Gaussian* family has the smallest MDL index of speed error both first and second level of resolution of the discrete wavelet transform (DWT). However, the filter bank realization of the proposed MRPID controller using the non-orthogonal *Gaussian* wavelet '*gaus*8' is not possible because it does not have scaling function. Therefore, the wavelet '*gaus*8' is not chosen for the proposed MRPID controller of the IPM motor drive system. The evaluation of Tables 4.1–4.3 also shows that the *Daubechies* wavelet functions ('*db*3', '*db*4', '*db*6', '*db*8') have the second smallest MDL indices of the speed error at both first and second level of resolution of the DWT. The MDL indices of speed error using the *Daubechies* wavelet functions ('*db*3', '*db*4', '*db*6', '*db*8') are almost identical at both first and second level of resolution. The filter lengths of the wavelet functions '*db*4', '*db*6', and '*db*8' are bigger than that of the wavelet filter '*db*3' for the real time implementation. So, more memory will be needed for the digital

TABLE 4.1

The MDL Indices of Speed Error of the IPMSM Drive System for the Command Speed of 188.6 rad/sec. (60 Hz)

Wavelet function	MDL (1st level)	MDL (2nd level)
*db*1	25.27	65.21
*db*3	25.23	65.12
*db*4	25.22	65.07
*db*6	25.23	65.00
*db*8	25.23	64.94
*coif*1	29.44	73.87
*coif*3	31.03	77.13
*coif*4	31.22	77.65
*coif*5	31.32	78.00
dmey	31.60	79.46
*sym*1	25.27	65.21
*sym*2	25.24	65.05
*sym*3	25.23	65.13
*sym*4	29.84	71.06
*bior*1.3	30.37	70.80
*bior*3.5	41.07	86.83
morl	4534.70	491.26
*gaus*1	7447.05	5141.26
*gaus*4	7398.23	3837.73
*gaus*8	0.35	0.50
mexh	4011.58	1729.4

TABLE 4.2

The MDL Indices of Speed Error of the IPMSM Drive System for the Command Speed of 50 rad/sec. (16 Hz)

Wavelet function	MDL (1st level)	MDL (2nd level)
*db*1	26.45	67.54
*db*3	26.40	67.42
*db*4	26.39	67.15
*db*6	26.39	66.94
*db*8	26.39	67.08
*coif*1	30.75	76.44
*coif*3	32.39	79.81
*coif*4	32.59	80.34
*coif*5	32.70	80.70
dmey	32.98	82.20
*sym*1	26.45	67.54
*sym*2	26.42	67.23
*sym*3	26.40	67.42
*sym*4	31.17	73.56
*bior*1.3	31.71	73.18
*bior*3.5	42.74	89.80
morl	4534.5	490.77
*gaus*1	7442.60	5138.95
*gaus*4	7400.01	3838.24
*gaus*8	0.32	0.71
mexh	4005.90	1726.03

TABLE 4.3

The MDL Indices of Speed Error of the IPMSM Drive System for the Command Speed of 250 rad/sec. (80 Hz)

Wavelet function	MDL (1st level)	MDL (2nd level)
*db*1	10.93	35.82
*db*3	10.90	35.77
*db*4	10.90	35.73
*db*6	10.91	35.67
*db*8	10.90	35.63
*coif*1	13.53	41.21
*coif*3	14.52	43.24
*coif*4	14.64	43.57
*coif*5	14.71	43.79
dmey	14.88	44.7
*sym*1	10.93	35.82
*sym*2	10.91	35.72
*sym*3	10.90	35.76
*sym*4	13.78	39.47
*bior*1.3	14.11	39.29
*bior*3.5	20.79	49.29
morl	3035.82	344.32
*gaus*1	4959.93	3415.46
*gaus*4	4512.46	2554.38
*gaus*8	0.8053	2.39
mexh	2670.11	1148.52

implementation of the wavelet filters '*db*4', '*db*6', and '*db*8'. On the other hand, the '*db*3' filter requires less memory for the real time implementation. The amplitude and phase responses of the '*db*3' high and low pass filters are shown in Figs. 4.8 and 4.9, respectively. The '*db*3' filters of Figs. 4.8–4.9 show minimum attenuation in the pass band and stop band frequencies. As a result, the proposed MRPID controller using the '*db*3' filters may perform smoother control than using other wavelet functions. The '*db*3' filters have linear phase response as shown in Figs. 4.8(*b*)-4.9(*b*). The amplitude responses of the '*db*3' filters of Figs. 4.8(*a*)-4.9(*a*) have changed monotonically from pass band to stop band frequencies. This property is useful to concentrate on specific frequency components and to remove the high frequency noise from the drive system. Therefore, the wavelet function '*db*3' is selected to carry out the multiresolution analysis (MRA) of the speed error signal of the proposed MRPID controller for the IPM motor drive system. The selected mother wavelet filter '*db*3' is used for both software and real time implementations of the proposed MRPID controller for the IPMSM drive system.

4.5 Number of Levels of Decomposition

The number of levels of decomposition of the speed error signal in the multiresolution analysis represents the number of tuning gains of the proposed MRPID controller for the IPMSM drive system. The number of decomposition levels depends on the signal and the type of the wavelet filter. The Shannon entropy based criterion is used in this work in order to find desired levels of decompositon of the speed error signal of the proposed MRPID controller. The entropy $H(x)$ of a signal $x[n]$ of length N is defined as [113]

$$H(x) = -\sum_{n=0}^{N-1} |x(n)|^2 \; log|x(n)|^2. \tag{4.40}$$

The entropy based criterion calculates the entropy of each subspace of the discrete wavelet transform (DWT). It compares the entropy of a parent subspace with those of its children's subspaces in order to find out the optimal levels of decomposition of a signal

using the optimum mother wavelet. The criterion states that if the entropy of a signal at a new level j is higher than that of the previous level j-1, i.e.

$$H(x)_j \geq H(x)_{j-1} \tag{4.41}$$

then the decomposition of the signal until level j of the DWT is not needed. The procedure is illustrated in Figs. 4.11, 4.12, and 4.13 for the command speeds of 188.6 rad/sec., 50 rad/sec., and 250 rad/sec. of the IPMSM drive system, respectively.

Figure 4.11 shows the entropy values of each subspace up to the third level of decomposition of the speed error using the selected mother wavelet '*db*3' for the command speed of 188.6 rad/sec. Figure 4.12 shows the entropy values of each subspace up to the third level of decomposition of the speed error using the selected mother wavelet '*db*3' for the command speed of 50 rad/sec. Figure 4.13 shows the entropy values of each subspace up to the third level of decomposition of the speed error using the selected mother wavelet '*db*3' for the command speed of 250 rad/sec. It is observed from Figs. 4.11–4.13 that the entropy values of the parent subspace are lower than those of its combined children's subspaces at first, second, and third level of resolution. Therefore, using the criterion of equations (4.40)–(4.41), the second and third level children's subspaces could be omitted from the DWT tree, which could provide the single level of resolution as the optimum level of speed error of the proposed wavelet controller. However, the speed error has been decomposed up to the second level of resolution for the precise control of the IPMSM drive system using the proposed wavelet based MRPID.

4.6 Wavelet Based Multiresolution PID Controller

In the fixed gain PID controller, the controller output u_{pid} is calculated from the error (e) between command and actual responses as

$$u_{pid} = k_p e + k_i \int e\,dt + k_d \frac{d}{dt} e \tag{4.42}$$

where the proportional (k_p), integral (k_i), and derivative (k_d) gains act on the error, integral of the error, and derivative of the error, respectively. In terms of frequency information, the proportional and integral of error has low frequency information of the error signal. The derivative of error has high frequency information of the error signal. The wavelet based mutliresolution PID (MRPID) controller for the IPMSM drive system decomposes the error (e) between command and actual speeds into its details (high frequency) components and approximations (low frequency) components up to the second level of resolution of the discrete wavelet function (DWT) using the selected mother wavelet "*db*3" as

$$e_{a^1}[n] = \sum_{k=0}^{N-1} g[k]\, e[n-k] \tag{4.43}$$

$$e_{d^1}[n] = \sum_{k=0}^{N-1} h[k]\, e[n-k] \tag{4.44}$$

$$e_{a^2}[n] = \sum_{k=0}^{N/2-1} g[k]\, e_{a^1}[2n-k] \tag{4.45}$$

$$e_{d^2}[n] = \sum_{k=0}^{N/2-1} h[k]\, e_{a^1}[2n-k] \tag{4.46}$$

where the selected wavelet function "*db*3" is used to generate the high pass filter coefficients $h[k]$ and low pass filter coefficients $g[k]$ in equations (4.43)–(4.46). The proposed MRPID controller filters the speed error in two stages. Each stage has a low pass filter (g) and a high pass filter (h). The filters g and h form quadrature mirror filter (QMF) bank for the multiresolution analysis (MRA) of the speed error.The filter coefficients $h[k]$ and $g[k]$ of the selected wavelet function "*db*3" for the MRPID controller are related to each other by the equation (4.36). These are determined as [108]

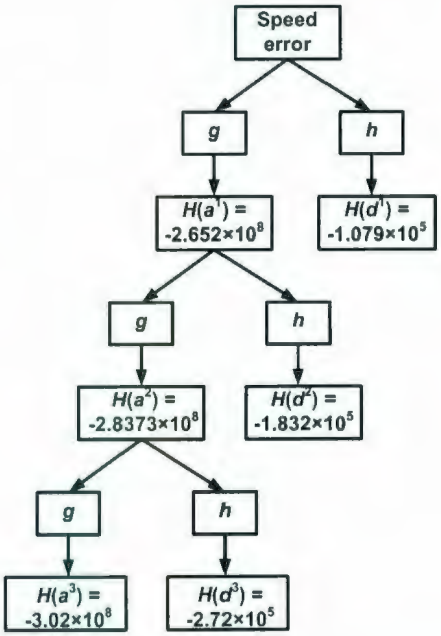

Figure 4.11: Entropy values (H) of the speed error at different level of resolution of the discrete wavelet transform (DWT) for the command speed of 188.6 rad/sec.

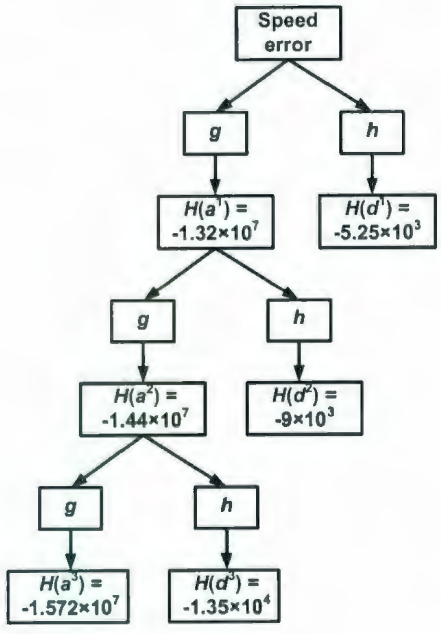

Figure 4.12: Entropy values (H) of the speed error at different level of resolution of the discrete wavelet transform (DWT) for the command speed of 50 rad/sec.

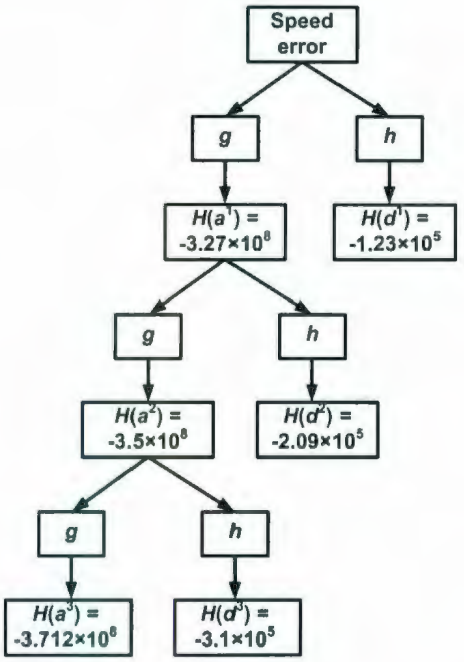

Figure 4.13: Entropy values (H) of the speed error at different level of resolution of the discrete wavelet transform (DWT) for the command speed of 250 rad/sec.

$$h[6] = [-0.3327\ 0.8069\ -0.4599\ -0.135\ 0.0854\ 0.0352] \tag{4.47}$$

$$g[6] = [0.0352\ -0.0854\ -0.135\ 0.4599\ 0.8069\ 0.3327]. \tag{4.48}$$

In the proposed MRPID controller, the control output u_{mrpid} is determined from the details and approximations of the speed error of equations (4.44)–(4.46) as [84]

$$u_{mrpid} = k_{d^1} e_{d^1} + k_{d^2} e_{d^2} + k_{a^2} e_{a^2}. \tag{4.49}$$

The proposed MRPID controller for the IPMSM drive system has three-gain parameters k_{d^1}, k_{d^2}, and k_{a^2} as the error signal is decomposed up to the second level of resolution of the DWT. The gains k_{d^1} and k_{d^2} are used for the tuning of high frequency components (e_{d^1}) and medium frequency components (e_{d^2}) of the speed error signal, respectively in

the DWT. The gain k_{a^2} is used for the tuning of low frequency components $\left(e_{a^2}\right)$ of the speed error signal in the DWT.

The performances of the IPMSM drive system can be affected by extraneous disturbances or noise during the operation. Therefore, the effects of disturbance and noise are considered in the design of an optimum control system for the IPMSM drive. The disturbance and command signals are low frequency signals. The noises are high frequency signals. Therefore, it is very difficult to minimize the effects of these uncertainties simultaneously. The MRPID controller can perform extremely well under these conditions. Figures 4.14–4.16 show the comparison of signals determined using the PID control and the multiresolution decomposition of the speed error signal. The proportional error using the PID control and the low frequency (high scale) components of error using the multiresolution decomposition are shown in Figs. 4.14(*a*) and 4.14(*b*), respectively. The low frequency components of speed error of Fig. 4.14(*b*) using the multiresolution decomposition are identical to the proportional error of Fig. 4.14(*a*) using the PID control. Therefore, the gain k_{a^2} for the low frequency components can be increased in order to reduce the settling time response and to improve the disturbance rejection of the drive system.

Figures 4.15(*a*) and 4.15(*b*) show the integral of error using the PID control and the medium frequency (medium scale) components of error using the multiresolution decomposition, respectively. The medium frequency components of speed error of Fig. 4.15(*b*) approximate the integral of speed error of Fig. 4.15(*a*) with low gain in the transient region and high gain in the steady state region. Therefore, the gain k_{d^2} for the medium frequency components can be increased in the steady state operating region to minimize the steady state speed error. Figures 4.16(*a*) and 4.16(*b*) show the differential of error using the PID control and the high frequency (low scale) components of error using the multiresolution decomposition, respectively.

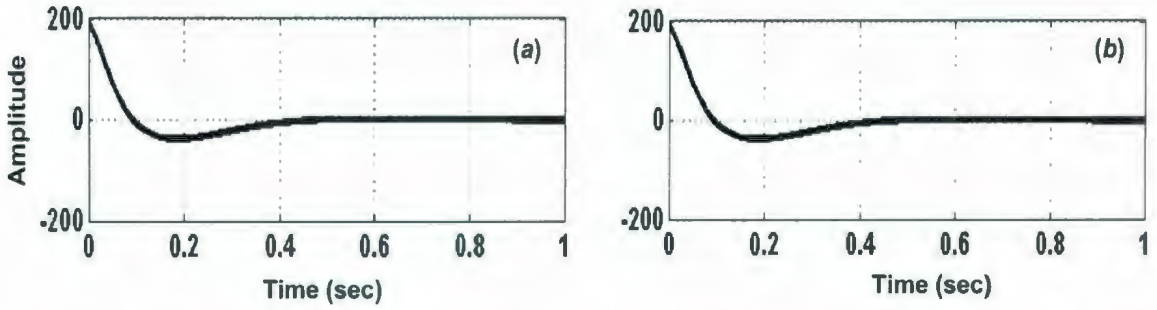

Figure 4.14: Comparison of PID control and multiresolution decomposition of error signal: (*a*) proportional error and (*b*) low frequency components of error.

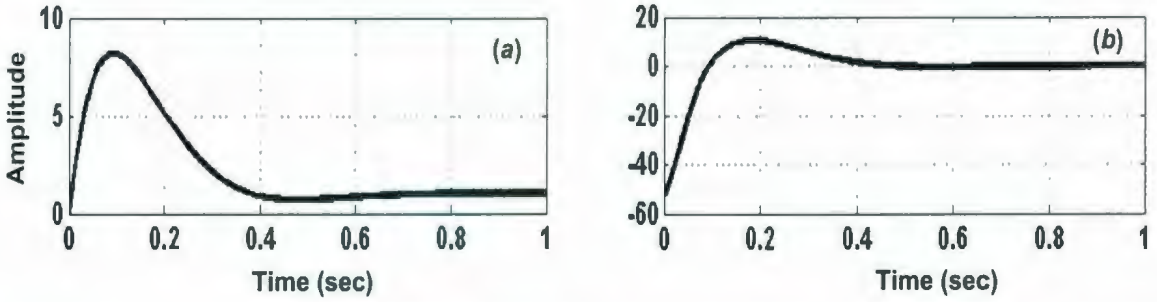

Figure 4.15: Comparison of PID control and multiresolution decomposition of error signal: (*a*) integral of error and (*b*) medium frequency components of error.

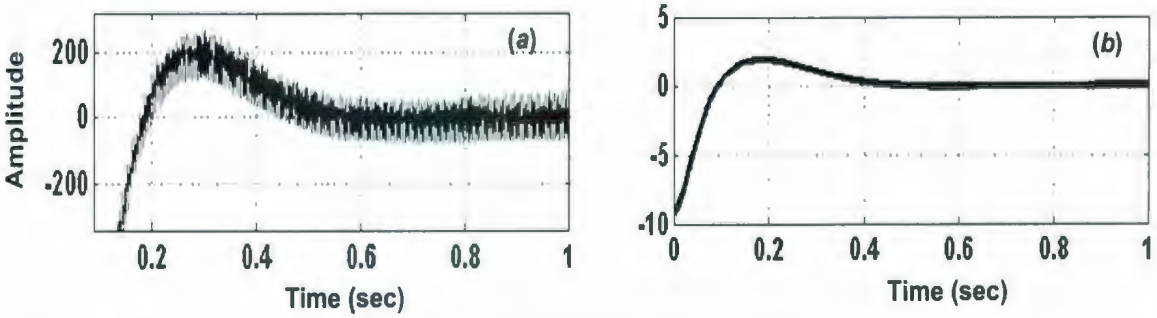

Figure 4.16: Comparison of PID control and multiresolution decomposition of error signal: (*a*) derivative of error and (*b*) high frequency components of error.

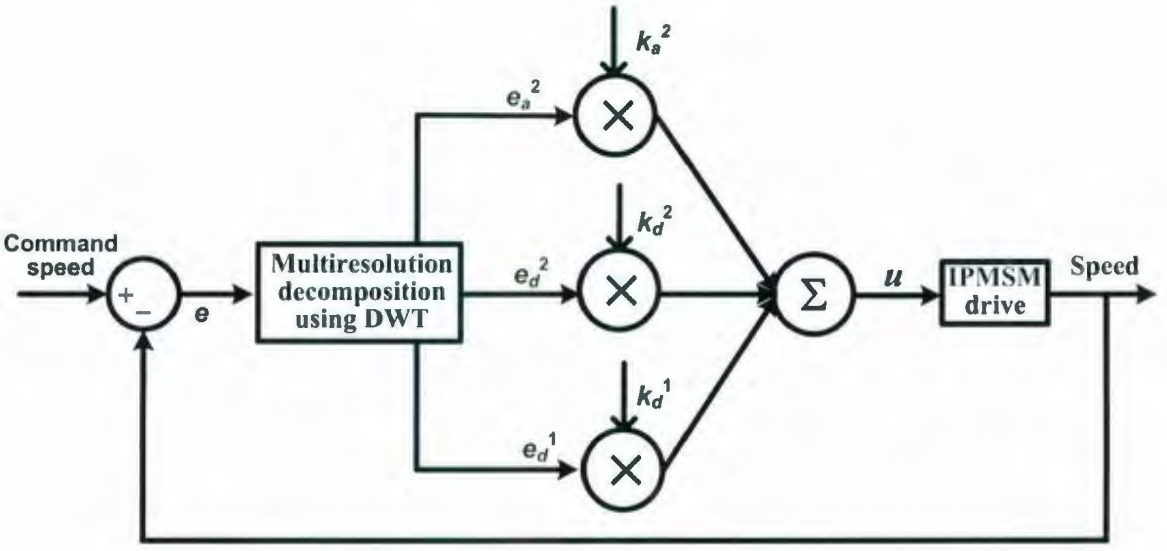

Figure 4.17: Specific schematic of the wavelet based MRPID controller for the IPMSM drive systems.

The high frequency components of speed error of Fig. 4.16(*b*) approximate the derivative of error of Fig. 4.16(*a*) with high gain. So, the gain k_{d^1} for the high frequency components can be increased to improve the transient response and to reduce the overshoot/undershoot in order to produce a smooth control signal for the drive system. Figure 4.17 shows the specific schematic of the wavelet based MRPID controller for the IPMSM drive system.

4.7 Concluding Remarks

In this chapter, the wavelet based multiresolution PID (MRPID) controller for the IPMSM drive system has been developed. The wavelet transforms and multiresolution analysis have been defined and illustrated at the beginning of the chapter. Then, the procedures for selecting optimum mother wavelet and for determining optimal levels of decomposition of the speed error signal of the MRPID controller have been presented and implemented for the interior permanent magnet synchronous motor (IPMSM) drive system. The mother wavelet function '*db*3' has been selected as the optimum wavelet

function for the proposed MRPID controller. The second level of resolution has been selected as the optimal levels of decomposition of the speed error of the proposed MRPID controller. Finally, the mathematical formulations and structure of the proposed MRPID controller have been defined and presented. The MRPID controller has been proposed as the robust speed controller for the IPMSM drive system in order to deal with parameter uncertainties and system disturbances. The simulated performances of the IPMSM drive system incorporating the proposed wavelet based MRPID controller have been presented in the next chapter.

Chapter 5

Implementation of Wavelet Based Control of the IPMSM Drive

The criteria of the high performance drive (HPD) systems are their ability to offer fast and accurate speed response, quick recovery of speed from disturbances, insensitivity to parameter variations and system noise, etc. These features are important to avoid the malfunction of the electric components connected to the drive system. Because of the nonlinearities of the interior permanent magnet synchronous motor (IPMSM) that may include magnetic saturation and parameter uncertainties, the precise control of the IPM motor is difficult for HPD applications. Therefore, special attention is needed for the control of the IPM motor for HPD applications. In a high performance IPMSM drive system, the speed controller generates the necessary command torque to cause the drive to follow the command speed for a wide range of operating conditions. The command speed can be tracked rapidly and precisely using the high performance speed controllers regardless of parameter variations and unexpected load excursions in the drive system. The conventional fixed gain PI and PID controllers are widely used as speed controllers due to their simple and easy implementation. However, these controllers show poor performances because of their high sensitivity to parameter variations, load changes, system disturbances, etc. Researchers have developed and implemented adaptive control techniques such as model reference adaptive control (MRAC), sliding mode control

(SMC), variable structure control (VSC), and self-tuning regulator (STR) to overcome some of the aforementioned problems. However, real time implementations of these adaptive controllers are very difficult and majority of them suffer from chattering, overreaching, and steady state errors. Moreover, the designs of the above mentioned controllers require exact modeling of the controlled drives. Furthermore, the traditional quantitative approaches of system modeling have significant limitations. In addition, it is difficult to develop a model that describes exactly the non-linear behavior of the IPMSM drive due to unpredictable dynamics, mutual interactions, and other phenomena. As a result, an intelligent speed controller is essential for the IPMSM to be used in the HPD systems.

This chapter presents a novel approach of speed control of the IPMSM drive system incorporating the proposed wavelet based multiresolution proportional integral derivative (MRPID) controller. Based on motor dynamics and non-linear load characteristics a new specific MRPID controller is developed and implemented for the maximum torque per ampere (MTPA) and flux weakening (FW) control of the IPMSM drive system. The MRPID controller is used in the outer loop of the FW control scheme. The hysteresis controller is used in the inner loop as a current controller. In order to predict the performances of the proposed drive system under various operating conditions, simulation and experimental performance tests of the drive system incorporating the proposed MRPID controller are presented and discussed in this chapter.

5.1 Modeling of the IPMSM for the MRPID Controller

The dynamics of the IPMSM are used to select the input and output variables of the proposed MRPID controller. Moreover, the maximum torque per ampere (MTPA) and flux weakening (FW) control scheme is incorporated with the MRPID controller in order to generate the maximum torque and to operate the drive over the rated speed of the IPMSM. The dynamics of the IPMSM in the synchronously rotating d^r-q^r frame are obtained as [93]–[94]

$$v_q^r = R\, i_q^r + P\,\omega_r \left(L_d\, i_d^r + \lambda_M\right) + L_q \frac{d}{dt} i_q^r \tag{5.1}$$

$$v_d^r = R\, i_d^r - P\,\omega_r\, L_q\, i_q^r + L_d \frac{d}{dt} i_d^r \tag{5.2}$$

where v_d^r, v_q^r are the *d-q* axis voltages, i_d^r, i_q^r are the *d-q* axis currents, L_d, L_q are the *d-q* axis inductances, λ_M is the permanent magnet flux linkage, ω_r is the rotor mechanical speed in rad/sec., R is the stator resistance per phase, and P is the number of pole pairs. The electromagnetic torque is defined as

$$T_e = \frac{3}{2} P\left(\lambda_M\, i_q^r + i_d^r\, i_q^r \left(L_d - L_q\right)\right) \tag{5.3}$$

and the motor dynamics using the load torque is defined as

$$T_e = J_m \frac{d\omega_r}{dt} + B_m\, \omega_r + T_L \tag{5.4}$$

where T_L is the load torque in N-m, B_m is the friction damping coefficient in N-m/rad/sec, and J_m is the rotor inertia constant in kg-m^2. The electromagnetic torque of equation (5.3) is a function of both i_d^r and i_q^r. The *d*-axis magnetizing current i_d^r is modeled as function of *q*-axis torque current i_q^r for the MTPA and FW control of the IPMSM drive system in chapter three. The motor dynamics of equation (5.4) can be represented as

$$\frac{d\omega_r}{dt} = \frac{1}{J_m}\left[T_e - T_l - B_m \omega_r\right]. \tag{5.5}$$

The load torque of equation (5.5) is non-linear and unpredictable in real time. The following equation can be used to model a non-linear load [91], [114]

$$T_L = A\,\omega_r^2 + B\,\omega_r + C \tag{5.6}$$

where A, B, and C are arbitrary constants, which implies that the load torque can be a constant value or linear and quadratic functions of rotor speed (ω_r). A laboratory

electrodynamometer, which is coupled to the shaft of the motor, is used as the load of the IPMSM drive.

The IPMSM dynamics can be expressed as a single input single output system in the continuous time domain by combining equations (5.5)–(5.6). The single input single output continuous time system is formed as

$$J_m \frac{d\omega_r}{dt} = T_e - (B_m + B)\omega_r - A\omega_r^2 - C. \tag{5.7}$$

A small incremental change ΔT_e of the electromagnetic torque T_e results in a corresponding change $\Delta\omega_r$ of the speed ω_r. Thus, the equation (5.7) can be rewritten as

$$J_m \frac{d(\Delta\omega_r)}{dt} = \Delta T_e - (B_m + B)\Delta\omega_r - A(\Delta\omega_r)^2. \tag{5.8}$$

The discrete time model of the IPMSM with nonlinear load is obtained by replacing all continuous quantities by their finite differences as

$$\Delta T_e(n) = \frac{J_m}{T_s}\Delta e(n) + (B_m + B)\Delta\omega_r(n) + A(\Delta\omega_r(n))^2 \tag{5.9}$$

$$\text{Therefore, } T_e(n) = \int_{discrete} \Delta T_e(n)dn = f(\Delta\omega_r(n), \Delta e(n)) \tag{5.10}$$

where $\Delta\omega_r(n)=\omega_r^*(n)-\omega_r(n)$ is the present sample of speed error, $\Delta\omega_r(n-1)$ is the past sample of speed error, $\Delta e(n)=\Delta\omega_r(n)-\Delta\omega_r(n-1)$ is the change of speed error, $\omega_r(n)$ is the present sample of actual speed, $\omega_r^*(n)$ is the present sample of command speed, T_s is the sampling time interval, and f is the nonlinear function. The purpose of using the MRPID controller for the IPMSM drive system is to map the nonlinear functional relationship between the electromagnetic torque $T_e(n)$ and the speed $\omega_r(n)$.

5.2 MRPID Controller Based IPMSM Drive System

The IPMSM model of equation (5.10) is used to define the input and output variables of the proposed MRPID controller. The input of the MRPID controller is the present sample of speed error $\Delta\omega_r(n)$. The output of the MRPID controller is the electromagnetic command torque T_e^* for the IPMSM drive system. The controller model of equations (4.37)–(4.43) are used to determine the command torque (T_e^*). The q-axis command current (i_q^*) is calculated from the command torque using the IPMSM model of equations (5.1)–(5.4). The q-axis command current component i_q^* provides the necessary torque to track the command speeds quickly under different operating conditions. The rotor position and the q-axis command current i_q^* are used in inverse Park's transformation to generate the command *a-b-c* phase currents for the IPMSM [93]. The command phase currents are compared with actual motor currents in a hysteresis current controller. The current controller generates the necessary switching pulses for the employed three-phase six-pulse inverter switches. Figure 5.1 shows the block diagram of the proposed new IPMSM control system incorporating the wavelet based MRPID controller. After the input and output variables of the proposed controller are chosen, the gains $\left(k_{d^1}, k_{d^2}, k_{a^2}\right)$ of the MRPID controller are selected. The gains k_{d^1}, k_{d^2}, and k_{a^2}, which are defined in chapter 4, are used for the tuning of high frequency components $\left(e_{d^1}\right)$, medium frequency components $\left(e_{d^2}\right)$, and low frequency components $\left(e_{a^2}\right)$ of speed error signal of equations (4.44)–(4.46) of chapter 4, respectively. In this work, the gains for the proposed controller are initially selected as $k_{d^1} = 0.0001$, $k_{d^2} = 1.2$, and $k_{a^2} = 0.4$ in order to get optimal performances of the drive system.

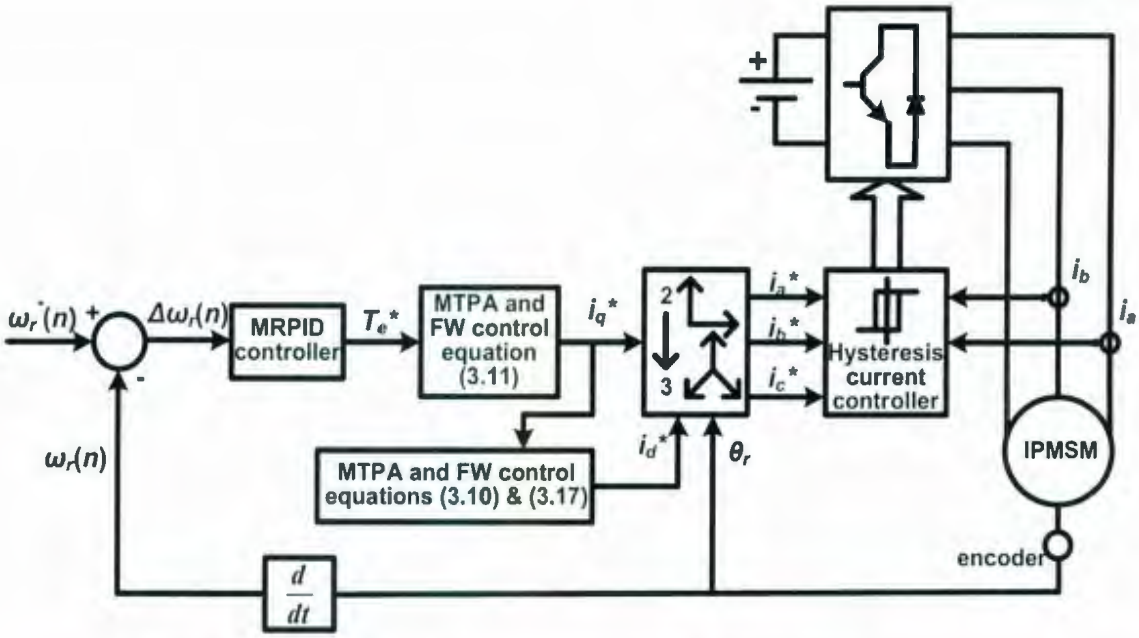

Figure 5.1: Schematic of the new IPMSM control system using the proposed wavelet based MRPID controller.

5.3 Implementation of the MRPID Controller Based IPMSM Drive System

Extensive simulation and experimental tests have been carried out in order to predict the performances of the IPMSM drive system using the proposed MRPID controller. The drive system has been simulated using the M-file format of the MATLAB software package [90]. The dSPACE ds1102 digital signal processor (DSP) board [103] has been used for the real time implementation of the IPMSM drive system. Both simulated and experimental performance test results have been presented in the chapter. The laboratory 1-hp IPMSM with rated load torque of 2 N-m has been used in the implementation of IPMSM drive system. The complete IPMSM drive system using the MRPID controller has been operated at different conditions including low and high starting command speeds, step changes of command speeds, variation of system parameters, and changes of load torque.

The drive system has been simulated to predict the speed responses at rated command speed of 188.6 rad/sec., at low command speed of 50 rad/sec., and at high command speed of 250 rad/sec. under no load and rated load conditions. The speed and current responses under these operating conditions have been shown in Figures 5.2–5.7. The proposed drive system has followed the low, high and rated command speeds very quickly without any overshoot and with minor steady state error. The steady state *d-q* axis command currents (i_d^*, i_q^*) have shown smooth response under these conditions. The steady state phase currents of the drive system have been sinusoidal under various operating speeds and loading conditions. Therefore, the proposed MRPID controller based IPMSM drive system can operate at wide range of speeds at various loading conditions.

The proposed drive system has been simulated with step changes in command speeds at both no load and rated load conditions. The speed and current responses of the drive system for step increase (from 150 rad/sec. to 250 rad/sec.) and for step decrease (from 250 rad/sec. to 188.6 rad/sec.) of command speeds at no load condition have been shown in Figures 5.8(*a*)–5.8(*d*). The speed and current responses of the drive system for step increase (from 150 rad/sec. to 250 rad/sec.) and for step decrease (from 250 rad/sec. to 188.6 rad/sec.) of command speeds at rated load condition have been shown in Figures 5.9(*a*)–5.9(*d*). The proposed MRPID controller based IPMSM drive system has followed the command speed quickly without overshoot, undershoot, and steady state error for step changes of command speeds at both no load and rated load conditions. The proposed MRPID controller has generated the necessary *d-q* axis command currents (i_d^*, i_q^*) to operate the drive system at the command speeds.

The proposed MRPID controller based IPM motor drive system has been simulated to predict its performance for a sudden impact of load. The speed, phase-*a* current, *q*-axis command current, and *d*-axis command current of the drive system have been shown in Figs. 5.10(*a*)–5.10(*d*), respectively for a sudden impact of load at the rated speed. Initially, the IPMSM drive has been started at the rated command speed at no load condition. Then, the load has been suddenly increased to rated load of 2 N-m at t = 0.5

sec. The drive system has shown sensitive performance for this change in load. The speed response has dropped significantly at the instant of load impact. In addition, the system has shown steady state speed error after the load has been changed.

The control performances of the IPMSM drive system can be influenced by system uncertainties. These uncertainties include parameter variations due to magnetic saturation and temperature variation due to high starting current. The performances of the proposed drive system have been investigated for a change in stator resistance at rated load condition. The speed and current responses of the drive system have been shown in Figs. 5.11(*a*)–5.11(*d*) when the stator resistance has been doubled at rated load and rated speed conditions. The drive system has followed the command speed accurately. The starting performances of the proposed drive system have been investigated with increased inertia at rated load condition. The starting speed response, phase-*a* current, *q*-axis command current, and *d*-axis command current have been shown in Figs. 5.12(*a*)–5.12(*d*), respectively for doubled rotor inertia at rated load and rated speed conditions. The drive system has followed the command speed smoothly with doubled rotor inertia at rated load condition. However, the system has taken slightly higher settling time of 0.1 sec to reach the steady state command speed because of the increased inertia.

The air gap flux distribution of an IPM motor can be distorted significantly because of the saturation of rotor iron around the permanent magnets. Therefore, the inductances of the IPMSM, especially the *q*-axis inductance (L_q), vary as a function of current magnitude and phase angle of the IPM motor [115]. The performance of the proposed drive system has been investigated for the variation of *q*-axis inductance (L_q). The starting speed response, phase-*a* current, *q*-axis command current, and *d*-axis command current of the IPMSM drive system have been shown in Figs. 5.13(*a*)–5.13(*d*), respectively when L_q has been reduced by 25% at rated speed and rated load conditions. The proposed MRPID controller based drive has tackled the variation of inductances effectively at rated load condition.

The experimental starting responses of the MRPID controller based IPMSM drive system at rated speed and rated load conditions have been shown in Fig. 5.14. The experimental starting responses of the MRPID controller based IPMSM drive system at low speed and rated load conditions have been shown in Figure 5.15. The proposed controller has taken 2 sec. to reach the steady state rated command speed of 188.6 rad/sec. It has taken less than 1 sec. to reach the steady state low command speed of 50 rad/sec. But the proposed controller has shown steady state speed error for both rated and low command speed conditions. The experimental starting responses of the MRPID controller based IPMSM drive system for step increase in command speeds (from 130 rad/sec. to 150 rad/sec. and from 150 rad/sec. to 188.6 rad/sec.) and for step decrease in command speeds (from 188.6 rad/sec. to 175 rad/sec.) at rated load condition have been shown in Figure 5.16. The drive system has shown significant undershoots, overshoots, and steady state speed error for step changes in command speeds.

The speed and current responses of the MRPID controller based IPMSM drive system for a step change in load have been shown in Figure 5.17. The proposed controller has shown sensitive responses for this step change in load. The speed of the drive system has dropped after the load has been changed. The experimental starting responses of the MRPID controller based IPMSM drive system for change in inertia at rated speed and rated load conditions have been shown in Figure 5.18. The experimental starting responses of the MRPID controller based IPMSM drive system for change in stator resistance at rated speed and rated load conditions have been shown in Fig. 5.19. The proposed controller has taken about 6 sec. and 4 sec. to reach to the steady state rated command speed for change in inertia and for change in stator resistance, respectively. The proposed controller has also responded slowly for changes in system parameters.

The speed responses of the IPM motor drive system of Figs. 5.14(a) and 5.18(a) using the fixed gain MRPID controller have experienced spikes before the motor speed reaches the command speed. The starting speed response of the drive system at the rated speed and rated load has been shown in Fig. 5.14(a). The starting speed response for change in inertia under the same operating condition has been shown in Fig. 5.18(a). The

spikes of the starting speed response of Figs. 5.14(*a*) and 5.18(*a*) have been caused because of the momentary variation of the voltage control knob to the motor terminal for a short period of time. The variable voltage control knob, which has been connected to the diode bridge rectifier, has been varied by hand as quickly as possible in order to apply proper voltage to the motor. However, because of the use of hand, the variation of the control knob could not be done smoothly and uniformly in all cases. Therefore, spikes have been generated in the starting speed responses of Figs. 5.14(*a*) and 5.18(*b*) for a short period of time. However, the performances of the drive system have not been affected significantly due to these spikes.

The steady state current spikes have been observed in the phase current responses of Figs. 5.14–5.19. The current spikes have been generated because of the electromagnetic torque ripples of the drive system. The current spikes have also been created by the vibration of the IPM motor. The initial current responses Figs. 5.14–5.19 have been varied with the operating conditions of the drive system. The difference between the initial current responses of Figs. 5.15(*a*) and 5.19(*b*) has been due to a variation in stator resistance at the starting of the drive system. The resistance has been increased to six times of the original resistance at the starting of the drive system of Fig. 5.19(*b*).

It is to be noted that the symbols Y1 and Y2 have been used to represent the speed response and the phase current response of the IPMSM drive system, respectively in Figs. 5.14–5.15, 5.18–5.19. It is also to be mentioned that the symbols Y1, Y2, and Y3 has been used to represent the speed response, the q-axis command current response, and the phase current response of the IPMSM drive system, respectively in Figs. 5.16–5.17.

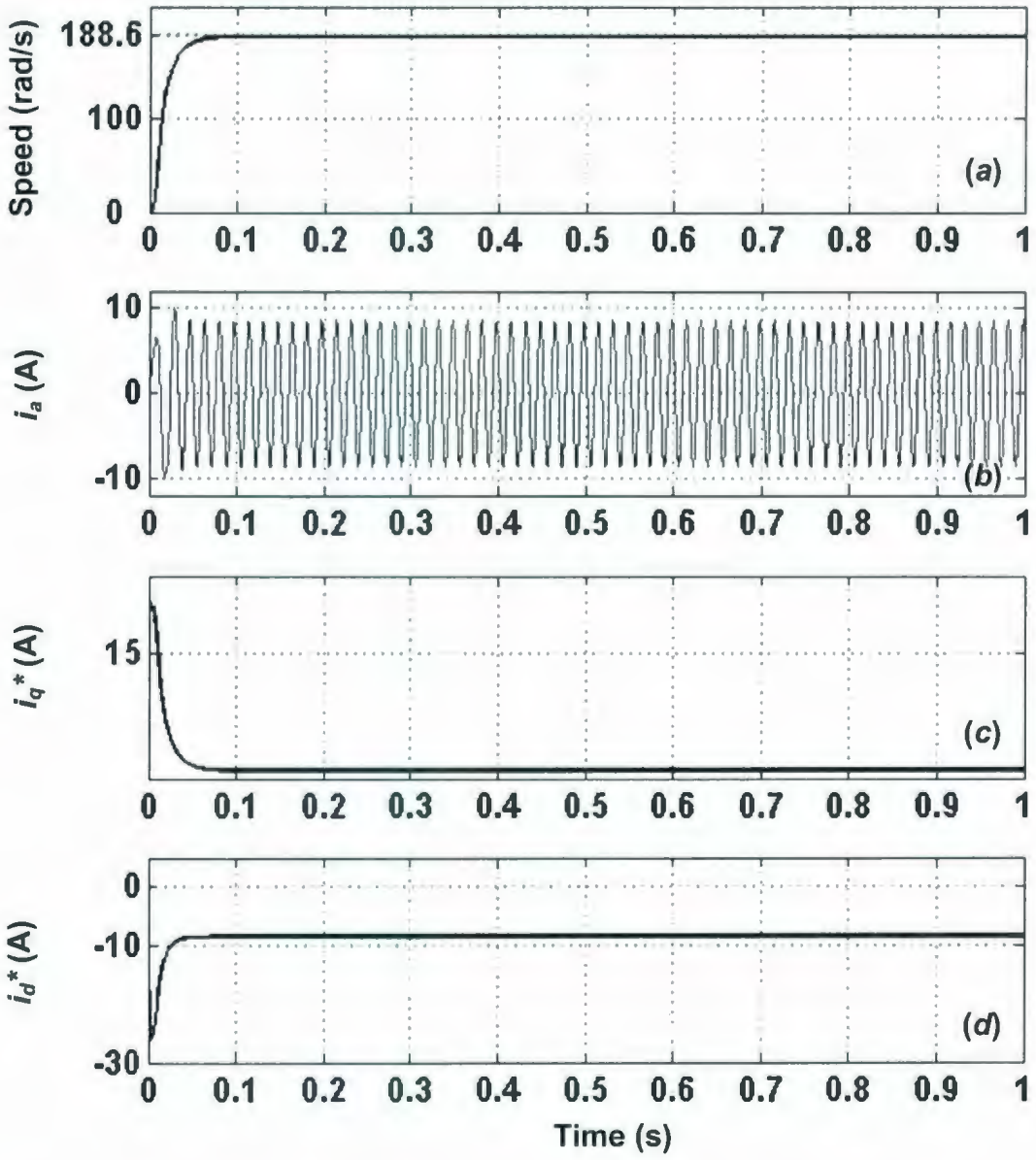

Figure 5.2: Simulated starting responses of the proposed MRPID controller based IPMSM drive system under no load and rated speed (188.6 rad/sec.) conditions: (*a*) speed, (*b*) phase current (i_a), (*c*) *q*-axis command current (i_q^*), and (*d*) *d*-axis command current (i_d^*).

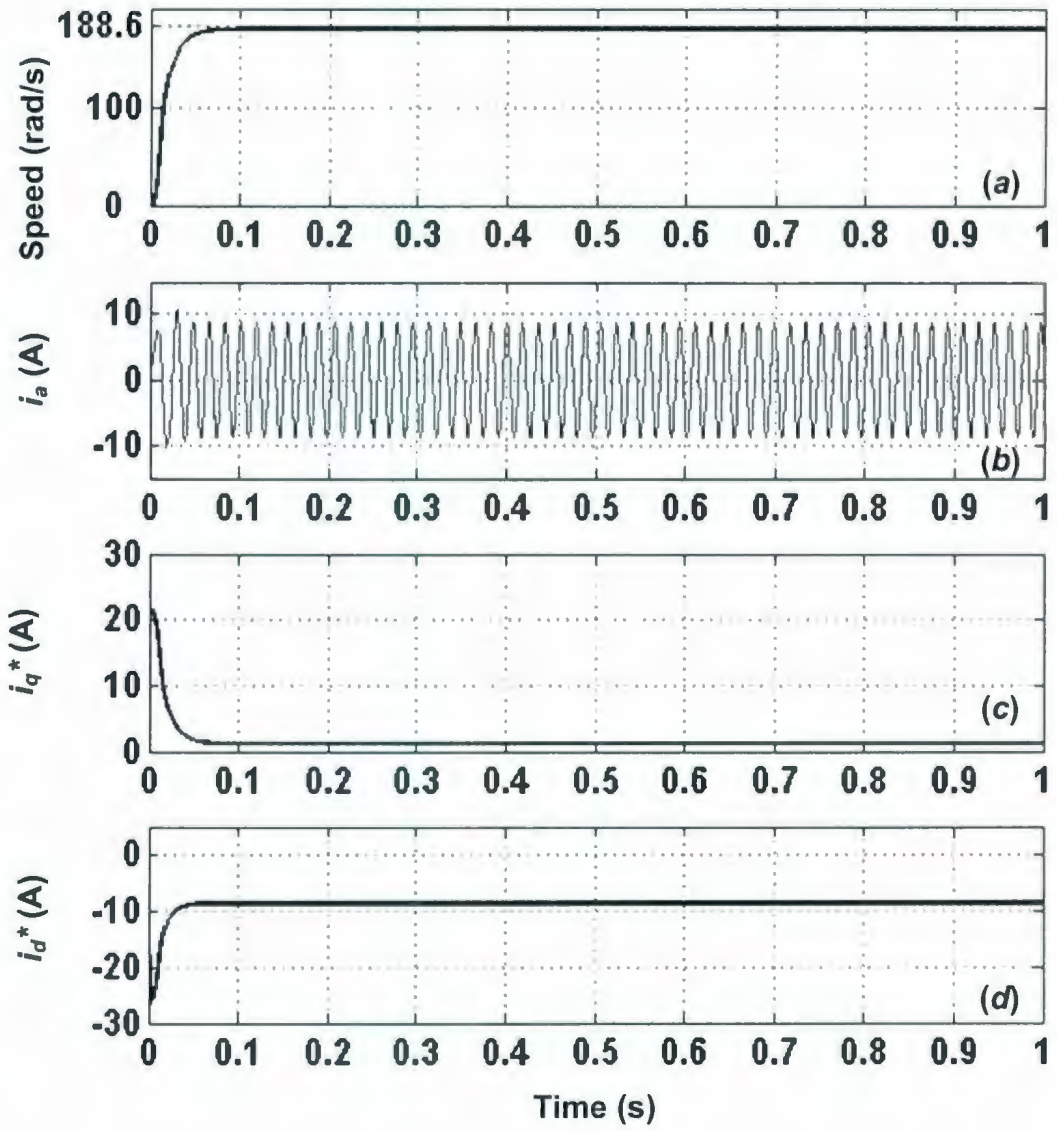

Figure 5.3: Simulated starting responses of the proposed MRPID controller based IPMSM drive system under rated load and rated speed (188.6 rad/sec.) conditions: (*a*) speed, (*b*) phase current (i_a), (*c*) *q*-axis command current (i_q^*), and (*d*) *d*-axis command current (i_d^*).

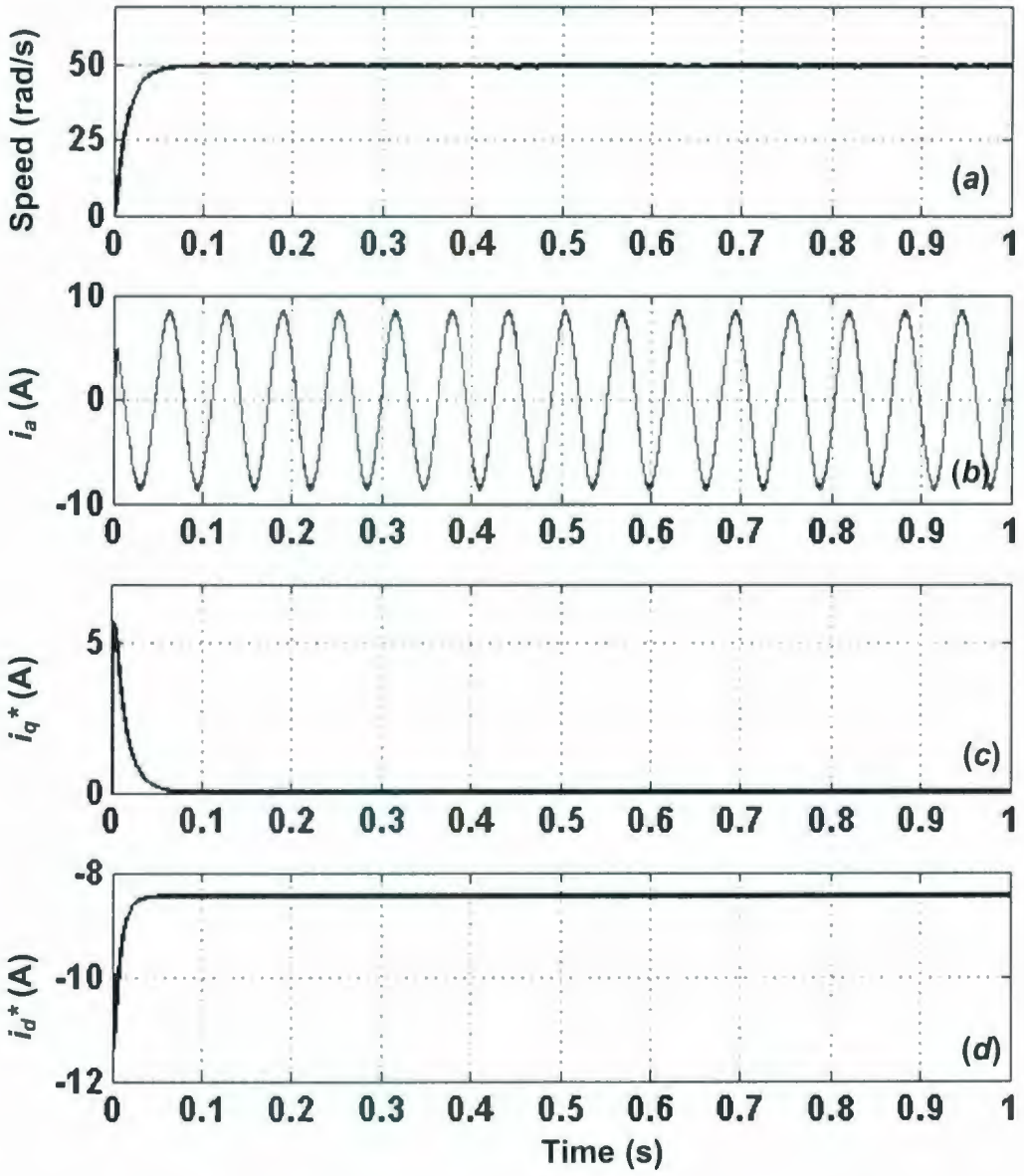

Figure 5.4: Simulated starting responses of the proposed MRPID controller based IPMSM drive system under no load and low speed (50 rad/sec.) conditions: (*a*) speed, (*b*) phase current (i_a), (*c*) *q*-axis command current (i_q^*), and (*d*) *d*-axis command current (i_d^*).

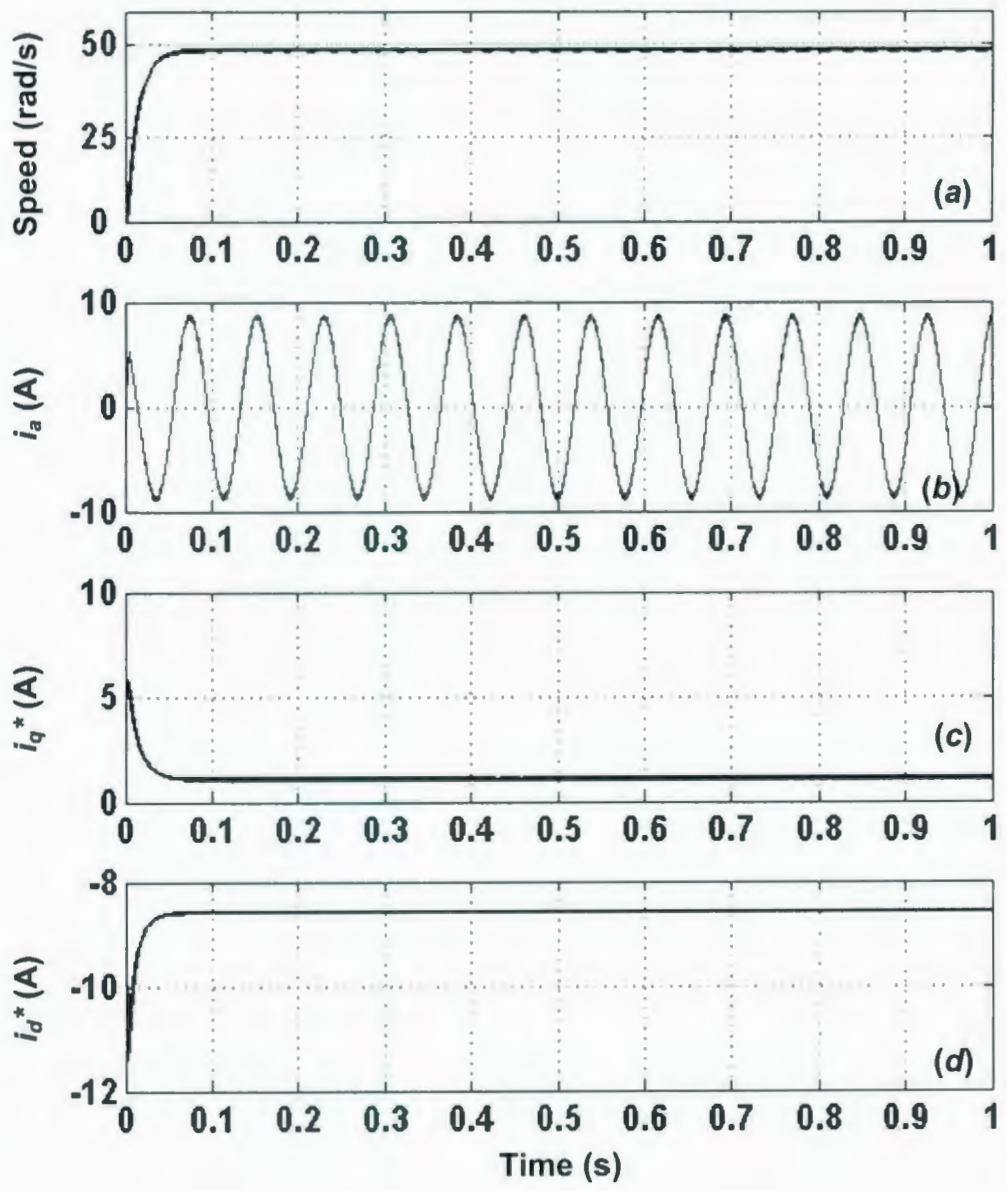

Figure 5.5: Simulated starting responses of the proposed MRPID controller based IPMSM drive system under rated load and low speed (50 rad/sec.) conditions: (*a*) speed, (*b*) phase current (i_a), (*c*) *q*-axis command current (i_q^*), and (*d*) *d*-axis command current (i_d^*).

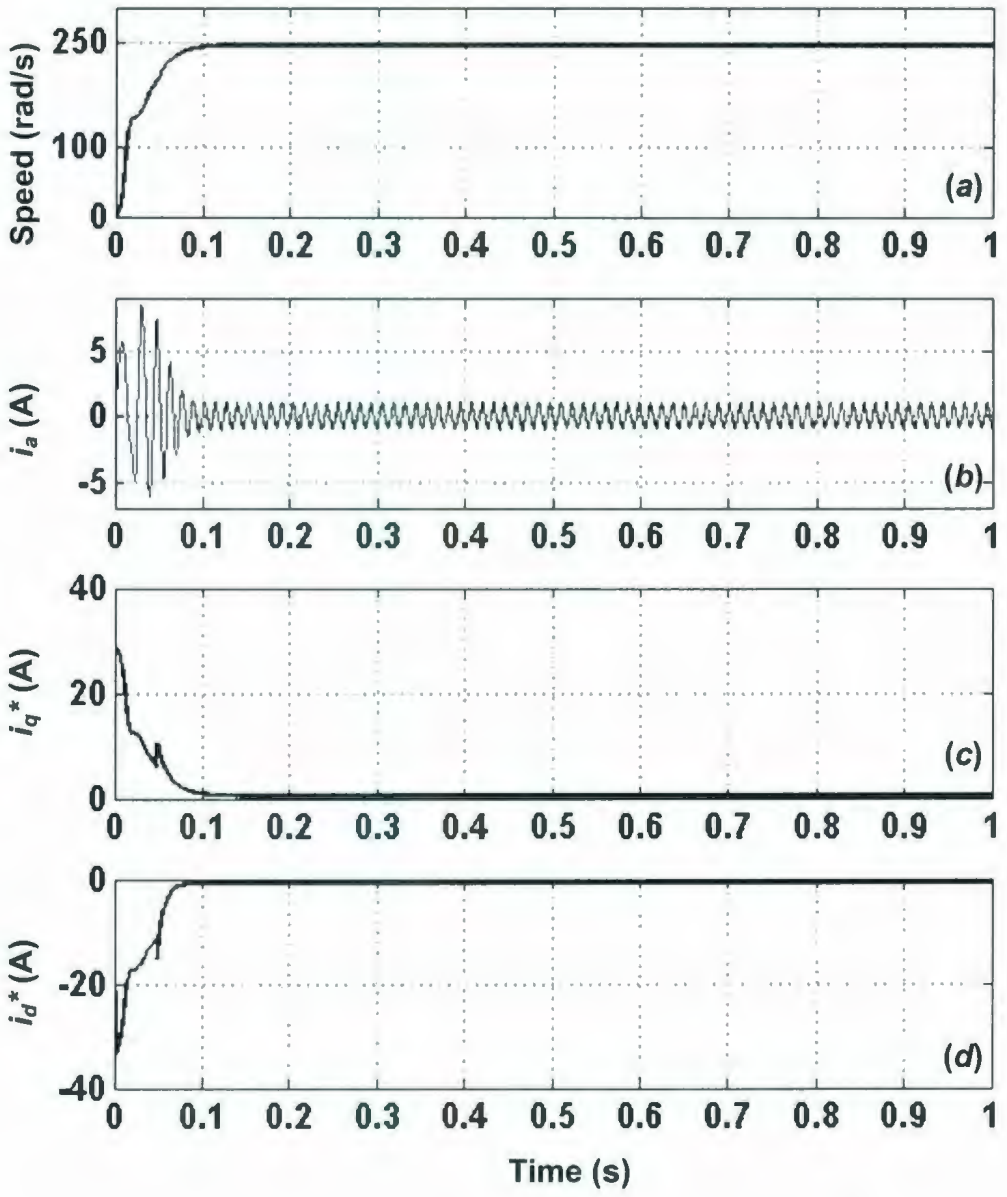

Figure 5.6: Simulated starting responses of the proposed MRPID controller based IPMSM drive system under no load and high speed (250 rad/sec.) conditions: (*a*) speed, (*b*) phase current (i_a), (*c*) *q*-axis command current (i_q^*), and (*d*) *d*-axis command current (i_d^*).

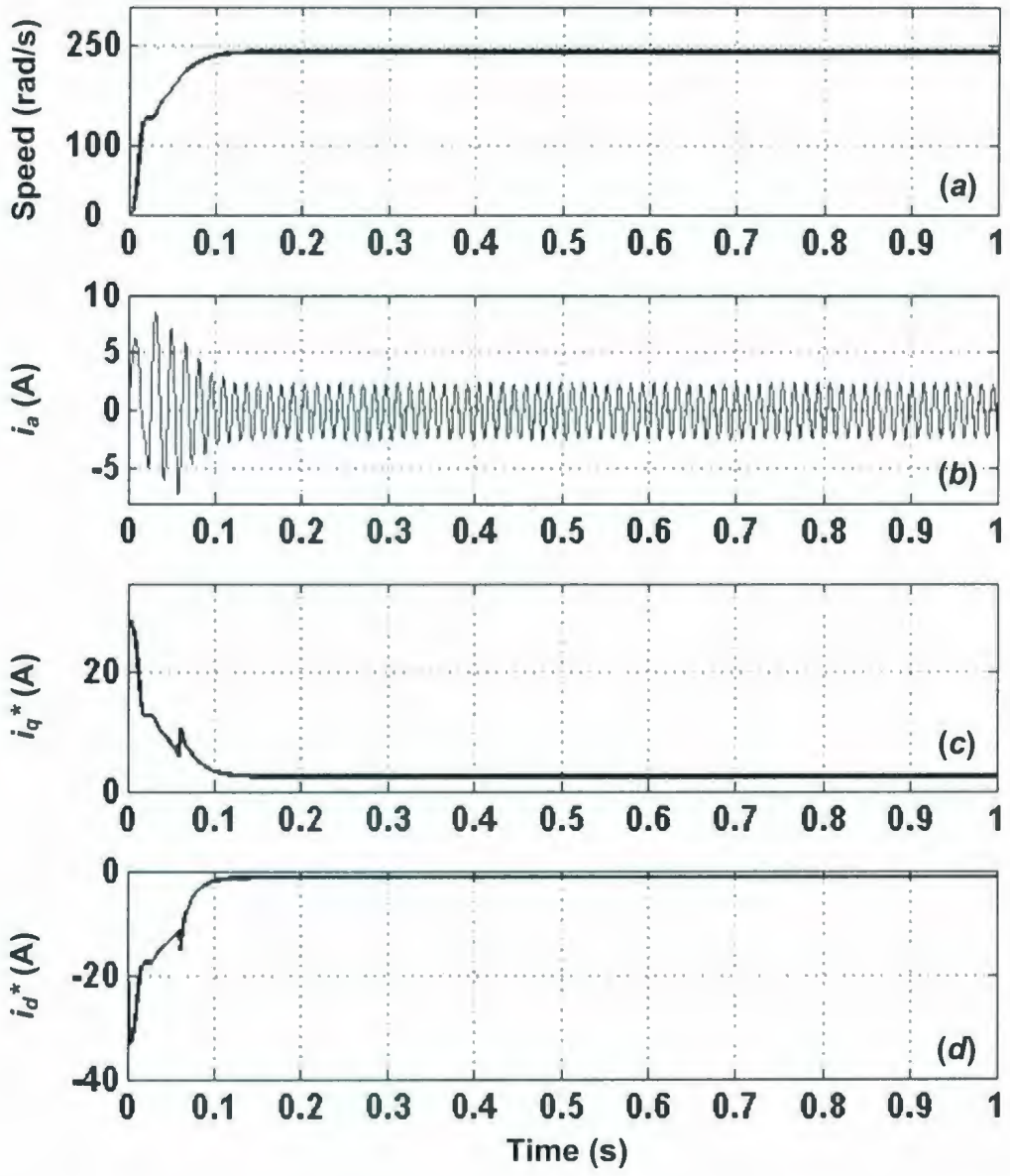

Figure 5.7: Simulated starting responses of the proposed MRPID controller based IPMSM drive system under rated load and high speed (250 rad/sec.) conditions: (*a*) speed, (*b*) phase current (i_a), (*c*) *q*-axis command current (i_q^*), and (*d*) *d*-axis command current (i_d^*).

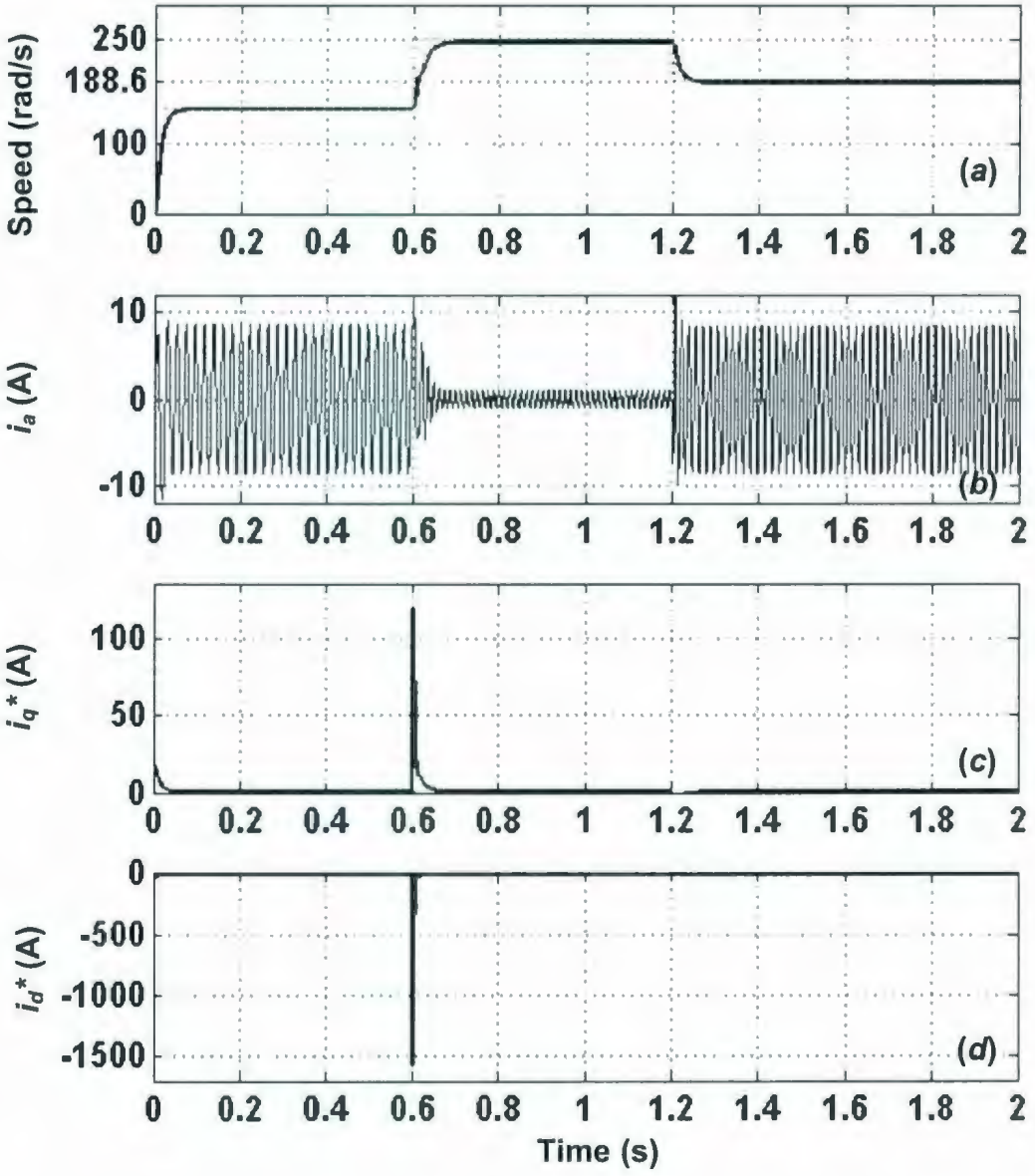

Figure 5.8: Simulated responses of the proposed MRPID controller based IPMSM drive system for step increase (from 150 rad/sec. to 250 rad/sec.) and step decrease (from 250 rad/sec. to 188.6 rad/sec.) of command speeds under no load condition: (*a*) speed, (*b*) phase current (i_a), (*c*) *q*-axis command current (i_q^*), and (*d*) *d*-axis command current (i_d^*).

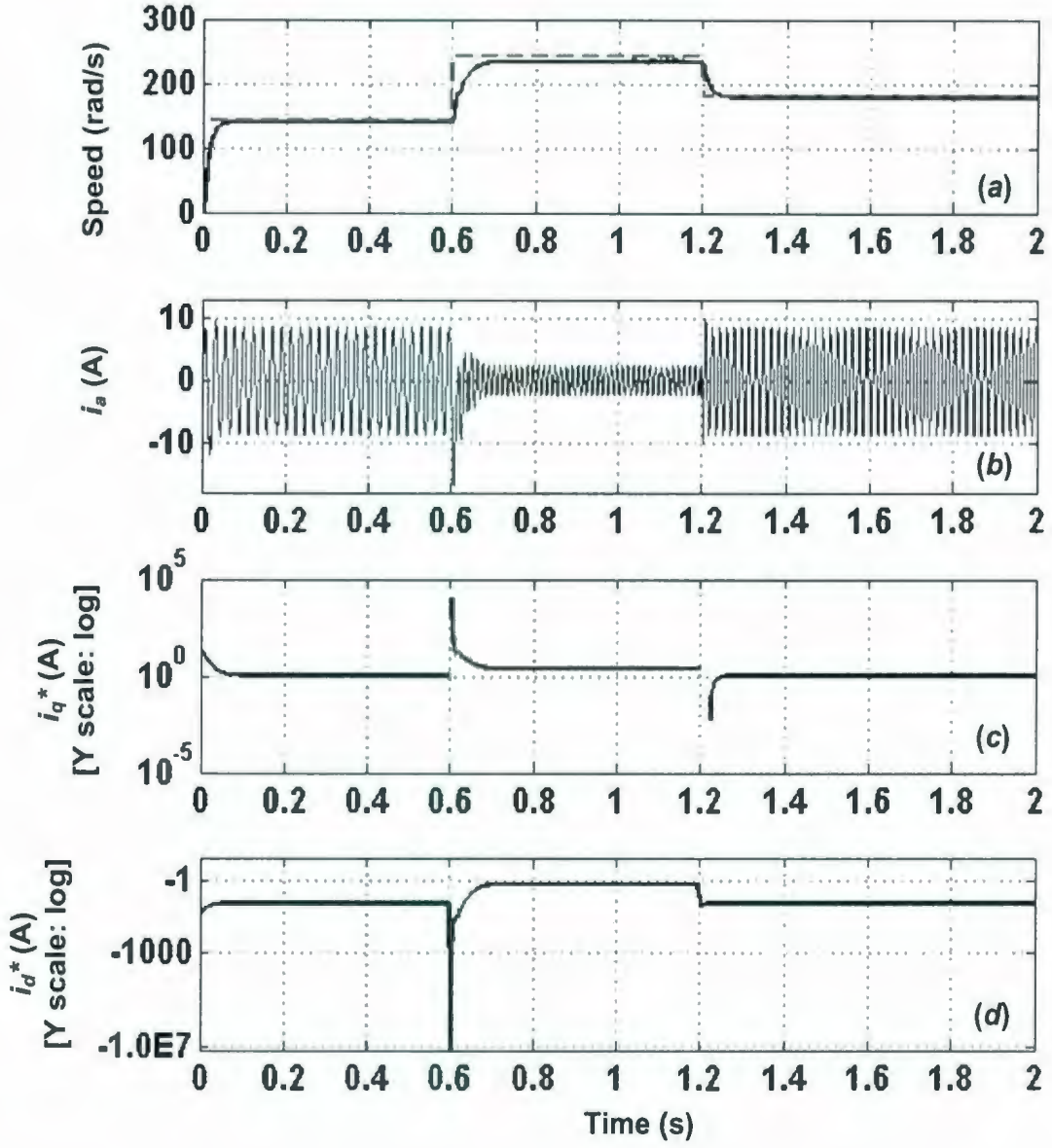

Figure 5.9: Simulated responses of the proposed MRPID controller based IPMSM drive system for step increase (from 150 rad/sec. to 250 rad/sec.) and step decrease (from 250 rad/sec. to 188.6 rad/sec.) of command speeds under rated load condition: (*a*) speed, (*b*) phase current (i_a), (*c*) *q*-axis command current (i_q^*), and (*d*) *d*-axis command current (i_d^*).

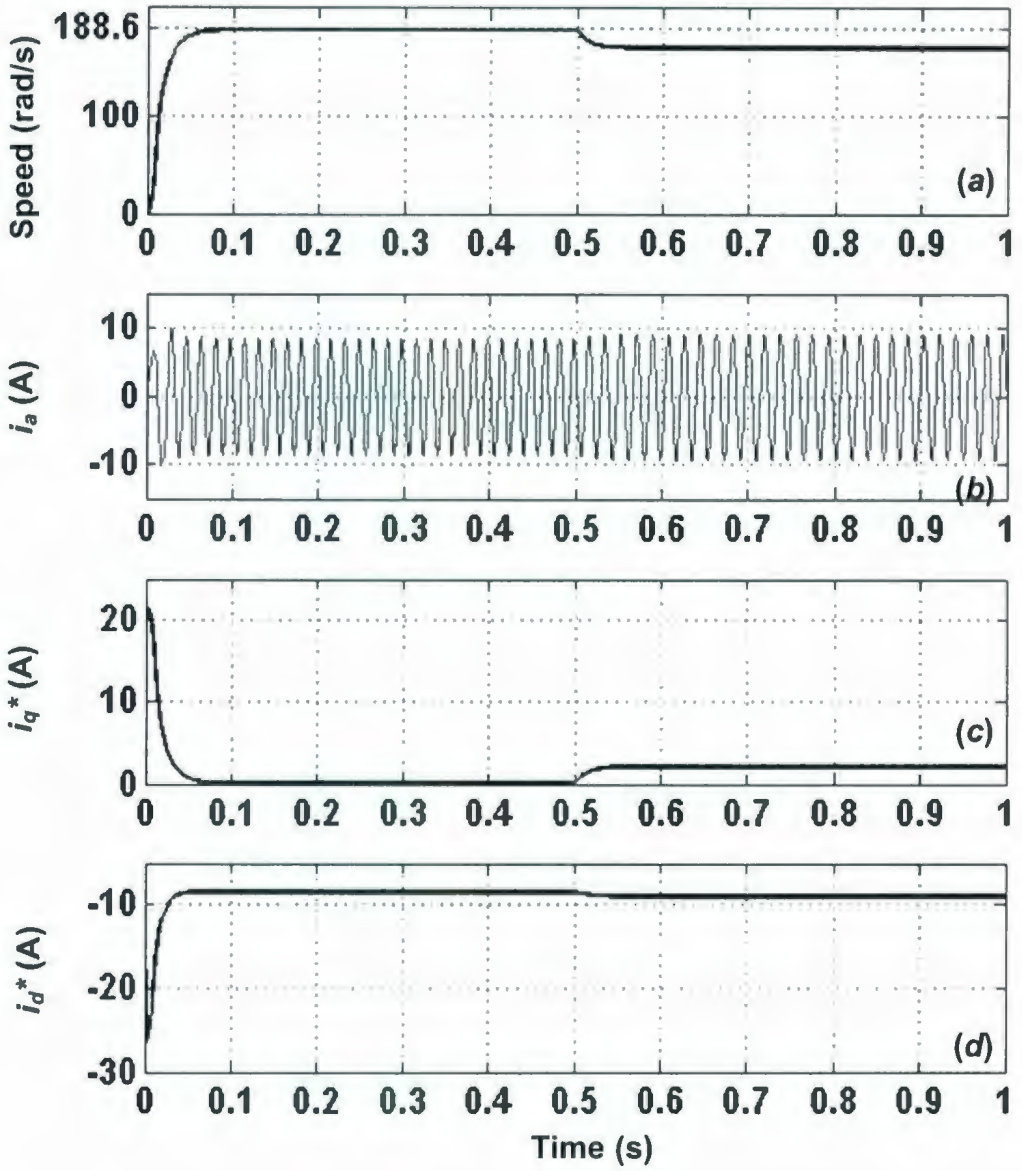

Figure 5.10: Simulated responses of the proposed MRPID controller based IPMSM drive system when load is changed at t = 0.5 second from no load to rated load under rated command speed (188.6 rad/sec.) condition: (*a*) speed, (*b*) phase current (i_a), (*c*) q-axis command current (i_q^*), and (*d*) d-axis command current (i_d^*).

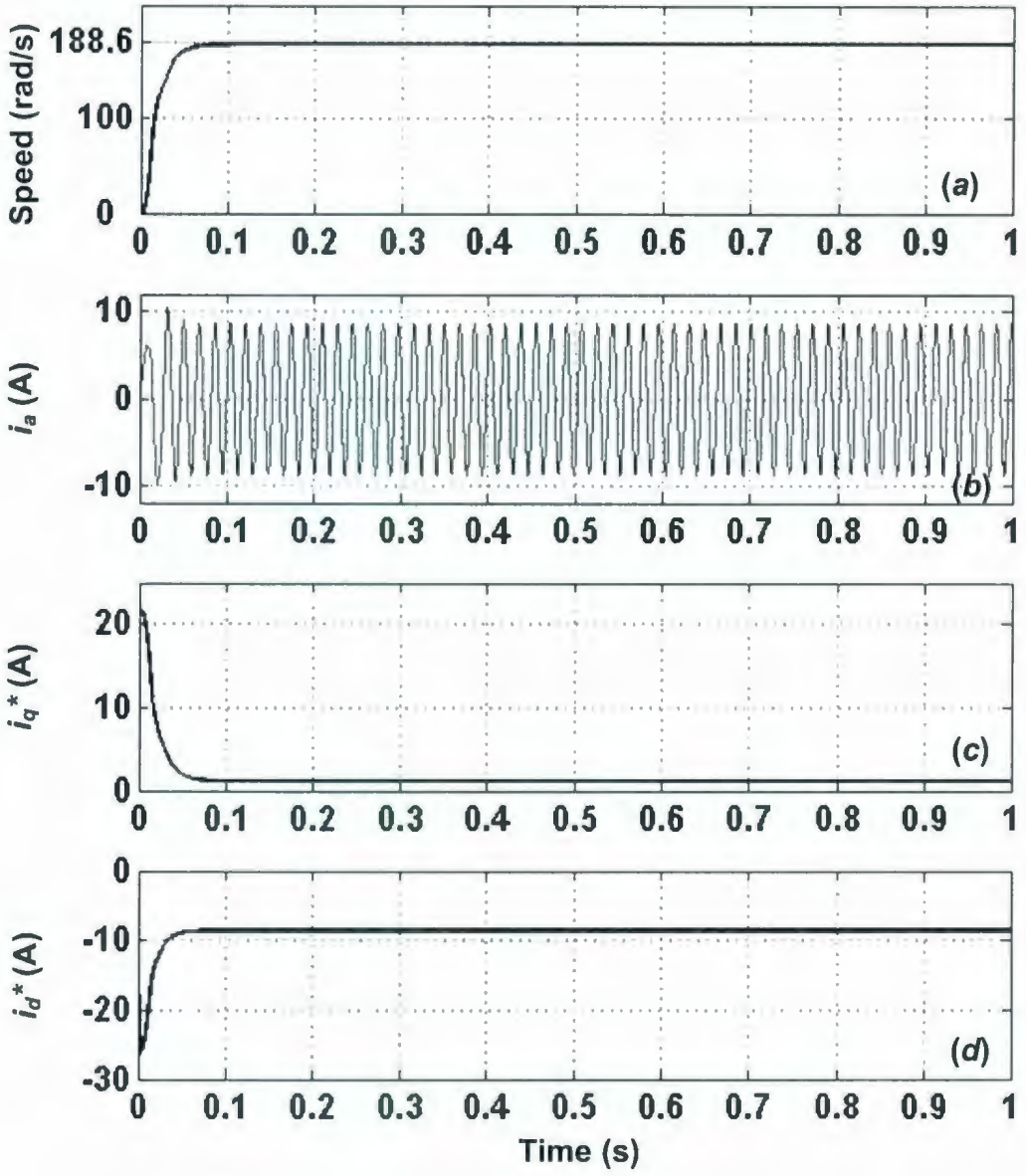

Figure 5.11: Simulated starting responses of the proposed MRPID controller based IPMSM drive system for change in stator resistance ($R_1 = 2*R$) under rated load and rated command speed (188.6 rad/sec.) conditions: (*a*) speed, (*b*) phase current (i_a), (*c*) *q*-axis command current (i_q^*), and (*d*) *d*-axis command current (i_d^*).

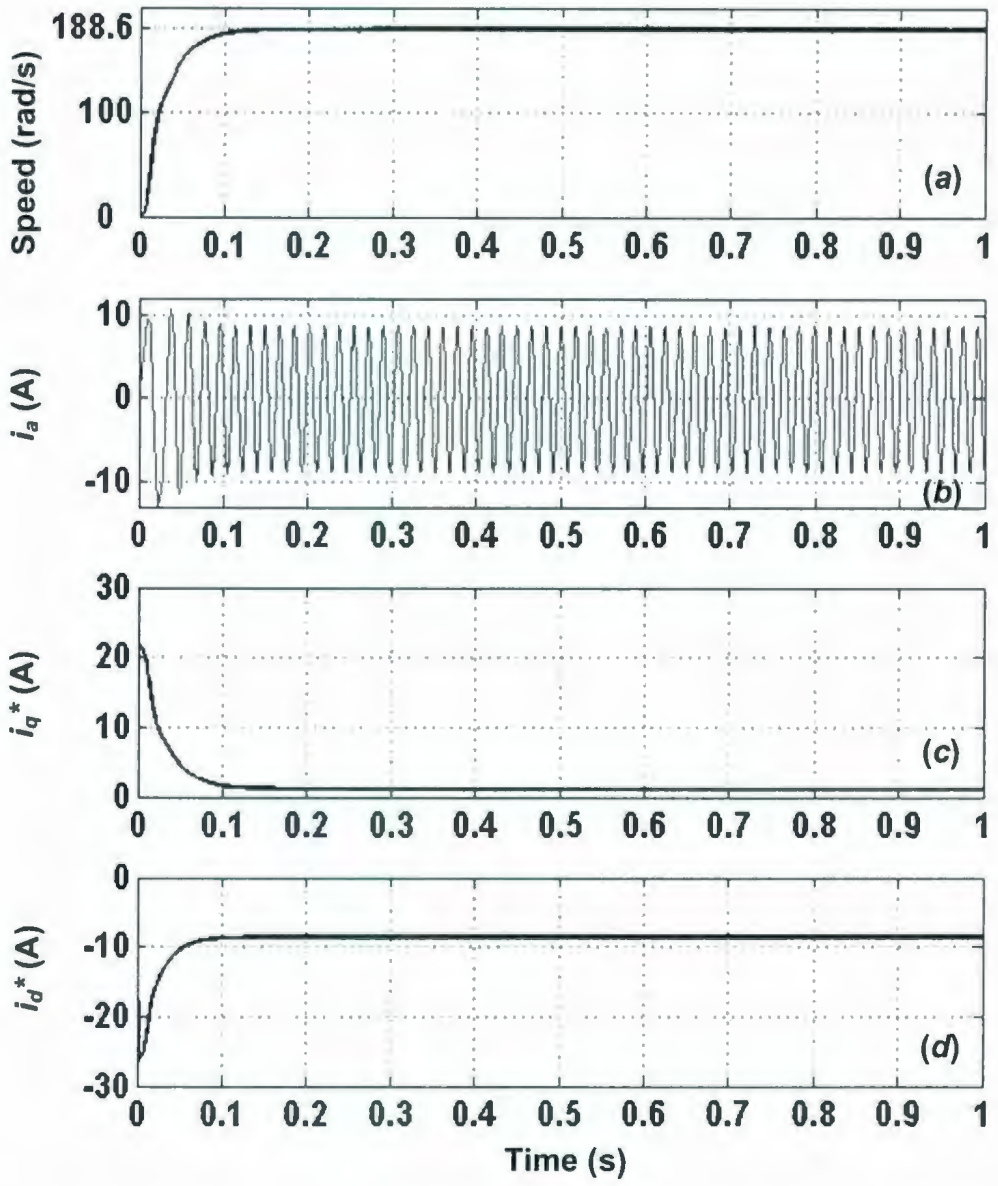

Figure 5.12: Simulated starting responses of the proposed MRPID controller based IPMSM drive system for change in rotor inertia (J_1 = 2*J) under rated load and rated command speed (188.6 rad/sec.) conditions: (*a*) speed, (*b*) phase current (i_a), (*c*) q-axis command current (i_q*), and (*d*) d-axis command current (i_d*).

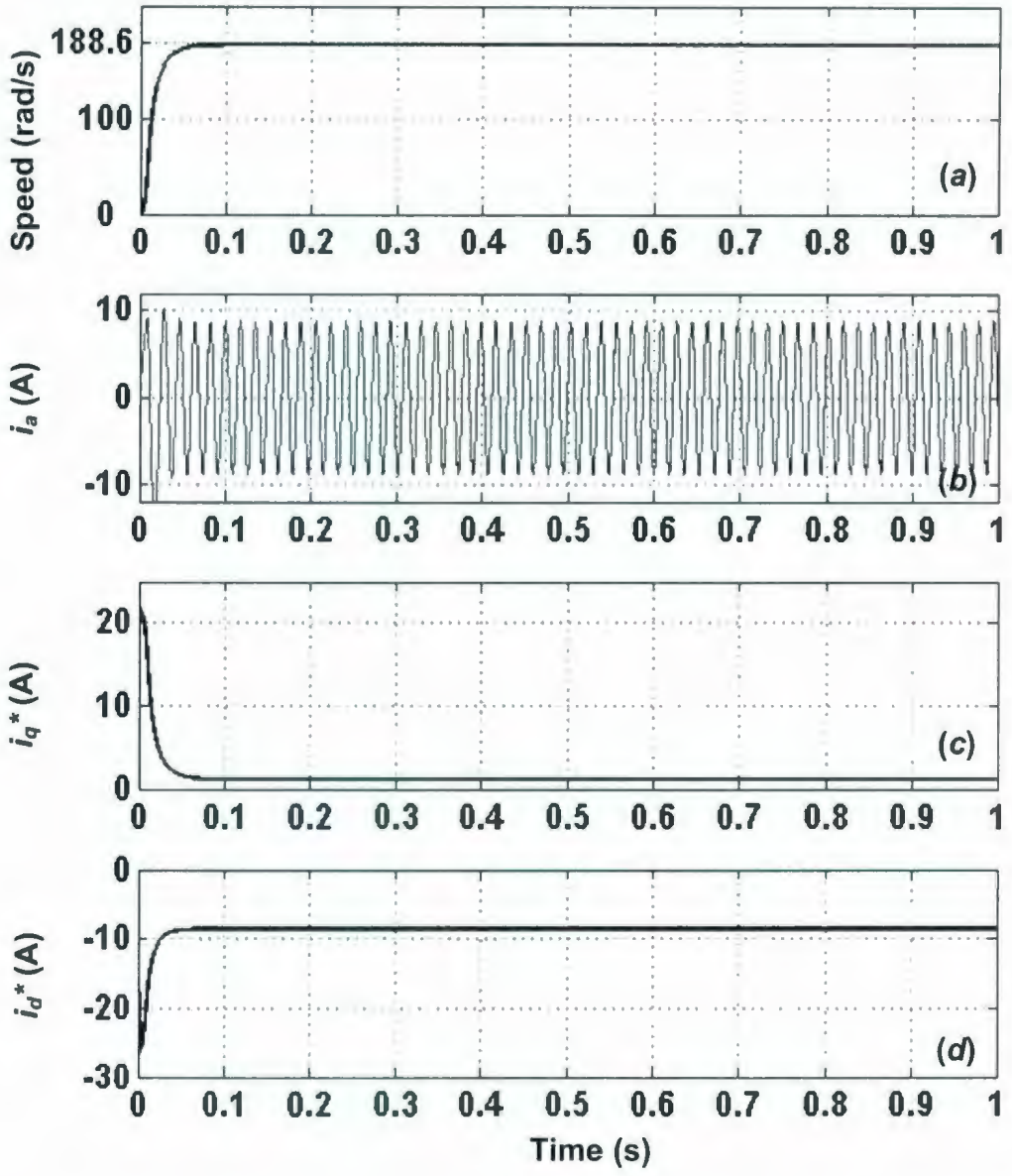

Figure 5.13: Simulated starting responses of the proposed MRPID controller based IPMSM drive system when L_q is reduced by 25% under rated load and rated command speed (188.6 rad/sec.) conditions: (*a*) speed, (*b*) phase current (i_a), (*c*) *q*-axis command current (i_q^*), and (*d*) *d*-axis command current (i_d^*).

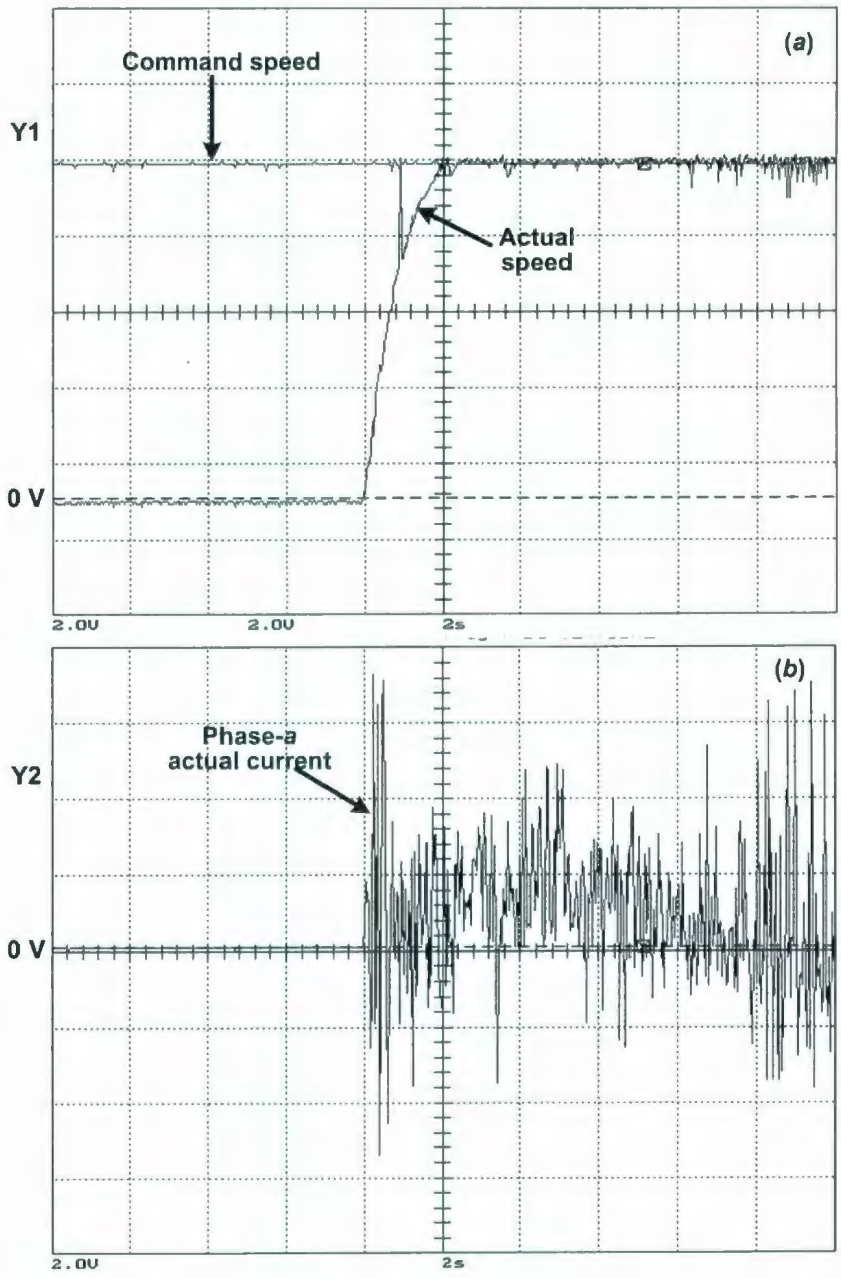

Figure 5.14: Experimental starting responses of the proposed MRPID controller based IPMSM drive system under rated load and rated speed (188.6 rad/sec.) conditions: (*a*) speed response (Y1: 2 V/div., 1V = 20 rad/sec., time: 2 sec./div.) and (*b*) current response (Y2: 2 V/div., 1V = 0.933 A, time: 2 sec./div.).

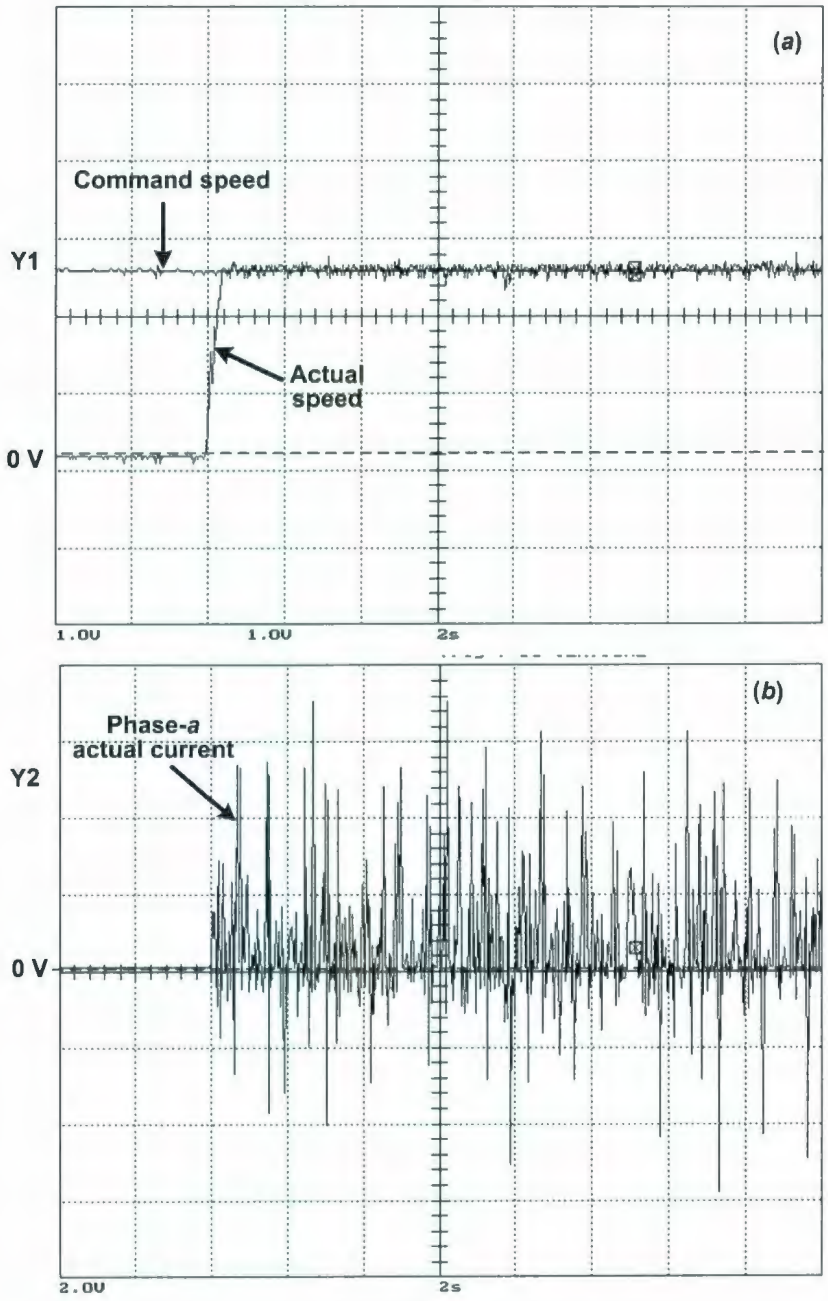

Figure 5.15: Experimental starting responses of the proposed MRPID controller based IPMSM drive system under rated load and low speed (50 rad/sec.) conditions: (*a*) speed response (Y1: 1 V/div., 1V = 20 rad/sec., time: 2 sec./div.) and (*b*) current response (Y2: 2 V/div., 1V = 0.933 A, time: 2 sec./div.).

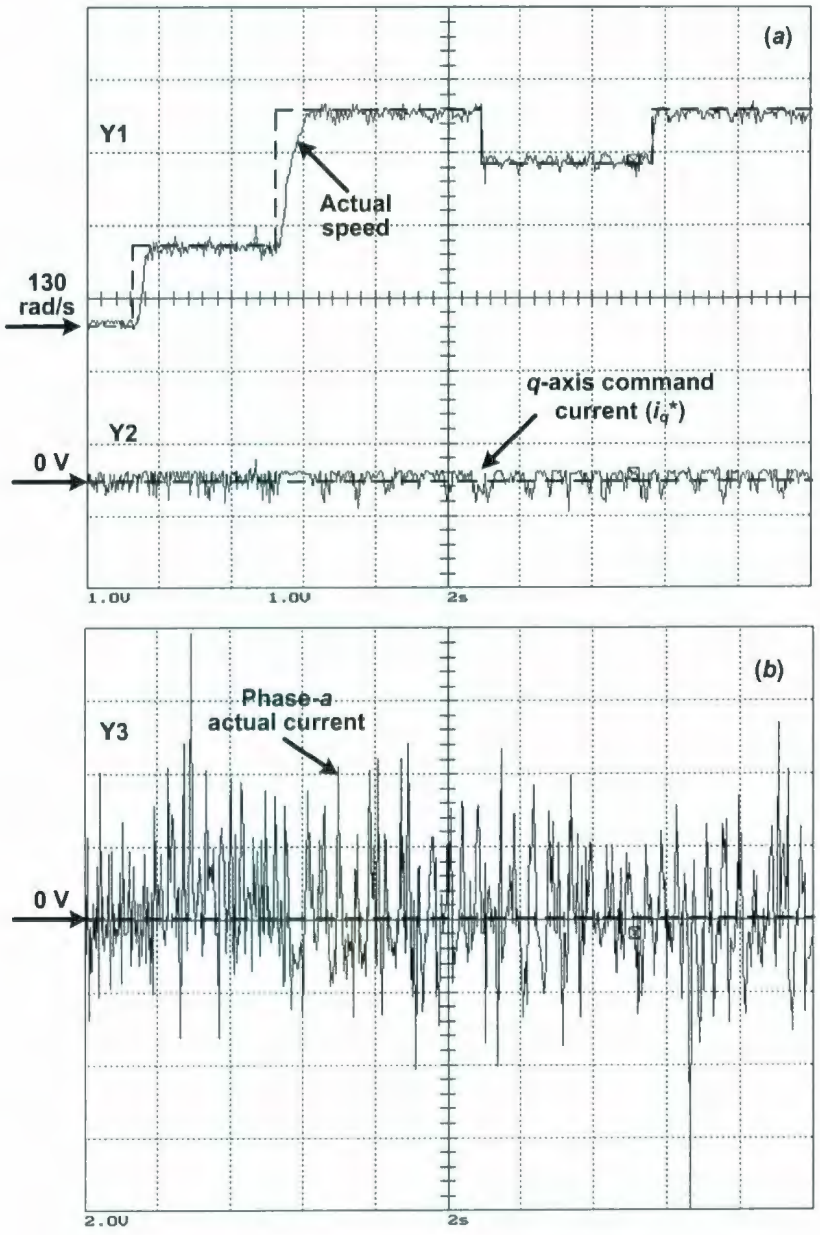

Figure 5.16: Experimental responses of the proposed MRPID controller based IPMSM drive system for step changes in command speeds (130 rad/sec. to 150 rad/sec., 150 rad/sec. to 188.6 rad/sec., 188.6 rad/sec. to 175 rad/sec., 175 rad/sec. to 188.6 rad/sec.) at rated load condition: (*a*) speed and *q*-axis command current responses (Y1: 1 V/div., 1V = 20 rad/sec., Y2: 1 V/div., 1V = 1.6 A, time: 2 sec./div.) and (*b*) phase current response (Y3: 2 V/div., 1V = 0.933 A, time: 2 sec./div.).

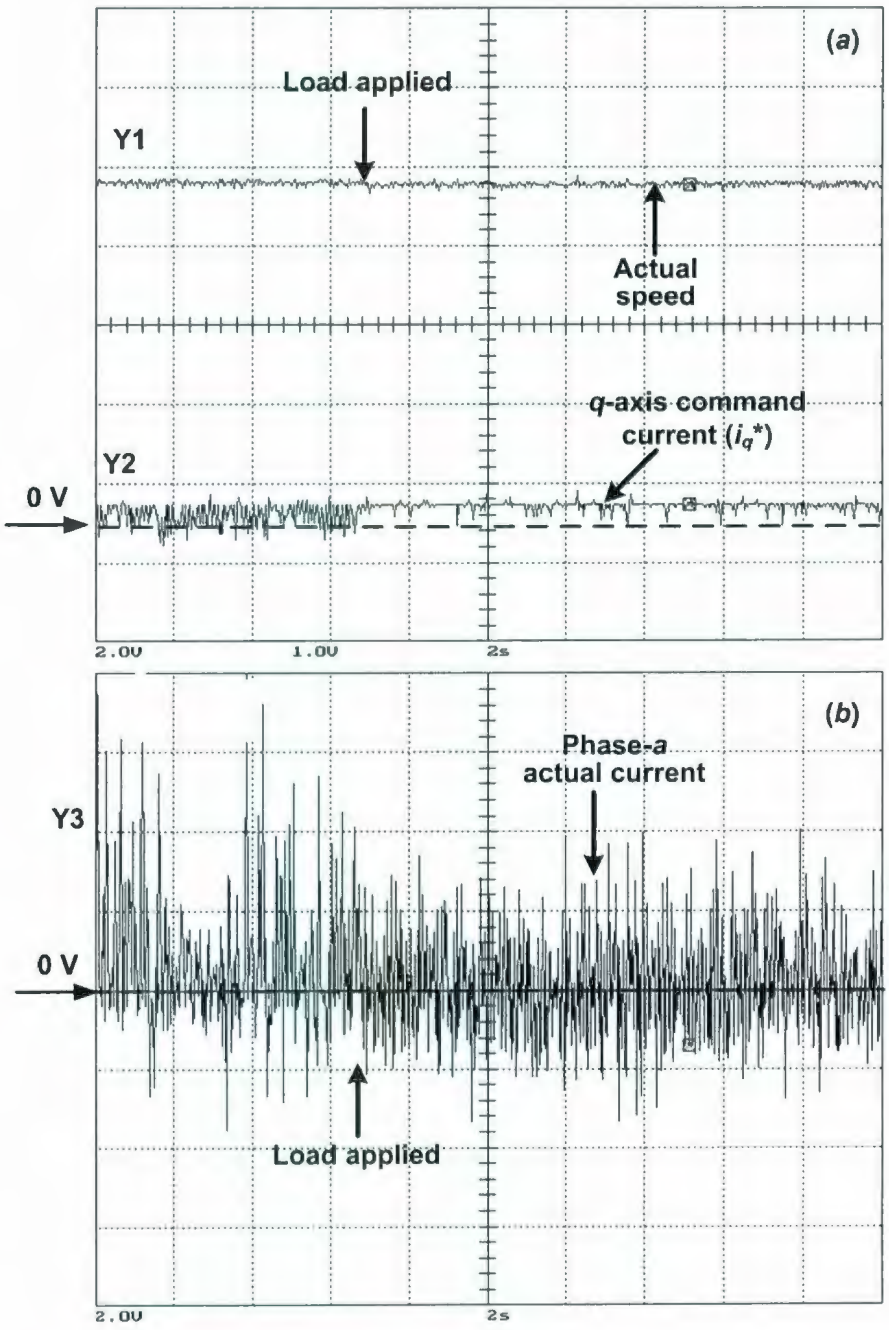

Figure 5.17: Experimental responses of the proposed MRPID controller based IPMSM drive system for a step change in load under command speed of 150 rad/sec.: (*a*) speed and *q*-axis command current responses (Y1: 2 V/div., 1V = 20 rad/sec., Y2: 1 V/div., 1V = 1.6 A, time: 2 sec./div.) and (*b*) phase current response (Y3: 2 V/div., 1V = 0.933 A, time: 2 sec./div.).

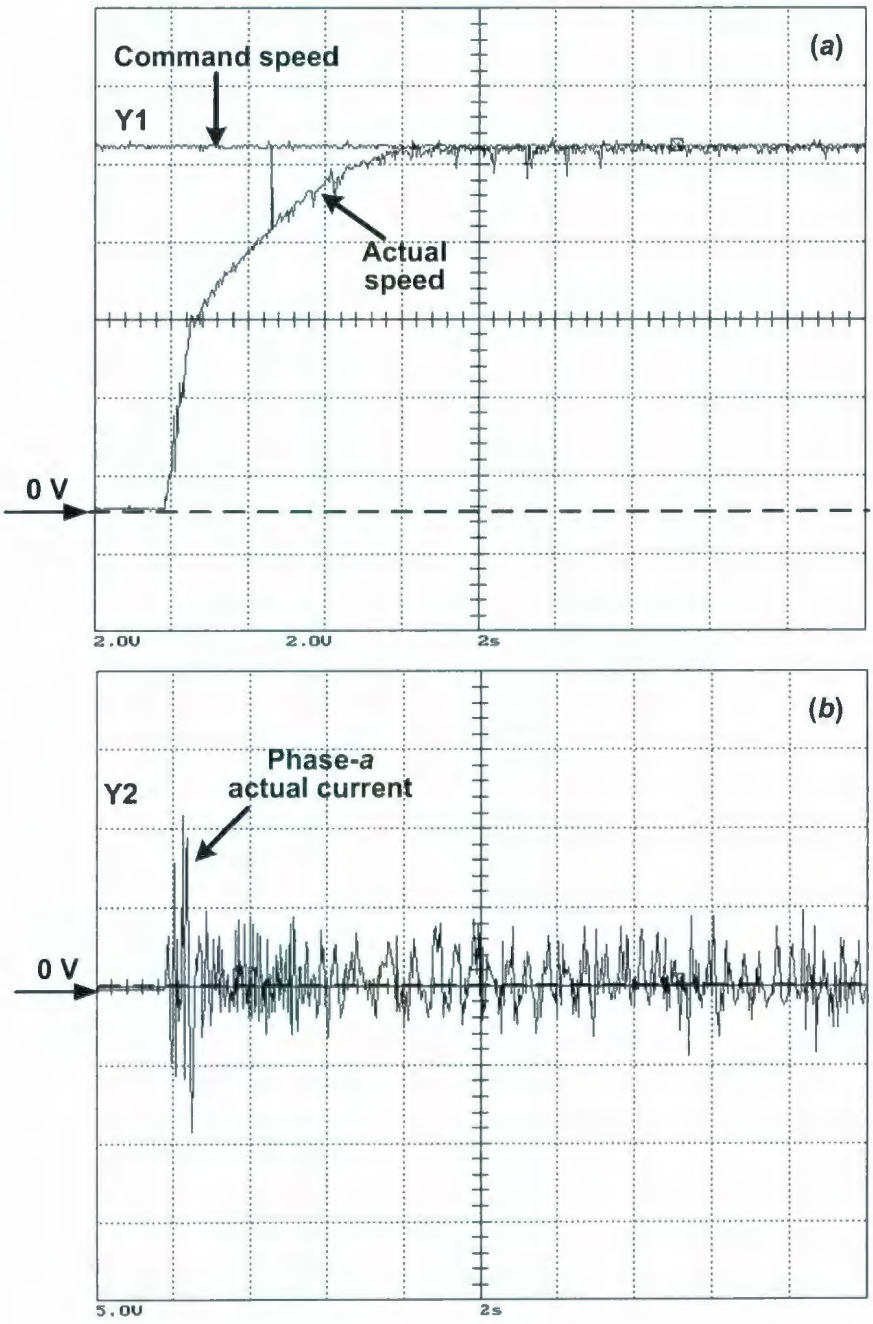

Figure 5.18: Experimental starting responses of the proposed MRPID controller based IPMSM drive system for change in inertia under rated load and rated speed (188.6 rad/sec.) conditions: (*a*) speed response (Y1: 2 V/div., 1V = 20 rad/sec., time: 2 sec./div.) and (*b*) current response (Y2: 5 V/div., 1V = 0.933 A, time: 2 sec./div.).

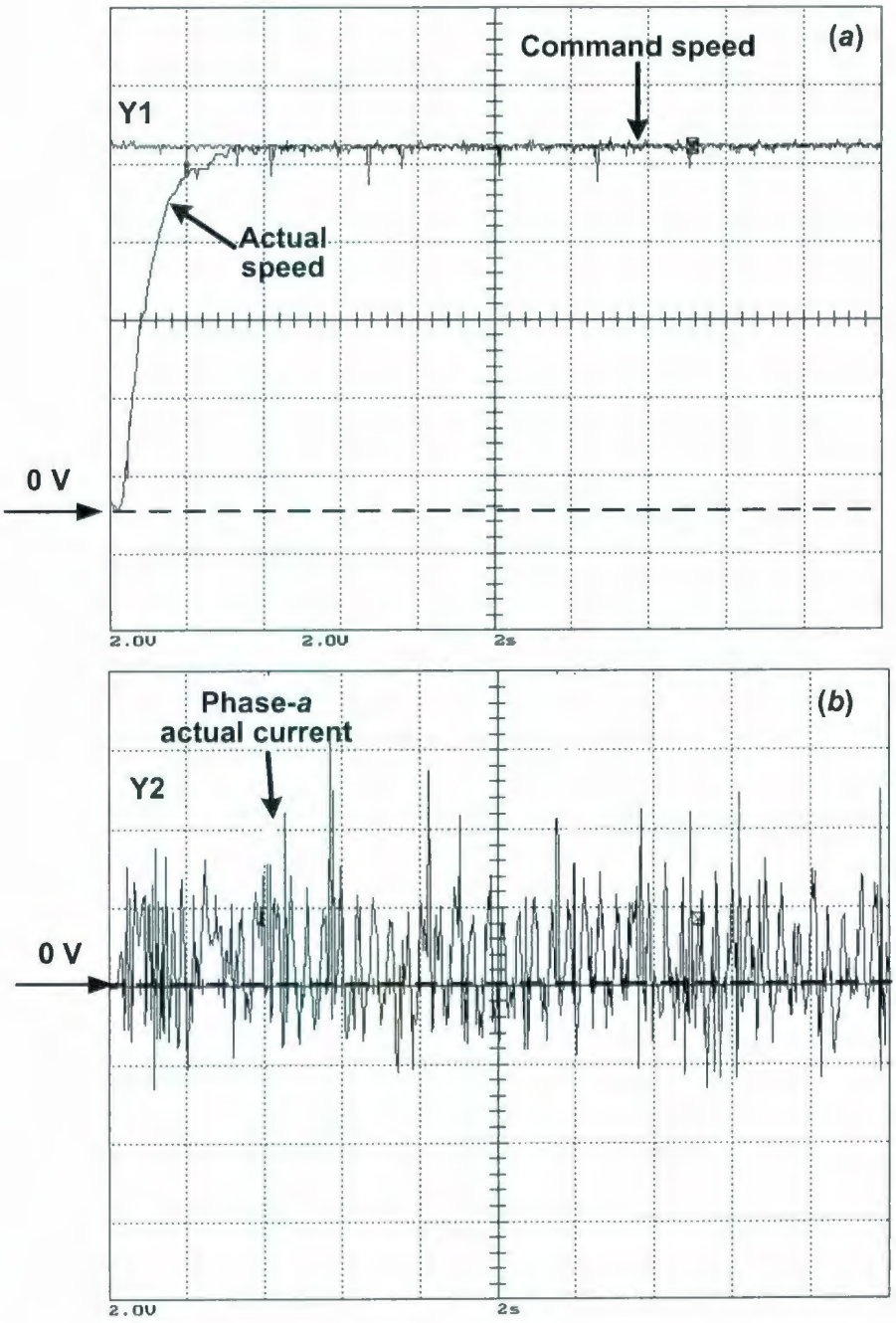

Figure 5.19: Experimental starting responses of the proposed MRPID controller based IPMSM drive system for change in resistance under rated load and rated speed (188.6 rad/sec.) conditions: (*a*) speed response (Y1: 2 V/div., 1V = 20 rad/sec., time: 2 sec./div.) and (*b*) current response (Y2: 2 V/div., 1V = 0.933 A, time: 2 sec./div.).

5.4 Concluding Remarks

In this chapter, the specific MRPID controller for the IPMSM drive system has been developed and implemented. The MATLAB has been used for the software implementation of the proposed controller. The proposed MRPID controller has responded almost accurately with small steady state speed error for different operating conditions of the drive system. These operating conditions include low and high starting command speeds, and step changes of command speeds of the drive system. However, the controller has responded slowly for changes in system parameters at rated command speed condition. In addition, the proposed controller has showed sensitive performances for a sudden impact of load. The speed of the MRPID based drive has dropped significantly at the instant of load impact. The drive system has showed steady state speed error after the load has been changed.

The performances of the proposed MRPID controller could be improved using high order wavelet function and higher levels of resolution of the controller. As a result, the computational complexity of the proposed controller would increase. On the other hand, the gains of the MRPID controller have shown significant effects on the performances of the drive system. So, the gains of the proposed controller have been updated with the operating conditions of the IPMSM drive. The wavelet neural network (WNN) has been used in the next chapter for the on-line updating of the gains of the MRPID controller in order to get optimal performances of the drive system. The development and implementation of the wavelet neural network (WNN) based self-tuning MRPID controller for the IPMSM drive system have been presented in next chapter. The performances of the self-tuning MRPID controller have been investigated in simulation in chapter six before the real time implementation. The simulated performance test results have been presented in the next chapter.

Chapter 6

Self-Tuning MRPID Control of the IPMSM Drive

The previous chapter has presented the simulated and experimental performance test results of the interior permanent magnet (IPM) motor drive using the fixed gain multiresolution proportional integral derivative (MRPID) controller. The fixed gain MRPID controller has shown sensitive performances to parameter variations and step change in load of the drive system. The performances of the drive system have been affected due to the use of fixed gain of the proposed MRPID controller. The wavelet neural network (WNN) based self-tuning MRPID controller for the interior permanent magnet synchronous motor (IPMSM) drive system has been presented in this chapter. The gains of the proposed MRPID controller for the IPM motor drive system have been tuned on-line using the proposed WNN based tuning approach. The proposed self-tuning algorithm has been implemented for the optimal and on-line tuning of the proposed MRPID controller. The mathematical formulations and the pertinent structure of the proposed WNN have been described and presented at the beginning of the chapter. The WNN parameters have been updated on-line using a suitable training algorithm. The training mechanism of the proposed WNN have been developed and illustrated through

mathematical formulations in the middle of the chapter. The stability of the proposed self-tuning MRPID controller based drive system including the convergence of the speed tracking error has been verified using the discrete Lyapunov stability theorem [97], [122]. The performances of the proposed self-tuning MRPID controller based IPMSM drive system have been investigated in simulations before the real time implementation of the drive system. The simulated performances have been presented at the end of the chapter.

6.1 Wavelet Neural Network

In the past few years, several research works have been done on the applications of wavelet neural networks. The wavelet neural network provides the capability of artificial neural networks of learning from processes, and the capability of wavelet decomposition for identification and control of dynamic systems [116]–[118]. The notation of wavelet neural network, which is based on the wavelet transform and the neural network theories, has been introduced as an alternative to feed forward neural networks for approximating arbitrary nonlinear functions. In this work, a four-layer wavelet neural network (WNN) has been used for the proposed self-tuning multiresolution proportional integral derivative (MRPID) controller of the IPMSM drive system. The proposed structure of a four-layer WNN for the self-tuning MRPID controller has been shown in Figure 6.1. The proposed WNN has an input layer (i), a mother wavelet layer (j), a wavelet layer (k), and an output layer (o). The speed error ($e(n)$) and change in speed error ($e(n)$-$e(n$-1)) have been used as the inputs of the WNN. The variable n of $e(n)$ has been used to define the discrete time integer. The speed error has been calculated from the difference between the command and actual motor speeds. The gains (k_d^1, k_d^2, k_a^2) of the proposed MRPID controller have been selected as the outputs of the WNN. These gains have been defined in chapter 4.

A family of wavelets has been generated from the translations and dilations of the mother wavelet function at the mother wavelet layer of the WNN. The input signal at each node of the mother wavelet layer has been processed through the translated and dilated wavelet functions. The *Morlet* wavelet function, which is the first derivative of

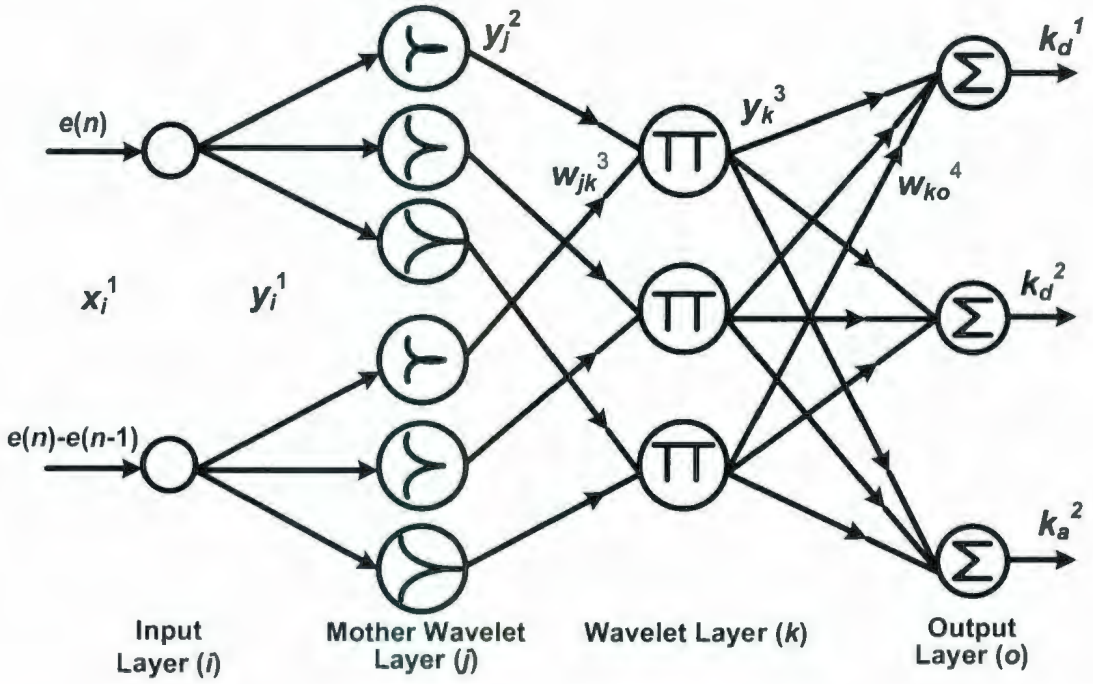

Figure 6.1: Proposed structure of a four-layer wavelet neural network of the self-tuning MRPID controller of the IPMSM drive system.

the Gaussian function, has been used as the mother wavelet function of the mother wavelet layer. The *Morlet* wavelet function can be mathematically expressed as [104]

$$\psi(x) = -xe^{-\frac{x^2}{2}}. \tag{6.1}$$

At every node of the input layer (i) of the wavelet neural network (WNN), the net input and the net output are expressed as

$$net_i^1 = x_i^1 \tag{6.2}$$

$$y_i^1 = net_i^1 = x_i^1, i = 1, 2 \tag{6.3}$$

where, $x_1^1 = e(n)$ and $x_2^1 = e(n)$-$e(n$-1). The variables $e(n)$ and $e(n$-1) have been used to represent the present and past samples of speed error, respectively. It is to be noted that the superscript and subscript of input and output variables of a layer denote the number of

layer and the number of inputs, respectively. In the mother wavelet layer (j) of the WNN, the net input and the net output are expressed as

$$x_i^2 = y_i^1, \; i = 1, 2 \tag{6.4}$$

$$net_j^2 = \frac{x_i^2 - m_{ij}}{\sigma_{ij}}, \; i = 1,2, \; j = 1...6 \tag{6.5}$$

$$y_j^2 = \psi_j\left(net_j^2\right) \tag{6.6}$$

where m_{ij} and σ_{ij} are the translation and the dilation parameters of the WNN, respectively in the *j-th* term of the *i-th* input (x_i^2) to the node of mother wavelet layer (j). In the *k-th* node of the wavelet layer (k), the input signals are multiplied, and the results of the product are forwarded to the output layer (o). In the wavelet layer, the net input and the net output are expressed as

$$x_j^3 = y_j^2 \tag{6.7}$$

$$net_k^3 = \prod_j w_{jk}^3 \, x_j^3 \tag{6.8}$$

where, $w_{jk}^3 = 1, \; j = 1...6, \; k = 1...3$

$$y_k^3 = net_k^3 \tag{6.9}$$

where x_j^3 represents the *j-th* input to the node of the wavelet layer, and w_{jk}^3 are the connection weights between the mother wavelet layer(j) and the wavelet layer (k). In the *o-th* node of the fourth output layer (o), the net input and the net output are expressed as

$$x_k^4 = y_k^3 \tag{6.10}$$

$$net_o^4 = \sum_k w_{ko}^4 \, x_k^4, \; o = 1...3 \tag{6.11}$$

$$y_o^4 = net_o^4 \tag{6.12}$$

where w_{ko}^4 are the connection weights between the wavelet layer (k) and the output layer (o) of the WNN, x_k^4 represents the *k-th* input to the node of the output layer (o). The outputs of the WNN are defined as $y_1^4 = k_d^1$, $y_2^4 = k_d^2$, and $y_3^4 = k_a^2$. The gains of the proposed MRPID controller are provided from the WNN of Fig. 6.1 using equations (6.1) –(6.12).

6.1.1 Adaptive on-line training of the wavelet neural network

The wavelet neural network (WNN) is trained on-line using the supervised back propagation learning algorithm. The central part of the training algorithm is to obtain a gradient vector recursively. The gradient vector for each parameter is defined as the derivative of a performance function with respect to the parameter of the network. The gradient vector is calculated in the direction opposite to the output flow of each node of the WNN.

In the supervised gradient descent on-line training technique of the WNN, a performance function is used at the beginning. This is defined as [97], [118]

$$E = \frac{1}{2}e^2 \tag{6.13}$$

In the output layer of the WNN, the error term to be propagated is determined as [118]

$$\begin{aligned} \delta_o^4 &= -\frac{\partial E}{\partial y_o^4} = -\left[\frac{\partial E}{\partial e}.\frac{\partial e}{\partial y_o^4}\right], \quad o = 1...3 \\ &\approx e(n) + e(n) - e(n-1) \\ &\approx 2e(n) - e(n-1) \end{aligned} \tag{6.14}$$

The connection weights between the output and the wavelet layer are updated as

$$\begin{aligned} \Delta w_{ko}^4 &= -\eta_w \frac{\partial E}{\partial w_{ko}^4} \\ &= \left[-\eta_w \frac{\partial E}{\partial y_o^4}\right] \times \left[\frac{\partial y_o^4}{\partial net_o^4} \times \frac{\partial net_o^4}{\partial w_{ko}^4}\right] \end{aligned} \tag{6.15}$$

Now,

$$net_o^4 = \sum_k w_{ko}^4 x_k^4 = y_o^4 \tag{6.16}$$

So,

$$\frac{\partial net_o^4}{\partial w_{ko}^4} = x_k^4 \text{ and } \frac{\partial y_o^4}{\partial net_o^4} = 1 \tag{6.17}$$

As a result,

$$\begin{aligned} \Delta w_{ko}^4 &= \left[-\eta_w \frac{\partial E}{\partial y_o^4} \right] \times 1 \times x_k^4 \\ &= \eta_w \delta_o^4 x_k^4 \end{aligned} \tag{6.18}$$

So, the weights of the output layer of the WNN are updated as

$$w_{ko}^4 (N+1) = w_{ko}^4 (N) + \Delta w_{ko}^4 \tag{6.19}$$

where N denotes the number of iterations, and the factor η_w is the learning rate for the output weights of the network.

In the wavelet layer of the WNN, the error term to be propagated is determined as

$$\begin{aligned} \delta_k^3 &= -\frac{\partial E}{\partial net_k^3} \\ &= \left[-\frac{\partial E}{\partial y_o^4} \right] \times \left[\frac{\partial y_o^4}{\partial net_o^4} \times \frac{\partial net_o^4}{\partial y_k^3} \times \frac{\partial y_k^3}{\partial net_k^3} \right] \\ &= \left[\delta_o^4 \right] \times \left[1 \times w_{ko}^4 \times 1 \right] \\ &= \delta_o^4 w_{ko}^4 \end{aligned} \tag{6.20}$$

In the mother wavelet layer of the WNN, the error term to be propagated is determined as

$$\begin{aligned}
\delta_j^2 &= -\frac{\partial E}{\partial net_j^2} \\
&= \left[-\frac{\partial E}{\partial y_o^4} \times \frac{\partial y_o^4}{\partial net_o^4} \times \frac{\partial net_o^4}{\partial y_k^3} \times \frac{\partial y_k^3}{\partial net_k^3} \right] \times \left[\frac{\partial net_k^3}{\partial y_j^2} \times \frac{\partial y_j^2}{\partial net_j^2} \right] \\
&= \left[-\frac{\partial E}{\partial y_o^4} \times 1 \times w_{ko}^4 \times 1 \right] \times \left[1 \times \frac{\partial y_j^2}{\partial net_j^2} \right] \\
&= \left[\delta_o^4 \times w_{ko}^4 \right] \times \left[\frac{\partial y_j^2}{\partial net_j^2} \right] \\
&= \left[\sum_k \delta_k^3 \right] \times \left[\left\{ \left(net_j^2 \right)^2 - 1 \right\} \times e^{-\frac{\left(net_j^2 \right)^2}{2}} \right]
\end{aligned} \tag{6.21}$$

The update law for the translation parameter (m_{ij}) of the WNN is expressed as

$$\begin{aligned}
\Delta m_{ij} &= -\eta_m \frac{\partial E}{\partial m_{ij}} \\
&= \left[-\eta_m \times \frac{\partial E}{\partial net_j^2} \times \frac{\partial net_j^2}{\partial m_{ij}} \right]
\end{aligned} \tag{6.22}$$

Here,

$$-\frac{\partial E}{\partial net_j^2} = \delta_j^2, \quad \frac{\partial net_j^2}{\partial m_{ij}} = -\frac{1}{\sigma_{ij}} \tag{6.23}$$

So,

$$\begin{aligned}
\Delta m_{ij} &= \left[-\eta_m \times \frac{\partial E}{\partial net_j^2} \times \frac{\partial net_j^2}{\partial m_{ij}} \right] \\
&= -\eta_m \delta_j^2 \frac{1}{\sigma_{ij}}
\end{aligned} \tag{6.24}$$

The update law for the dilation parameter (σ_{ij}) of the WNN is expressed as

$$\begin{aligned}\Delta\sigma_{ij} &= -\eta_\sigma \frac{\partial E}{\partial \sigma_{ij}} \\ &= \left[-\eta_\sigma \times \frac{\partial E}{\partial net_j^2} \times \frac{\partial net_j^2}{\partial \sigma_{ij}} \right]\end{aligned} \tag{6.25}$$

Here,

$$-\frac{\partial E}{\partial net_j^2} = \delta_j^2, \quad \frac{\partial net_j^2}{\partial \sigma_{ij}} = \frac{m_{ij} - x_i^2}{\left(\sigma_{ij}\right)^2} \tag{6.26}$$

So,

$$\begin{aligned}\Delta\sigma_{ij} &= \left[-\eta_\sigma \times \frac{\partial E}{\partial net_j^2} \times \frac{\partial net_j^2}{\partial \sigma_{ij}} \right] \\ &= \eta_\sigma \delta_j^2 \frac{m_{ij} - x_i^2}{\left(\sigma_{ij}\right)^2}\end{aligned} \tag{6.27}$$

Using equations (6.22)–(6.27), the translation and dilation parameters of the mother wavelet function are updated as

$$m_{ij}(N+1) = m_{ij}(N) + \Delta m_{ij} \tag{6.28}$$

$$\sigma_{ij}(N+1) = \sigma_{ij}(N) + \Delta\sigma_{ij} \tag{6.29}$$

where η_m and η_σ are the learning rates for the translation and dilation parameters of the wavelet neural network (WNN), respectively.

6.1.2 Stability analysis

The wavelet neural network (WNN) has been used to provide the gains of the proposed MRPID controller for the interior permanent magnet (IPM) motor drive system. The performances and stability of a WNN have been affected by the selection of learning rates. The convergence of network parameters has been delayed using small learning rate.

On the other hand, the network has become unstable with high learning rate. As a result, the learning rates of the WNN has significant effects on the performance and stability of the proposed self-tuning MRPID controller based nonlinear IPMSM drive system In order to determine the optimal learning rates of the WNN, a discrete type Lyapunov function has been used in this work. The stability analyses in this section have included the formulation of optimal learning rates for the WNN parameters of the proposed self-tuning MRPID controller to confirm the convergence of the speed tracking error of the IPM motor drive system. The following theorems have been used to derive adaptive learning rates of the WNN in order to confirm the stability of the drive system. It is to be noted that the mathematical formulations of the following stability theorems have been developed from the reference [118].

Theorem 1:

The stability is confirmed if the learning rate η_w is defined as [118]

$$\eta_w = \frac{\lambda}{P_{w\max}^2} = \frac{\lambda}{R_u} \tag{6.30}$$

where λ is a positive constant and R_u is the number of nodes in the wavelet layer of the WNN. The factor $P_{w\max}$ is defined as

$$P_{w\max} \equiv \max_N \left\| P_w(N) \right\| \tag{6.31}$$

where $P_w(N) = \frac{\partial y_o^4}{\partial w_{ko}^4}$ and $\|.\|$ is the Euclidean norm in the real number $\mathbb{R}^n$.

Proof of Theorem 1:

Since $P_w(N) = \frac{\partial y_o^4}{\partial w_{ko}^4} = x_k^4$, so $\left\| P_w(N) \right\| < \sqrt{R_u}$. Now, a discrete type Lyapunov function is defined as [118], [122]

$$V(N)=\frac{e^2(N)}{2} \tag{6.32}$$

where the variable e is used to represent the speed error between the actual and command speeds of the IPM motor.

The finite difference in the Lyapunov function is obtained as

$$\begin{aligned}\Delta V(N) &= V(N+1)-V(N)\\ &=\frac{e^2(N+1)}{2}-\frac{e^2(N)}{2}\end{aligned} \tag{6.33}$$

Now, the error difference can be represented as

$$\begin{aligned}e(N+1) &= e(N)+\Delta e(N)\\ &= e(N)+\left[\frac{\partial e(N)}{\partial w_{ko}^4}\right]^T \Delta w_{ko}^4\end{aligned} \tag{6.34}$$

where

$$\begin{aligned}\frac{\partial e(N)}{\partial w_{ko}^4} &= \frac{\partial e(N)}{\partial E}\times\frac{\partial E}{\partial y_o^4}\times\frac{\partial y_o^4}{\partial w_{ko}^4}\\ &=\frac{1}{e(N)}\times\left(-\delta_o^4\right)\times P_w(N)\\ &=\frac{-\delta_o^4}{e(N)}P_w(N)\end{aligned} \tag{6.35}$$

Now, $\Delta w_{ko}^4=\eta_w\delta_o^4\,x_k^4$ and $P_w(N)=x_k^4$.

so,

$$e(N+1)=e(N)-\left[\frac{\delta_o^4}{e(N)}P_w(N)\right]^T\eta_w\delta_o^4\,P_w(N) \tag{6.36}$$

The equation (6.36) can be rewritten as

$$\begin{aligned} e(N+1) &= e(N) - \eta_w \frac{\left(\delta_o^4\right)^2}{e(N)} P_w^T(N) P_w(N) \\ &= e(N)\left[1 - \eta_w \left(\frac{\delta_o^4}{e(N)}\right)^2 P_w^T(N) P_w(N)\right] \end{aligned} \tag{6.37}$$

$$\begin{aligned} \left\|e(N+1)\right\| &= \left\|e(N)\left[1 - \eta_w \left(\frac{\delta_o^4}{e(N)}\right)^2 P_w^T(N) P_w(N)\right]\right\| \\ &\le \left\|e(N)\right\| \left\|\left[1 - \eta_w \left(\frac{\delta_o^4}{e(N)}\right)^2 P_w^T(N) P_w(N)\right]\right\| \end{aligned} \tag{6.38}$$

If the learning rate η_w is chosen as $\eta_w = \frac{\lambda}{P_{w\max}^2} = \frac{\lambda}{R_u}$, then the term $\left[1 - \eta_w \left(\frac{\delta_o^4}{e(N)}\right)^2 P_w^T(N) P_w(N)\right]$ in equation (6.38) is less than 1, which ensures the Lyapunov function (V) and the time rate of change of Lyapunov function (ΔV) of equations (6.32)–(6.33) are greater than zero ($V>0$) and less than zero ($\Delta V<0$), respectively. Therefore, the stability of the learning rate η_w is confirmed using the Lyapunov functions of equations (6.32)–(6.33). The stable learning rate η_w is designed to provide the stable gains of the proposed MRPID controller of the IPMSM drive system.

Theorem 2:

The stability is confirmed if the learning rates η_m and η_σ of the WNN are defined as [118]

$$\eta_m = \frac{\eta_w}{\left[\left|w_{ko}^4\right|_{\max} \times \left(\frac{2e^{-0.5}}{\left|\sigma_{ij}\right|_{\min}}\right)\right]^2} \tag{6.39}$$

$$\eta_\sigma = \frac{\eta_w}{\left[\left|w_{ko}^4\right|_{\max} \times \left(\frac{2e^{0.5}}{\left|\sigma_{ij}\right|_{\min}}\right)\right]^2} \tag{6.40}$$

Here,

$$\left|w_{ko}^4\right|_{\max} = \max_N \left|w_{ko}^4(N)\right| \tag{6.41}$$

$$\left|\sigma_{ij}\right|_{\min} = \min_N \left|\sigma_{ij}(N)\right| \tag{6.42}$$

Proof of Theorem 2:

In order to prove theorem 2, the following conditions are used and defined as

Condition 1: If $p(r) = re^{-r^2}$, then $|p(r)| < 1,\ \forall r \in \mathbb{R}$

Condition 2: If $q(r) = \frac{(r^2-1)}{2} e^{\frac{(r^2-1)}{2}}$, then $|q(r)| < 1,\ \forall r \in \mathbb{R}$

The factors $P_{m\max}$ and $P_{\sigma\max}$ are defined as

$$P_{m\max} \equiv \max_N \left\|P_m(N)\right\| \tag{6.43}$$

$$P_{\sigma\max} \equiv \max_N \left\|P_\sigma(N)\right\| \tag{6.44}$$

where $P_m(N) = \frac{\partial y_o^4}{\partial m_{ij}}$ and $P_\sigma(N) = \frac{\partial y_o^4}{\partial \sigma_{ij}}$.

Now,

$$
\begin{aligned}
P_m(N) &= \frac{\partial y_o^4}{\partial m_{ij}} \\
&= \frac{\partial y_o^4}{\partial net_o^4} \times \frac{\partial net_o^4}{\partial y_k^3} \times \frac{\partial y_k^3}{\partial net_k^3} \times \frac{\partial net_k^3}{\partial y_j^2} \times \frac{\partial y_j^2}{\partial m_{ij}} \\
&= 1 \times w_{ko}^4 \times 1 \times 1 \times \frac{\partial y_j^2}{\partial m_{ij}} \\
&= w_{ko}^4 \frac{\partial y_j^2}{\partial m_{ij}}
\end{aligned}
\tag{6.45}
$$

where

$$
\begin{aligned}
\frac{\partial y_j^2}{\partial m_{ij}} &= \frac{\partial y_j^2}{\partial net_j^2} \times \frac{\partial net_j^2}{\partial m_{ij}} \\
&= \left[\left(net_j^2\right)^2 - 1\right] \times e^{\frac{\left(net_j^2\right)^2}{2}} \times \left(-\frac{1}{\sigma_{ij}}\right) \\
&= \frac{1}{2}\left[\left(\frac{x_i^2 - m_{ij}}{\sigma_{ij}}\right)^2 - 1\right] \times e^{\frac{\left(\frac{x_i^2 - m_{ij}}{\sigma_{ij}}\right)^2 - 1}{2}} \times \left(-\frac{2e^{-0.5}}{\sigma_{ij}}\right)
\end{aligned}
\tag{6.46}
$$

Now replacing the value of $\frac{\partial y_j^2}{\partial m_{ij}}$ from the equation (6.46) into the equation (6.45), the factor $P_m(N)$ can be represented as

$$
\begin{aligned}
P_m(N) &= w_{ko}^4 \frac{\partial y_j^2}{\partial m_{ij}} \\
&\le \left|w_{ko}^4\right| \times \max\left|\frac{\partial y_j^2}{\partial m_{ij}}\right| \\
&\le \left|w_{ko}^4\right| \times \max\left\{\left|\frac{1}{2}\left[\left(\frac{x_i^2 - m_{ij}}{\sigma_{ij}}\right)^2 - 1\right] \times e^{\frac{\left(\frac{x_i^2 - m_{ij}}{\sigma_{ij}}\right)^2 - 1}{2}}\right| \times \left|\left(-\frac{2e^{-0.5}}{\sigma_{ij}}\right)\right|\right\}
\end{aligned}
\tag{6.47}
$$

Using condition two, the equation (6.47) can be rewritten as

$$P_m(N) \le \left|w_{ko}^4\right| \times \max\left\{\left|\frac{1}{2}\left[\left(\frac{x_i^2 - m_{ij}}{\sigma_{ij}}\right)^2 - 1\right] \times e^{\frac{\left(\frac{x_i^2 - m_{ij}}{\sigma_{ij}}\right)^2 - 1}{2}}\right| \times \left|\left(-\frac{2e^{-0.5}}{\sigma_{ij}}\right)\right|\right\}$$
$$\le \left|w_{ko}^4\right| \times \max\left\{\left|\left(-\frac{2e^{-0.5}}{\sigma_{ij}}\right)\right|\right\} = \left|w_{ko}^4\right| \times \left(\frac{2e^{-0.5}}{\left|\sigma_{ij}\right|_{\min}}\right) \tag{6.48}$$

So, $\left\|P_m(N)\right\| < \sqrt{R_u} \times \left|w_{ko}^4\right|_{\max} \times \left(\frac{2e^{-0.5}}{\left|\sigma_{ij}\right|_{\min}}\right)$

Now, the error difference can be represented as

$$\begin{aligned} e(N+1) &= e(N) + \Delta e(N) \\ &= e(N) + \left[\frac{\partial e(N)}{\partial m_{ij}}\right]^T \Delta m_{ij} \end{aligned} \tag{6.49}$$

where

$$\begin{aligned} \frac{\partial e(N)}{\partial m_{ij}} &= \frac{\partial e(N)}{\partial E} \times \frac{\partial E}{\partial y_o^4} \times \frac{\partial y_o^4}{\partial m_{ij}} \\ &= \frac{1}{e(N)} \times \left(-\delta_o^4\right) \times P_m(N) \\ &= \frac{-\delta_o^4}{e(N)} P_m(N) \end{aligned} \tag{6.50}$$

Now, $\Delta m_{ij} = -\eta_m \frac{\partial E}{\partial m_{ij}} = \eta_m \delta_o^4 P_m(N)$

so,

$$e(N+1)=e(N)-\left[\frac{\delta_o^4}{e(N)}P_m(N)\right]^T \eta_m \delta_o^4 P_m(N) \tag{6.51}$$

The equation (6.51) can be rewritten as

$$\begin{aligned} e(N+1) &= e(N)-\eta_m \frac{\left(\delta_o^4\right)^2}{e(N)} P_m^T(N) P_m(N) \\ &= e(N)\left[1-\eta_m\left(\frac{\delta_o^4}{e(N)}\right)^2 P_m^T(N) P_m(N)\right] \end{aligned} \tag{6.52}$$

So,

$$\begin{aligned} \left\|e(N+1)\right\| &= \left\|e(N)\left[1-\eta_m\left(\frac{\delta_o^4}{e(N)}\right)^2 P_m^T(N) P_m(N)\right]\right\| \\ &\le \left\|e(N)\right\|\left\|\left[1-\eta_m\left(\frac{\delta_o^4}{e(N)}\right)^2 P_m^T(N) P_m(N)\right]\right\| \end{aligned} \tag{6.53}$$

If the learning rate η_m is chosen as

$$\eta_m = \frac{\eta_w}{\left[\left|w_{ko}^4\right|_{\max} \times \left(\frac{2e^{-0.5}}{\left|\sigma_{ij}\right|_{\min}}\right)\right]^2},$$

then the term $\left[1-\eta_m\left(\frac{\delta_o^4}{e(N)}\right)^2 P_m^T(N) P_m(N)\right]$ in equation (6.53) is less than 1, which ensures the Lyapunov function (V) and the time rate of change of Lyapunov function (ΔV) of equations (6.32)–(6.33) are greater than zero ($V>0$) and less than zero ($\Delta V<0$), respectively. Therefore, the stability of the learning rate η_m is confirmed using the Lyapunov functions of equations (6.32)–(6.33). The stable learning rate η_m is designed to provide the stable gains of the proposed MRPID controller of the IPMSM drive system.

Now,

$$
\begin{aligned}
P_{\sigma}(N) &= \frac{\partial y_o^4}{\partial \sigma_{ij}} \\
&= \frac{\partial y_o^4}{\partial net_o^4} \times \frac{\partial net_o^4}{\partial y_k^3} \times \frac{\partial y_k^3}{\partial net_k^3} \times \frac{\partial net_k^3}{\partial y_j^2} \times \frac{\partial y_j^2}{\partial \sigma_{ij}} \\
&= 1 \times w_{ko}^4 \times 1 \times 1 \times \frac{\partial y_j^2}{\partial \sigma_{ij}} \\
&= w_{ko}^4 \frac{\partial y_j^2}{\partial \sigma_{ij}}
\end{aligned}
\tag{6.54}
$$

where

$$
\begin{aligned}
\frac{\partial y_j^2}{\partial \sigma_{ij}} &= \frac{\partial y_j^2}{\partial net_j^2} \times \frac{\partial net_j^2}{\partial \sigma_{ij}} \\
&= \left[\left(net_j^2 \right)^2 - 1 \right] \times e^{\frac{\left(net_j^2 \right)^2}{2}} \times \left(\frac{-x_i^2 + m_{ij}}{\left(\sigma_{ij} \right)^2} \right) \\
&= \left(\frac{x_i^2 - m_{ij}}{\sigma_{ij}} \right) \times e^{-\left(\frac{x_i^2 - m_{ij}}{\sigma_{ij}} \right)^2} \times \frac{1}{2} \left[1 - \left(\frac{x_i^2 - m_{ij}}{\sigma_{ij}} \right)^2 \right] \times e^{\frac{1 - \left(\frac{x_i^2 - m_{ij}}{\sigma_{ij}} \right)^2}{2}} \times \left(\frac{2e^{0.5}}{\sigma_{ij}} \right)
\end{aligned}
\tag{6.55}
$$

Now replacing the value of $\frac{\partial y_j^2}{\partial \sigma_{ij}}$ from the equation (6.55) into the equation (6.54), the factor $P_\sigma(N)$ can be represented as

$$P_\sigma(N) = w_{ko}^4 \frac{\partial y_j^2}{\partial \sigma_{ij}}$$

$$\leq \left|w_{ko}^4\right| \times \max \left|\frac{\partial y_j^2}{\partial \sigma_{ij}}\right| \tag{6.56}$$

$$\leq \left|w_{ko}^4\right| \times \max \left\{ \left| \left(\frac{x_i^2 - m_{ij}}{\sigma_{ij}}\right) \times e^{-\left(\frac{x_i^2 - m_{ij}}{\sigma_{ij}}\right)^2} \times \frac{1}{2}\left[1 - \left(\frac{x_i^2 - m_{ij}}{\sigma_{ij}}\right)^2\right] \times e^{\frac{1-\left(\frac{x_i^2 - m_{ij}}{\sigma_{ij}}\right)^2}{2}} \right| \times \left| \left(\frac{2e^{0.5}}{\sigma_{ij}}\right) \right| \right\}$$

Using conditions one and two, the above equation (6.56) can be rewritten as

$$P_\sigma(N) \leq \left|w_{ko}^4\right| \times \max \left\{ \left| \left(\frac{x_i^2 - m_{ij}}{\sigma_{ij}}\right) \times e^{-\left(\frac{x_i^2 - m_{ij}}{\sigma_{ij}}\right)^2} \times \frac{1}{2}\left[1 - \left(\frac{x_i^2 - m_{ij}}{\sigma_{ij}}\right)^2\right] \times e^{\frac{1-\left(\frac{x_i^2 - m_{ij}}{\sigma_{ij}}\right)^2}{2}} \right| \times \left| \left(\frac{2e^{0.5}}{\sigma_{ij}}\right) \right| \right\} \tag{6.57}$$

$$\leq \left|w_{ko}^4\right| \times \max \left\{ \left| \left(\frac{2e^{0.5}}{\sigma_{ij}}\right) \right| \right\} = \left|w_{ko}^4\right| \times \left(\frac{2e^{0.5}}{\left|\sigma_{ij}\right|_{\min}}\right)$$

So, $\left\|P_\sigma(N)\right\| < \sqrt{R_u} \times \left|w_{ko}^4\right|_{\max} \times \left(\frac{2e^{0.5}}{\left|\sigma_{ij}\right|_{\min}}\right)$.

Now, the error difference can be represented as

$$\begin{aligned} e(N+1) &= e(N) + \Delta e(N) \\ &= e(N) + \left[\frac{\partial e(N)}{\partial \sigma_{ij}}\right]^T \Delta\sigma_{ij} \end{aligned} \tag{6.58}$$

where

$$\begin{aligned} \frac{\partial e(N)}{\partial \sigma_{ij}} &= \frac{\partial e(N)}{\partial E} \times \frac{\partial E}{\partial y_o^4} \times \frac{\partial y_o^4}{\partial \sigma_{ij}} \\ &= \frac{1}{e(N)} \times \left(-\delta_o^4\right) \times P_\sigma(N) \\ &= \frac{-\delta_o^4}{e(N)} P_\sigma(N) \end{aligned} \tag{6.59}$$

Now, $\Delta\sigma_{ij} = -\eta_\sigma \dfrac{\partial E}{\partial \sigma_{ij}} = \eta_\sigma \delta_o^4 P_\sigma(N)$

So,

$$e(N+1) = e(N) - \left[\frac{\delta_o^4}{e(N)} P_\sigma(N)\right]^T \eta_\sigma \delta_o^4 P_\sigma(N) \tag{6.60}$$

The equation (6.60) can be rewritten as

$$\begin{aligned} e(N+1) &= e(N) - \eta_\sigma \frac{\left(\delta_o^4\right)^2}{e(N)} P_\sigma^T(N) P_\sigma(N) \\ &= e(N)\left[1 - \eta_\sigma \left(\frac{\delta_o^4}{e(N)}\right)^2 P_\sigma^T(N) P_\sigma(N)\right] \end{aligned} \tag{6.61}$$

So,

$$\begin{aligned}\left\|e(N+1)\right\| &= \left\|e(N)\left[1-\eta_\sigma\left(\frac{\delta_o^4}{e(N)}\right)^2 P_\sigma^T(N)P_\sigma(N)\right]\right\| \\ &\le \left\|e(N)\right\|\left\|\left[1-\eta_\sigma\left(\frac{\delta_o^4}{e(N)}\right)^2 P_\sigma^T(N)P_\sigma(N)\right]\right\|\end{aligned} \tag{6.62}$$

If the learning rate η_σ is chosen as

$$\eta_\sigma = \frac{\eta_w}{\left[\left|w_{ko}^4\right|_{\max} \times \left(\frac{2e^{0.5}}{\left|\sigma_{ij}\right|_{\min}}\right)\right]^2},$$

then the term $\left[1-\eta_\sigma\left(\frac{\delta_o^4}{e(N)}\right)^2 P_\sigma^T(N)P_\sigma(N)\right]$ in equation (6.62) is less than 1, which ensures the Lyapunov function (V) and the time rate of change of Lyapunov function (ΔV) of equations (6.32)–(6.33) are greater than zero ($V>0$) and less than zero ($\Delta V<0$), respectively. Therefore, the stability of the learning rate η_σ is confirmed using the Lyapunov functions of equations (6.32)–(6.33). The stable learning rate η_σ is designed to provide the stable gains of the proposed MRPID controller of the IPMSM drive system.

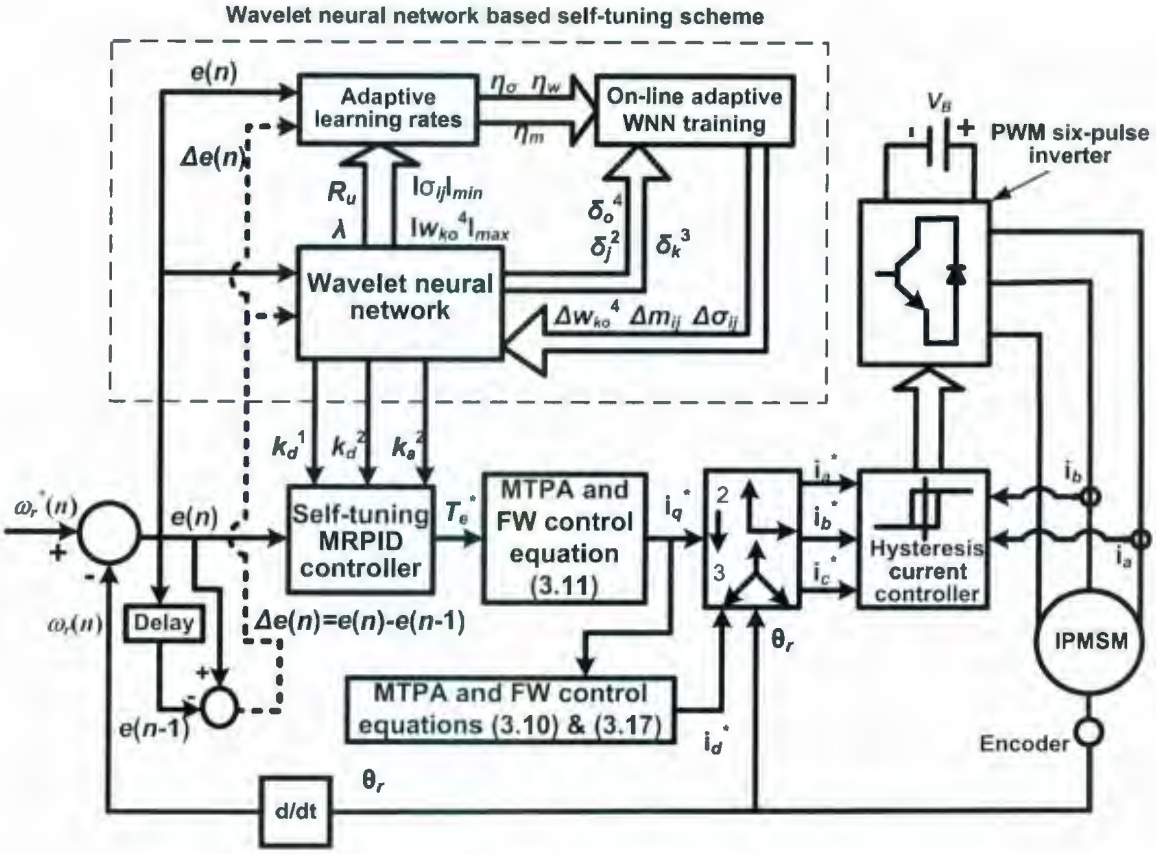

Figure 6.2: Schematic of the IPMSM drive system incorporating the WNN based self-tuning MRPID controller.

6.2 Software Implementation of the WNN based Self-Tuning MRPID Controller

The schematic of the interior permanent magnet synchronous motor (IPMSM) drive system incorporating the wavelet neural network (WNN) based self-tuning multiresolution proportional integral derivative (MRPID) controller has been shown in Fig. 6.2. The self-tuning MRPID controller block of Fig. 6.2 has been used as the speed controller to process the speed error (e) between the actual speed (ω_r) and the command speed (ω_r^*) of the IPM motor. Using equations (4.44)–(4.46), the proposed MRPID controller with the optimal gains has been used to generate the electromagnetic command

torque (T_e^*) for the drive system. The WNN based tuning scheme of Fig. 6.2 has provided the optimal gains (k_d^1, k_d^2, k_a^2) of the proposed MRPID controller under different operating conditions of the IPM motor drive system. The on-line training scheme of the WNN for the proposed MRPID controller has been illustrated in the flow chart of Fig. 6.3. The output weights and their changes (Δw_{ko}), the translation and dilation parameters and their changes (Δm_{ij}, $\Delta \sigma_{ij}$) have been initialized at the beginning of the flow chart of Fig. 6.3. Then, the output weights and the translation and dilation parameters have been updated using the initial values. The learning rates of the WNN have been determined from the updated values of output weights and dilation parameters. The error propagations of different layers of the WNN have been determined from the speed error and the updated values of the WNN parameters. The output of the wavelet layer, the error propagation of different layers, and the learning rates have been used to determine the changes of the output weights, and the changes of the translation and dilation parameters of the WNN. The change of weights and the changes of the translation and dilation parameters have been added with the current weights, and the current translation and dilation parameters to determine the new weights and the new translation and dilation parameters of the WNN.

The maximum torque per ampere (MTPA) and the flux weakening (FW) control block of Fig. 6.2 with equation (3.11) has been used to generate the q-axis command current (i_q^*) of the drive system. The q-axis command current (i_q^*) has been used in the MTPA and FW control block of Fig. 6.2 with equations (3.10) and (3.17) in order to generate the d-axis command current (i_d^*) of the drive system. The d-q axis command currents have been transformed to the a-b-c command phase currents using inverse Park transformation in the coordinate transformation block Fig. 6.2. The command phase currents have been compared with the actual phase currents in the hysteresis current control block in order to generate the switching pulses for the used three-phase six-pulse pulse width modulated (PWM) inverter. The PWM six-pulse inverter block of Fig. 6.2 has provided the appropriate stator phase voltages in order to operate the drive system to the specific command speed.

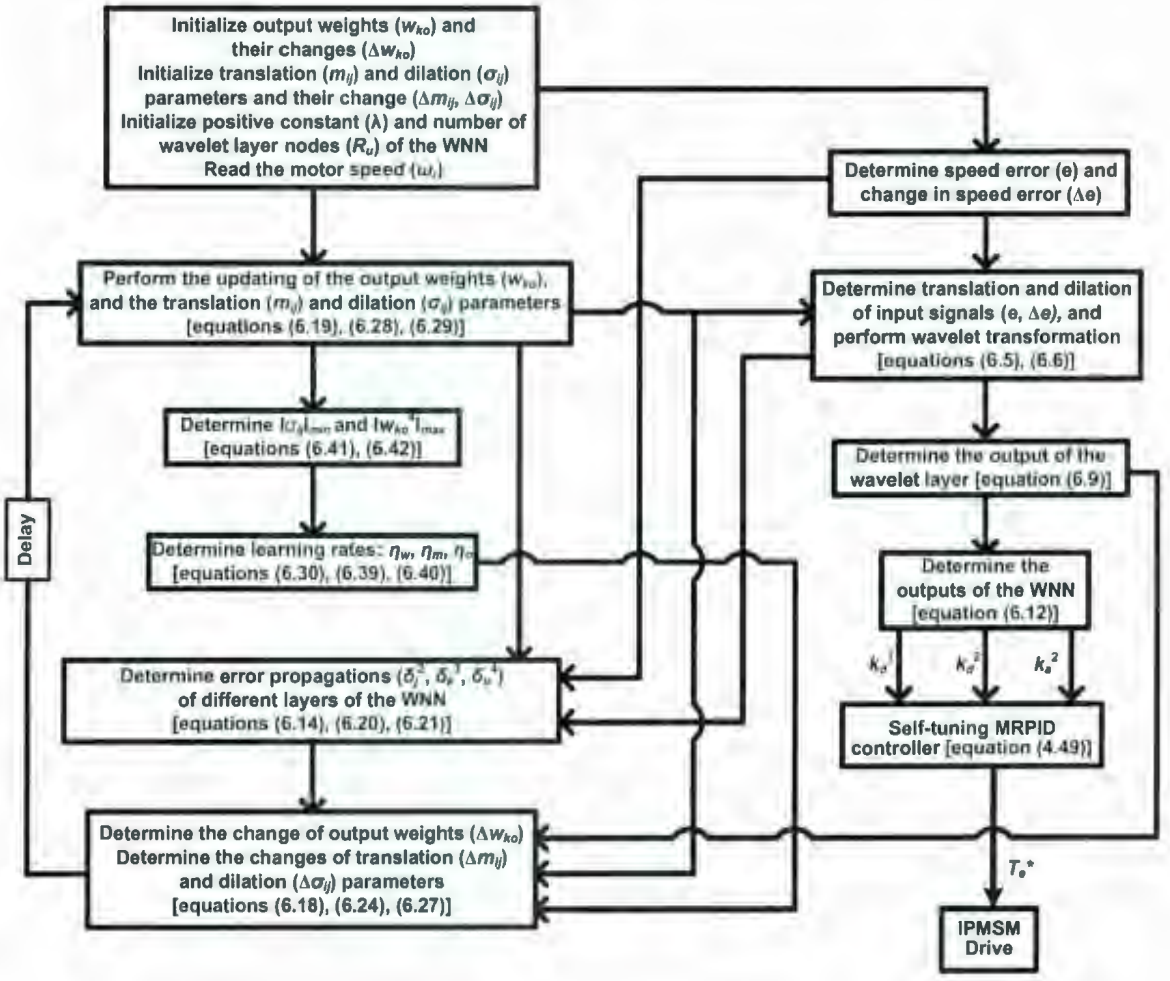

Figure 6.3: Flow chart for the on-line training of the WNN for the self-tuning of the proposed MRPID controller of the IPM motor drive system.

The performances of the IPMSM drive system have been investigated in simulation at different operating conditions of the IPM motor drive system. The performances of the proposed drive system have been investigated for step changes of command speeds, for step change of load, and for variation of system parameters. The performance indices of the proposed controller have been selected as the rise time, the speed overshoot and undershoot, and the steady state speed error. The starting performances of the drive system using the self-tuning MRPID controller have been investigated for the rated command speed of 188.6 rad/sec. at both no load and rated load conditions. The starting performances of the self-tuning MRPID controller based drive system have been shown in Figs. 6.4 and 6.5 for the rated command speed of 188.6 rad/sec. at no load and rated load conditions, respectively. The drive system has followed the command speed quickly with small steady state error at both no load and rated load conditions without large undershoots and overshoots. The proposed MRPID controller has taken less than 0.1 sec. to arrive at the rated command speed of 188.6 rad/sec. at both no load and rated load conditions. However, the starting speed responses of Figs. 6.4(*a*) and 6.5(*a*) have experienced a small speed dipping at 0.02 sec. These speed dipping has been due to the adaptive nature of learning of the wavelet neural network (WNN) parameters including the adaptive learning of the output weights, and the translation and dilation parameters. The command torque current (i_q^*) and command flux current (i_d^*) of Figs. 6.4–6.5 have shown smooth response and have forced the drive system quickly to operate at the rated command speed at both no load and rated load conditions. It is to be mentioned that log scale has been used to display the amplitude values (y-axis) of the command torque current and the command flux current of Figs. 6.5(*c*) and 6.5(*d*), respectively in order to zoom in the steady state current values of i_q^* and i_d^* at the rated load condition. The i_q^* and i_d^* currents have settled down to the constant values in the steady state operating region at the rated load condition of the drive system.

Figures 6.6 and 6.7 have shown the starting performances of the self-tuning MRPID controller based drive system for the low command speed of 50 rad/sec. at no load and rated load conditions, respectively. The drive system has followed the low

command speed of 50 rad/sec. very quickly in less than 0.05 sec. at both no load and rated load conditions with a small speed overshoot and small steady state speed error. The command torque current and command flux current have increased rapidly at the beginning to provide the sufficient starting torque of the drive system. The command torque current of Fig. 6.7(*c*) has provided the necessary torque at the rated load condition of the drive system. In Figs. 6.8 and 6.9, the starting performances of the self-tuning MRPID controller based drive system have been given for the high command speed of 250 rad/sec. at no load and rated load conditions, respectively. Again, the drive system has successfully tracked the high command speed of 250 rad/sec. quickly in less than 0.1 sec. at both no load and rated load conditions. The negative command flux currents of Figs. 6.8(*d*) and 6.9(*d*) have demagnetized the permanent magnet flux in order to operate the drive system above the rated speed (188.6 rad/sec.) of the IPM motor. Therefore, the IPMSM drive system using the self-tuning MRPID controller has been found quick and robust for tracking different command speeds including low and high command speeds at both no load and rated load conditions.

The performances of the self-tuning MRPID based drive system have been investigated for step changes in command speeds for both no load and rated load conditions. Figures 6.10 and 6.11 have displayed the simulated performances of the self-tuning MRPID controller based drive system for step increase of command speeds (from 188.6 rad/sec. to 350 rad/sec.) at no load and rated load conditions, respectively. The proposed self-tuning MRPID controller based IPMSM drive system has successfully followed the step changes in command speeds quickly in less than 0.1 sec. at both no load and rated load conditions. The command torque currents of Figs. 6.10(*c*) and 6.11(*c*) have provided more initial torque at t = 0.5 sec. than at t = 0 sec due to the step change in command speeds from 188.6 rad/sec. to 350 rad/sec. The command flux currents of Figs. 6.10(*d*) and 6.11(*d*) have become negative at t = 0.5 sec. to demagnetize the main flux in order to operate the IPM motor at the command speed of 350 rad/sec. Therefore, the performances of the self-tuning MRPID based drive system have not been affected by the sudden changes in command speeds.

It is to be noted that the initial command torque and flux current (i_q^*, i_d^*) responses of Figs. 6.8–6.11 have shown higher amplitude in the order of 100 kA for a very short interval of time. The high initial i_q^*, i_d^* currents have been created due to the high frequency components of speed error of the proposed MRPID controller. The high frequency components could be removed using the zero gain in the proposed MRPID controller, but it would increase the drive response time as well as the speed overshoot of the drive system. However, these high initial i_q^*, i_d^* have not affected the performances of the IPM motor drive system using the proposed MRPID controller. It is to be mentioned that the log scale has been used for i_q^*, i_d^* currents in the simulated responses of Figs. 6.8–6.11. When the log scale has been used, it has been highlighted on the amplitude axis (y-axis) of the simulated responses of Figs. 6.4–6.18.

The performances of the self-tuning MRPID based drive system have been investigated for a step change in load. Figure 6.12 has displayed the performances of the self-tuning MRPID controller based drive system for a step change in load. Initially, the drive has been started at no load condition, and then at t = 0.5 sec. the load has been suddenly increased to the rated load of 2 N-m. The drive system has handled this impact of load change effectively. The system has shown almost zero steady state speed error after the load has been changed. At t = 0.5 sec, the command torque current of Fig. 6.12(*c*) has changed to a new level in order to handle the load torque of the drive system. The command flux current of Fig. 6.12(*d*) has not been changed after the load has been changed at t = 0.5 sec.

The performances of the drive system using the self-tuning MRPID controller have been investigated for change in system and motor parameters, which include variations in stator resistance, *q*-axis inductance (L_q), and rotor inertia. Initially, the performances of the drive system have been investigated for variation in stator resistance. The starting current, which is four or five times of the rated current, has caused large copper losses in the IPM motor. These losses have dissipated as heat in the stator winding. So, the temperature of the winding has increased. As a result, the resistance of the stator winding has increased. The starting performances of the proposed drive system have been

investigated for doubled stator resistance at both no load and rated load conditions. The doubled stator resistance has been chosen arbitrarily for the simulation of the IPM drive system. Figures 6.13 and 6.14 have shown the speed and current responses of the IPM drive system for doubled stator resistance ($R_l = 2*R$) at no load and rated load conditions, respectively at the rated command speed of 188.6 rad/sec. The drive system has followed the rated command speed quickly and accurately in less than 0.1 sec under these operating conditions. Both command torque current and command flux current have shown smooth response, and these have provided appropriate torque and flux to operate the drive system for doubled stator resistance at both no load and rated load conditions.

The starting performances of the proposed drive system have been investigated for increased inertia to prototype the effect of a high inertia machine connected to the IPM motor at both no load and rated load conditions. Figures 6.15 and 6.16 have shown the starting speed and current responses for doubled rotor inertia ($J_l = 2*J$) at no load and rated load conditions, respectively. The drive system has followed the command speed accurately for doubled rotor inertia at both no load and rated load conditions. However, the drive system has taken slightly higher settling times of 0.12 sec and 0.22 sec at no load and rated load conditions, respectively to arrive at the rated command speed of 188.6 rad/sec. because of the increased inertia. The command torque current response of Fig. 6.16(c) has shown steady state current ripple at the rated load condition. The increased inertia has added current ripple in the torque response of the IPM motor drive system.

The performances of the proposed drive system have also been investigated for the variation of q-axis inductance (L_q) to consider the effects of magnetic saturation. The effective air gap length in the q-axis is smaller than that in the d-axis of the IPM motor. Therefore, the effects of magnetic saturation have been found more prevalent in the q-axis. As a result, the q-axis inductance (L_q) has varied with the q-axis current (i_q) of the IPM motor. But, the variation of d-axis inductance (L_d) with d-axis current (i_d) has not been reported widely. It has been reported in reference [99] that the q-axis inductance (L_q) of the IPM motor decreases with the increase in q-axis torque current. In this work, the q-axis inductance (L_q) has been reduced arbitrarily by 25% to illustrate the effects of

magnetic saturation. Figures 6.17 and 6.18 have displayed the starting speed and current responses of the IPMSM drive system when L_q has been reduced by 25% at no load and rated load conditions, respectively at the rated command speed of 188.6 rad/sec. The proposed self-tuning MRPID controller has tracked the command speed in less than 0.1 sec. for change in q-axis inductance (L_q) at both no load and rated load conditions. A small speed dip at t = 0.03 sec. has been spotted in the starting speed responses of Figs. 6.17(a) and 6.18(a) at no load and rated load conditions. The speed dip in the starting speed responses of Figs. 6.17(a) and 6.18(a) have been generated due to the adaptive learning of the wavelet neural network (WNN) parameters.

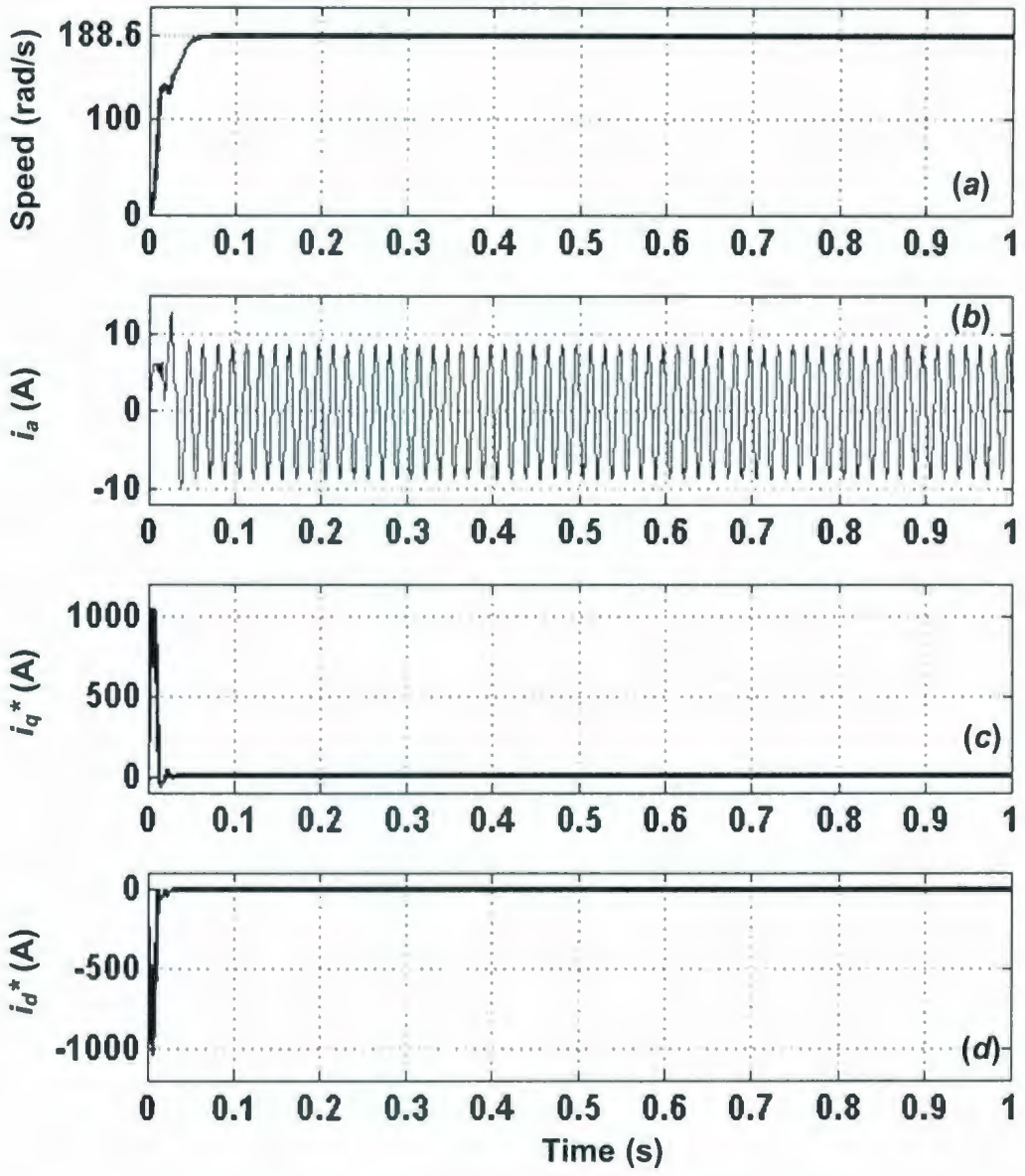

Figure 6.4: Simulated starting responses of the proposed self-tuning MRPID controller based IPMSM drive system under no load and rated speed (188.6 rad/sec.) conditions: (*a*) speed, (*b*) phase current (i_a), (*c*) *q*-axis command current (i_q*), and (*d*) *d*-axis command current (i_d*).

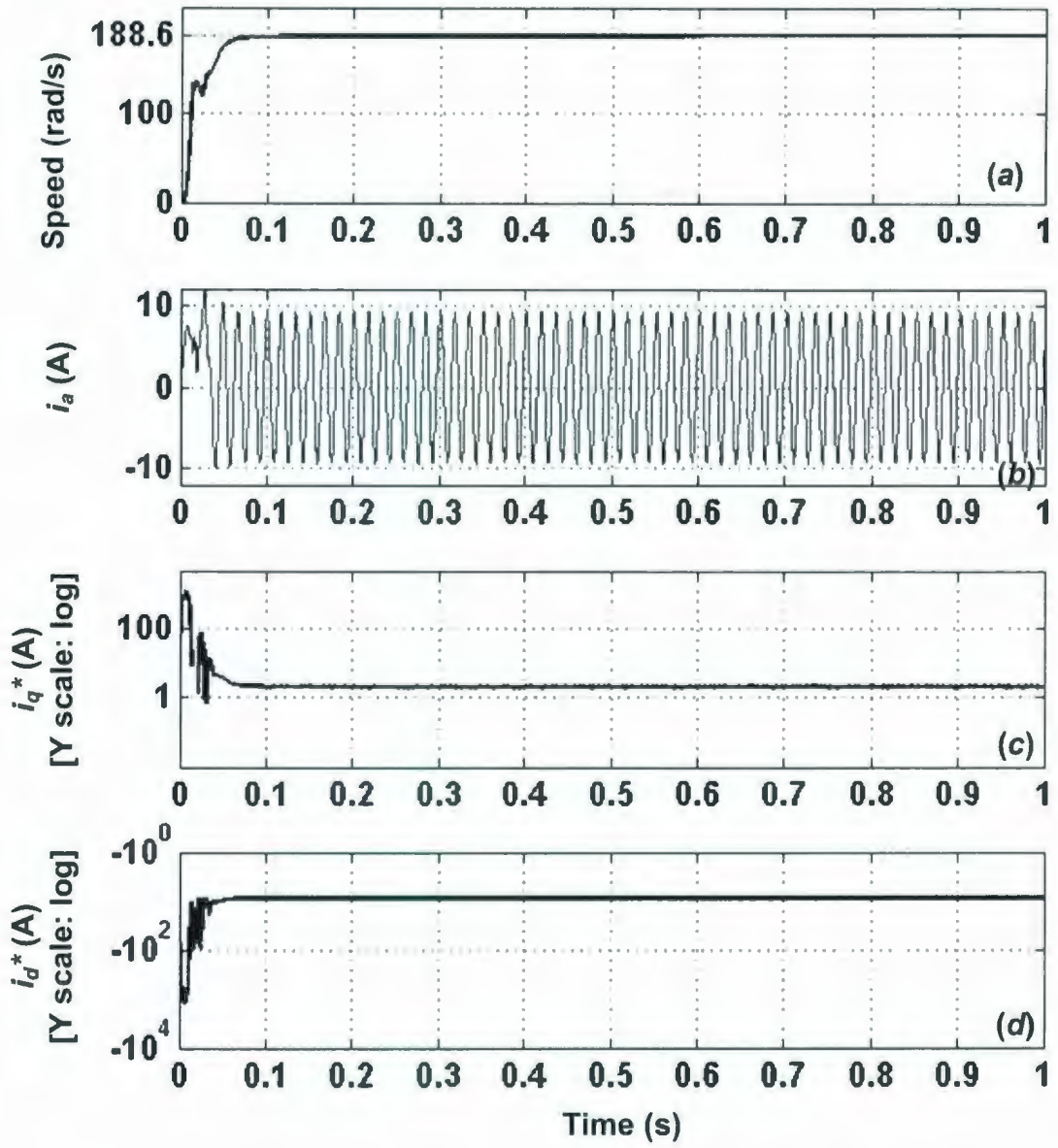

Figure 6.5: Simulated starting responses of the proposed self-tuning MRPID controller based IPMSM drive system under rated load and rated speed (188.6 rad/sec.) conditions: (*a*) speed, (*b*) phase current (i_a), (*c*) *q*-axis command current (i_q^*), and (*d*) *d*-axis command current (i_d^*).

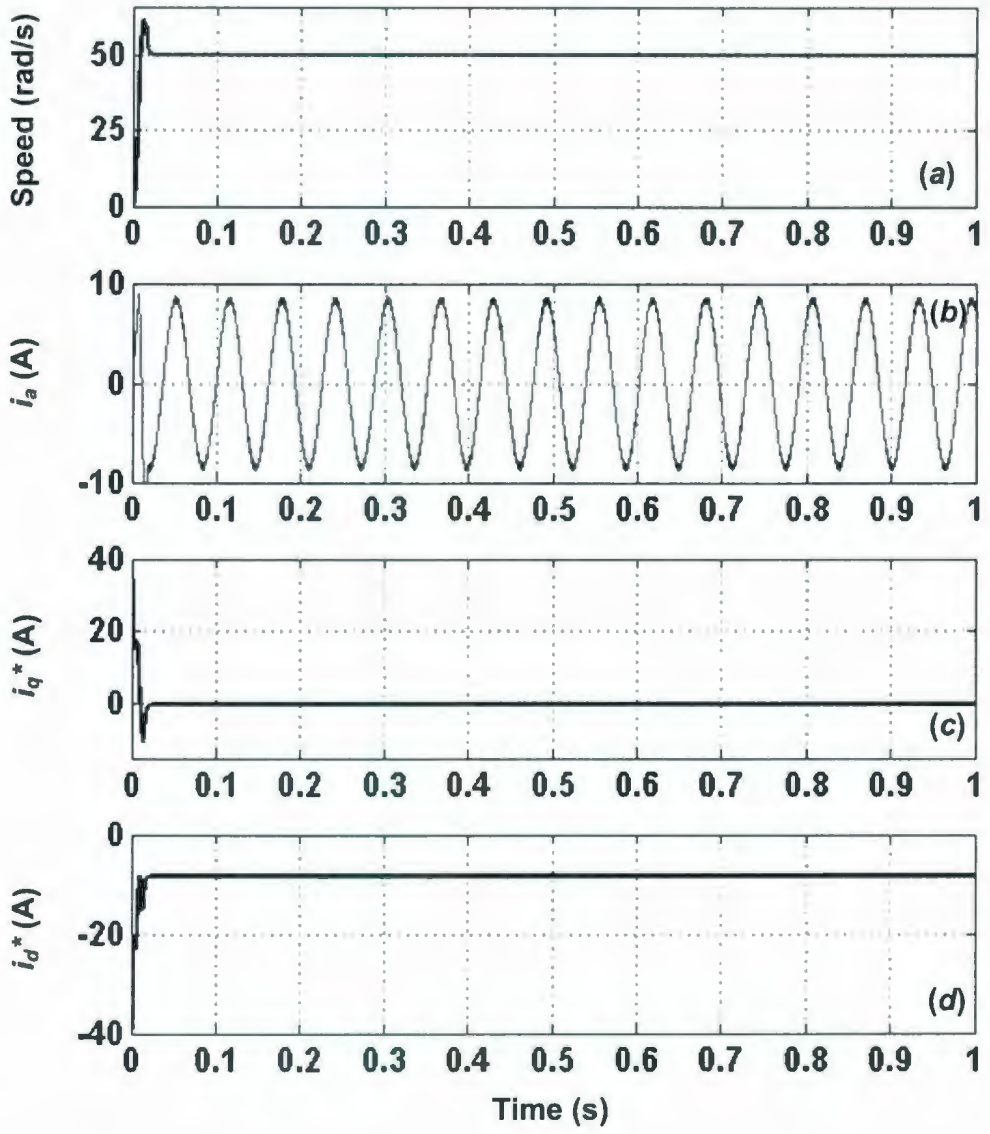

Figure 6.6: Simulated starting responses of the proposed self-tuning MRPID controller based IPMSM drive system under no load and low speed (50 rad/sec.) conditions: (*a*) speed, (*b*) phase current (i_a), (*c*) *q*-axis command current (i_q^*), and (*d*) *d*-axis command current (i_d^*).

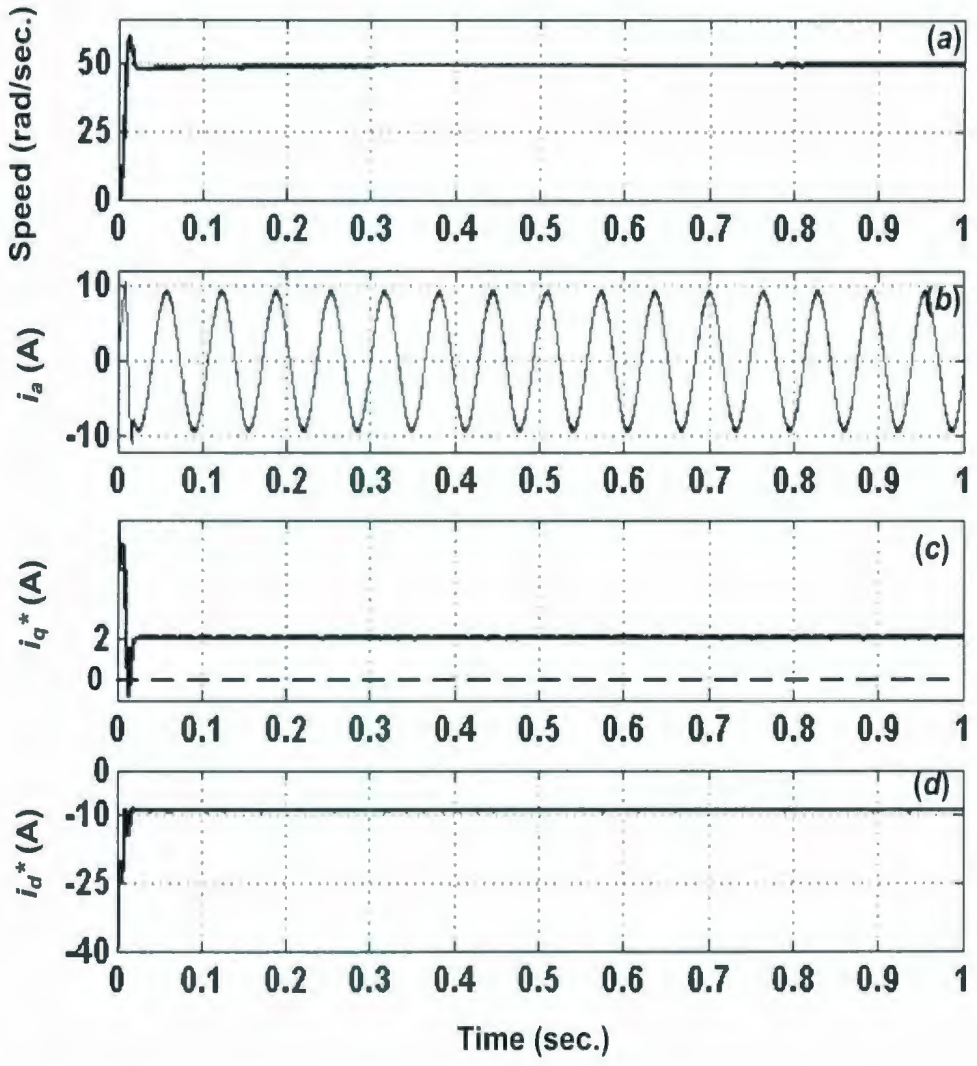

Figure 6.7: Simulated starting responses of the proposed self-tuning MRPID controller based IPMSM drive system under rated load and low speed (50 rad/sec.) conditions: (*a*) speed, (*b*) phase current (i_a), (*c*) *q*-axis command current (i_q^*), and (*d*) *d*-axis command current (i_d^*).

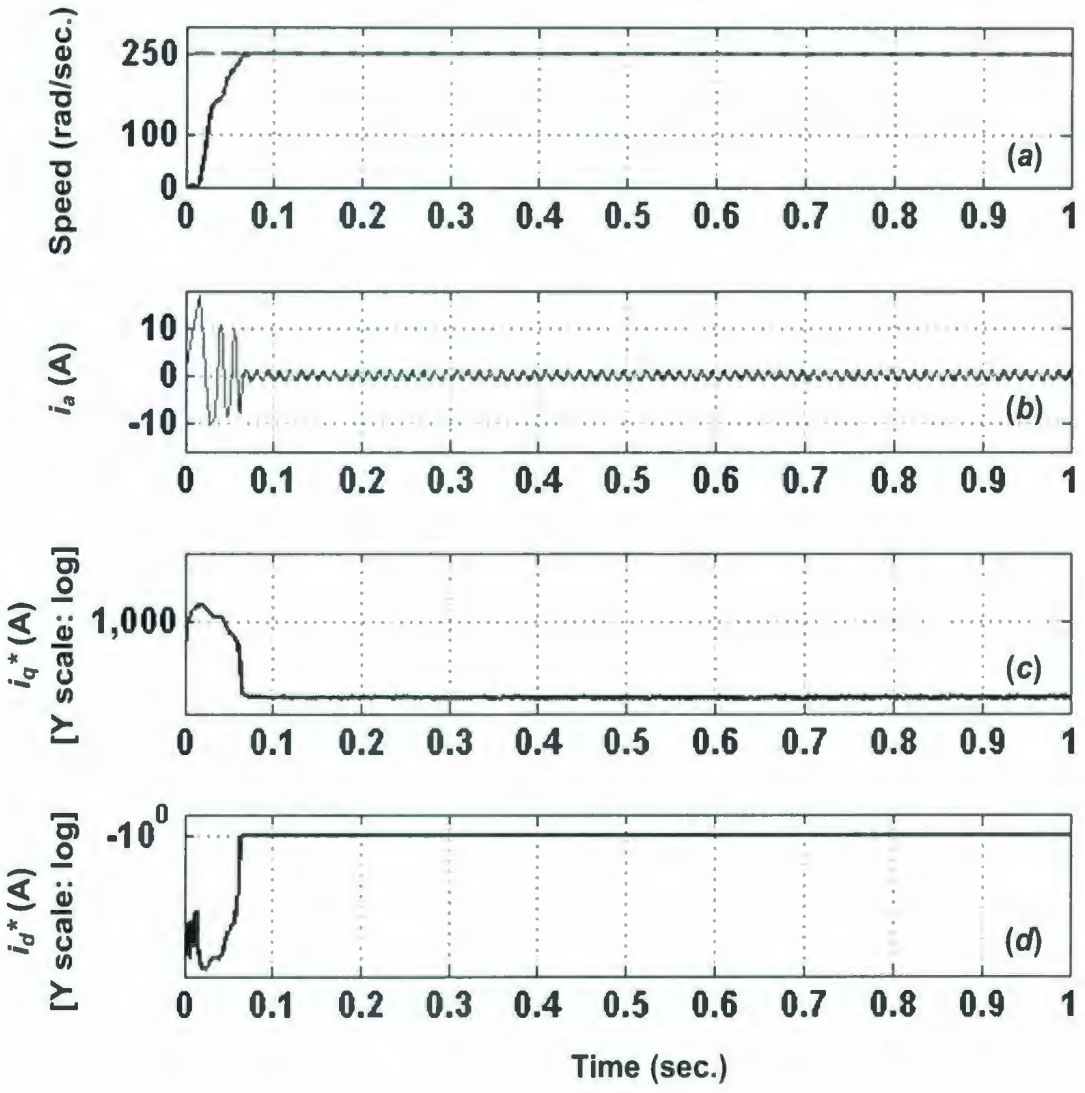

Figure 6.8: Simulated starting responses of the proposed self-tuning MRPID controller based IPMSM drive system under no load and high speed (250 rad/sec.) conditions: (*a*) speed, (*b*) phase current (i_a), (*c*) *q*-axis command current (i_q^*), and (*d*) *d*-axis command current (i_d^*).

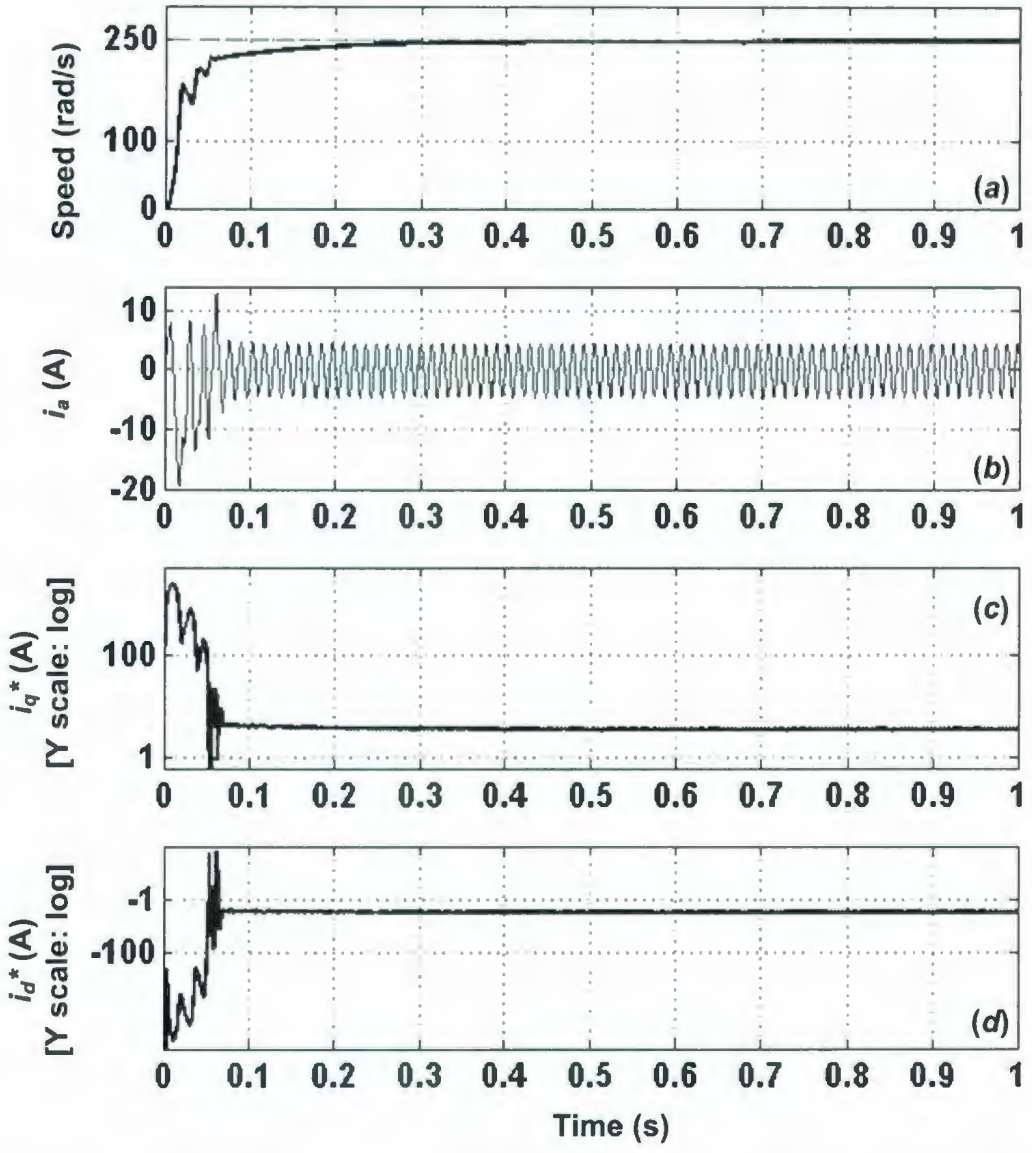

Figure 6.9: Simulated starting responses of the proposed self-tuning MRPID controller based IPMSM drive system under rated load and high speed (250 rad/sec.) conditions: (*a*) speed, (*b*) phase current (i_a), (*c*) *q*-axis command current (i_q^*), and (*d*) *d*-axis command current (i_d^*).

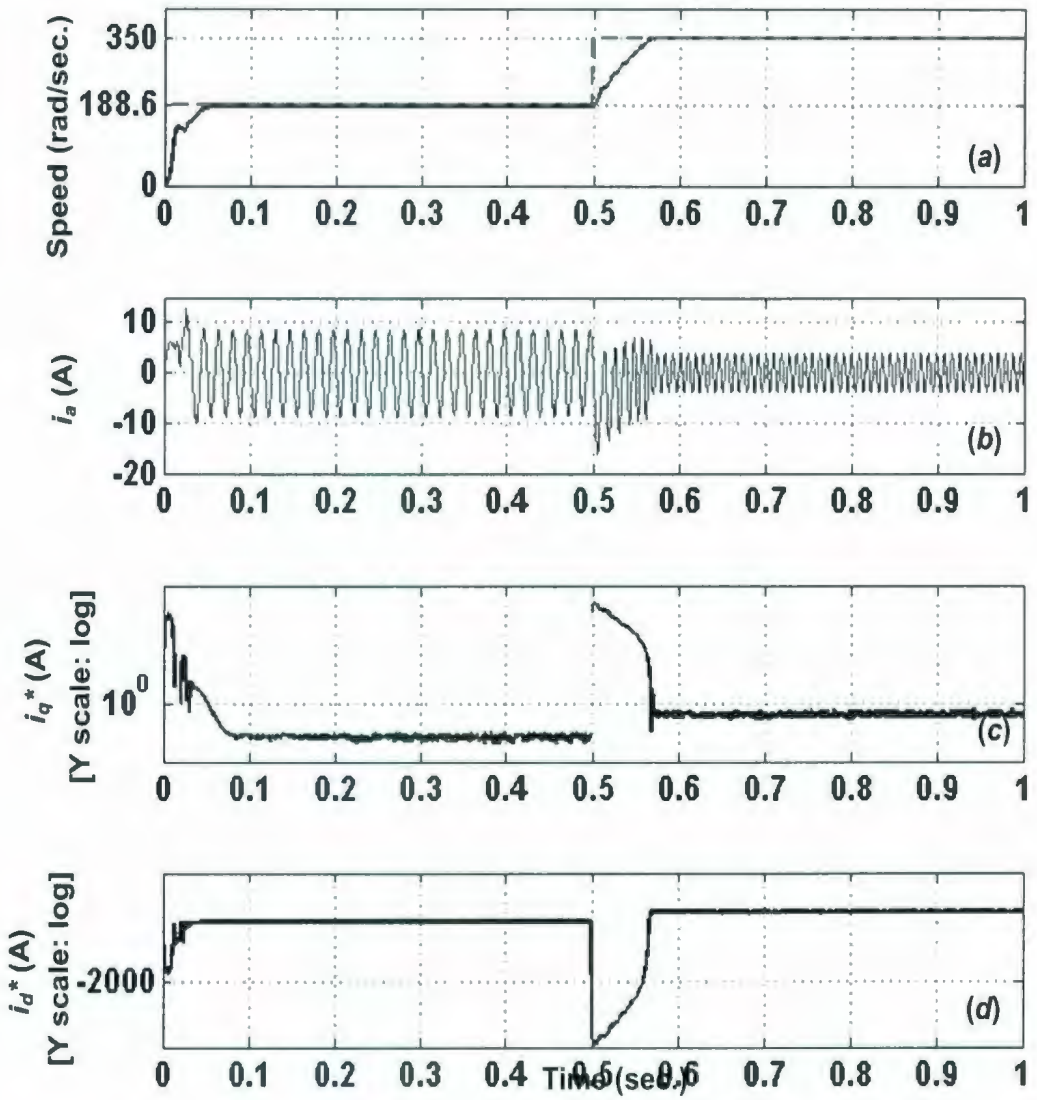

Figure 6.10: Simulated starting responses of the proposed self-tuning MRPID controller based IPMSM drive system for step increase in command speeds (from 188.6 rad/sec. to 350 rad/sec.) under no load condition: (*a*) speed, (*b*) phase current (i_a), (*c*) *q*-axis command current (i_q^*), and (*d*) *d*-axis command current (i_d^*).

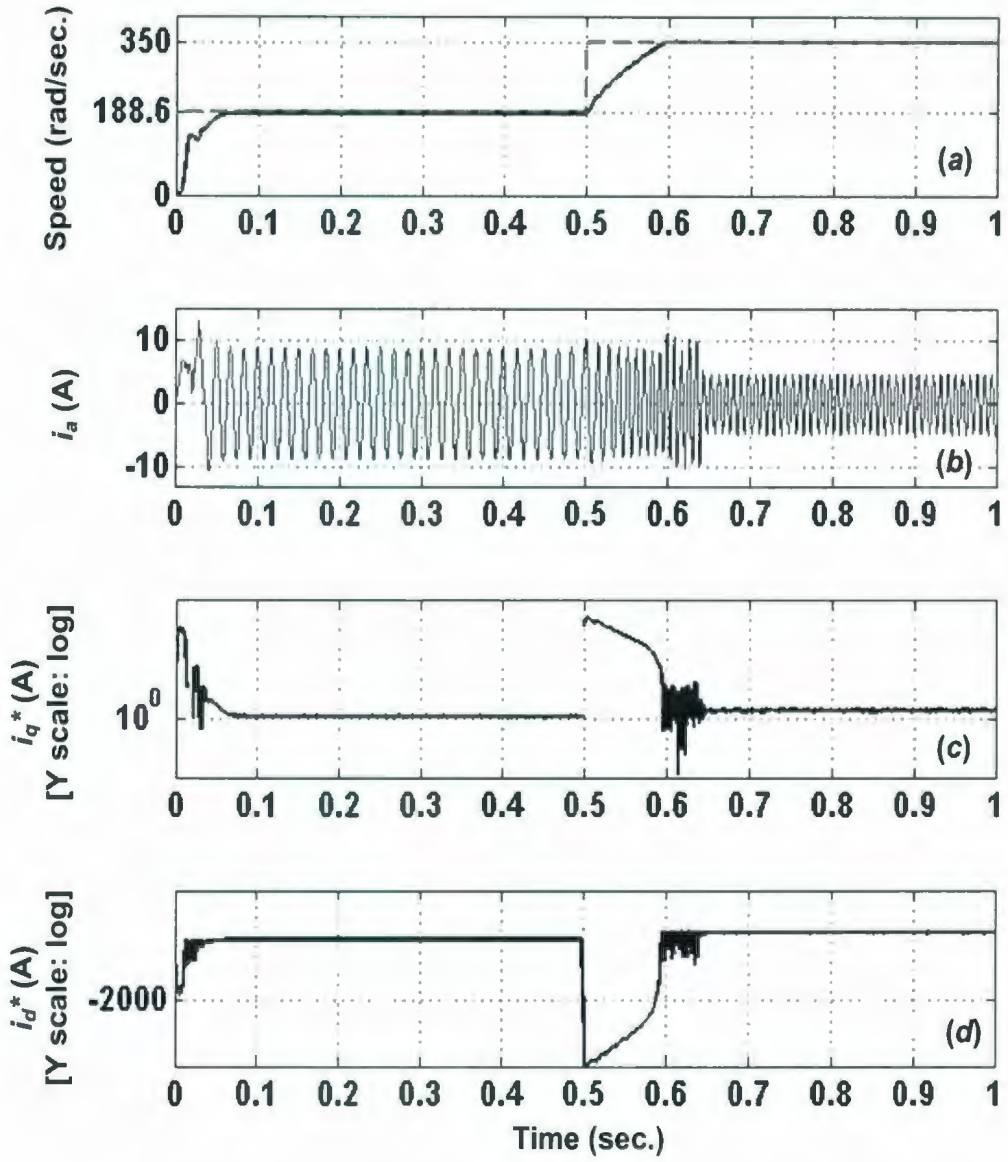

Figure 6.11: Simulated starting responses of the proposed self-tuning MRPID controller based IPMSM drive system for step increase in command speeds (from 188.6 rad/sec. to 350 rad/sec.) under rated load condition: (*a*) speed, (*b*) phase current (i_a), (*c*) *q*-axis command current (i_q^*), and (*d*) *d*-axis command current (i_d^*).

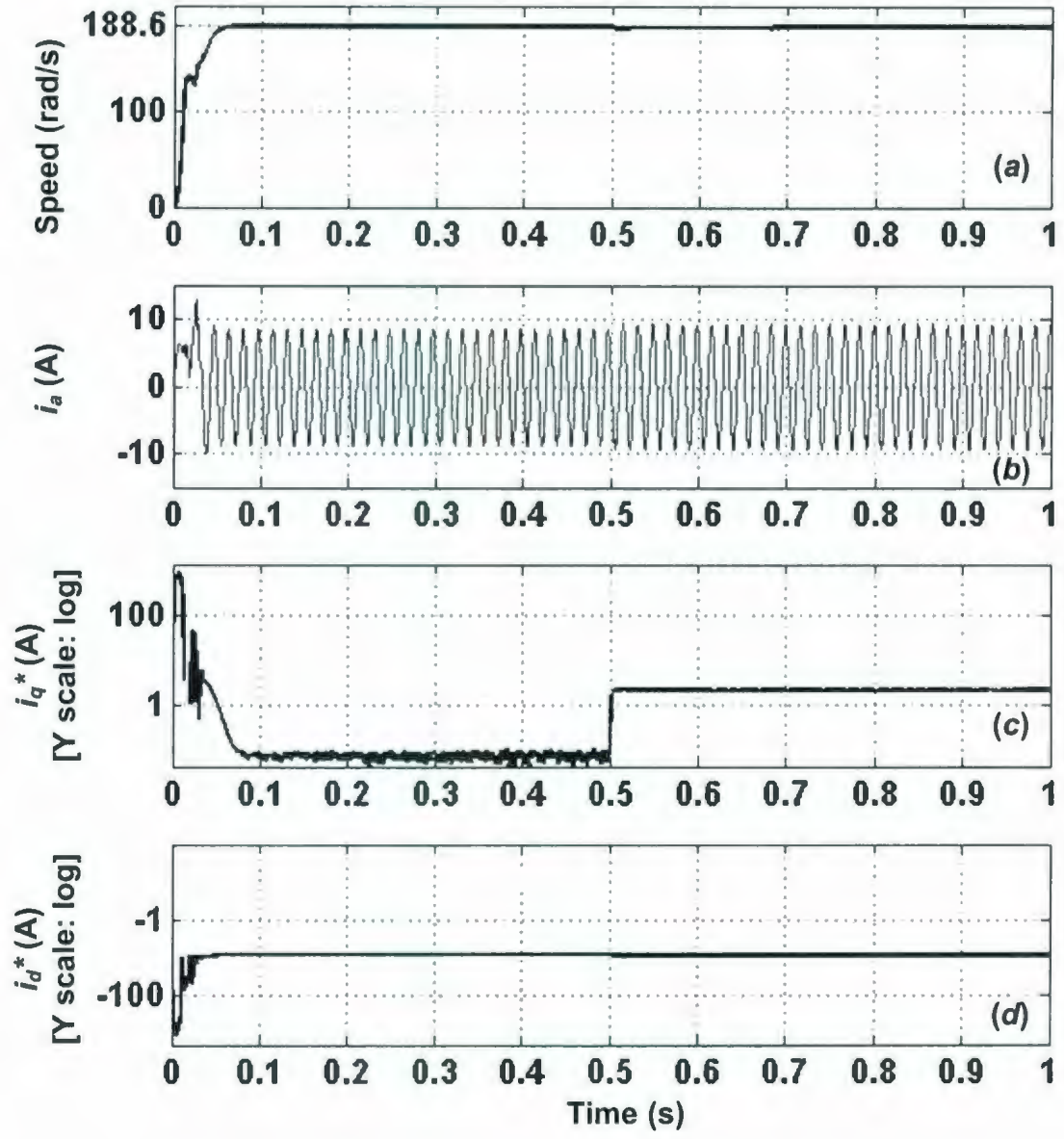

Figure 6.12: Simulated responses of the proposed self-tuning MRPID controller based IPMSM drive system when load is changed at $t = 0.5$ second from no load to rated load under rated speed (188.6 rad/sec.) condition: (*a*) speed, (*b*) phase current (i_a), (*c*) q-axis command current (i_q^*), and (*d*) d-axis command current (i_d^*).

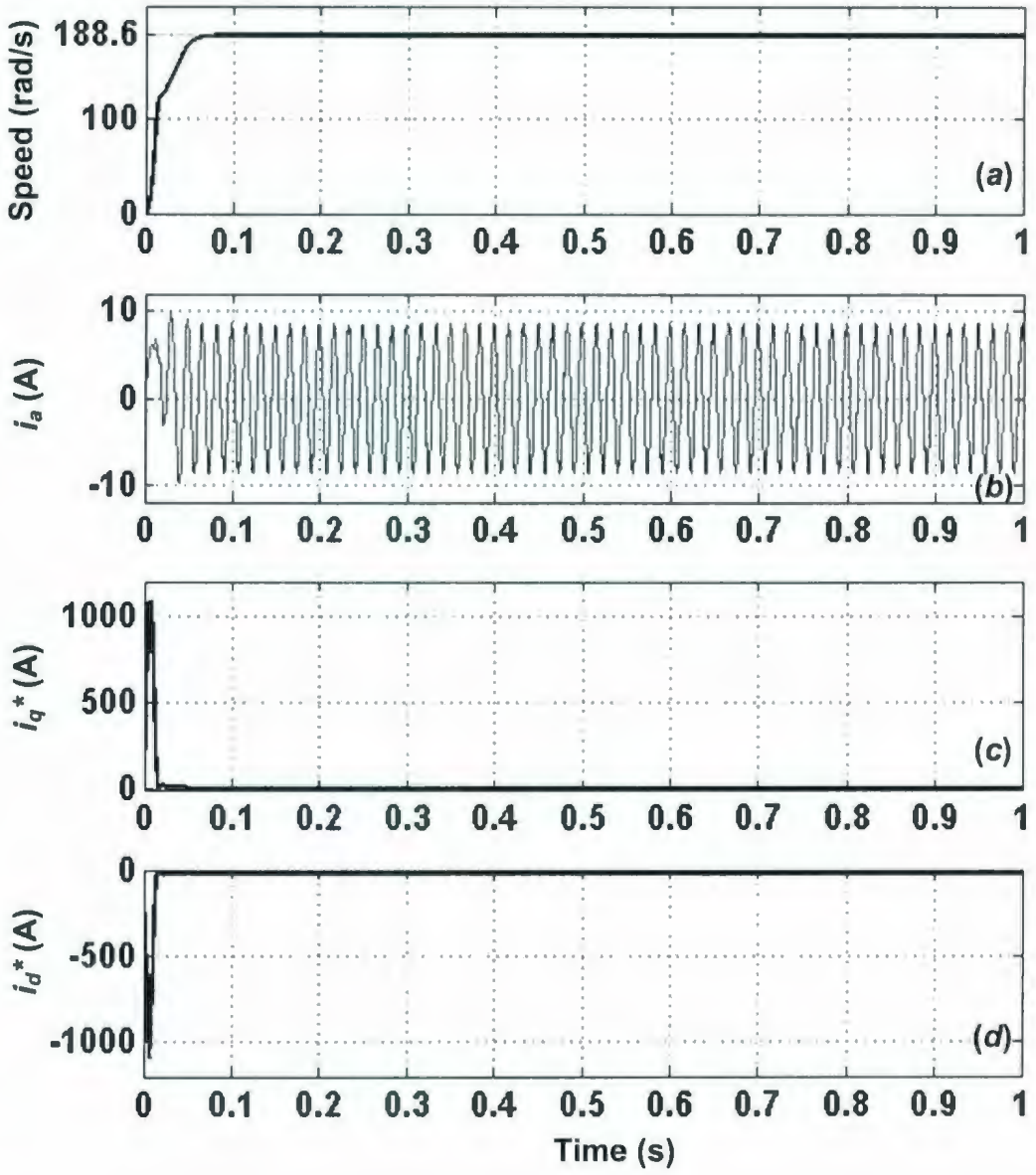

Figure 6.13: Simulated starting responses of the proposed self-tuning MRPID controller based IPMSM drive system for change in stator resistance ($R_l = 2*R$) under no load and rated speed (188.6 rad/sec.) conditions: (*a*) speed, (*b*) phase current (i_a), (*c*) *q*-axis command current (i_q*), and (*d*) *d*-axis command current (i_d*).

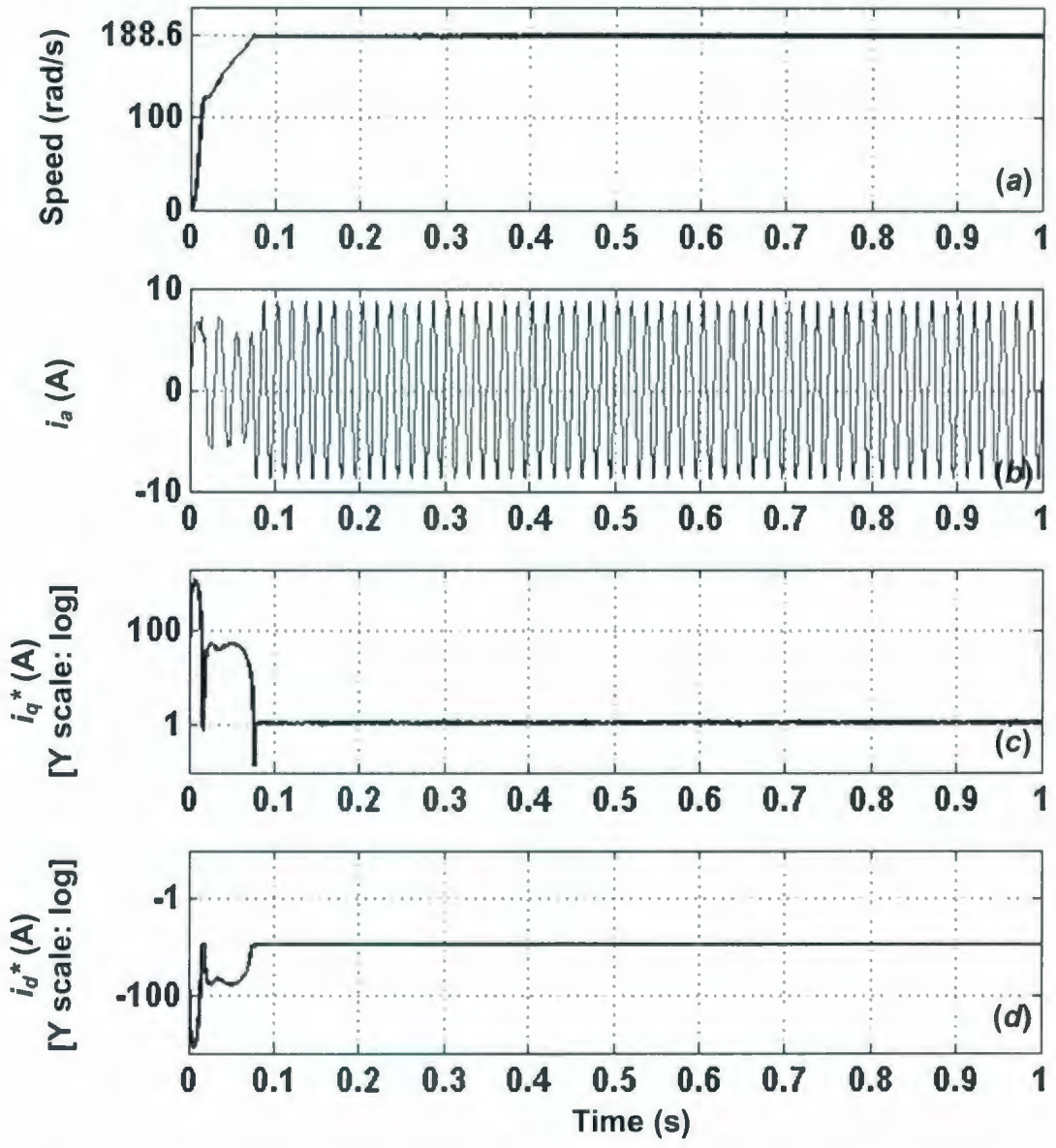

Figure 6.14: Simulated starting responses of the proposed self-tuning MRPID controller based IPMSM drive system for change in stator resistance (R_l = 2*R) under rated load and rated speed (188.6 rad/sec.) conditions: (*a*) speed, (*b*) phase current (i_a), (*c*) q-axis command current (i_q*), and (*d*) d-axis command current (i_d*).

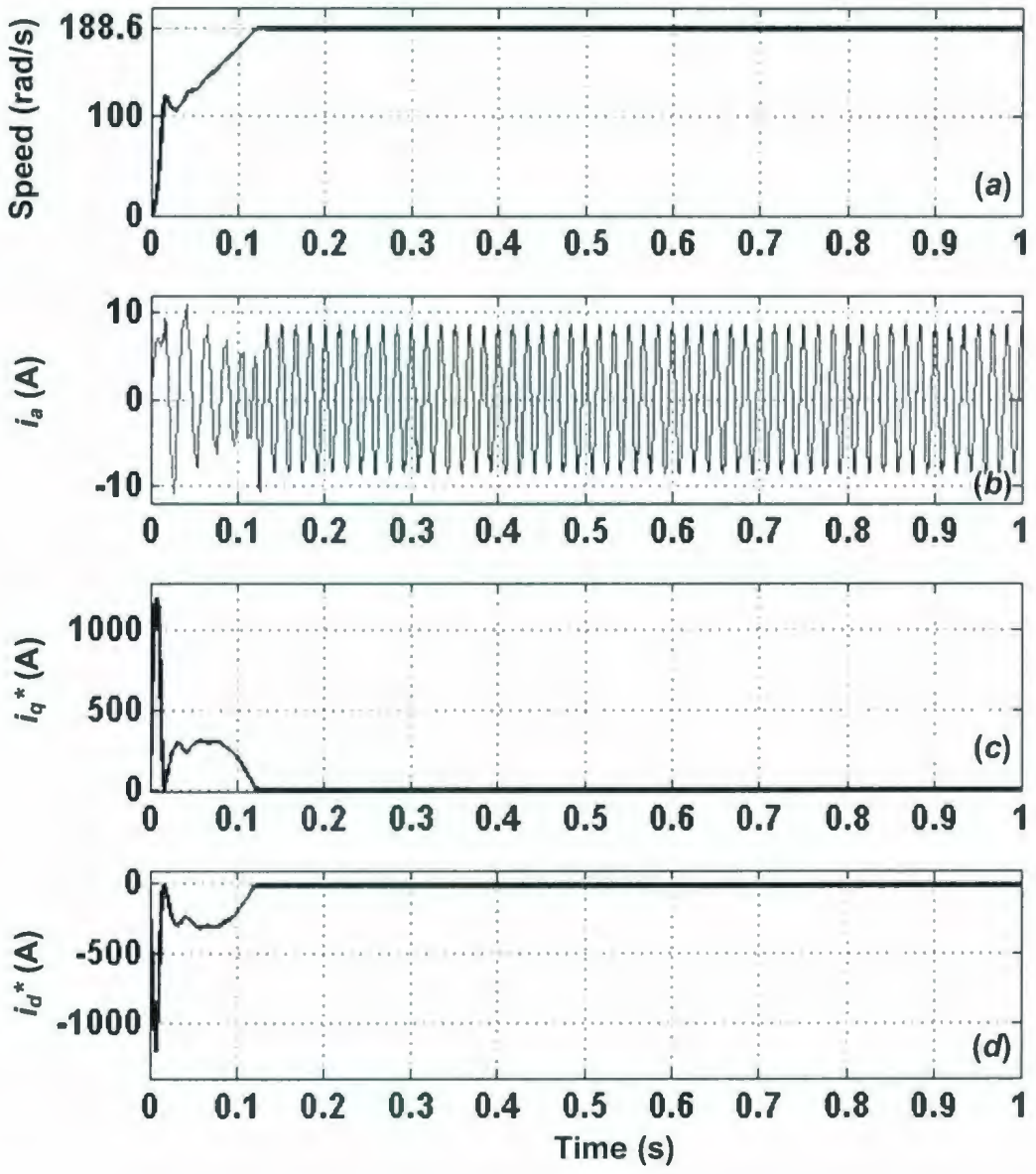

Figure 6.15: Simulated starting responses of the proposed self-tuning MRPID controller based IPMSM drive system for change in rotor inertia ($J_1 = 2*J$) under no load and rated speed (188.6 rad/sec.) conditions: (*a*) speed, (*b*) phase current (i_a), (*c*) *q*-axis command current (i_q*), and (*d*) *d*-axis command current (i_d*).

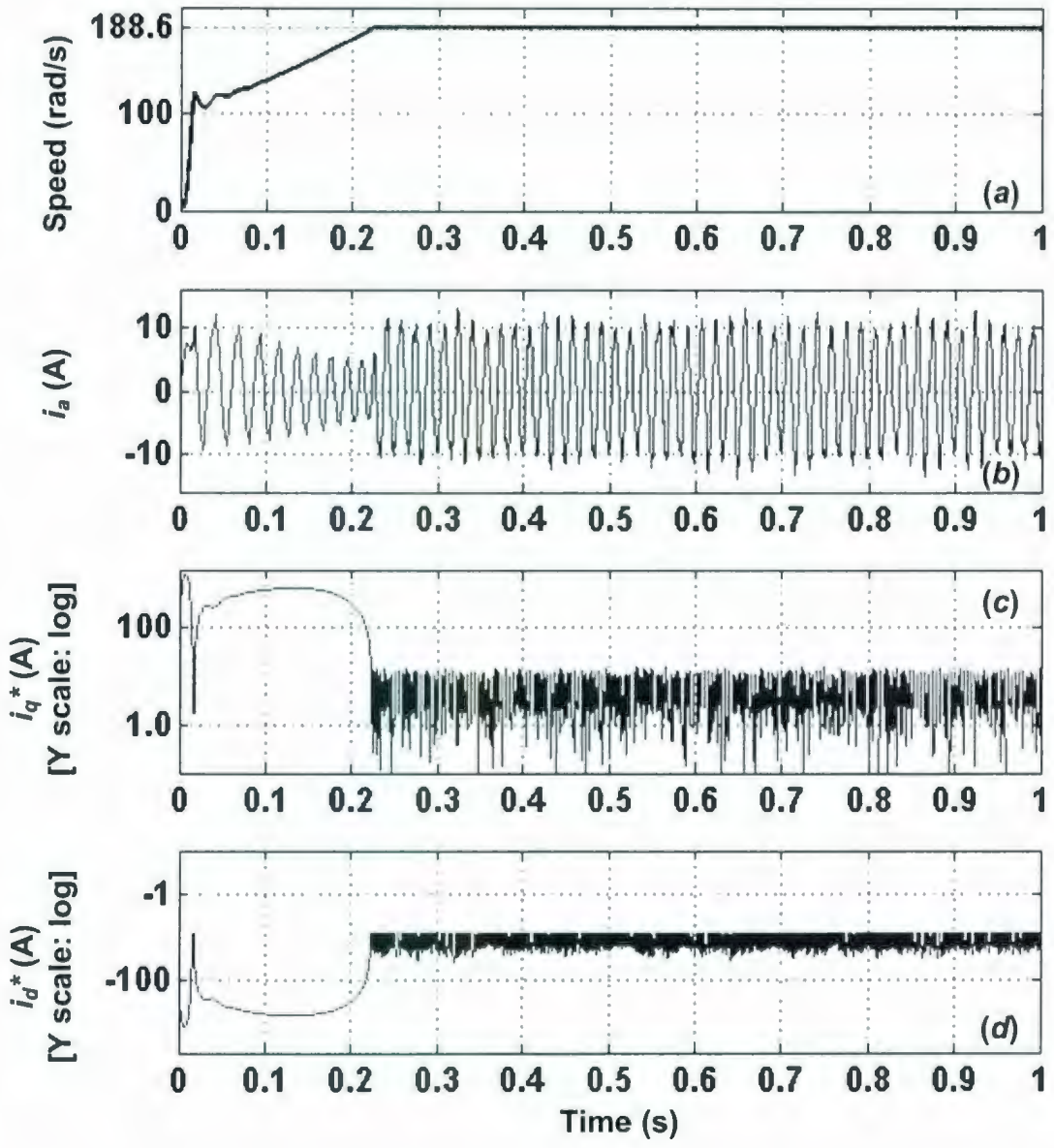

Figure 6.16: Simulated starting responses of the proposed self-tuning MRPID controller based IPMSM drive system for change in rotor inertia ($J_1 = 2*J$) under rated load and rated speed (188.6 rad/sec.) conditions: (*a*) speed, (*b*) phase current (i_a), (*c*) *q*-axis command current (i_q^*), and (*d*) *d*-axis command current (i_d^*).

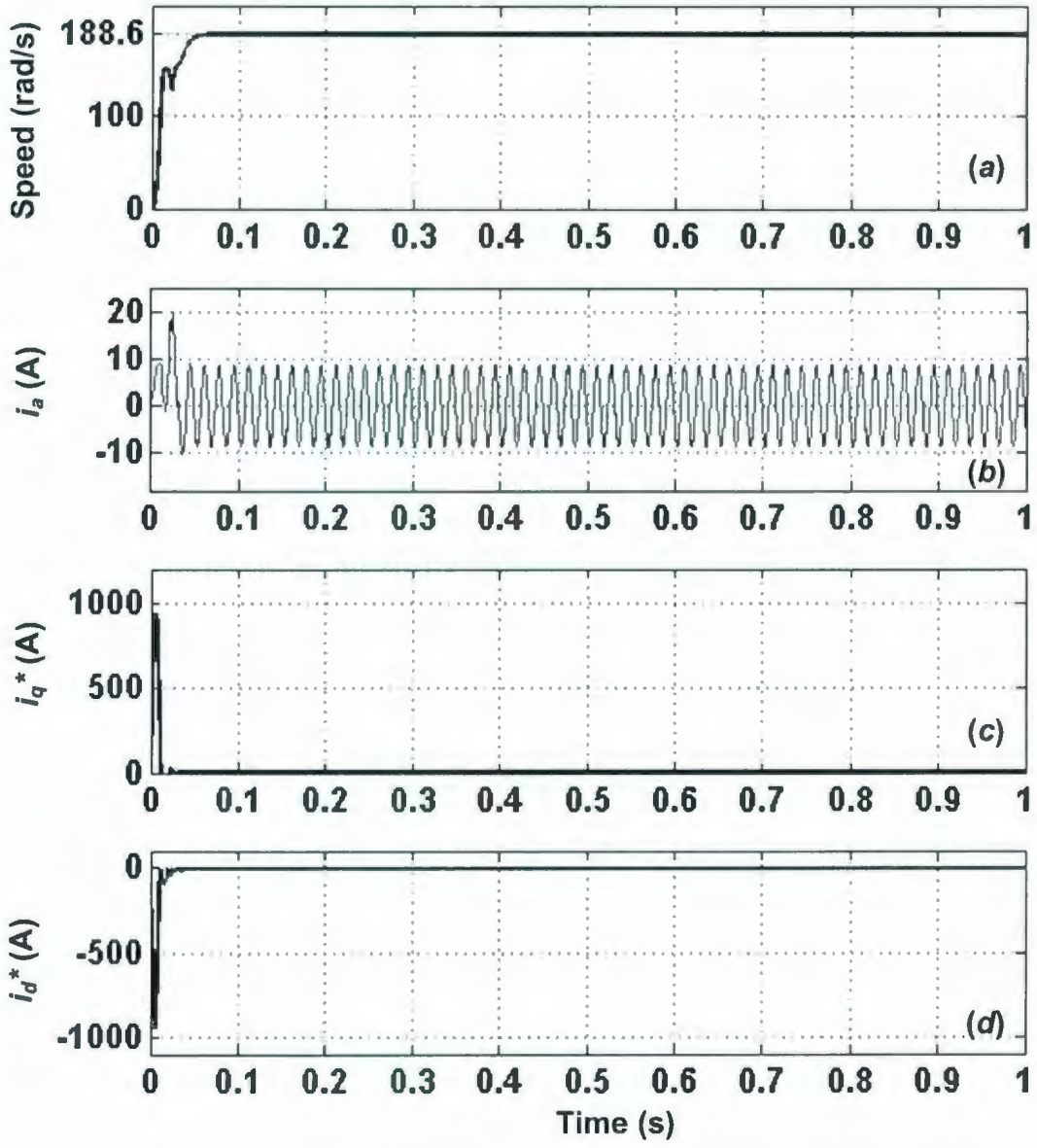

Figure 6.17: Simulated starting responses of the proposed self-tuning MRPID controller based IPMSM drive system when L_q is reduced by 25% under no load and rated speed (188.6 rad/sec.) conditions: (*a*) speed, (*b*) phase current (i_a), (*c*) *q*-axis command current (i_q^*), and (*d*) *d*-axis command current (i_d^*).

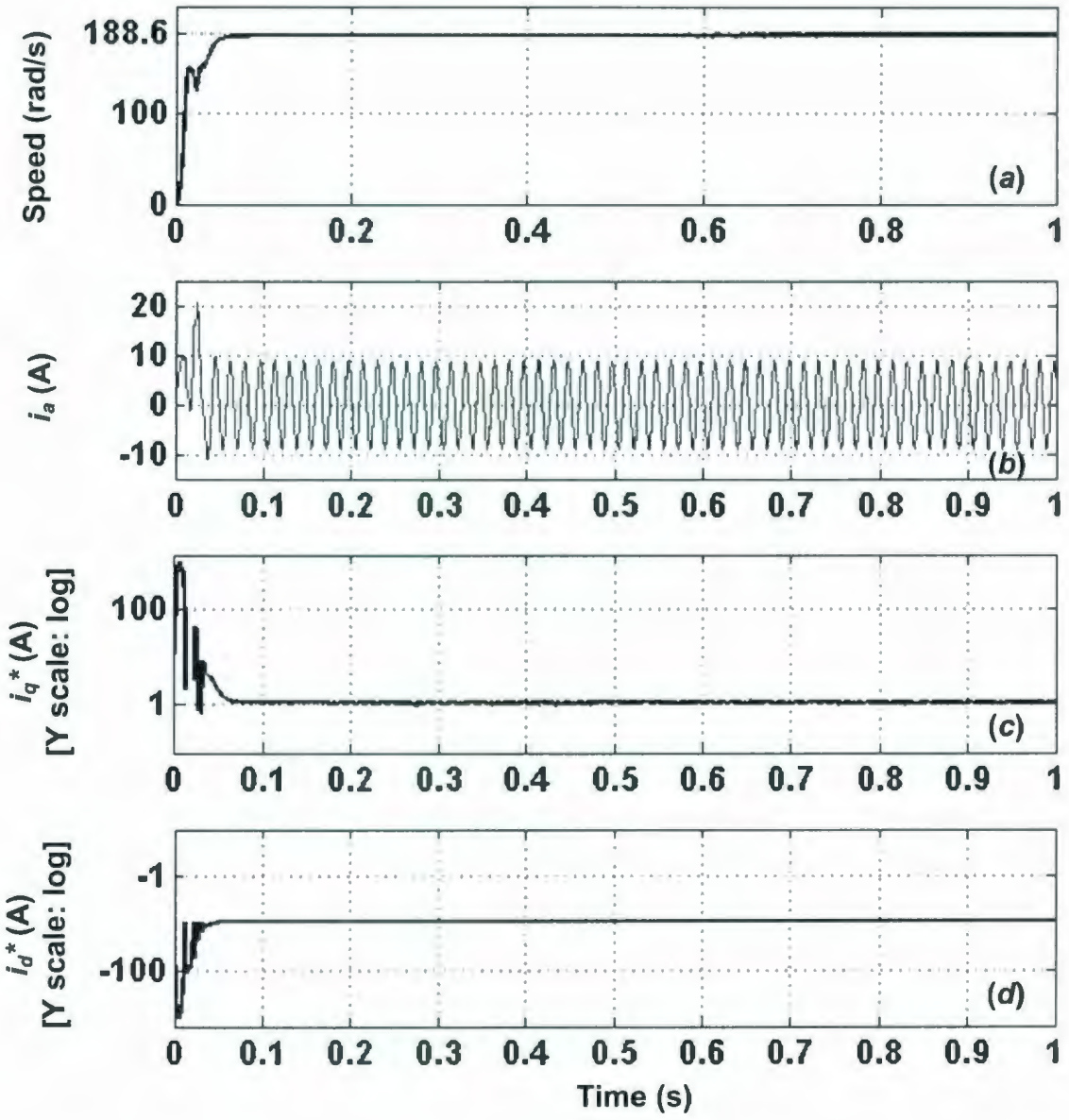

Figure 6.18: Simulated starting responses of the proposed self-tuning MRPID controller based IPMSM drive system when L_q is reduced by 25% under rated load and rated speed (188.6 rad/sec.) conditions: (*a*) speed, (*b*) phase current (i_a), (*c*) *q*-axis command current (i_q^*), and (*d*) *d*-axis command current (i_d^*).

6.3 Concluding Remarks

In this chapter, a novel wavelet neural network (WNN) based self-tuning multiresolution proportional integral derivative (MRPID) controller for the IPMSM drive system has been developed and implemented. A new structure of the WNN has been developed for the proposed self-tuning MRPID controller to ensure optimal drive performances under different system uncertainties. The on-line stability of the proposed control technique has been achieved by a novel adaptive learning of the WNN. In order to predict the performances of the proposed self-tuning MRPID controller, the drive system has been implemented in the MATLAB software. The proposed self-tuning MRPID based IPMSM drive system has shown fast speed responses for different starting command speeds and for step change in command speeds. The IPMSM drive system using the self-tuning MRPID controller has also shown insensitive performances to the step change in load. The self-tuning MRPID based drive system has stabilized quickly to the initial command speed after the sudden change has been load. The system has shown almost zero steady state speed error after the load has been applied.

The performances of the proposed drive system have been investigated for changes in system and motor parameters. The self-tuning MRPID control technique has performed excellent speed tracking for variations in parameters. The simulated performance test results of the proposed controller based IPM motor drive system have been found better than those of the fixed gain controllers based IPMSM drive systems. In the next chapter, the performances of the proposed self-tuning MRPID controller based IPMSM drive system have been investigated experimentally in real time using the dSPACE ds1102 digital signal processor (DSP) board. The real time implementation techniques and the experimental performance test results of the proposed self-tuning MRPID controller based IPMSM drive system have been presented in the next chapter.

Chapter 7

Real Time Implementation of the Wavelet Based Self-Tuning MRPID Controller

The pervious chapter has presented the simulated performance test results of the wavelet neural network (WNN) based self-tuning multiresolution proportional integral derivative (MRPID) controller for the interior permanent magnet (IPM) motor drive system. The simulated performances of the proposed WNN based self-tuning MRPID controller have been found satisfactory and encouraging. This chapter has presented the real time implementation of the interior permanent magnet synchronous motor (IPMSM) drive system incorporating the WNN based proposed self-tuning MRPID controller. The real time implementation of the proposed self tuning MRPID based IPMSM drive system has involved both software and hardware implementation of the drive system. The dSPACE ds1102 digital signal processor (DSP) controller board has been used for the implementation and execution of the self-tuning MRPID control algorithm. Other hardware components such as amplifier and isolation circuits, six-pulse voltage source inverter, and current transducers have been used for the real time implementation of the drive system. This chapter has presented a detailed experimental implementation procedure of the IPMSM drive system using the proposed self-tuning MRPID controller.

The experimental test results of the proposed drive system using the self-tuning MRPID controller have been presented with pertinent discussions.

7.1 Laboratory Setup for the Real Time Implementation of the IPMSM Drive

The laboratory setup for the real time implementation of the interior permanent magnet synchronous motor (IPMSM) drive system has been shown in Fig. 7.1. In the drive system, a laboratory 1-hp interior permanent magnet (IPM) motor has been used. The IPM motor has been coupled to an electro dynamometer using the rubber belt. The dynamometer has been used for the loading for the IPM motor. The rotor position of the IPMSM has been measured by an optical incremental encoder. The encoder has been directly mounted on the rotor shaft using a flexible coupler. The actual motor currents have been measured using the Hall-effect current transducers. These transducers have been rated with maximum current of 30 A, and these have good frequency responses up to 20 kHz. A three-phase six-pulse Darlington pair bipolar junction transistor (BJT) inverter has been used to supply the test IPM motor with its stator voltages. The details of the BJT inverter have been provided in Appendix B.

The switching pulses generated on digital output port of the DSP board have been fed to a six-channel opto-coupler amplifier driving circuit before being applied on gates of the inverter BJT switches. The details of the opto-coupler driving circuit have been provided in Appendix C. The amplifier section of the driving circuit has been used to increase the power level of the switching pulses for the BJT inverter. The opto-coupler driving circuit has also provided isolation between the low power control circuit and the high power drive system. A three-phase diode rectifier has been used to provide the dc bus voltage for the BJT inverter from a three-phase 208 V variable power supply. The ds1102 digital signal processor (DSP) board has been installed in a personal computer (PC). A digital storage oscilloscope has been used to capture the speed response and the current response of the IPM motor drive system.

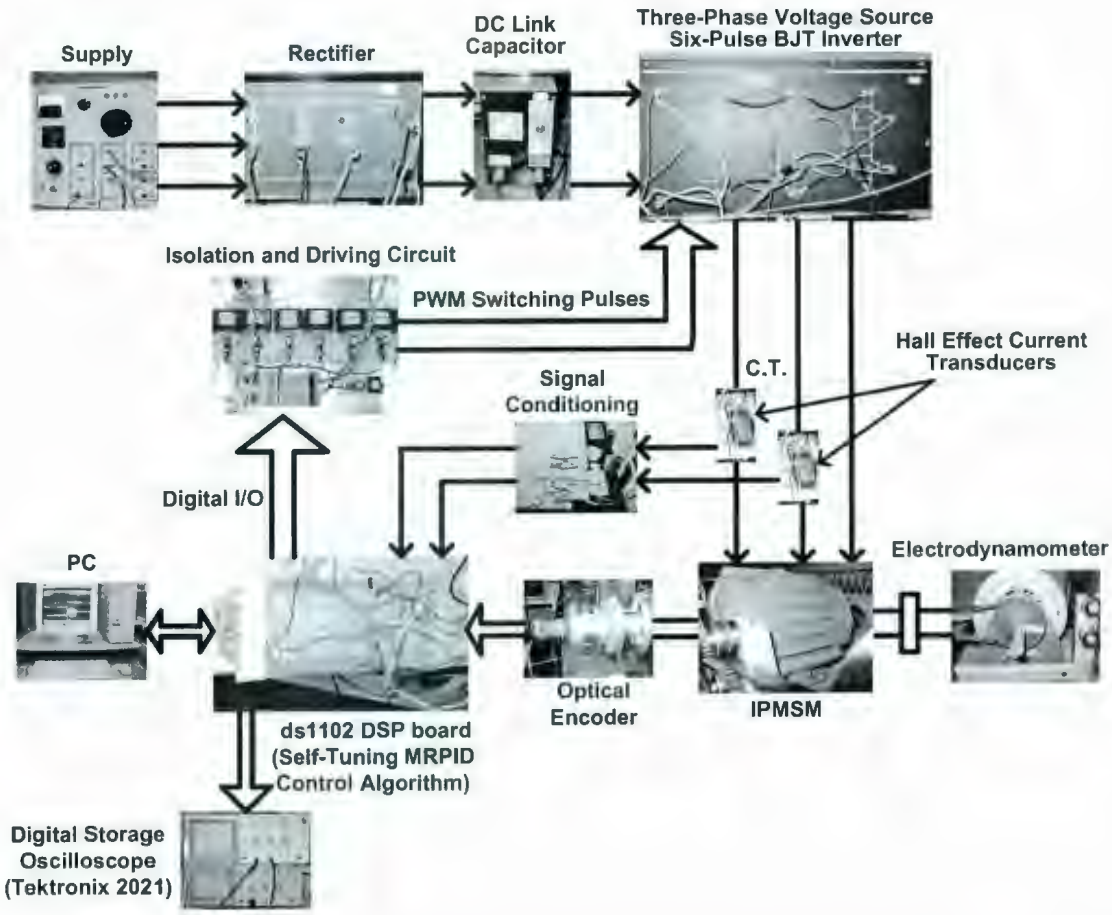

Figure 7.1: Laboratory setup for the real time implementation of the IPMSM drive system.

7.2 Hardware Components for the Real time Implementation of the IPMSM Drive

The proposed self-tuning MRPID controller has been implemented through the dSPACE ds1102 DSP controller board in real time. The hardware schematic for the real time implementation of the proposed IPM motor drive system using the ds1102 DSP board has been shown in Fig. 7.2. The main processor of the DSP board is the Texas Instrument 32 bit floating point digital signal processor TMS320C31. The DSP board consists of a set of on-board peripherals such as analog to digital (A/D) converter, digital to analog (D/A) converter, and incremental encoder interfaces. The board has one four-channel A/D (two 16-bit and two 12-bit) converter, one four-channel D/A (each of 12-bit) converter, and two 16-bit incremental encoder subsystems. The board also has a DSP microcontroller based digital I/O subsystem. The fixed point Texas Instrument slave processor TMS320P14 has been used for the execution of the subsystem [103]. The software *dSPACE control desk* has been used to edit and download the proposed self-tuning MRPID control algorithm in the DSP board. The *control desk* software has also been used to change the command speeds and to change the index pulses of the encoder from the keyboard. The block diagram of the DSP controller board has been shown in Fig. 7.3.

The motor currents have been fed to the DSP board through the A/D converter. The rotor position angle has been measured by an absolute incremental encoder mounted on the rotor shaft and then fed to the board through the encoder interface. The encoder has generated 4096 pulses per revolution of the rotor. The output of the encoder has been increased to 4×4096 pulses per revolution by a built-in pulse multiplier to get a better resolution. The 24-bit built-in position counter has been used to count the number of pulses from the encoder. The position counter has been reset once per revolution by the index pulse from the encoder. The motor speed has been computed from the rotor position angle using the numerical differentiation. The hysteresis controller has been used as the current controller of the IPMSM drive system. The speed controller has been used

to generate the command torque for the drive system. The digital outputs of the DSP board have been used as the switching pulses for the BJT inverter. These digital outputs have been fed to the BJT inverter through the opto-coupler driving circuit.

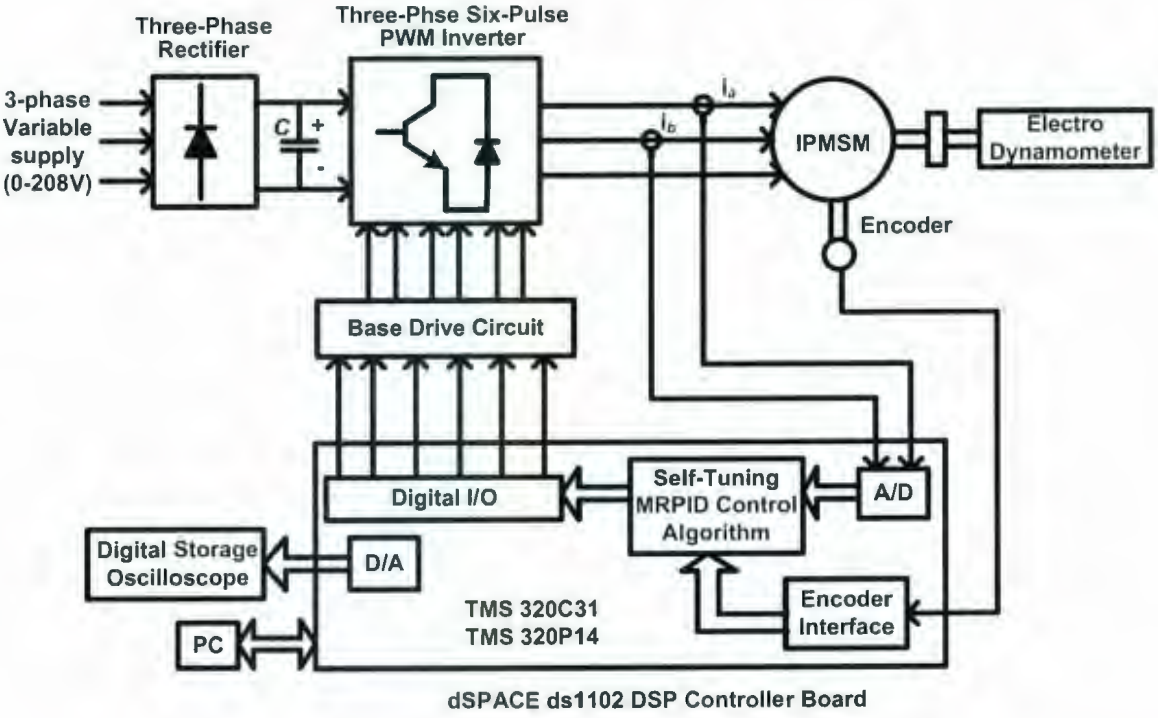

Figure 7.2: Hardware schematic for the real time implementation of the IPMSM drive system using the dSPACE ds1102 DSP controller board.

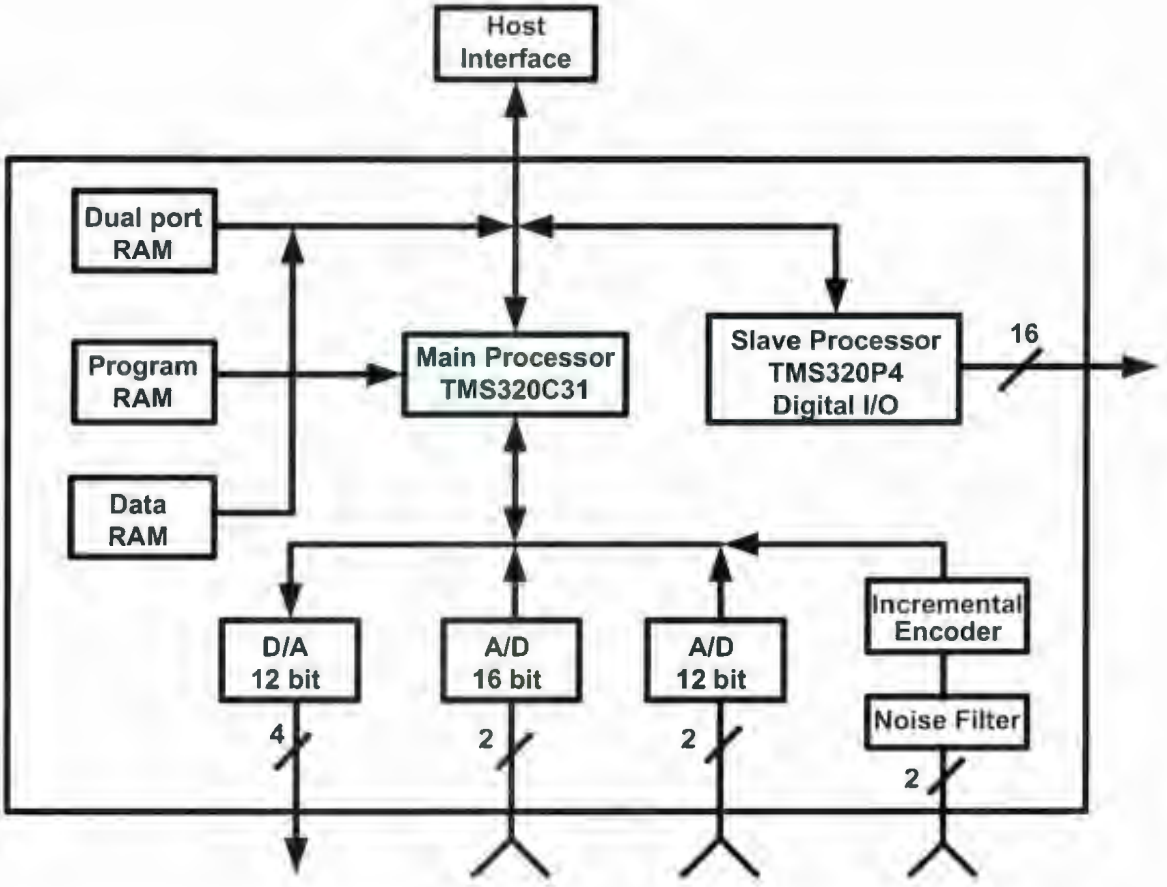

Figure 7.3: Block diagram of the dSPACE ds1102 DSP controller board [103].

7.3 Software Development for the Real Time Implementation of the IPMSM Drive

The proposed self-tuning MRPID control algorithm for the IPMSM drive system has been implemented through software by developing a computer program in high level Tourbo-*C* programming language. The program has been compiled by the Texas Instrument (TI) *C* compiler in order to generate the object codes. The generated object codes have been downloaded to the DSP board through the dSPACE utilities. The control algorithm has loaded the output weights, the translation parameter, the dilation parameter, and the filter coefficients at the beginning. After initializing the required variables and the functions, the A/D converter of the DSP board has been used to read the motor currents. At the same time, the encoder subsystem has been used to read the rotor position. The motor speed has been calculated from the measured rotor position. The speed error and the change of speed error have been determined from the actual speed and the command speeds.

The low pass and high pass filters of the selected wavelet '*db*3' have been used for the implementation of the proposed MRPID control algorithm. The speed error has been filtered up to the second level of resolution of the discrete wavelet transform (DWT). The discrete samples of speed error have been placed into an input buffer of size six. The current and past samples of speed error have been used in the input buffer. The samples of the input buffer have been updated using the first in first out (FIFO) operation. The filter coefficients of the '*db*3' low pass and high pass filters have been placed into two separate arrays of size six. The speed samples have been circularly convolved with the low pass and high pass filter coefficients at first level of resolution. Then the convoluted samples have been down sampled by two. The down sampling operation has produced first level approximations and details of the speed error. The first level approximations have been convolved circularly again with the low pass and high pass filter coefficients. The convolution operations at this stage have produced the second level details and approximations of the speed error. The second level details and approximations, and the first level approximations have been multiplied with the gains

and then these have been added together to generate the command torque for the drive system.

The wavelet neural network (WNN) has been used for the self-tuning of the proposed MRPID controller. The discrete samples of speed error and change of speed error have been processed in the four-layer WNN to generate the optimal gains for the proposed self-tuning MRPID controller. An adaptive on-line training of the WNN has been used. The *d-q* axis command currents have been determined from the command torque using the maximum torque per ampere (MTPA) and flux weakening (FW) control algorithm. The inverse Park transformation has been applied on the *d-q* axis command currents to determine the three-phase command currents for the drive system. The three-phase command currents have been compared with actual motor current samples within a hysteresis band in order to generate the switching pulses for the Darlington pair bipolar junction transistor (BJT) inverter.

The A/D and D/A conversions, the digital logic signal generation, the executions of the proposed speed control and the hysteresis current control algorithms, and the *d-q* transformations have been performed under one sampling period. The sampling frequency of 3.3 kHz has been used for the real time implementation of the IPM motor drive system using the DSP board. The procedure to implement the proposed self-tuning MRPID control algorithm for the IPMSM drive system in real time using the ds1102 DSP board has been shown in the flow chart of Fig. 7.4.

7.3.1 Peripheral initialization

The macro functions have been used in order to initialize and to access the on-board peripherals of the ds1102 DSP controller board. The macro function *init*() has been used to initialize the DAC subsystem of the DSP controller board. It has also been used to reset the interrupt request bit. The macro functions *timer*0() and *timer*1() have been used to initialize the TMS320C31's on chip timers in order to generate timer interrupts at the predefined sampling rate. The I/O macro functions have been used to read the four-channel A/D converters and to initialize the 16-bit I/O subsystem of the DSP board [103].

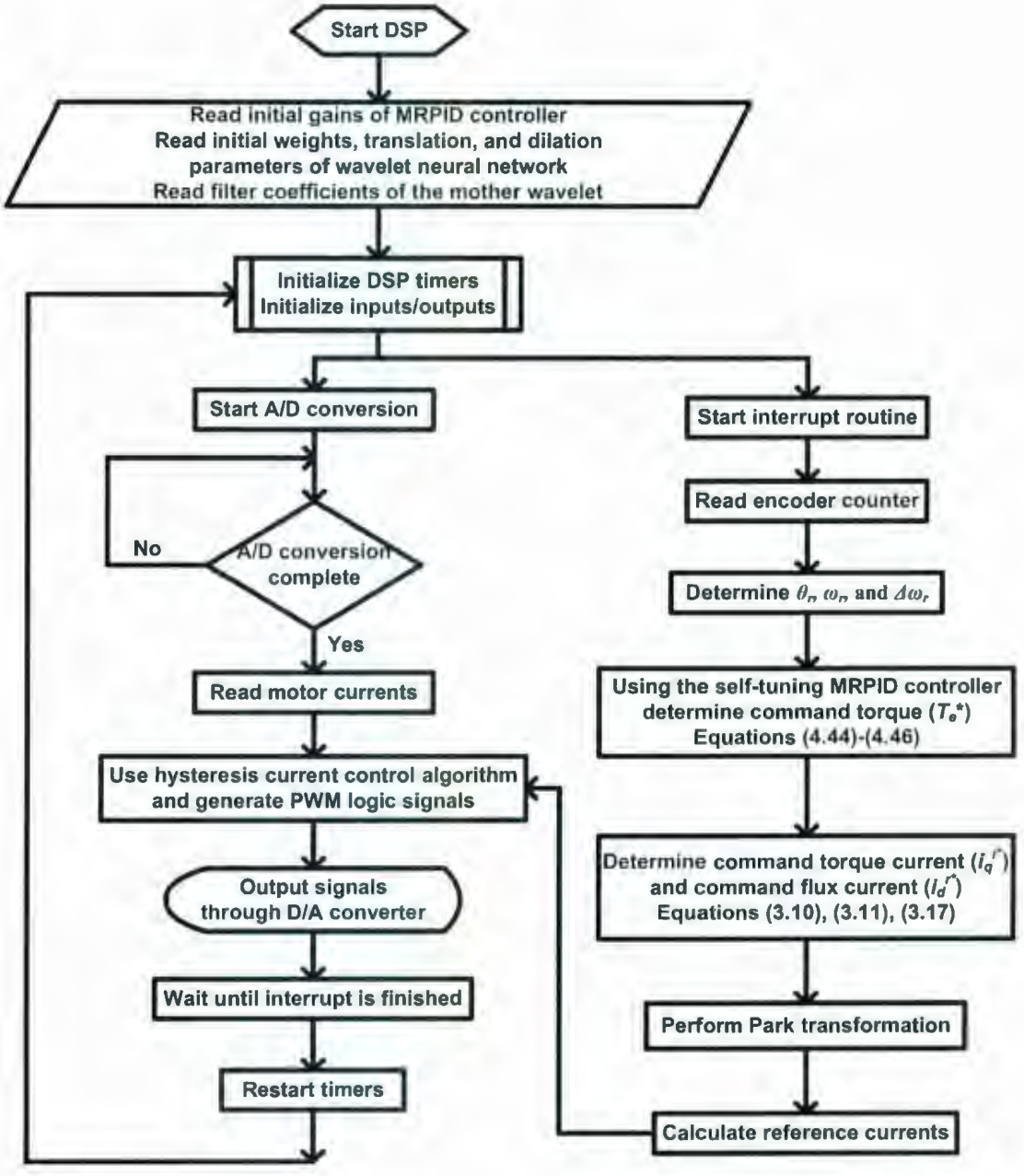

Figure 7.4: Flow chart for the real time implementation of the proposed self-tuning MRPID controller based IPMSM drive system using the dSAPCE ds1102 DSP controller board.

7.3.2 Interrupt service routine

The interrupt service routine (ISR) has been used to read the actual motor currents and to read the rotor position at the predefined sampling rate of 300 μsec. During this routine, the A/D conversions have been initialized, the rotor position has been measured, and the index line of the encoder has been generated in order to clear the counter. The incremental encoder interface of the DSP board has a 24 bit counter. The output of the optical encoder has been expanded to 4×4096 pulses per revolution using a multiplier [103]. The encoder has generated a significant index pulse at the starting of the drive system. The encoder counter has been reset to zero during the starting using a subroutine to limit the maximum rotor angle equal to 2π. The subroutine has been disabled after few seconds of the starting.

7.4 Experimental Results and Discussions

Extensive experimental tests have been carried out in real time to investigate the performances of the proposed wavelet based self-tuning MRPID control scheme for the IPMSM drive system. Tests have been performed under no load and rated load conditions at low, rated, and high command speeds. The tests have also been carried out for step changes in command speeds and for step change in load, and for parameter variations under no load and rated load conditions. An electrodynamometer has been used for the loading of the IPM motor during the laboratory performance evaluation of the proposed wavelet based self-tuning MRPID controller. The dynamometer has been connected to the shaft of the IPM motor through a coupling belt. The input knob of the dynamometer has been varied in order to change the loading of the motor. The knob has been connected to the 120 V fixed supply. When the drive has reached the steady state command speed, the control knob has been changed in a step wise manner during the step change in load on the drive system. The knob has been set to some initial value before the motor has started during the starting performance evaluations of the drive system at the rated load condition. The speed control loop of the IPMSM drive system has also been

experimentally implemented with a fixed gain PI controller in order to compare the performances with the proposed self-tuning MRPID controller based drive system. In order to make a fair judgment, the gains of the PI controller have been optimized using the Ziegler and Nichols criteria [119] for quick and smooth response of the drive system. The experimental PI controller has been optimized under the rated command speed and the rated load conditions of the IPM motor drive system. The experimental responses of the fixed gain PI controller and the proposed self-tuning MRPID controller based IPMSM drive systems have been shown in Figs. 7.5–7.22.

The experimental starting speed and current responses of the PI controller based IPMSM drive system under no load and rated command speed (188.6 rad/sec.) conditions have been in shown in Figs. 7.5(*a*) and 7.5(*b*), respectively. The experimental starting speed and current responses of the proposed self-tuning MRPID controller based IPMSM drive system under the same operating condition have been in shown in Figs. 7.6(*a*) and 7.6(*b*), respectively. The experimental starting speed and current responses of the drive system using the fixed gain PI and the self-tuning MRPID controllers have been shown in Figs. 7.7 and 7.8, respectively at rated load and rated command speed (188.6 rad/sec.) conditions. The PI controller has tracked the rated command speed of 188.6 rad/sec. in more than 1 sec. with small speed undershoot and overshoot at both no load and rated load conditions. The proposed self-tuning MRPID controller has taken less than 1 sec. to arrive at the rated command speed of 188.6 rad/sec with small speed undershoot and overshoot at both no load and rated load conditions. The PI controller based system has shown steady state speed error at both no load and rated load conditions. But the proposed self-tuning MRPID controller based system has shown small steady state speed error only at the rated load condition. Therefore, the real time starting performances of the proposed self-tuning MRPID controller have been found better than those of the PI controller based system.

The performances of the drive system have been investigated over the rated speed of the IPM motor. The experimental starting speed and current responses of the PI controller and the self-tuning MRPID controller based drive systems have been shown in

Figs. 7.9 and 7.10, respectively for the high command speed of 250 rad/sec. at no load condition. The starting speed and current responses of the fixed gain PI and the self-tuning MRPID drive systems have been shown in Figs. 7.11 and 7.12, respectively for the high command speed of 250 rad/sec. at the rated load condition. The PI controller has taken about 1 sec. to arrive at the high command speed of 250 rad/sec. at both no load and rated load conditions. The proposed controller has tracked the high command speed of 250 rad/sec. within 0.5 sec. at both no load and rated load conditions. Both PI controller and proposed self-tuning MRPID controller based systems have shown zero steady state speed error, and zero speed undershoot or overshoot for this high command speed of 250 rad/sec. Therefore, the performances of the self-tuning MRPID controller based drive system have been found faster than with the PI based system for the high command speed of 250 rad/sec. at both no load and rated load conditions. It is to be noted that the laboratory current responses of Figs. 7.5-7.8 for the rated command speed of 188.6 rad/sec. have been found lower than those of Figs. 7.9-7.12 for the high command speed of 250 rad/sec. The current responses of Figs. 7.9-7.12 have been found higher because of the higher voltage induced in the air gap for the high command speed of 250 rad/sec.

The performances of the drive have been investigated for step increase and for step decrease of command speeds at no load and rated load conditions. The speed response, the q-axis command current response, and the phase current response of the IPM motor drive system using the PI controller have been shown in Fig. 7.13 for step increase (from 130 rad/sec. to 150 rad/sec. and from 150 rad/sec. to 188.6 rad/sec.) and for step decrease (from 188.6 rad/sec. to 175 rad/sec.) of command speeds at no load condition. The speed response, the q-axis command current response, and the phase current response of the IPM motor drive system using the self-tuning MRPID controller under the same operating condition have been shown in Fig. 7.14.

The experimental performances of the IPMSM drive system using the fixed gain PI and the proposed self-tuning MRPID controllers have been shown in Figs. 7.15 and 7.16, respectively for a similar step change in command speeds at the rated load

condition. The PI controller based system responses of Figs. 7.13(a) and 7.15(a) have shown significant speed undershoots and overshoots at the instant of step changes of command speeds for both no load and rated load conditions. The proposed self-tuning MRPID controller based system responses of Figs. 7.14(a) and 7.16(a) have shown negligible speed undershoots and overshoots at the instant of step changes of command speeds for both no load and rated load conditions. However, both the PI and the MRPID based systems have generated steady state speed error at the rated load condition. The performances of the IPMSM drive system of Figs. 7.14 and 7.16 have confirmed that the proposed self-tuning MRPID controller can handle step increase and step decrease of command speeds quickly with small speed overshoot and undershoot, and with small steady state speed error at both no load and rated load conditions.

The performances of the IPMSM drive system have been experimentally investigated for a step change of load torque. Initially, the IPM motor drive has been started for the rated command speed of 188.6 rad/sec. at no load condition. After the drive system has reached the steady state command speed, the load has been changed from no load to rated load condition. The experimental speed response, the q-axis command current response, and the phase current response of the IPMSM drive system using the PI controller and the proposed self-tuning MRPID controller for a step change in load torque have been shown in Figs. 7.17 and 7.18, respectively. The proposed self-tuning MRPID controller based system has shown more robust performances than the PI controller based system for the case of sudden change of load torque. The motor speed has dropped significantly at the instant of load change for the case of the PI based drive. On the other hand, the self-tuning MRPID based system has shown almost insensitive performances for the step change in load.

The experimental performances of the PI and the proposed MRPID based drive systems have been investigated for variations of system parameters such as change in rotor inertia and change in stator winding resistance. The performance of the IPM motor drive has been investigated for change in inertia to show the effect of a high inertia machine connected to the IPM motor. The inertia of the IPM motor has been varied using

an inertia wheel connected to the shaft of the dynamometer. The inertia wheel has been connected to the shaft of the dynamometer before the drive system has started. A screw has been connected between the inner and the outer parts of the wheel. The position of the screw has been changed in order to vary the amount of inertia on the IPM motor.

Figures 7.19(*a*) and 7.19(*b*) have shown the speed and current responses of the PI controller based drive system, respectively for change in inertia under rated speed and rated load conditions. Figures 7.20(*a*) and 7.20(*b*) have shown the starting speed and current responses of the MRPID controller based drive system, respectively under the same operating condition. The PI controller based system of Fig. 7.19 has taken almost 5 sec. to arrive at the rated command speed of 188.6 rad/sec. with large steady state speed error. On the other hand, the proposed self-tuning MRPID controller based system of Fig. 7.20 has taken almost 3 sec. to reach the rated command speed of 188.6 rad/sec. with small steady state speed error under the same operating condition.

In an IPM motor, the copper loss dissipates as heat in the stator winding. The heat increases the temperature of the stator winding. So, the stator winding resistance of the IPM motor changes with change in temperature. The performances of the IPM motor drive system have been investigated for change in stator resistance. The per phase stator resistance of the IPM motor has been changed by connecting an external resistance between the BJT inverter and the IPM motor. The value of this resistance, which is six times the original per phase resistance, has been chosen arbitrarily. The experimental performances of the IPMSM drive system using the PI controller and the proposed self-tuning MRPID controller for change in stator resistance ($R_1 = 6*R$) have been shown in Figs. 7.21 and 7.22, respectively under rated load and rated speed conditions. The proposed MRPID controller based drive system of Fig. 7.22 has tracked the command speed within 1 sec. But the PI controller based system of Fig. 7.21 has taken 2 sec. under the same operating condition.

It is to be mentioned that both PI and MRPID based systems of Figs. 7.5–7.22 have generated noise and spikes in the phase current responses of the drive system for different operating conditions at no load and rated load conditions. These noise and

spikes have been generated due to the non-sinusoidal flux distribution in air gap during the real time implementation. The non-sinusoidal flux distribution has contributed ripples in the electromagnetic torque of the IPM motor. Due to the electromagnetic torque ripple, the motor has faced vibration during the normal operating condition. The vibrations have generated noise and spikes in the phase current responses of the IPM motor drive system of Figs. 7.5–7.22. The dc offsets have also been noted in the current responses of Figs. 7.5-7.22. These dc offsets have been created due to the offset of current transformers, which have been connected in series with the IPM motor for sensing the actual current.

It has been established from the test results of Figs. 7.5–7.22 that the proposed self-tuning MRPID controller can track a command speed quickly and smoothly with small steady state speed error, and small speed undershoot and overshoot for different dynamic operating conditions of the IPM motor drive system. On the other hand, the PI controller has shown significant speed overshoots and undershoots, and large steady state speed error under the identical operating conditions of the IPMSM drive. In addition, the starting responses of the PI controller based system have been found slower than with the proposed self-tuning MRPID controller based system. The proposed self-tuning MRPID controller has generated the necessary command torque quickly to operate the drive for different conditions such as step changes in command speeds, step change in load torque, and parameter variations. Thus, the proposed self-tuning MRPID based IPMSM drive system has been found superior to the conventional PI controller based drive system. The proposed self-tuning MRPID controller has also been found a robust controller for wide spread applications in high performance industrial motor drive systems. It is to be noted that the symbols Y1 and Y2 of Figs. 7.5–7.12, Figs. 7.19–7.22 have been used to represent the speed response and the phase current response, respectively. It is also to be mentioned that the symbols Y1, Y2, and Y3 of Figs. 7.13–7.18 have been used to represent the speed response, the q-axis command current response, and the phase current response of the IPMSM drive system, respectively.

The laboratory time performance test responses of the IPM motor drive system have been found slower than the simulated performances because of the limitation of the sampling frequency of the ds1102 DSP board. The maximum sampling frequency of 3.3 kHz has been used for the real time implementation of the proposed control algorithm using the ds1102 DSP board. On the other hand, the simulation has been performed using the m-file format of the MATLAB software package. The MATLAB software has been installed on a Microsoft XP 32 bit operating system with the clock frequency equal to 1.16 GHz. Moreover, the difference between simulated and laboratory performance test results have been due to use of a simplified model of the voltage source inverter (VSI) during the simulation. In the simplified model of the VSI, the inverter switching losses have been ignored.

The comparative performances of the IPMSM drive system using the PI controller, the fixed gain MRPID controller, and the proposed WNN based self-tuning MRPID controller have been given in Tables 7.1–7.4. The rise time, speed overshoot/undershoot, and steady state speed error of the IPM drive system have been used in the comparative analysis. The starting performance characteristics of the fixed gain and proposed controllers based IPM motor drive system have been shown in Table 7.1 for the rated command speed of 188.6 rad/sec. at both no load and rated load conditions. The starting performance characteristics of the fixed gain and proposed controllers have been shown in Table 7.2 for the high command speed of 250 rad/sec. at both no load and rated load conditions. The step change in load performance characteristics of the fixed gain and proposed controllers have been shown in Table 7.3 for the rated command speed of 188.6 rad/sec. at both no load and rated load conditions. The starting performance characteristics of the fixed gain and proposed controllers for change in inertia have been shown in Table 7.4 for the rated command speed of 188.6 rad/sec at both no load and rated load conditions.

The proposed self-tuning MRPID controller has shown better performances than the PI and fixed gain MRPID controllers in Tables 7.1–7.4. The proposed controller has provided faster response and has shown smaller steady state speed error than the PI and

fixed gain MRPID controllers in all cases. It has also provided smaller speed overshoot/undershoot than the fixed gain controllers. However, the proposed controller has shown higher speed undershoot and overshoot than the PI controller in Tables 7.1 and 7.4 for the change in inertia at the rated load condition. But the overall performances of the proposed self-tuning MRPID controller have been found better than the fixed gain controllers. The harmonics of phase current response of the drive system have been investigated. The harmonic spectra of the phase current of the IPMSM drive system using the fixed gain PI controller and the proposed self-tuning MRPID controller have been shown in Figs. 7.23(*a*) and 7.23(*b*), respectively. The phase current response using the fixed gain PI controller has significant second and third harmonics of fundamental current as shown in Fig. 7.23(*a*). On the other hand, the phase current response of Fig. 7.23(*b*) using the proposed self-tuning MRPID controller has generated second harmonic only.

Table 7.1: Starting Performance Comparisons of the IPMSM Drive System at the Rated Command Speed of 188.6 rad/sec.

Type of Controllers	Unloaded Condition			Loaded Condition		
	Rise Time (sec.)	% Overshoot/ Undershoot	Steady State Error (rad/sec.)	Rise Time (sec.)	% Overshoot/ Undershoot	Steady State Error (rad/sec.)
PI	0.95	2.02	6	1.36	0.87	15
Fixed Gain MRPID	2.23	7.64	2	2.12	9.45	2
Self Tuning MPRID	0.95	0	2	0.95	2.12	4

Table 7.2: Starting Performance Comparisons of the IPMSM Drive System at the High Command Speed of 250 rad/sec.

Type of Controllers	Unloaded Condition			Loaded Condition		
	Rise Time (sec.)	% Overshoot/ Undershoot	Steady State Error (rad/sec.)	Rise Time (sec.)	% Overshoot/ Undershoot	Steady State Error (rad/sec.)
PI	1.25	1.58	4	1.06	0	2
Fixed Gain MRPID	0.98	5.2	2	1.02	0	4
Self Tuning MPRID	0.87	0	0	0.98	0	3

Table 7.3: Performance Comparisons of the IPMSM Drive System for Step Change in Load at the Rated Command Speed of 188.6 rad/sec.

Type of Controllers	% Overshoot/ Undershoot	Steady State Error (rad/sec.)
PI	1.91	6
Fixed Gain MRPID	0	3
Self Tuning MPRID	0	2

Table 7.4: Starting Performance Comparisons of the IPMSM Drive System for Change in Rotor Inertia at the Rated Command Speed of 188.6 rad/sec.

Type of Controllers	Unloaded Condition			Loaded Condition		
	Rise Time (sec.)	% Overshoot/ Undershoot	Steady State Error (rad/sec.)	Rise Time (sec.)	% Overshoot/ Undershoot	Steady State Error (rad/sec.)
PI	3.98	-9.4	0	5.68	-2.65	2
Fixed Gain MRPID	6.4	9.44	2	8.07	0	2
Self Tuning MPRID	3.41	-7	1	3.18	-7.7	0

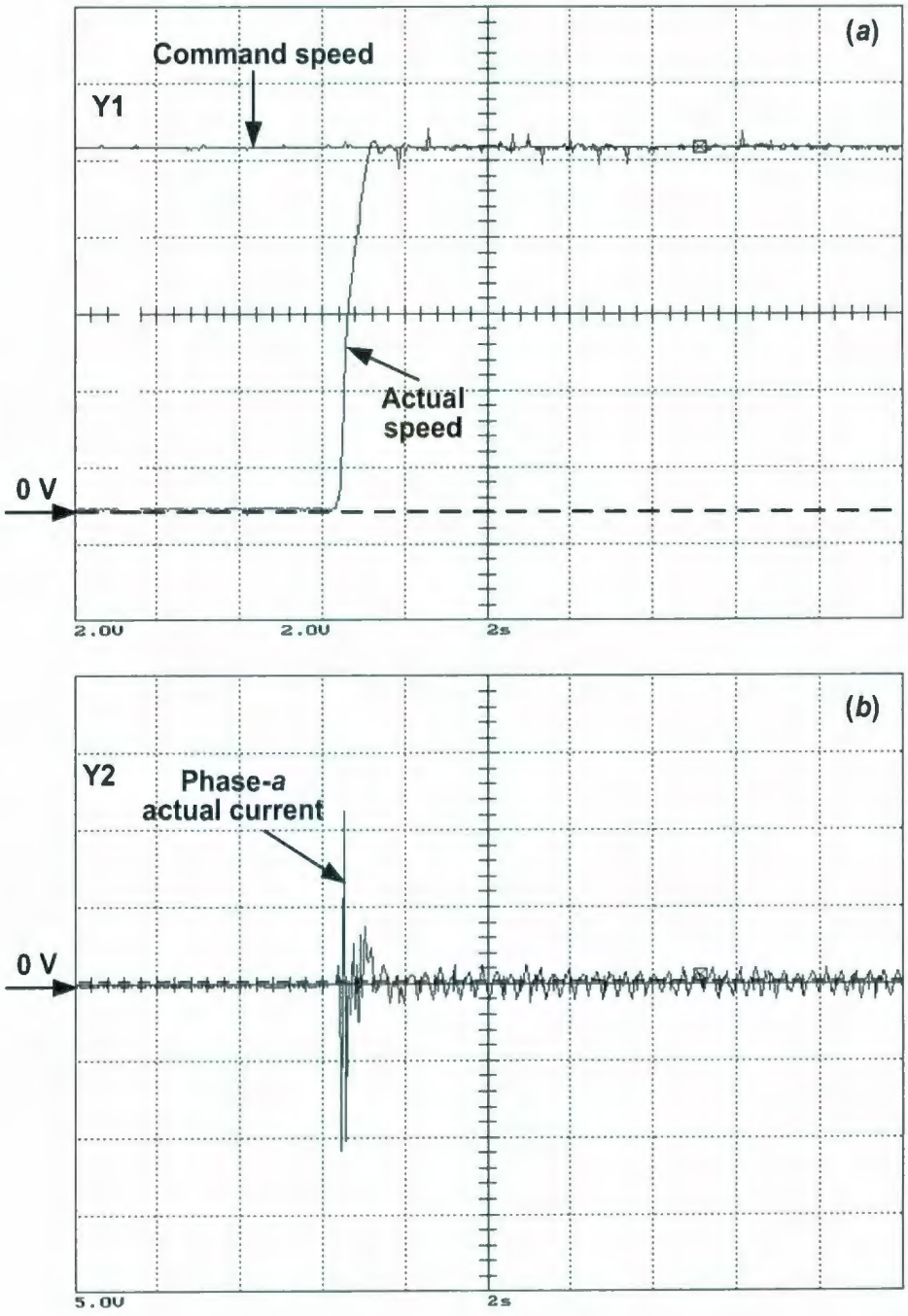

Figure 7.5: Experimental starting responses of the fixed gain PI controller based IPMSM drive system under no load and rated speed (188.6 rad/sec.) conditions: (*a*) speed response (Y1: 2 V/div., 1V = 20 rad/sec., time: 2 sec./div.) and (*b*) current response (Y2: 5 V/div., 1V = 0.933 A, time: 2 sec./div.).

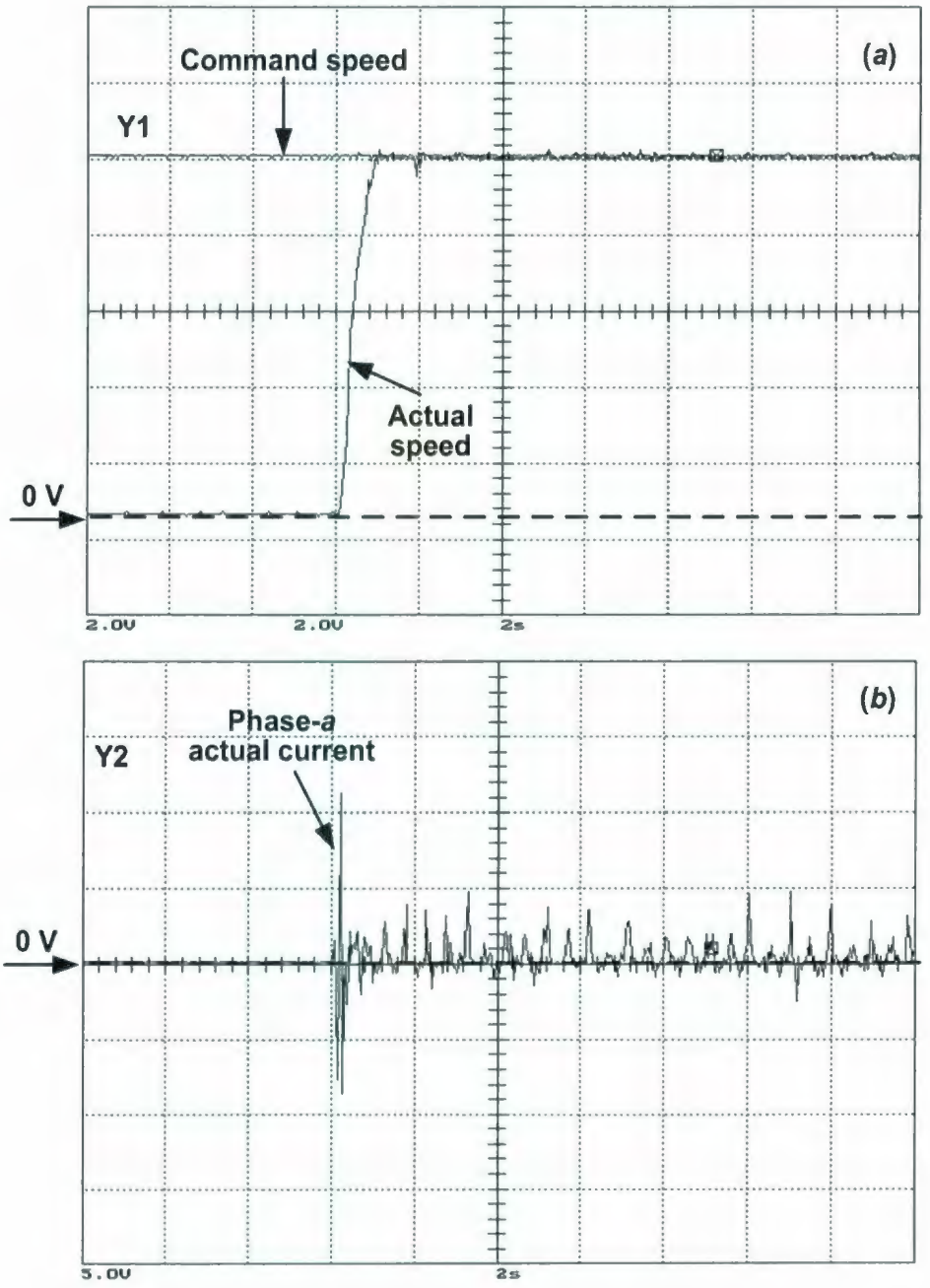

Figure 7.6: Experimental starting responses of the proposed self-tuning MRPID controller based IPMSM drive system under no load and rated speed (188.6 rad/sec.) conditions: (*a*) speed response (Y1: 2 V/div., 1V = 20 rad/sec., time: 2 sec/div.) and (*b*) current response (Y2: 5 V/div., 1V = 0.933 A, time: 2 sec/div.).

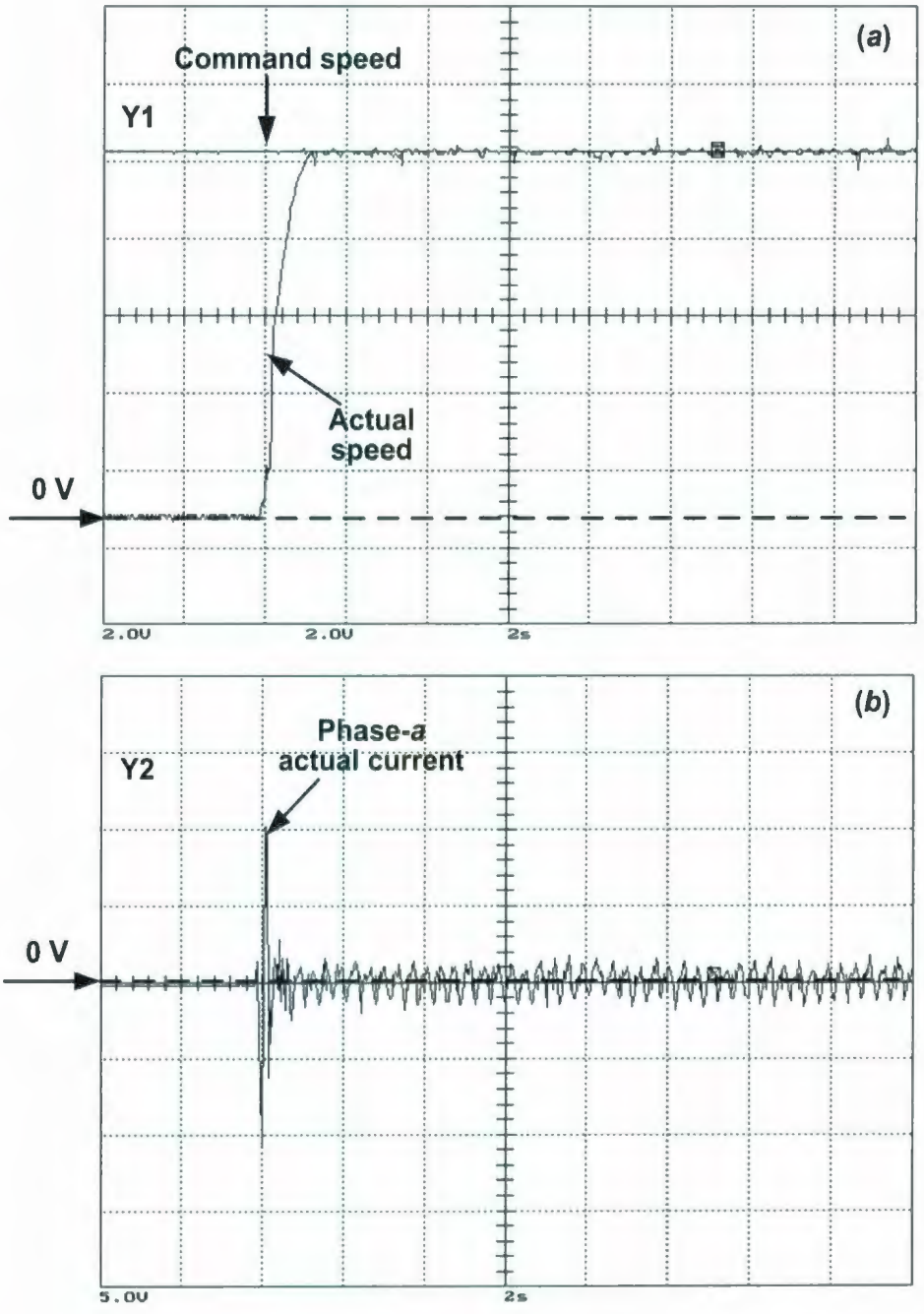

Figure 7.7: Experimental starting responses of the fixed gain PI controller based IPMSM drive system under rated load and rated speed (188.6 rad/sec.) conditions: (*a*) speed response (Y1: 2 V/div., 1V = 20 rad/sec., time: 2 sec/div.) and (*b*) current response (Y2: 5 V/div., 1V = 0.933 A, time: 2 sec/div.).

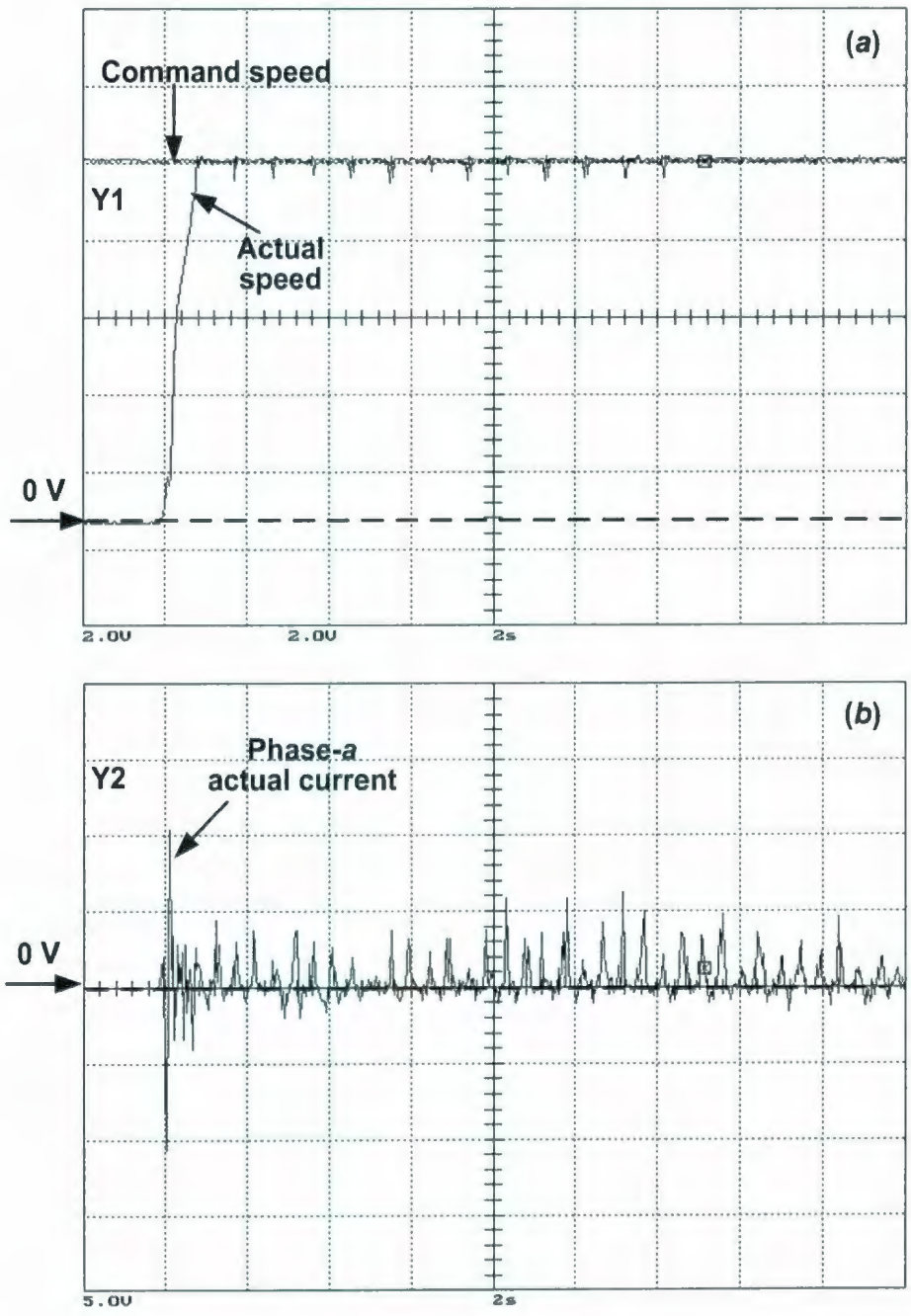

Figure 7.8: Experimental starting responses of the proposed self-tuning MRPID controller based IPMSM drive system under rated load and rated speed (188.6 rad/sec.) conditions: (*a*) speed response (Y1: 2 V/div., 1V = 20 rad/sec., time: 2 sec/div.) and (*b*) current response (Y2: 5 V/div., 1V = 0.933 A, time: 2 sec/div.).

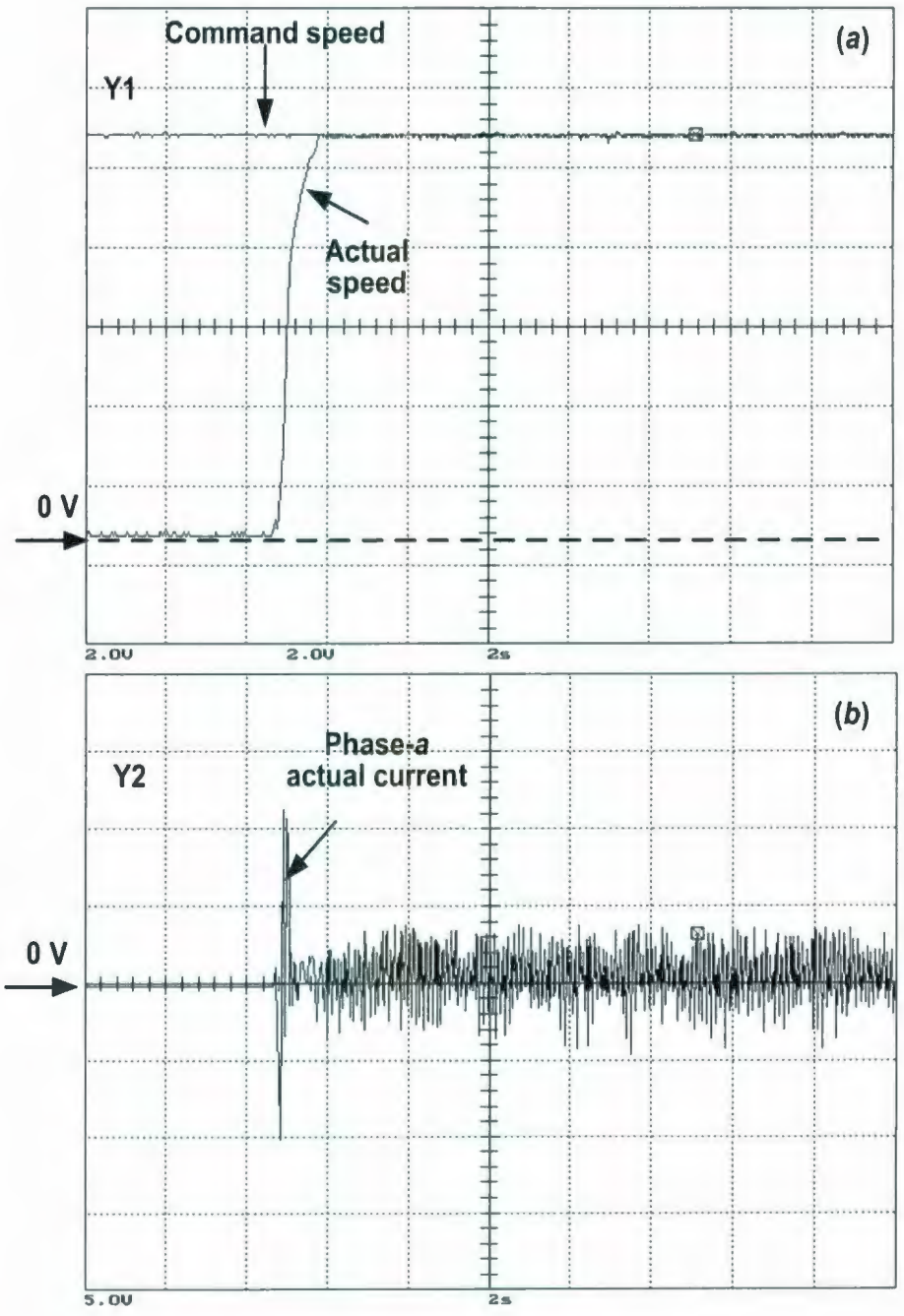

Figure 7.9: Experimental starting responses of the fixed gain PI controller based IPMSM drive system under no load and high speed (250 rad/sec.) conditions: (*a*) speed response (Y1: 2 V/div., 1V = 25 rad/sec., time: 2 sec/div.) and (*b*) current response (Y2: 5 V/div., 1V = 0.933 A, time: 2 sec/div.).

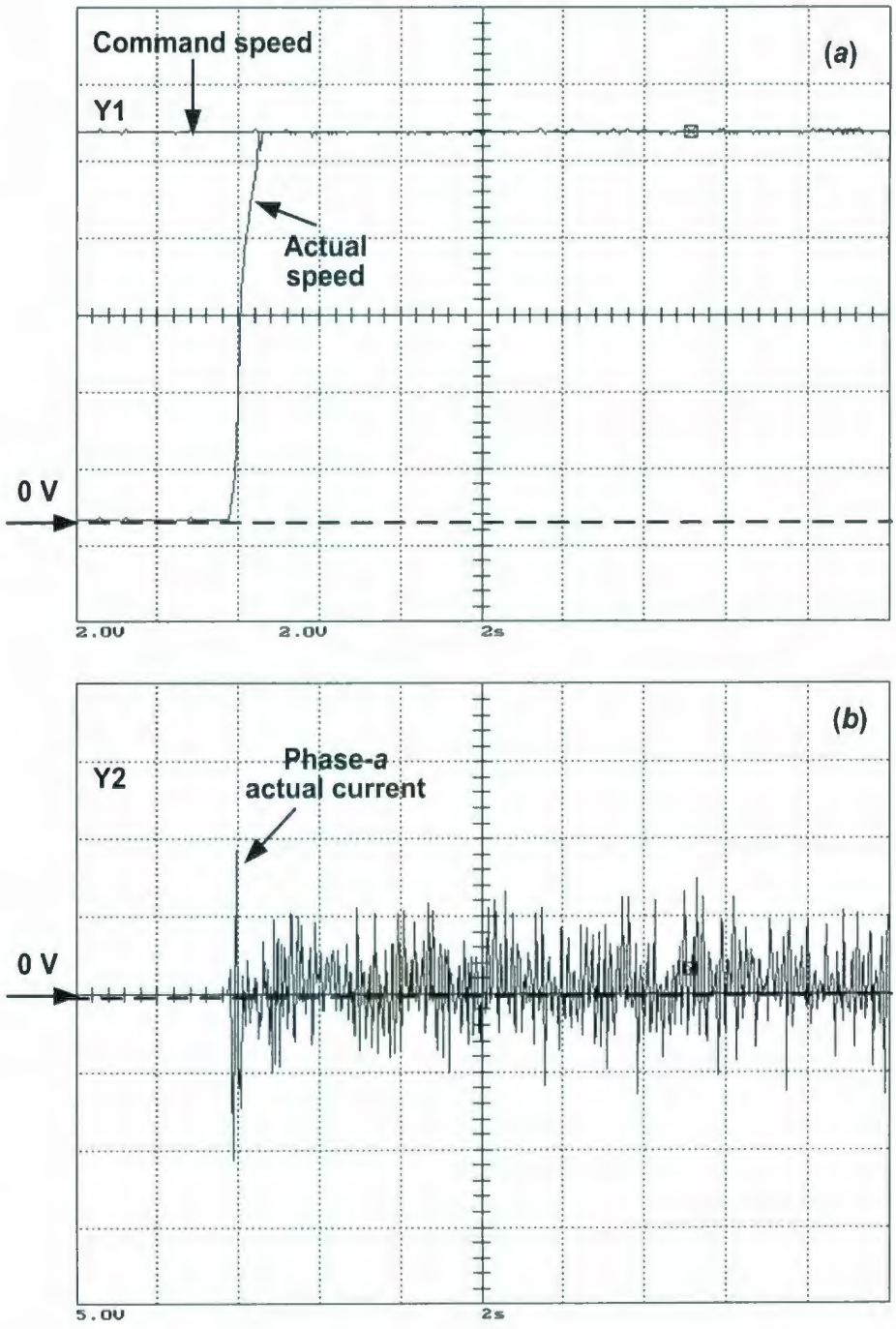

Figure 7.10: Experimental starting responses of the proposed self tuning MRPID controller based IPMSM drive system under no load and high speed (250 rad/sec.) conditions: (*a*) speed response (Y1: 2 V/div., 1V = 25 rad/sec., time: 2 sec/div.) and (*b*) current response (Y2: 5 V/div., 1V = 0.933 A, time: 2 sec/div.).

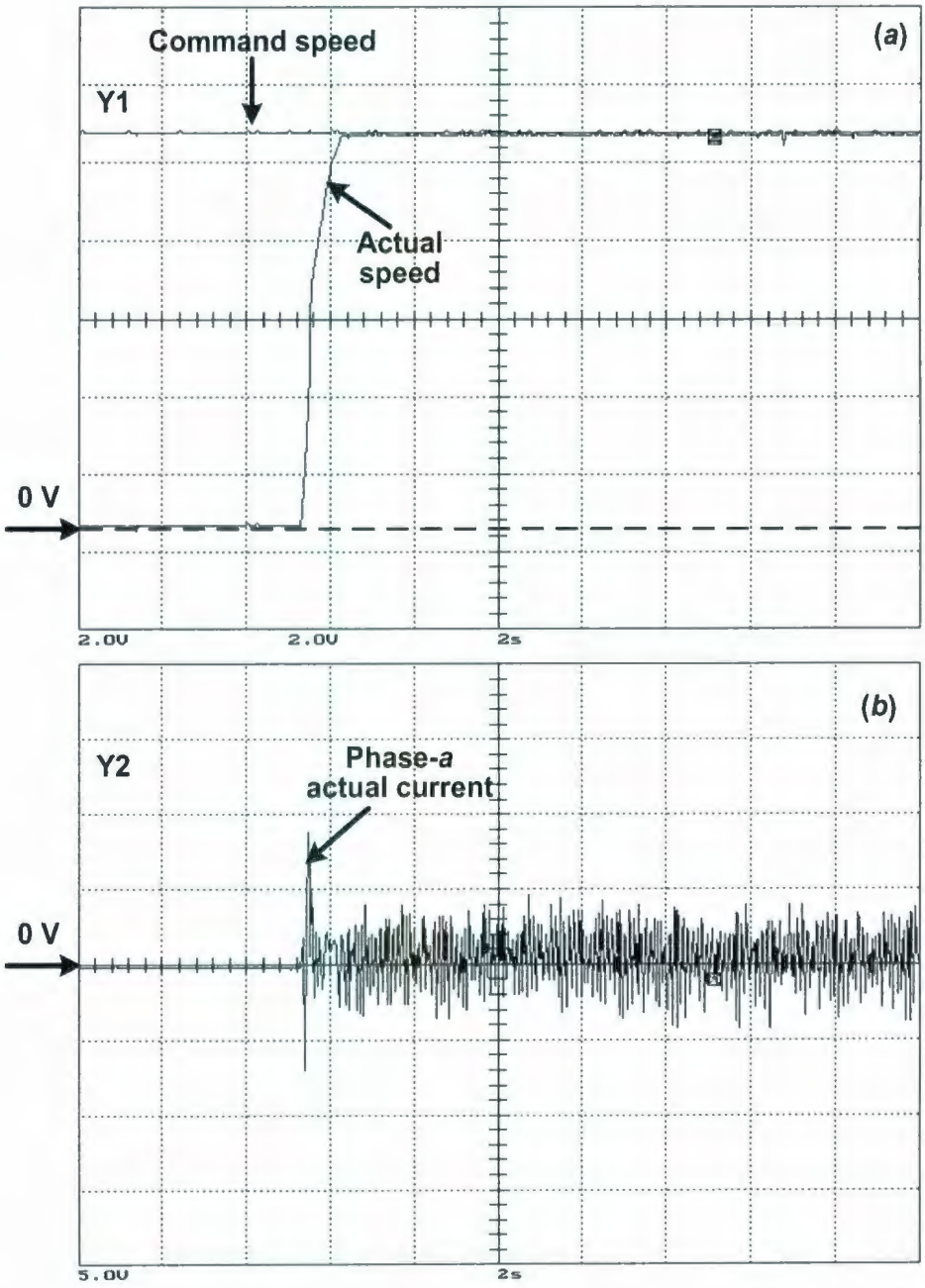

Figure 7.11: Experimental starting responses of the fixed gain PI controller based IPMSM drive system under rated load and high speed (250 rad/sec.) conditions: (*a*) speed response (Y1: 2 V/div., 1V = 25 rad/sec., time: 2 sec/div.) and (*b*) current response (Y2: 5 V/div., 1V = 0.933 A, time: 2 sec/div.).

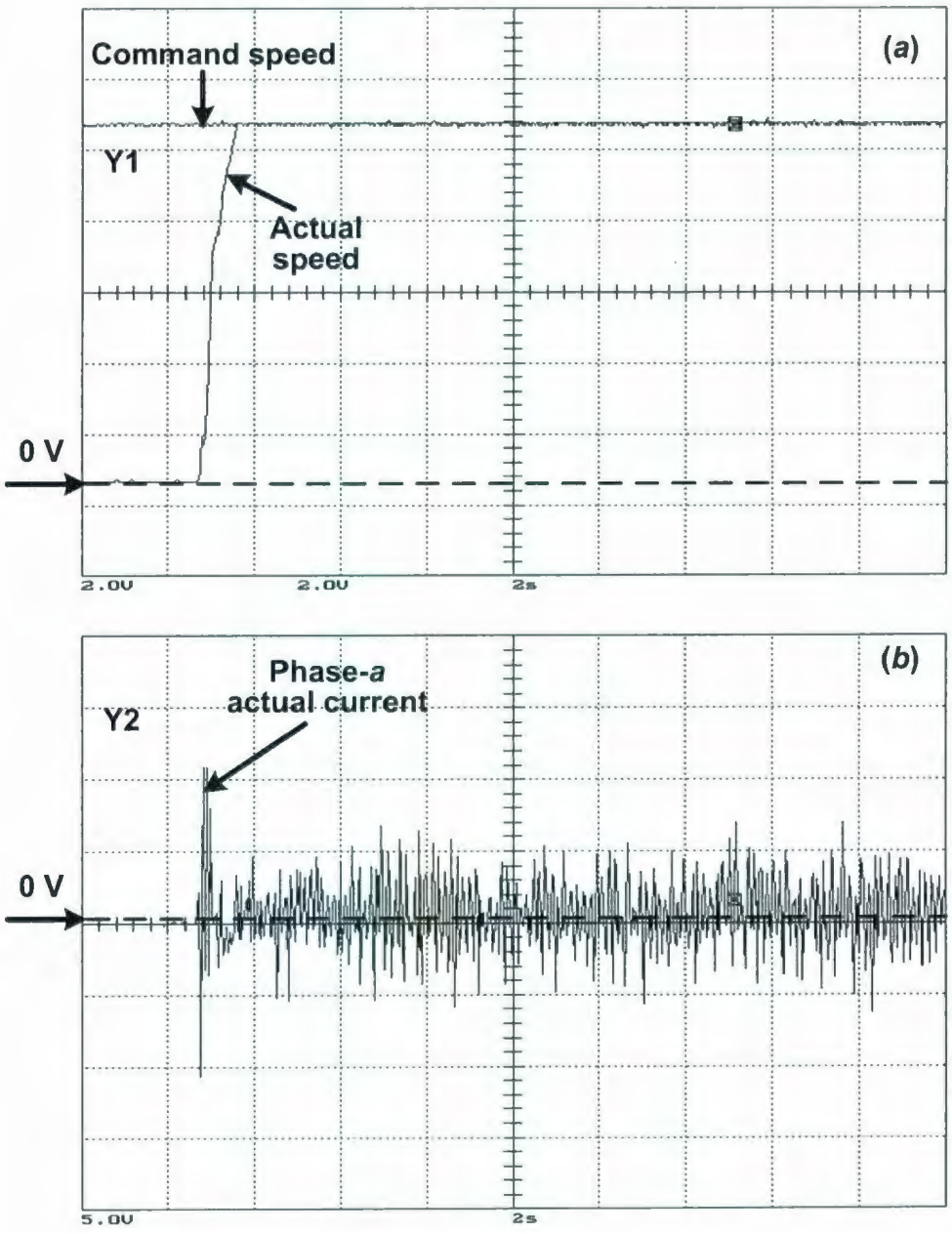

Figure 7.12: Experimental starting responses of the proposed self-tuning MRPID controller based IPMSM drive system under rated load and high speed (250 rad/sec.) conditions: (*a*) speed response (Y1: 2 V/div., 1V = 25 rad/sec., time: 2 sec/div.) and (*b*) current response (Y2: 5 V/div., 1V = 0.933 A, time: 2 sec/div.).

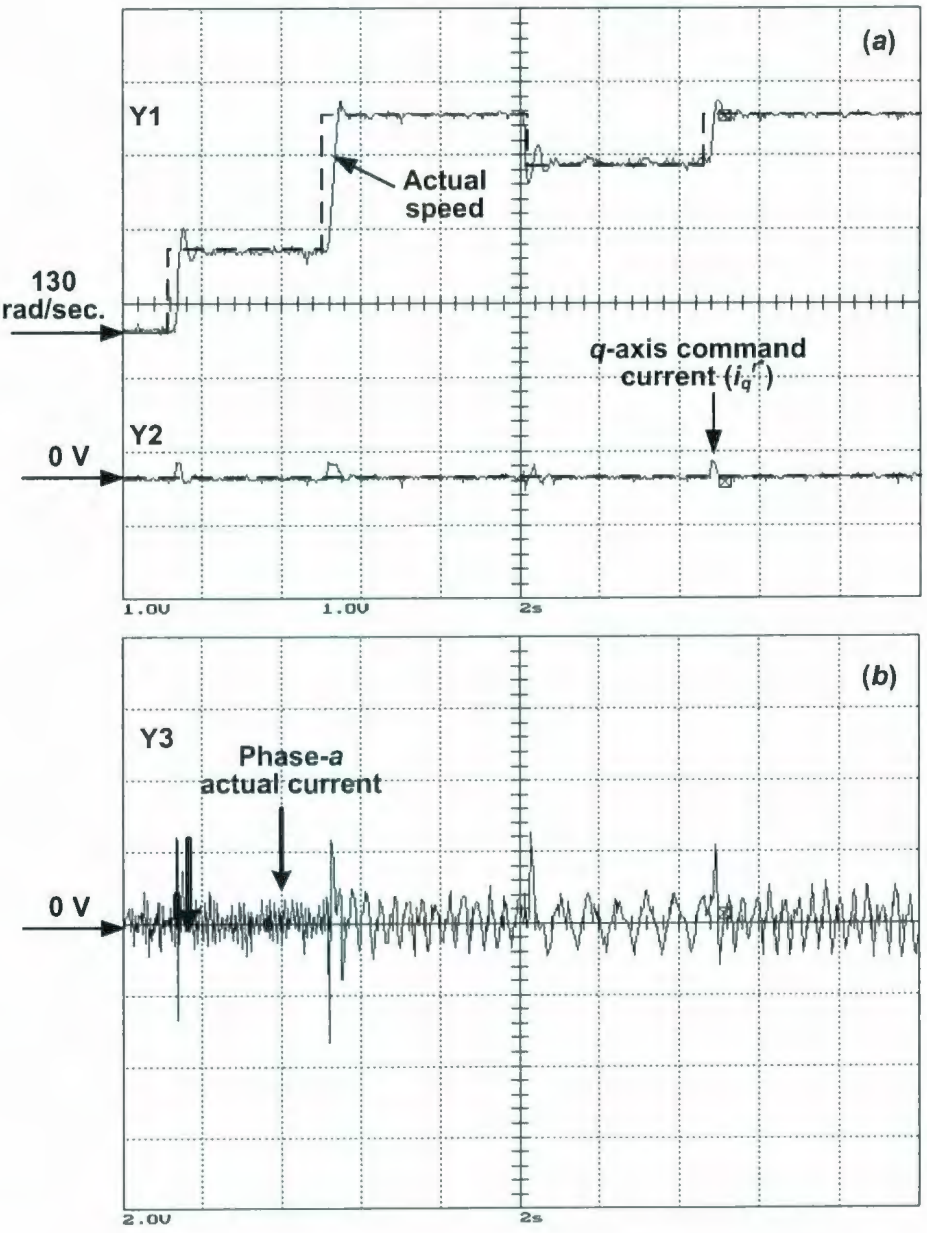

Figure 7.13: Experimental responses of the fixed gain PI controller based IPMSM drive system for step changes in command speeds (from 130 to 150 rad/sec., from 150 to 188.6 rad/sec., from 188.6 to 175 rad/sec., from 175 to 188.6 rad/sec.) at no load condition: (*a*) speed and *q*-axis command current responses (Y1: 1 V/div., 1V = 20 rad/sec., Y2: 1 V/div., 1V = 1.6 A, time: 2 sec/div.) and (*b*) phase current response (Y3: 2 V/div., 1V = 0.933 A, time: 2 sec/div.).

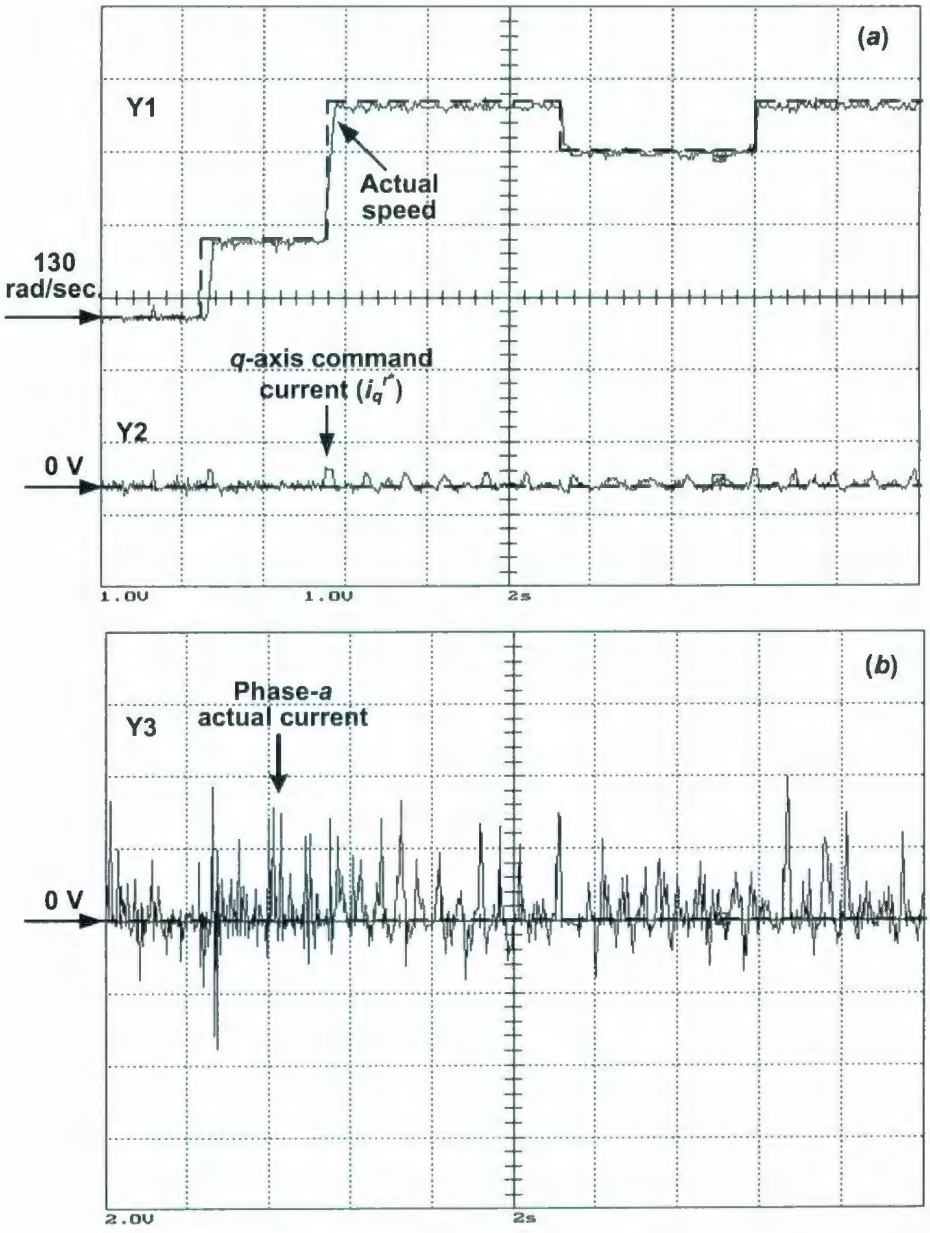

Figure 7.14: Experimental responses of the proposed self-tuning MRPID controller based IPMSM drive system for step changes in command speeds (from 130 to 150 rad/sec., from 150 to 188.6 rad/sec., from 188.6 to 175 rad/sec., from 175 to 188.6 rad/sec.) at no load condition: (*a*) speed and *q*-axis command current responses (Y1: 1 V/div., 1V = 20 rad/sec., Y2: 1 V/div., 1V = 1.6 A, time: 2 sec/div.) and (*b*) phase current response (Y3: 2 V/div., 1V = 0.933 A, time: 2 sec/div.).

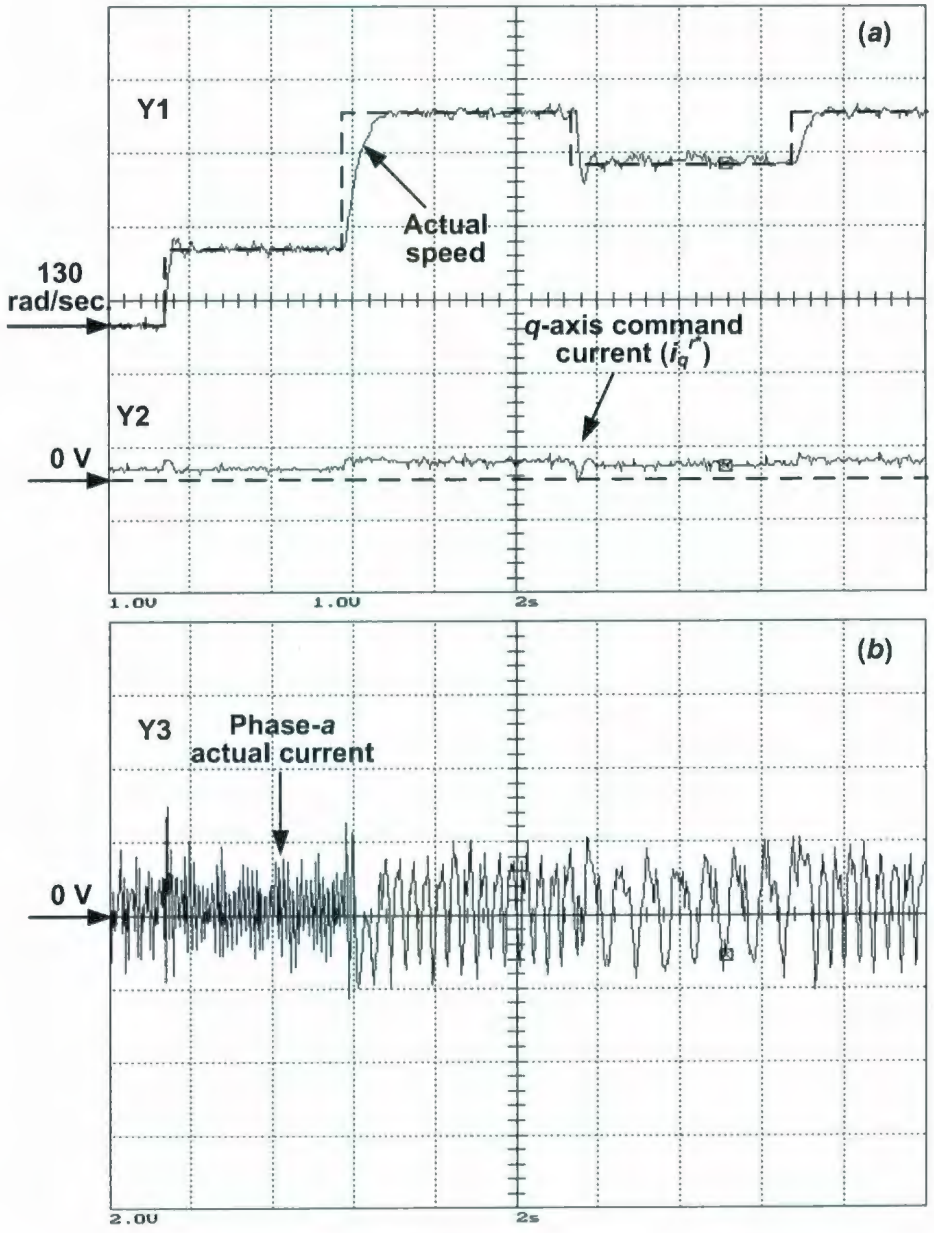

Figure 7.15: Experimental responses of the fixed gain PI controller based IPMSM drive system for step changes in command speeds (from 130 to 150 rad/sec., from 150 to 188.6 rad/sec., from 188.6 to 175 rad/sec., from 175 to 188.6 rad/sec.) at rated load condition: (*a*) speed and *q*-axis command current responses (Y1: 1 V/div., 1V = 20 rad/sec., Y2: 1 V/div., 1V = 1.6 A, time: 2 sec/div.) and (*b*) phase current response (Y3: 2 V/div., 1V = 0.933 A, time: 2 sec/div.).

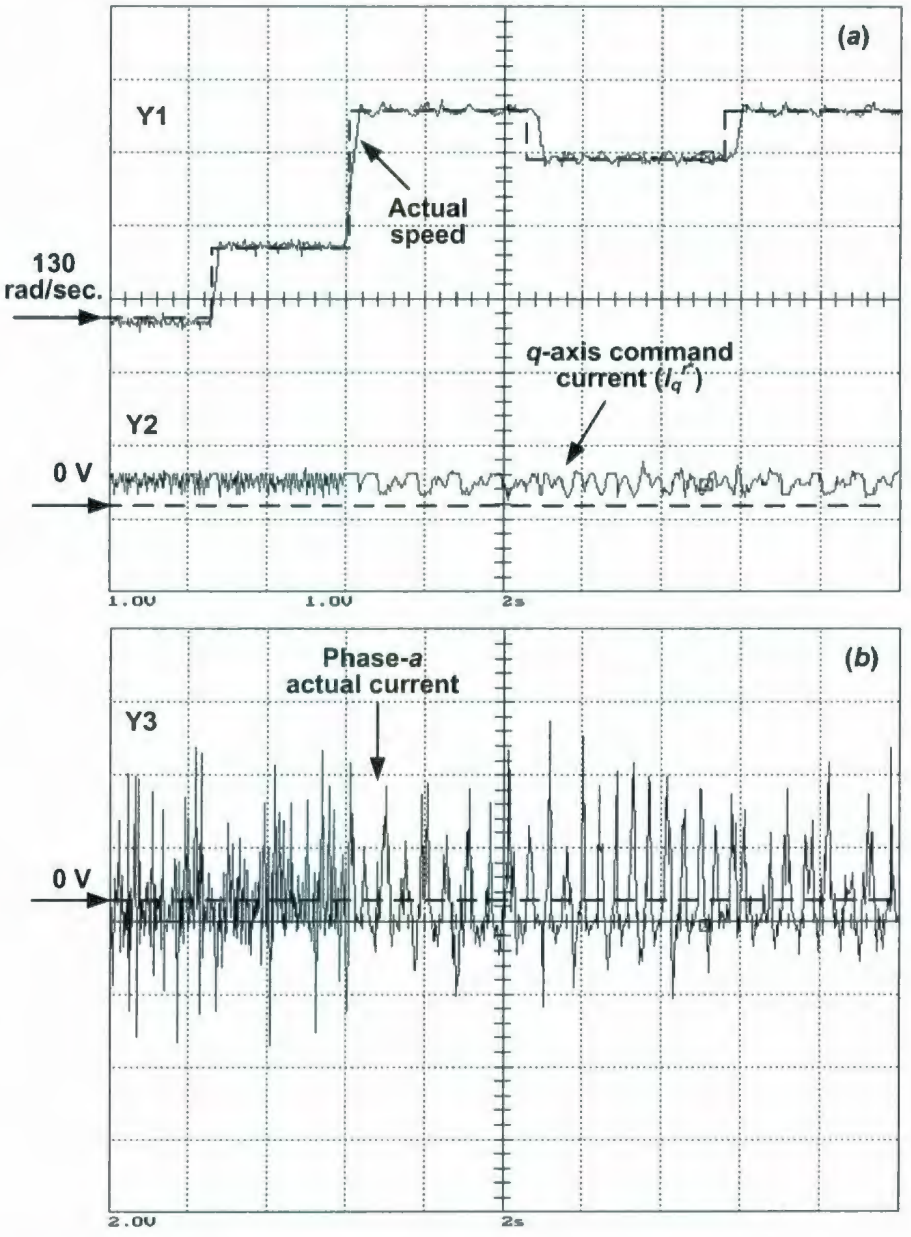

Figure 7.16: Experimental responses of the proposed self-tuning MRPID controller based IPMSM drive system for step changes in command speeds (from 130 to 150 rad/sec., from 150 to 188.6 rad/sec., from 188.6 to 175 rad/sec., from 175 to 188.6 rad/sec.) at rated load condition: (*a*) speed and *q*-axis command current responses (Y1: 1 V/div., 1V = 20 rad/sec., Y2: 1 V/div., 1V = 1.6 A, time: 2 sec/div.) and (*b*) phase current response (Y3: 2 V/div., 1V = 0.933 A, time: 2 sec/div.).

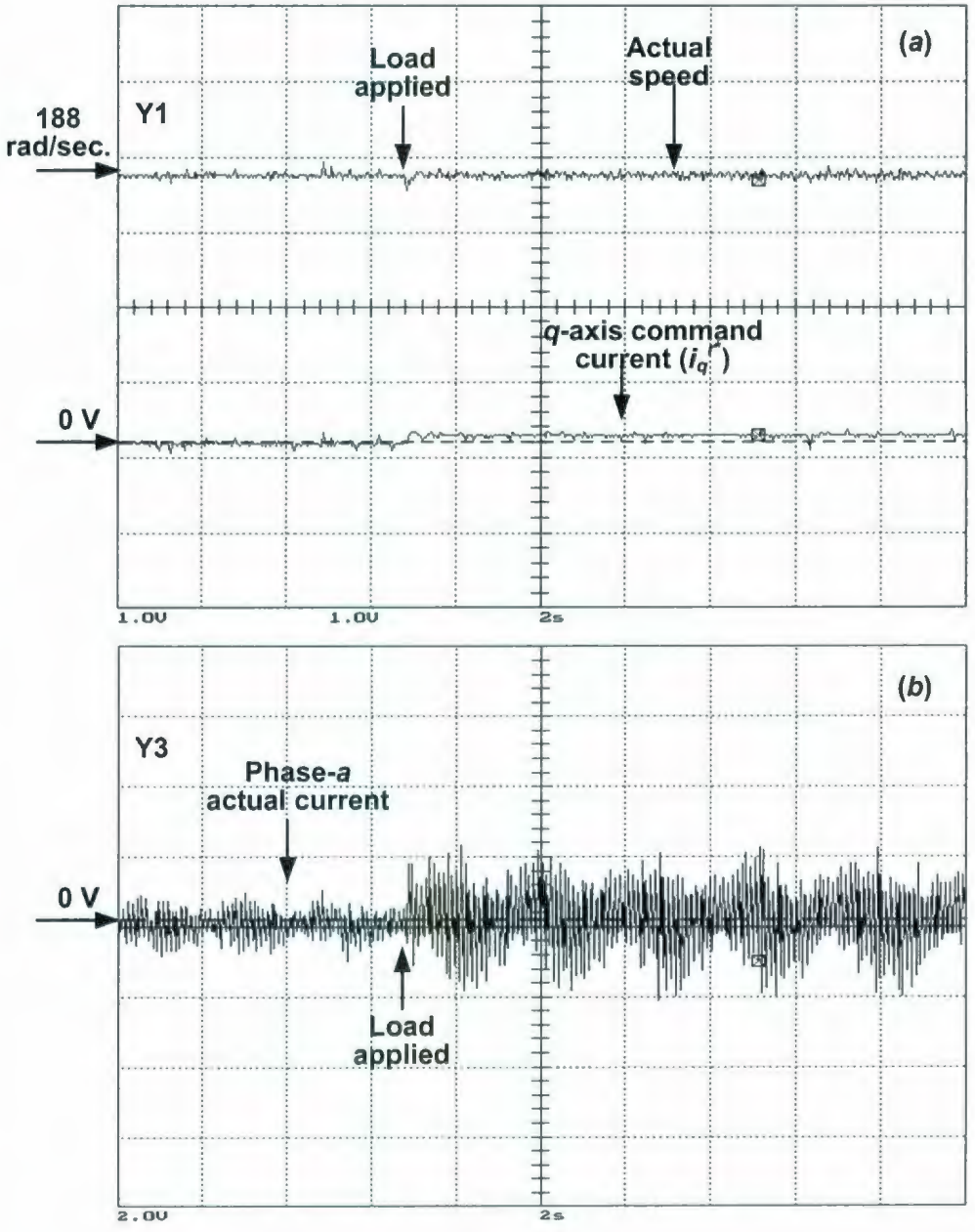

Figure 7.17: Experimental responses of the fixed gain PI controller based IPMSM drive system for a change in load at rated speed (188.6 rad/sec.) condition: (*a*) speed and *q*-axis command current responses (Y1: 1 V/div., 1V = 20 rad/sec., Y2: 1 V/div., 1V = 1.6 A, time: 2 sec/div.) and (*b*) phase current response (Y3: 2 V/div., 1V = 0.933 A, time: 2 sec/div.).

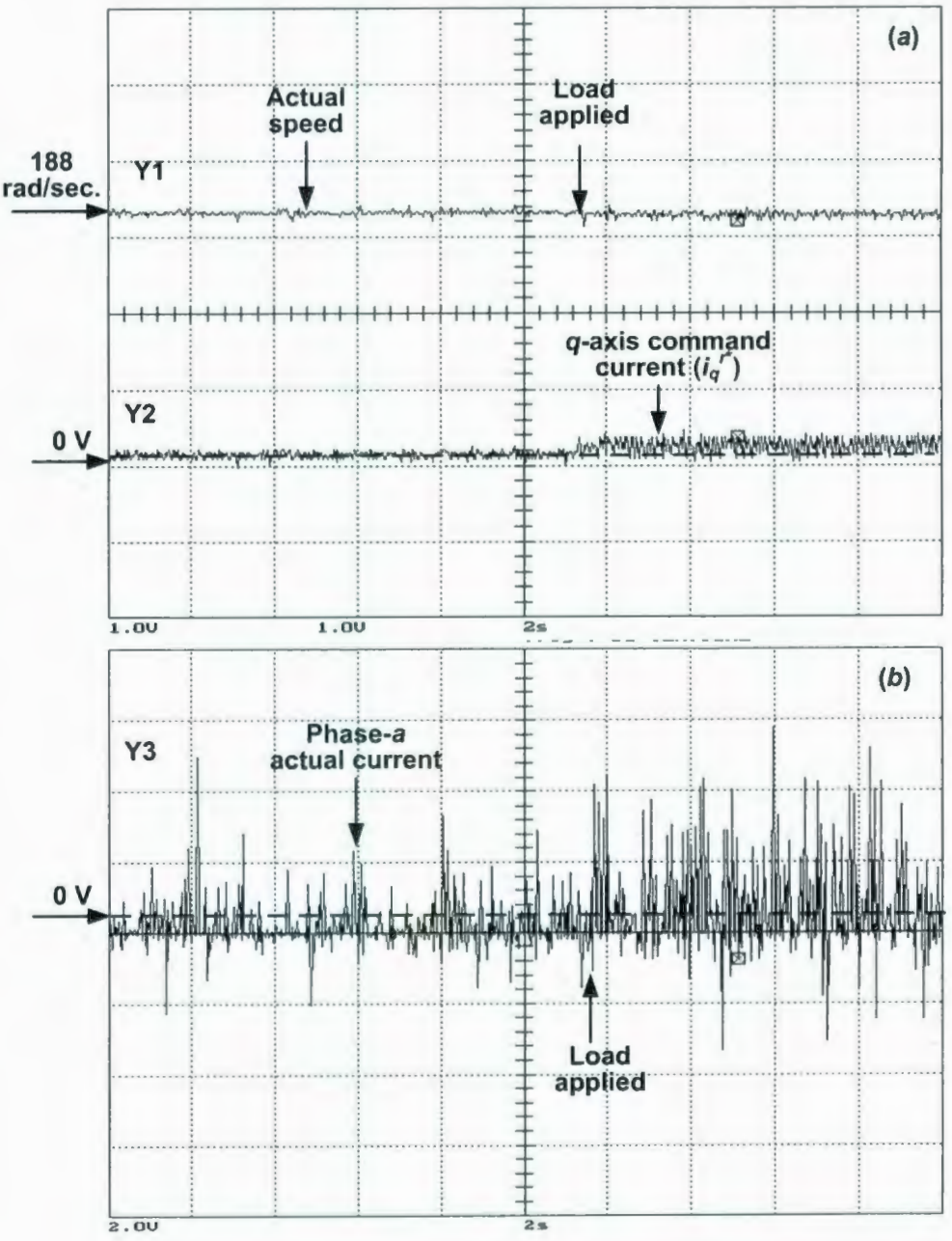

Figure 7.18: Experimental responses of the proposed self-tuning MRPID controller based IPMSM drive system for a change in load at rated speed (188.6 rad/sec.) condition: (*a*) speed and *q*-axis command current responses (Y1: 1 V/div., 1V = 20 rad/sec., Y2: 1 V/div., 1V = 1.6 A, time: 2 sec/div.) and (*b*) phase current response (Y3: 2 V/div., 1V = 0.933 A, time: 2 sec/div.).

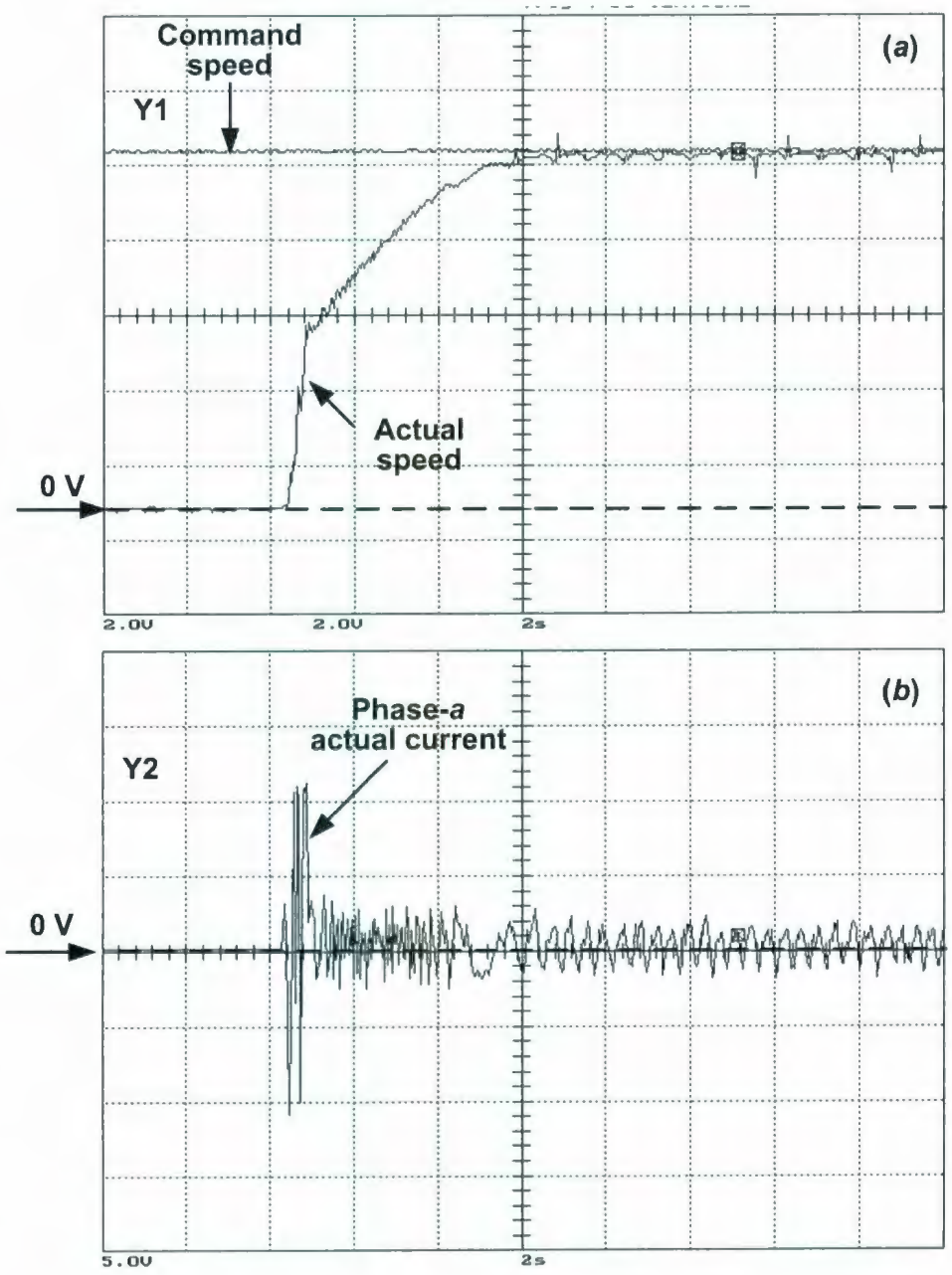

Figure 7.19: Experimental starting responses of the fixed gain PI controller based IPMSM drive system for change in rotor inertia under rated load and rated speed (188.6 rad/sec.) conditions: (*a*) speed response (Y1: 2 V/div., 1V = 20 rad/sec., time: 2 sec/div.) and (*b*) current response (Y2: 5 V/div., 1V = 0.933 A, time: 2 sec/div.).

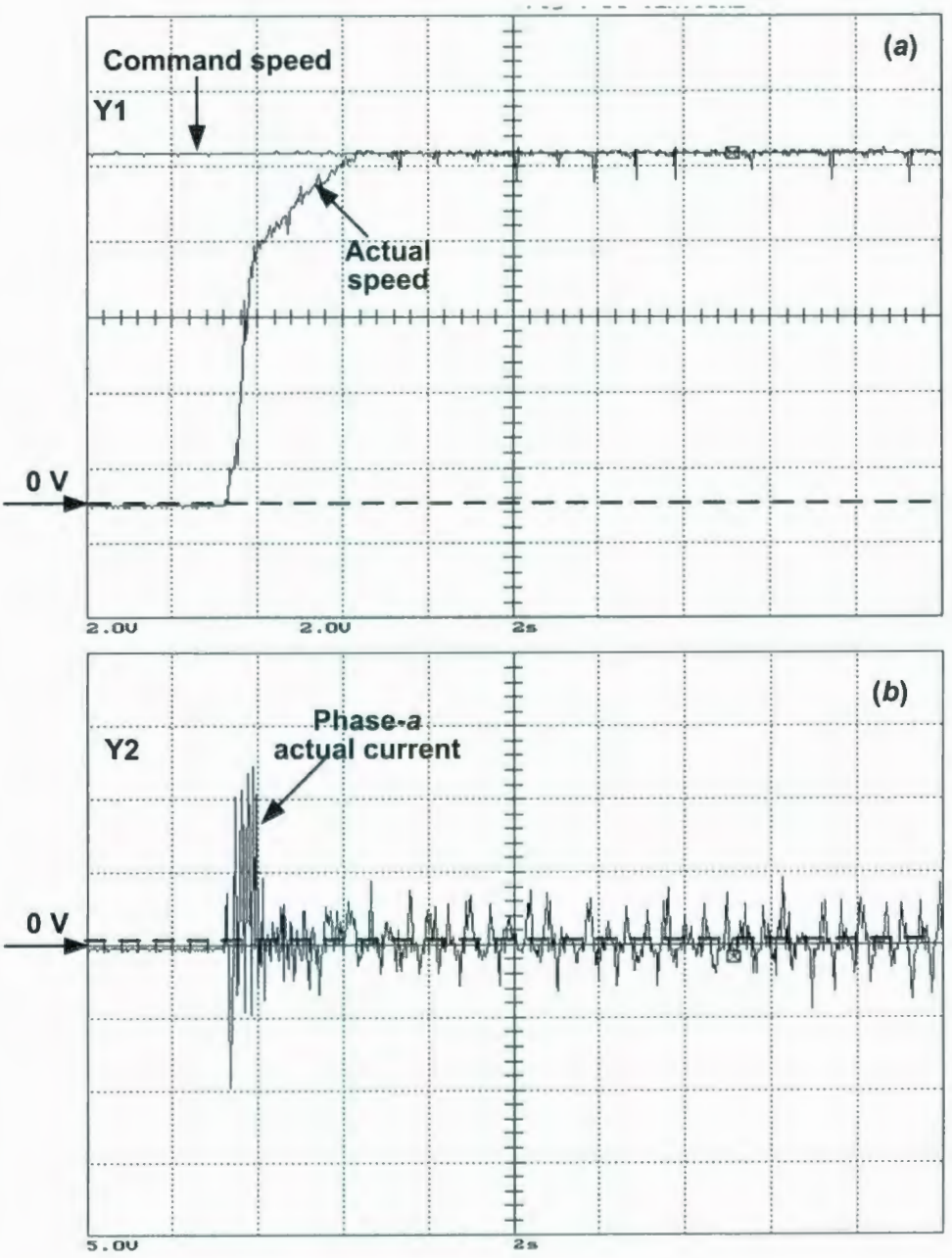

Figure 7.20: Experimental starting responses of the proposed self-tuning MRPID controller based IPMSM drive system for change in rotor inertia under rated load and rated speed (188.6 rad/sec.) conditions: (*a*) speed response (Y1: 2 V/div., 1V = 20 rad/sec., time: 2 sec/div.) and (*b*) current response (Y2: 5 V/div., 1V = 0.933 A, time: 2 sec/div.).

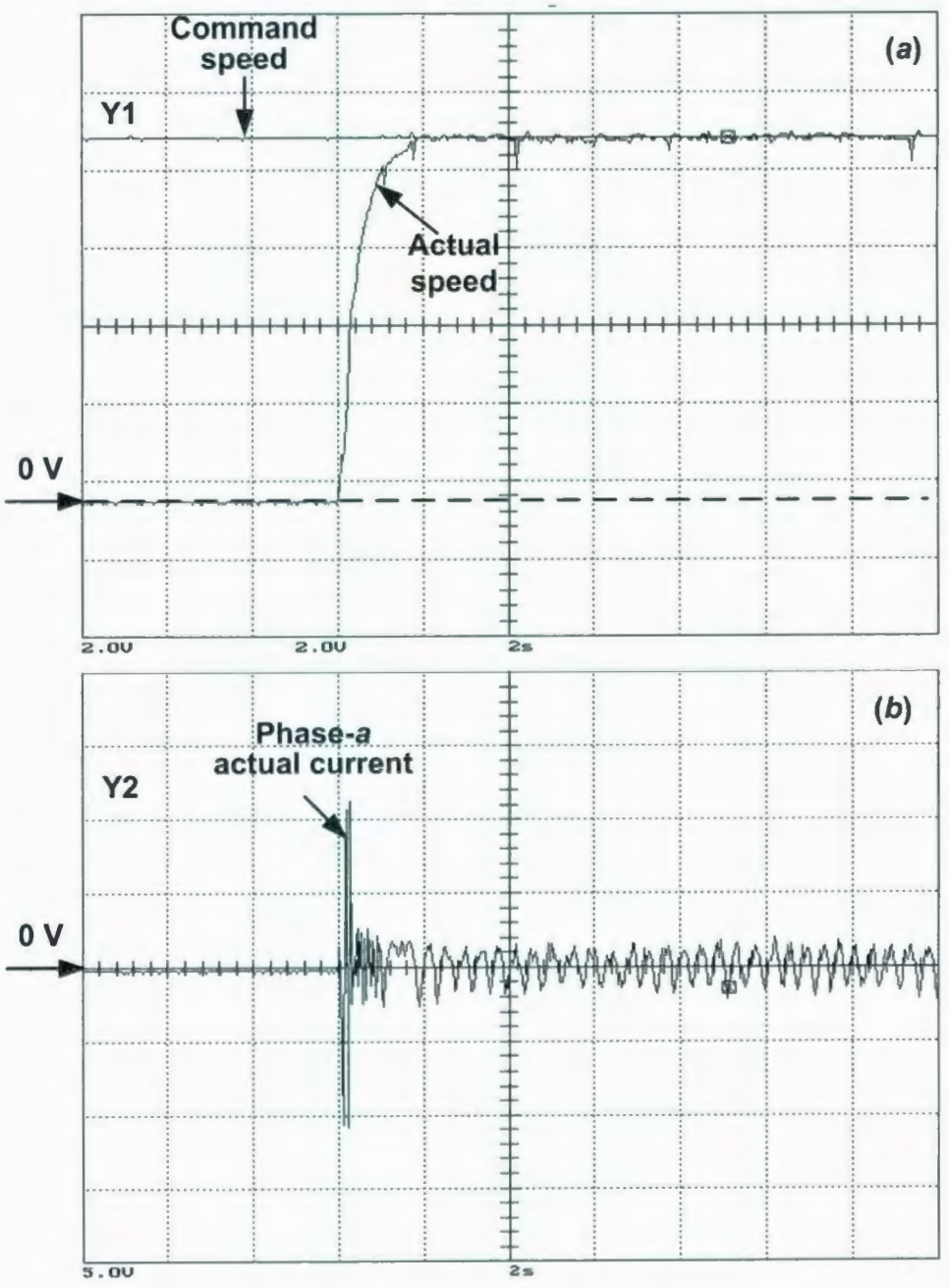

Figure 7.21: Experimental starting responses of the fixed gain PI controller based IPMSM drive system for change in stator resistance under rated load and rated speed (188.6 rad/sec.) conditions: (*a*) speed response (Y1: 2 V/div., 1V = 20 rad/sec., time: 2 sec/div.) and (*b*) current response (Y2: 5 V/div., 1V = 0.933 A, time: 2 sec/div.).

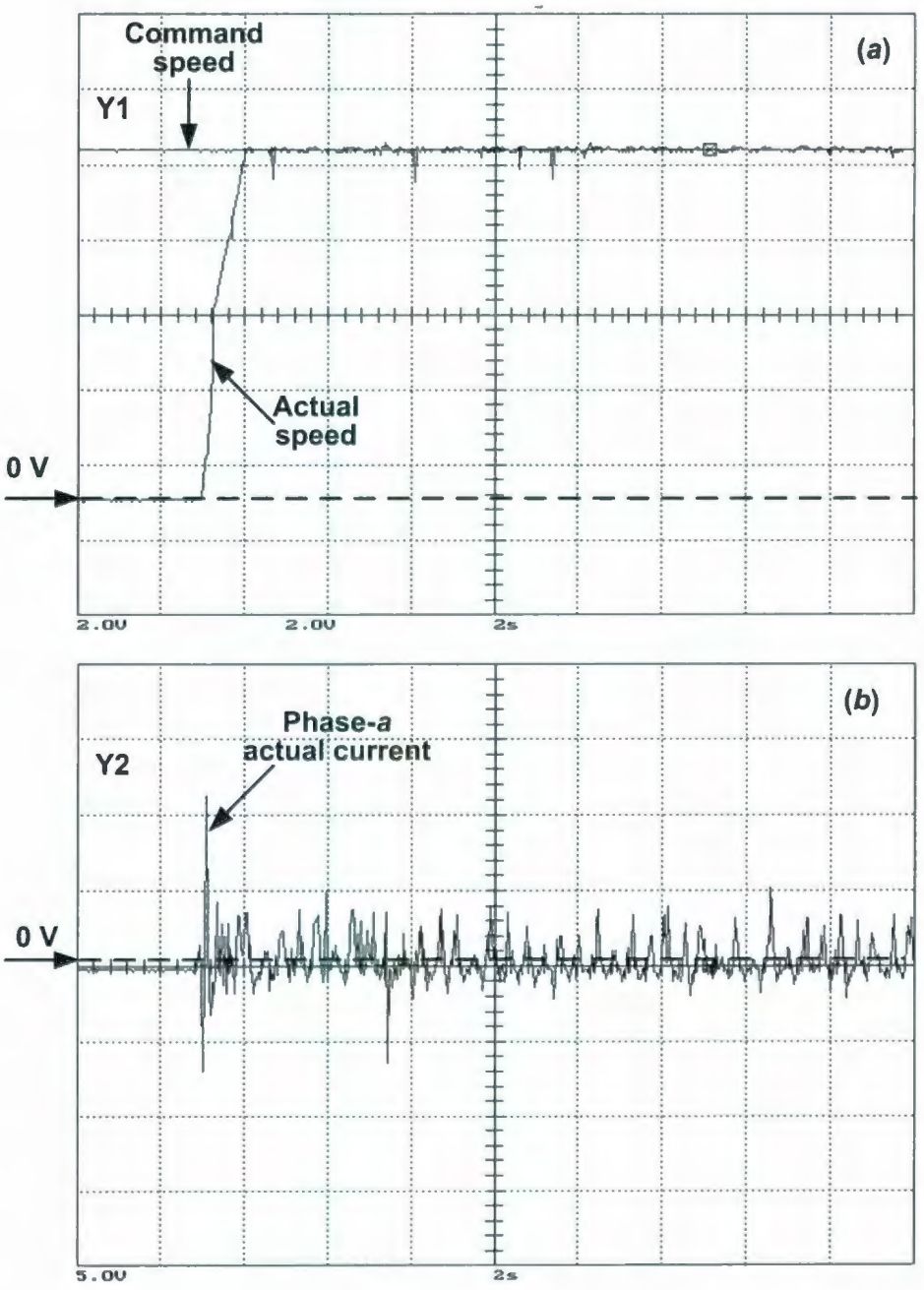

Figure 7.22: Experimental starting responses of the proposed self-tuning MRPID controller based IPMSM drive system for change in stator resistance under rated load and rated speed (188.6 rad/sec.) conditions: (*a*) speed response (Y1: 2 V/div., 1V = 20 rad/sec., time: 2 sec/div.) and (*b*) current response (Y2: 5 V/div., 1V = 0.933 A, time: 2 sec/div.).

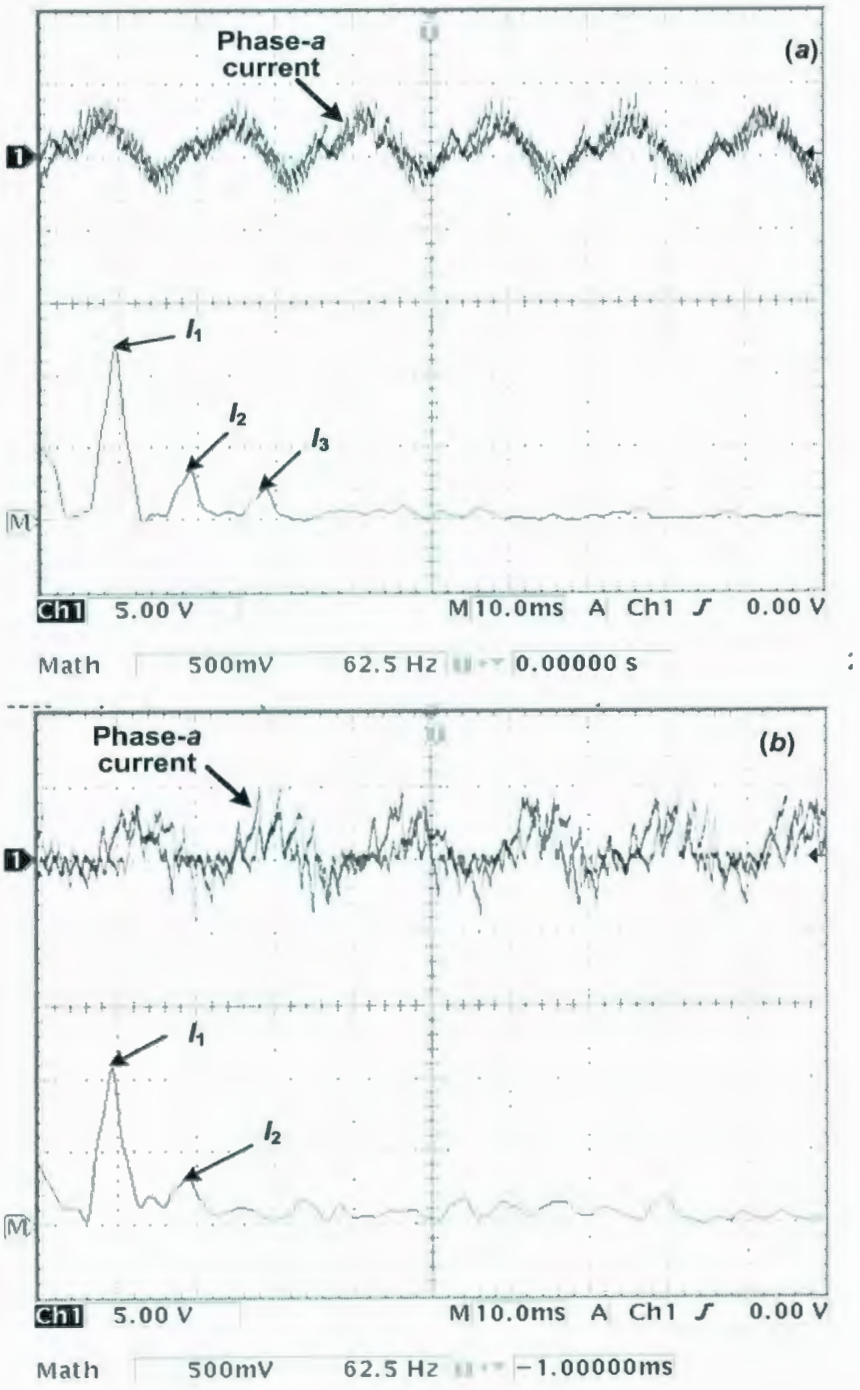

Figure 7.23: Harmonic spectra of the phase current response of the IPMSM drive system at the rated command speed and rated load conditions: (*a*) PI controller and (*b*) self-tuning MRPID controller.

7.5 Concluding Remarks

In this chapter, the wavelet neural network based self-tuning multiresolution proportional integral derivative (MRPID) controller has been successfully implemented and tested on the laboratory 1-hp interior permanent magnet synchronous motor (IPMSM). The IPMSM drive system using the proposed self-tuning MRPID controller has been experimentally implemented in real time using the ds1102 DSP controller board. The performances of the proposed drive system have been investigated at different dynamic operating conditions including the step change of command speeds, the step change in load, and the parameter variations. The performances of the proposed self-tuning MRPID based drive system have been experimentally compared with the standard PI controller based IPMSM drive system under identical operating conditions. The experimental performances of the proposed self-tuning MRPID based IPMSM drive system have been found more robust than the conventional PI controller based IPMSM drive system.

Chapter 8

Summary and Conclusions

The interior permanent magnet synchronous motor (IPMSM) with a suitable speed controller can meet the required criteria of high performance motor drive systems. The conventional constant gain controllers have been widely used for the speed control of the IPMSM drive systems due to their simple implementation scheme. However, the gains of such controllers require adequate tuning for acceptable motor speed response. Moreover, the design of a fixed gain control system has been normally based on an accurate mathematical model of the system dynamics. Furthermore, even if the system model is well known, building an accurate mathematical model is a very difficult task due to unavoidable conditions such as saturation, parameter variations, system noise, temperature changes, etc. Therefore, the performances of the fixed gain controller based drive systems are unpredictable under dynamic operating conditions. In addition, the fixed gain controllers have suffered from occasional instability due to unknown nonlinear load dynamics. In order to achieve robustness against disturbances and parameter variations, several modern controllers have been developed for high performance IPMSM drive systems. These modern controllers include model reference adaptive controller (MRAC), sliding mode controller (SMC), variable structure controller (VSC), and self tuning regulator (STR). However, these intelligent controllers are difficult to design and implement in real time when the accurate model of a system is unavailable. Moreover, the design of these intelligent control techniques relies on system parameters. The signals for these controllers are usually periodic and stationary types.

In recent years, the wavelet transforms have been used for the adaptive control of electric motor drives. The wavelet transform (WT) can decompose non stationary and non periodic signals into time and frequency localized parameters. The WT uses longer time windows for low frequencies and shorter time windows for high frequencies to meet conditions of frequency resolution. This thesis has introduced a novel wavelet neural network (WNN) based self-tuning multiresolution proportional integral derivative (MRPID) controller for speed control of high performance IPMSM drive systems. The wavelet based self-tuning MRPID speed controller in the IPMSM drive systems has been used to overcome the limitations of conventional controllers used in high performance motor drive systems. In order to verify the feasibility of using the proposed controller as a speed controller for high performance drive systems, the WNN based self-tuning MRPID controller for an IPMSM drive system has been simulated using the MATLAB software package. It has been found that the proposed self-tuning MRPID speed controller can track the command speed adaptively for dynamic operating conditions such as step change in command speeds, step change in load, parameter variations, etc. The simulated performance test results of the IPMSM drive system using the self-tuning MRPID speed controller have demonstrated encouraging performances. These encouraging performances have provided the motivation to extend the testing of the proposed self-tuning speed controller in real time for the IPMSM drive system.

Chapter 1 has presented an extensive literature survey on variable speed ac motor drives incorporating various control techniques. The survey has presented a clear picture of the problems related with the high performance interior permanent magnet (IPM) motor drive systems. Therefore, problems related with the precise speed control of an IPMSM drive system have also been identified. A wavelet neural network (WNN) based self-tuning multiresolution proportional integral (MRPID) controller has been proposed to overcome these problems. The wavelet transforms have become a popular choice for system identification and speed control of electric motor drives in recent years.

In chapter 2, the vector control technique of a voltage source inverter (VSI) fed IPMSM drive system has been presented. The vector control scheme has been integrated with the mathematical model of the IPMSM. The fixed gain PI, PID speed controllers and adaptive neural network (NN) speed controller have been developed and implemented for the vector control of the IPMSM drive. The performances of the fixed gain and adaptive speed controllers have been investigated in simulation. The simulation studies have provided a basis for further investigation on using the modern speed controllers for high performance IPMSM drive system.

Chapter 3 has discussed the wide speed control of the IPMSM drive system incorporating the maximum torque per ampere (MTPA) and flux weakening (FW) control algorithms. The comparative performances of the proposed flux weakening control (FW) control and the vector control for an IPMSM drive system have been investigated for both simulation and experimental performances. The FW control technique has been found more robust and realistic than the $i_d = 0$ control technique over a wide speed range of the IPM synchronous motor.

Chapter 4 has introduced a novel wavelet based multiresolution proportional integral derivative (MRPID) controller for the IPMSM drive systems. The mathematical formulations of the proposed MRPID speed controller for the IPMSM drive have been presented. In the proposed MRPID controller, the speed error signal has been decomposed by the discrete wavelet transform (DWT) using the selected wavelet function. The number of levels of decomposition of the speed error signal has been incorporated to determine the number of gains of the proposed MRPID controller. The minimum description length (MDL) data criterion and the entropy based criterion have been utilized in this work for selecting the mother wavelet function and for determining the desired levels of decomposition of the speed error, respectively. A tuning approach has been outlined for the proposed MRPID controller of the IPMSM drive system. The approach has been based on the comparative performance analysis of the PID decomposition and the multiresolution decomposition of the speed error signal.

In chapter 5, a specific MRPID controller for the IPMSM drive system has been presented. The specific MRPID controller based IPMSM drive system has been developed and implemented in both simulation and real time. In real time, the specific MRPID controller has been implemented for a laboratory IPMSM drive. The performances of the MRPID controller have been investigated for dynamic operating conditions such as rated and high starting command speeds, step change in command speeds, sudden change in load torque, and parameter variations with different initial conditions. The simulation and experimental test results have facilitated a platform for application of a wavelet neural network based self-tuning MRPID controller for the high performance IPMSM drive system.

In chapter 6, a self-tuning MRPID controller based on the wavelet neural network (WNN) has been developed and implemented for precise speed control of an IPMSM drive system. Initially the structure and the mathematical formulations of the specific WNN for the self-tuning control of the IPMSM drive system have been derived. Later the mathematical model and the specific schematic of the proposed self-tuning MRPID controller for an IPMSM drive system have been presented. The back propagation training algorithm has been used for the on-line training of the WNN parameters. The outline of the training algorithm has been developed and discussed. The stability of the proposed control system has been guaranteed as the learning rates of the WNN have been derived on the basis of the discrete Lyapunov function. Extensive simulations of the IPMSM drive system using the proposed self-tuning MRPID controller have been carried out. The simulation results show encouraging performances for the real time implementation of the IPMSM drive system using the proposed self-tuning MRPID controller.

Chapter 7 has provided the details of the real time implementation of the IPMSM drive system incorporating the WNN based self-tuning MRPID controller. The software and hardware components for the real-time implementation of the IPMSM drive system have been described. The performances of the proposed self-tuning MRPID controller based IPMSM drive system have been investigated experimentally on a laboratory 1-hp

IPM motor at dynamic operating conditions. The experimental test results have validated the simulated performance test results of the proposed controller of chapter 6. The performances of the proposed self-tuning MRPID controller have also been compared experimentally with the fixed gain PI controller based IPMSM drive system under the same operating conditions. The performances of the proposed self-tuning MRPID speed controller based drive system have been found more robust as compared to those of the conventional PI controller based drive system. The flux weakening (FW) control technique with $i_d \neq 0$ condition has been integrated in the proposed control technique in order to operate the drive above the rated speed of the IPMSM.

8.1 Major Contributions of the Thesis

The major contributions of the thesis have been outlined in the followings:

- The detailed mathematical formulations of a vector controlled voltage source inverter (VSI) fed interior permanent magnet synchronous motor (IPMSM) drive system have been presented. The fixed band hysteresis current controller has been developed and implemented for an IPMSM drive system in both simulation and experiments.
- The comparative performances of the fixed gain PI and PID speed controllers based IPMSM drive system, and an adaptive NN speed controller based IPMSM drive system have been presented.
- The maximum torque per ampere (MTPA) and flux weakening (FW) control techniques have been implemented and tested for wide speed control of the IPMSM drive system. The FW control $i_d \neq 0$ has been compared with the $i_d = 0$ control technique. The performances of the FW control technique have been found more robust as compared to those of the $i_d = 0$ control technique.
- A novel wavelet based multiresolution proportional integral derivative (MRPID) controller has been developed for the precise speed control of the IPMSM drive system. In the wavelet based MRPID controller, the error

between actual and command speeds has been decomposed up to the second level of resolution of the discrete wavelet transform (DWT) using the selected mother wavelet function. The wavelet transformed coefficients of the speed error signal at different frequency sub-bands of the DWT have been scaled by their respective gains, and then these have been added together to generate the control signal for the drive system.

- In the development of the MRPID controller, the minimum description length (MDL) data criterion and the entropy based criterion have been successfully utilized in order to select an optimum mother wavelet function and to find the optimal levels of decomposition of the speed error signal, respectively.
- The specific MRPID controller incorporating the maximum torque per ampere (MTPA) control and flux weakening (FW) control with $i_d \neq 0$ of the IPMSM drive system has been presented. The applicability of the MRPID controller for the speed control of the IPMSM drive has been evaluated by simulations, and verified experimentally in a laboratory test IPM motor drive.
- A new wavelet neural network (WNN) based self-tuning MRPID controller for the IPMSM drive system has been developed. The performances of the proposed controller have been evaluated in both simulations and experiments.
- A new specific WNN structure for the optimum tuning of the proposed MRPID controller has been presented. The on-line stability of the proposed control system has been achieved using a novel adaptive learning of the WNN.
- The proposed self-tuning MRPID controller using maximum torque per ampere (MTPA) and flux weakening (FW) control schemes for the IPMSM drive has been successfully implemented in real time for the first time on a laboratory 1-hp IPMSM using the digital signal processor (DSP) board ds1102. The procedures for the real time implementation of the proposed self-tuning MRPID based IPMSM drive system have also been presented.

- The performances of the IPMSM drive system incorporating the proposed self-tuning MRPID controller have been experimentally investigated at different dynamic operating conditions. The performances of the proposed drive system have also been compared with the conventional PI controller based drive system in real time under the same operating conditions. It has been found that the proposed self-tuning MRPID controller based drive system has superior performances over the PI controller based IPMSM drive system.
- The contents of the thesis so far have led to the publications of two journal papers and four conference papers. The chapters 2, 4, and 5 have been published in references [84] and [87]. The chapters 4, 6, and 7 have been published in references [85] and [86]. The proposed wavelet based MRPID controller of chapter 4 has been implemented for induction motor drives in references [88] and [89].

8.2 Future Scope of Work

This work focuses on the development and implementation of fixed gain and adaptive speed controllers for the IPMSM drive to be used in the high performance motor drives. The wavelet neural network (WNN) based self-tuning multiresolution proportional integral derivative (MRPID) controller has been successfully implemented in real time for the flux weakening (FW) control of the IPMSM drive system for the first time. The self-tuning MRPID based IPMSM drive system has provided the faster response than with the fixed gain PI, PID speed controllers and the adaptive neural network (NN) speed controllers.

The command torque current response of the IPMSM drive system using the proposed self-tuning MRPID controller has shown significant oscillations in real time. These oscillations have generated minor spikes in the actual speed and phase current responses of the proposed drive system. The number of level of decomposition of the speed error signal of the proposed controller could be increased in order to eliminate

these spikes. But it would increase the sampling frequency of the proposed control algorithm during the real time implementation. The ds1102 digital signal processor (DSP) board could not be used for the implementation of the proposed controller with high sampling frequency. As a future scope of this work, the proposed self-tuning MRPID controller should be implemented in real time using the new ds1104 DSP board. The maximum sampling frequency of 10 kHz can be used for the real time implementation of the proposed control algorithm using the ds1104 DSP controller board.

The IPMSM drive systems have been subjected to a wide variety of abnormal operating conditions including faults in inverters and motors. The fault currents of the IPMSM drive may consist of wideband, stationary, non stationary, and non periodic signals. The wavelet transform has a unique ability to decompose wide band, stationary and non stationary signals into time and frequency localized components. As another future scope of this work, the wavelet based fault tolerant control may be integrated with the proposed self-tuning MRPID controller based IPMSM drive system.

The efficiency of the IPMSM drive is a crucial performance characteristic because of the limitation of the dc power for the drive system. A detail study on the efficiency of the drive system using the proposed wavelet based MRPID controller will be conducted in the future. The computational time and memory requirements of the proposed MRPID controller have also influenced the performances of the drive system. So, the computational requirements of the proposed controller will be investigated in detail in the future. It has been shown that the losses of an IPM motor can be estimated using the time and frequency localized wavelet coefficients of phase currents and air gap induced voltage. As an additional future scope of this work, a wavelet based loss minimization control may be developed and integrated with the proposed self-tuning MRPID controller based IPMSM drive system.

The systematic developments of the IPMSM drive using the Fuzzy logic controller and the Neuro-Fuzzy controller should be undertaken. The comparative analysis of the self-tuning MRPID based IPMSM drive system with the Fuzzy controllers will be conducted as a future work.

8.3 Conclusions

The major points of the conclusions of the work are the followings:

- The wavelet neural network (WNN) based self-tuning multiresolution proportional integral derivative (MRPID) controller has been successfully implemented and effectively used for the high performance speed control of the interior permanent magnet synchronous motor (IPMSM) drive system. The proposed self-tuning MRPID controller has been found a robust speed controller to be used in industrial high performance motor drive systems.
- The wavelet neural network (WNN) has been utilized for the self-tuning of the proposed MRPID controller for the IPMSM drive system. The on-line stability of the proposed MRPID controller based IPM motor drive system has been verified through adaptive learning of the WNN parameters based on the discrete Lyapunov algorithm. The WNN based self-tuning control scheme has been found to be suitable for the high performance IPM motor drive system.
- The minimum description length (MDL) data criterion and the entropy based criterion have been used for selecting an optimum mother wavelet function and for finding the optimal levels of decomposition of the speed error signal, respectively in the development of the proposed MRPID controller for the IPM motor drive system. The MDL and entropy criteria have been found to be optimal selection algorithms in the development of proposed MRPID controller.
- The maximum torque per ampere (MTPA) and flux weakening (FW) control algorithms have been implemented for high speed control of the IPMSM drive. The MTPA and FW control algorithms have been found to be suitable for wide speed control of the IPM motor drive in both constant torque and constant power modes of operation.

- The performances of the proposed self-tuning MRPID speed controller have been found more robust as compared to those of the fixed gain PI, PID controllers and adaptive neural network speed controller. So, the fixed gain and adaptive speed controllers based IPM drive systems can be successfully replaced by the proposed self-tuning MRPID speed controller for the IPM motor drive system.
- The performances of the proposed self-tuning MRPID controller based IPMSM drive system have been found better than the fixed gain MRPID controller based IPMSM drive system for a sudden change in load and associated loading uncertainties of the drive system.

References

[1] G. R. Slemon, *Electric Machines and Drives*, Boston, MA: Addison-Wesley, 1992.

[2] B. K. Bose, *Modern Power Electronics: Evolution, Technology, and Applications*, Piscataway, NJ: IEEE Press, 1992.

[3] M. A. Rahman, "Permanent magnet synchronous motors – a review of the state of design art," in *Proceedings of International Conference on Electric Machines (ICEM)*, Athens, Greece, 15–17 September 1980, vol. 1, pp. 312–319.

[4] P. C. Sen, "Electric motor drives and control – past, present, and future," *IEEE Transactions on Industrial Electronics*, vol. 37, no. 6, December 1990, pp. 562–575.

[5] B. K. Bose, "Technology trends in microcomputer control of electrical machines," *IEEE Transactions on Industrial Electronics*, vol. 35, no. 1, February 1988, pp. 160–177.

[6] F. Blaschke, "The principle of field orientation as applied to the new transvector closed-loop control system for rotating field machines," *Siemens Review*, vol. 39, no. 5, May 1972, pp. 217–220.

[7] M. A. Rahman, "Modern electric motors in electronic world," in *Proceedings of IEEE International Conference on Industrial Electronics, Control, and Instrumentation (IECON)*, Hawaii, US, 15–19 November 1993, pp. 644–648.

[8] J. F. Gieras and M. Wing, *Permanent Magnet Motor Technology: Design and Applications*, Madison, NY: Marcel Dekker, 2002.

[9] M. A. Rahman, "Recent advances of IPM motor drives in power electronics world," in *Proceedings of IEEE International Conference on Power Electronics and Drive Systems (PEDS)*, Kuala Lumpur, Malaysia, 30 November – 02 December 2005, vol. 1, pp. 24–31.

[10] M. Rosu, J. Saitz, and A. Arkkio, "Hysteresis model for finite-element analysis of permanent magnet demagnetization in a large synchronous motor under a fault condition," *IEEE Transactions on Magnetics*, vol. 41, no. 6, June 2005, pp. 2118–2123.

[11] S. A. Nasar, I. Boldea, and L. E. Unnewehr, *Permanent Magnet, Reluctance, and Self-Synchronous motors*, Boca Raton, FL: CRC Press, 1993.

[12] T. M. Jahns, G. B. Kliman, and T. W. Neumann, "Interior permanent magnet synchronous motors for adjustable speed drives," *IEEE Transactions on Industry Applications*, vol. IA–22, no. 4, July/August 1986, pp. 738–747.

[13] T. Himei, S. Funabiki, Y. Agari, and M. Okada, "Analysis of voltage source inverter-fed permanent magnet synchronous motor taking account of converter performance," *IEEE Transactions on Industry Applications*, vol. IA-21, no. 1, January–February 1985, pp. 279–284.

[14] R. Dhaouadi and N. Mohan, "Analysis of current-regulated voltage source inverters for permanent magnet synchronous motor drives in normal and extended speed ranges," *IEEE Transactions on Energy Conversion*, vol. 5, no. 1, March 1990, pp. 137–144.

[15] M. N. Uddin, T. S. Radwan, G. H. George, and M. A. Rahman, "Performance of current controllers for VSI-fed IPMSM drive," *IEEE Transactions on Industry Applications*, vol. 36, no. 6, November 2000, pp. 1531–1538.

[16] A. V. Gumaste and G. R. Slemon, "Steady state analysis of a permanent magnet synchronous motor drive with voltage source inverter," *IEEE Transactions on Industry Applications*, vol. IA-17, no. 2, March–April 1981, pp. 143–151.

[17] G. R. Slemon and A. V. Gumaste, "Steady state analysis of a permanent magnet synchronous motor drive with current source inverter," *IEEE Transactions on Industry Applications*, vol. IA-19, no. 2, March–April 1983, pp. 190–197.

[18] A. K. Mohanty and P. K. Dash, "Steady state performance and dynamic stability of C. S. I. fed permanent magnet motor," *Journal of Electric Machines and Power Systems*, vol. 13, no. 1, July 1987, pp. 1–17.

[19] V. Nedic and T. A. Lipo, "Low cost current fed PMSM drive system with sinusoidal input currents," *IEEE Transactions on Industry Applications*, vol. 42, no. 3, May–June 2006, pp. 753–762.

[20] P. Snary, B. Bhangu, C. M. Bingham, D. A. Stone, and N. Schofield, "Matrix converters for sensorless control of PMSMs and other auxiliaries on deep sea ROVs," in *Proceedings IEE Electric Power Applications*, vol. 152, no. 2, March 2005, pp. 382–392.

[21] E. Levi, M. Jones, and S. N. Vukosavic, "A series-connected two-motor six-phase drive with induction and permanent magnet machines," *IEEE Transactions on Energy Conversion*, vol. 21, no. 1, March 2006, pp. 121–129.

[22] T. –H. Liu, C. –M. Young, and C. –H. Liu, "Microprocessor based controller design and simulation for a permanent magnet synchronous motor drive," *IEEE Transactions on Industrial Electronics*, vol. 35, no. 4, November 1988, pp. 516–523.

[23] P. Pillay and R. Krishnan, "Modeling, simulation, and analysis of permanent magnet motor drives- part I: the permanent magnet synchronous motor drive," *IEEE Transactions on Industry Applications*, vol. IA-25, no. 2, March–April 1989, pp. 265–273.

[24] A. A. Fardoun, E. F. Fuchs, and H. Huang, "Modeling and simulation of an electronically commutated permanent magnet machine drive system using SPICE," *IEEE Transactions on Industry Applications*, vol. 30, no. 4, July–August 1994, pp. 927–937.

[25] G. R. Slemon and X. Liu, "Modeling and design optimization of permanent magnet motors," *Journal of Electric Machines and Power Systems*, vol. 20, no. 2, March-April 1992, pp. 71–92.

[26] G. –H. Kang, J. –P. Hong, G. –T. Kim, and J. –W. Park, "Improved parameter modeling of interior permanent magnet synchronous motor based on finite element analysis," *IEEE Transactions on Magnetics*, vol. 36, no. 4, July 2000, pp. 1867–1870.

[27] O. A. Mohammed, S. Ganu, Z. Liu, N. Abed, and S. Liu, "High frequency modeling of permanent magnet synchronous motor drive," in *Proceedings of IEEE International Electric Machines and Drives Conference (IEMDC)*, Antalya, Turkey, 3–5 May 2007, vol. 1, pp. 318–321.

[28] W. Roshen, "Iron loss model for permanent magnet synchronous motors," *IEEE Transactions on Magnetics*, vol. 43, no. 8, August 2007, pp. 3428–3434.

[29] A. Consoli and A. Abela, "Transient performance of permanent magnet AC motor drives," *IEEE Transactions on Industry Applications*, vol. IA-22, no. 1, January–February 1986, pp. 32–41.

[30] K. Nakamura, K. Saito, and O. Ichinokura, "Dynamic analysis of interior permanent magnet motor based on a magnetic circuit model," *IEEE Transactions on Magnetics*, vol. 39, no. 5, September 2003, pp. 3250–3252.

[31] T. –H. Liu and C. –P. Cheng, "Controller design for a sensorless permanent magnet synchronous drive system," in *Proceedings IEE Electric Power Applications*, vol. 140, no. 6, November 1993, pp. 369–378.

[32] I. Birou, M. Imecs, and C. Rusu, "Robust control of field-oriented drive system with permanent magnet synchronous servomotor," in *Proceedings of IEEE International Electric Machines and Drives Conference (IEMDC)*, Seattle, US, 9–12 May 1999, pp. 144–146.

[33] M. Cheng, Q. Sun, K. T. Chau, and C. C. Chan, "Control and operation of a new 8/6-pole doubly salient permanent magnet motor drives," *IEEE Transactions on Industry Applications*, vol. 39, no. 5, September–October 2003, pp. 1363–1371.

[34] M. Cheng and Q. Sun, "Variable parameter PI control of a novel doubly salient permanent magnet motor drive," in *Proceedings of IEEE International Conference on Power Electronics and Drive Systems (PEDS)*, Singapore, 17–20 November 2003, vol. 1, pp. 698–703.

[35] J. A. Haylock, B. C. Mecrow, A. G. Jack, and D. J. Atkinson, "Enhanced current control of high-speed PM machine drives through the use of flux controllers," *IEEE Transactions on Industry Applications*, vol. 35, no. 5, September–October 1999, pp. 1030–1038.

[36] J. –X. Xu, S. K. Panda, Y. –J. Pan, T. H. Lee, and B. H. Lam, "A modular control scheme for PMSM speed control with pulsating torque minimization," *IEEE Transactions on Industrial Electronics*, vol. 51, no. 3, June 2004, pp. 526–536.

[37] S. K. Panda, J. M. S. Lim, P. K. Dash, and K. S. Lock, "Gain scheduled PI speed controller for PMSM drive," in *Proceedings of IEEE International Conference on Industrial Electronics, Control, and Instrumentation (IECON)*, New Orleans, LA, 9–14 November 1997, vol. 2, pp. 925–930.

[38] R. M. Lourde, L. Umanand, and N. J. Rao, "Design of robust optimal PI controller for PMSM servo drives," *Journal of the Indian Institute of Science*, vol. 77, no. 5, September–October 1997, pp. 469–489.

[39] J. –K. Seok, J. –K. Lee, and D. –C. Lee, "Sensorless speed control of non-salient permanent magnet synchronous motor using rotor position tracking PI controller," *IEEE Transactions on Industrial Electronics*, vol. 53, no. 2, April 2006, pp. 399–405.

[40] B. Hemici, L. Nezli, M. Tadjine, and M. S. Boucherit, "Robust PID/backstepping control design for permanent magnet synchronous motor drive," *Journal of Control and Intelligent Systems*, vol. 34, no. 3, March 2006, pp. 194–204.

[41] S. Dan and M. Jun, "A single neuron PID controller based PMSM DTC drive system fed by fault tolerant 4-switch 3-phase inverter," in *Proceedings of IEEE International Conference on Industrial Electronics and Applications (ICIEA)*, Singapore, 24–26 May 2006, pp. 1–5.

[42] D. Garcia, A. Karimi, and R. Longchamp, "Robust proportional integral derivative controller tuning with specifications on the infinity-norm of sensitivity functions," in *Proceedings IET Control Theory and Applications*, vol. 1, no. 1, January 2007, pp. 263–272.

[43] M. Tursini, F. Parasiliti, and D. Zhang, "Real-time gain tuning of PI controllers for high performance PMSM drives," *IEEE Transactions on Industry Applications*, vol. 38, no. 4, July–August 2002, pp. 1018–1026.

[44] X. Xiao, Y. Li, and M. Li, "Performance control of PMSM drives using self-tuning PID," in *Proceedings of IEEE International Electric Machines and Drives Conference (IEMDC)*, San Antonio, TX, 15–18 May 2005, pp. 1053–1057.

[45] S. Vaez–Zadeh, V. I. John, and M. A. Rahman, "An online loss minimization controller for interior permanent magnet motor drives," *IEEE Transactions on Energy Conversion*, vol. 14, no. 4, December 1999, pp. 1435–1440.

[46] E. Cerruto, A. Consoli, A. Raciti, and A. Testa, "A robust adaptive controller for PM motor drives in robotic applications," *IEEE Transactions on Power Electronics*, vol. 10, no. 1, January 1995, pp. 62–71.

[47] H. Ebrahimirad, S. Vaez–Zadeh, and M. J. –Kharaajoo, "Speed control of PM synchronous motors: comparison of sliding mode and PI controllers," in *Proceedings of IEEE International Conference on Control Applications*, Istanbul, Turkey, 23–25 June 2003, vol. 1, pp. 99–102.

[48] K. –K. Shyu, C. –K. Lai, Y. –W. Tsai, and D. –I. Yang, "A newly robust controller design for the position control of permanent-magnet synchronous motor," *IEEE Transactions on Industrial Electronics*, vol. 49, no. 3, June 2002, pp. 558–565.

[49] M. N. Uddin, M. A. Abido, and M. A. Rahman, "Development and implementation of a hybrid intelligent controller for interior permanent magnet synchronous motor drives," *IEEE Transactions on Industry Applications*, vol. 40, no. 1, January–February 2004, pp. 68–76.

[50] Y. Ming, G. Yang, D. –G. Xu, and Y. Yong, "On-line self-tuning of PI controller for PMSM drives based on the iterative learning control," in *Proceedings of IEEE Applied Power Electronics Conference and Exposition*, Austin, TX, 6–10 March 2005, vol. 3, pp. 1889–1893.

[51] T. Fukumoto, H. Hamane, and Y. Hayashi, "Performance improvement of the IPMSM position sensorless vector control system by the on-line motor parameter error compensation and the practical dead time compensation," in *Proceedings of IEEE Power Conversion Conference (PCC),* Nagoya, Japan, 2–5 April 2007, pp. 314–321.

[52] Y. A. –R. I. Mohamed, "A novel direct instantaneous torque and flux control with an ADALINE based motor model for a high performance DD-PMSM," *IEEE Transactions on Power Electronics*, vol. 22, no. 5, September 2007, pp. 2042–2049.

[53] S. Shinnaka, "New sensorless vector control using minimum order flux state observer in a stationary reference frame for permanent magnet synchronous motors," *IEEE Transactions on Industrial Electronics*, vol. 53, no. 2, April 2006, pp. 388–398.

[54] S. Shinnaka, "New D-state-observer based vector control for sensorless drive of permanent magnet synchronous motors," *IEEE Transactions on Industry Applications*, vol. 41, no. 3, May–June 2005, pp. 825–833.

[55] K. –H. Kim, "Nonlinear speed control for a PM synchronous motor with a sequential parameter auto tuning algorithm," in *Proceedings IEE Electric Power Applications*, vol. 152, no. 5, September 2005, pp. 1253–1262.

[56] M. Hasegawa and K. Matsui, "Position sensorless control for interior permanent magnet synchronous motor using adaptive flux observer with inductance identification," in *Proceedings IET Electric Power Applications*, vol. 3, no. 3, May 2009, pp. 209–217.

[57] Z. Ibrahim and E. Levi, "A comparative analysis of fuzzy logic and PI speed control in high performance AC drives using experimental approach," *IEEE Transactions on Industry Applications*, vol. 38, no. 5, September–October 2002, pp. 1210–1218.

[58] M. Cheng, Q. Sun, and E. Zhou, "New self-tuning fuzzy PI control of a novel doubly salient permanent magnet motor drive," *IEEE Transactions on Industrial Electronics*, vol. 53, no. 3, June 2006, pp. 814–821.

[59] M. Kadjoudj, R. Abdessemed, N. Golea, and M. E. Benbouzid, "Adaptive fuzzy logic control for high performance PM synchronous drives," *Journal of Electric Power Components and Systems*, vol. 29, no. 9, September 2001, pp. 789–807.

[60] B. Singh, C. L. P. Swamy, B. P. Singh, A. Chandra, and K. A. –Haddad., "Performance analysis of fuzzy logic controlled permanent magnet synchronous motor drive," in *Proceedings of IEEE International Conference on Industrial Electronics, Control, and Instrumentation (IECON)*, Orlando, FL, November 1995, vol. 1, pp. 399–405.

[61] C. B. Butt, M. A. Hoque, and M. A. Rahman, "Simplified fuzzy-logic based MTPA speed control of IPMSM drive," *IEEE Transactions on Industry Applications*, vol. 40, no. 6, November–December 2004, pp. 1529–1534.

[62] M. N. Uddin, M. A. Abido, and M. A. Rahman, "Real-time performance evaluation of a genetic-algorithm-based fuzzy logic controller for IPM motor drives," *IEEE Transactions on Industry Applications*, vol. 41, no. 1, January–February 2005, pp. 246–252.

[63] M. N. Uddin, T. S. Radwan, and M. A. Rahman, "Fuzzy logic controller based cost effective four-switch three-phase inverter fed IPM synchronous motor system," *IEEE Transactions on Industry Applications*, vol. 42, no. 1, January–February 2006, pp. 21–30.

[64] J. –S. Yu, S. –H. Kim, B. –K. Lee, C. –Y. Won, and J. Hur, "Fuzzy logic based vector control scheme for permanent magnet synchronous motors in elevator drive applications," *IEEE Transactions on Industrial Electronics*, vol. 54, no. 4, August 2007, pp. 2190–2200.

[65] Y. –S. Kung and M. –H. Tsai, "FPGA based speed control IC for PMSM drive with adaptive fuzzy control," *IEEE Transactions on Power Electronics*, vol. 22, no. 6, November 2007, pp. 2476–2486.

[66] M. A. Rahman and M. A. Hoque, "On-line adaptive artificial neural network based vector control of permanent magnet synchronous motors," *IEEE Transactions on Energy Conversion*, vol. 13, no. 4, December 1998, pp. 311–318.

[67] M. E. Elbuluk, L. Tong, and I. Husain, "Neural network based model reference adaptive systems for high performance motor drives and motion controls," *IEEE Transactions on Industry Applications*, vol. 38, no. 3, May–June 2002, pp. 879–886.

[68] Y. Yi, D. M. Vilathgamuwa, and M. A. Rahman, "Implementation of an artificial neural network based real-time adaptive controller for an interior permanent magnet motor drive," *IEEE Transactions on Industry Applications*, vol. 39, no. 1, January–February 2003, pp. 96–104.

[69] F. –J. Lin, C. –H. Lin, and P. –H. Shen, "Self constructing fuzzy neural network speed controller for permanent magnet synchronous motor drive," *IEEE Transactions on Fuzzy Systems*, vol. 9, no. 5, October 2001, pp. 751–759.

[70] C. Elmas, O. Ustun, and H. H. Sayan, "A neuro-fuzzy controller for speed control of a permanent magnet synchronous motor drive," *Journal of Expert Systems with Applications*, vol. 34, no. 1, January 2008, pp. 657–664.

[71] M. A. S. K. Khan and M. A. Rahman, "Development and implementation of a novel fault diagnostic and protection technique for IPM motor drives," *IEEE Transactions on Industrial Electronics,* vol. 56, no. 1, January 2009, pp. 85–92.

[72] M. A. S. K. Khan, T. S. Radwan, and M. A. Rahman, "Real-time implementation of wavelet packet transform based diagnosis and protection of three-phase induction motors," *IEEE Transactions on Energy Conversion*, vol. 22, no. 3, September 2007, pp. 647–655.

[73] F. Chaplais, P. Tsiotras, and D. Jung, "On-line wavelet de-noising with application to the control of a reaction wheel system," in *Proceedings of American Institute of Aeronautics and Astronautics (AIAA) Guidance, Navigation, and Control Conference*, Rhode Island, Greece, 16–19 August 2004, vol. 5, pp. 3058–3072.

[74] F. Chaplais, P. Tsiotras, and D. Jung, "Redundant wavelet processing on the half-axis with applications to signal denoising with small delays: theory and experiments," *Journal of Adaptive Control and Signal Processing*, vol. 20, no. 9, November 2006, pp. 447–474.

[75] S. Khorbotly, A. Khalil, J. Carletta, and I. Husain, "A wavelet based de-noising approach for real-time signal processing in switched reluctance motor drives," in *Proceedings of IEEE Industrial Electronics Society Annual Conference (IECON)*, North Carolina, US, 6–10 November 2005, pp. 1437–1442.

[76] Y. Song, F. Ponci, A. Monti, L. Gao, and R. A. Dougal, "A novel brushless DC motor speed estimator based on space frequency localized wavelet neural networks," in *Proceedings of IEEE Applied Power Electronics Conference and Exposition*, Austin, TX, 6–10 March 2005, vol. 2, pp. 927–932.

[77] M. Yilmaz, R. N. Tuncay, and O. Ustun, "A wavelet study of sensorless control of brushless DC motor through rapid prototyping approach," in *Proceedings of IEEE International Conference on Mechatronics*, Istanbul, Turkey, 3–5 June 2004, pp. 334–339.

[78] C. –Z. Cao, M. –P. Lu, Q. –D. Zhang, and Y. –C. Zhang, "Research on online identification of the stator resistance using wavelet neural network," in *Proceedings of IEEE International Conference on Machine Learning and Cybernetics*, Shanghai, China, 26–29 August 2004, vol. 5, pp. 3073–3077.

[79] R. –J. Wai and H. –H. Chang, "Backstepping wavelet neural network control for indirect field oriented induction motor drive," *IEEE Transactions on Neural Networks*, vol. 15, no. 2, March 2004, pp. 367–382.

[80] R. –J. Wai, "Robust control for nonlinear motor-mechanism coupling system using wavelet neural network," *IEEE Transactions on Systems, Man, and Cybernetics*, vol. 33, no. 3, June 2003, pp. 489–497.

[81] W. Jun, P. Hong, and X. Ling, "A fuzzy-wavelet-network based position control for PMSM," in *Proceedings of IEEE International Conference on Power Electronics and Motion Control (PEMC)*, Portoroz, Slovenia, August 30–September 1, 2006, vol. 2, pp. 1-4.

[82] M. Azadi, A. Rahideh, A. A. Safavi, and O. Mahdiyar, "Wavenet based vector control of a permanent magnet synchronous motor drive," in *Proceedings of IEEE International Electric Machines and Drives Conference (IEMDC)*, Antalya, Turkey, 3–5 May 2007, vol. 2, pp. 1663–1668.

[83] S. Parvez and Z. Gao, "A wavelet-based multiresolution PID controller," *IEEE Transactions on Industry Applications,* vol. 41, no. 2, March–April 2005, pp. 537–543.

[84] M. A. S. K. Khan and M. A. Rahman, "Implementation of a new wavelet controller for interior permanent magnet motor drives," *IEEE Transactions on Industry Applications,* vol. 44, no. 6, November–December 2008, pp. 1957–1965.

[85] M. A. S. K. Khan and M. A. Rahman, "A novel neuro-wavelet based self-tuned wavelet controller for IPM motor drives," in *Proceedings of IEEE Industry Applications Society Annual Meeting*, Edmonton, AB, 5–9 October 2008, pp. 1–8.

[86] M. A. S. K. Khan and M. A. Rahman, "An adaptive self-tuned wavelet controller for IPM motor drives," in *Proceedings of IEEE Power and Energy Society General Meeting*, Pittsburg, PA, 20–24 July 2008, pp. 1–4.

[87] M. A. S. K. Khan, G. H. George, and M. A. Rahman, "Intelligent speed controllers for IPM motor drives," in *Proceedings of IEEE Canadian Conference on Electrical and Computer Engineering (CCECE)*, St. John's, NL, 3–6 May 2009, pp. 833-836.

[88] M. A. S. K. Khan and M. A. Rahman, "A new wavelet based speed controller for induction motor drives," *Journal of Electric Power Components and Systems,* vol. 36, no. 12, December 2008, pp. 1282–1298. (*Taylor & Francis*)

[89] M. A. S. K. Khan and M. A. Rahman, "Real-time implementation of a wavelet based speed controller for induction motor drives," in *Proceedings of IEEE Canadian Conference on Electrical and Computer Engineering (CCECE)*, Vancouver, BC, 22–26 April 2007, pp. 546–549.

[90] *Matlab/Simulink User Guide*, Natick, MA: MathWorks, 2006.

[91] M. A. Hoque, "*Speed Control of High Performance Permanent Magnet Motors*," PhD Thesis, Memorial University of Newfoundland, St. John's, NL, Canada, June 1996.

[92] M. A. Rahman, R. M. Milasi, C. Lucas, B. N. Araabi, and T. S. Radwan, "Implementation of emotional controller for interior permanent-magnet synchronous motor drive," *IEEE Transactions on Industry Applications*, vol. 44, no. 5, September-October 2008, pp. 1466–1476.

[93] P. C. Krause, *Analysis of Electric Machinery*, NY: McGraw-Hill, 1986.

[94] T. Sebastian, G. R. Slemon, and M. A. Rahman, "Modeling of permanent magnet synchronous motors," *IEEE Transactions on Magnetics*, vol. 22, no. 5, September 1986, pp. 129–134.

[95] M. N. Uddin, "*Intelligent Control of An Interior Permanent Magnet Synchronous Motor Drive,*" PhD Thesis, Memorial University of Newfoundland, St. John's, NL, Canada, October 2000.

[96] Y. –S. Jeong, S. –K. Sul, S. Hiti, and K. M. Rahman, "Online minimum copper loss control of an interior permanent magnet synchronous machine for automotive applications," *IEEE Transactions on Industry Applications*, vol. 42, no. 5, September–October 2006, pp. 1222–1229.

[97] H. Haykin, *Neural Networks: A Comprehensive Foundation*, NJ: Wiley–IEEE, 1994.

[98] D. M. Brod and D. W. Novotny, "Current control of VSI-PWM inverters," *IEEE Transactions on Industry Applications*, vol. IA-21, no. 3, May–June 1985, pp. 562–570.

[99] S. Morimoto, M. Sanada, and Y. Takeda, "Effects and compensation of magnetic saturation in flux-weakening controlled permanent magnet synchronous motor drives," *IEEE Transactions on Industry Applications*, vol. 30, no. 6, November–December 1994, pp. 1632–1637.

[100] S. Morimoto, Y. Takeda, T. Hirasa, and K. Taniguchi, "Expansion of operating limits for permanent magnet motor by current vector control considering inverter capacity," *IEEE Transactions on Industry Applications*, vol. 26, no. 5, September-October 1990, pp. 866–871.

[101] M. N. Uddin, T. S. Radwan, and M. A. Rahman, "Performance of interior permanent magnet motor drive over wide speed range," *IEEE Transactions on Energy Conversion*, vol. 17, no. 1, March 2002, pp. 79–84.

[102] M. N. Uddin and M. A. Rahman, "High-speed control of IPMSM drives using improved fuzzy logic algorithms," *IEEE Transactions on Industrial Electronics*, vol. 54, no. 1, February 2007, pp. 190–199.

[103] dSPACE, *Digital Signal Processing and Control Engineering Manual Guide*, GmbH, Paderborn, Germany, 1996.

[104] P. S. Addison, *The Illustrated Wavelet Transform Handbook*, Bristol, UK: Institute of Physics Publishing, 2002.

[105] S. A. Saleh, C. R. Moloney, and M. A. Rahman, "Development and testing of wavelet modulation for single-phase inverters," *IEEE Transactions on Industrial Electronics*, vol. 56, no. 7, July 2009, pp. 2588–2599.

[106] P. L. Mao and R. K. Aggarwal, "A novel approach to the classification of the transient phenomena in power transformers using combined wavelet transform and neural network," *IEEE Transactions on Power Delivery*, vol. 16, no. 4, October 2001, pp. 654–660.

[107] G. Stang and T. Nguyen, *Wavelets and Wavelet Filter Banks*, Wellesley, MA: Wellesly–Cambridge, 1996.

[108] Mathworks, *Matlab: Wavelet Tool Box*, 2006, version r2006b.

[109] S. Santoso, E. J. Powers, W. M. Grady, and P. Hofmann, "Power quality assessment via wavelet transform analysis," *IEEE Transactions on Power Delivery,* vol. 11, no. 2, April 1996, pp. 924–930.

[110] M. A. S. K. Khan, "*A Wavelet Packet Transform Based On-line Technique for the Protection of Three-Phase Interior Permanent Magnet Motors*," M. Eng. Thesis, Memorial University of Newfoundland, St. John's, NL, Canada, June 2006.

[111] G. G. Yen and K. –C. Lin, "Wavelet packet feature extraction for vibration monitoring," *IEEE Transactions on Industrial Electronics,* vol. 47, no. 3, June 2000, pp. 650–667.

[112] S. G. Mallat, "A theory of multi-resolution signal decomposition: the wavelet representation," *IEEE Transactions on Pattern Analysis and Machine Intelligence*, vol. 11, no. 7, July 1989, pp. 674–693.

[113] E. Y. Hamid and Z. I. Kawasaki, "Wavelet based data compression of power system disturbances using the minimum description length criterion," *IEEE Transactions on Power Delivery*, vol. 17, no. 2, April 2002, pp. 460–466.

[114] M. A. El-Sharkawi, A. A. El-Samahy, and M. L. El-Sayed, "High performance drive of dc brushless motors using neural network," *IEEE Transactions on Energy Conversion*, vol. 9, no. 2, June 1994, pp. 317–322.

[115] Y. A. R. I. Mohamed and T. K. Lee, "Adaptive self-tuning MTPA vector controller for IPMSM drive system," *IEEE Transactions on Energy Conversion*, vol. 21, no. 3, September 2006, pp. 636–644.

[116] Q. Zhang and A. Benveniste, "Wavelet networks," *IEEE Trans. Neural Networks*, vol. 3, no. 6, Nov. 1992, pp. 889–898.

[117] Y. C. Pati and P. S. Krishnaprasad, "Analysis and synthesis of feed forward neural networks using discrete affine wavelet transformations," *IEEE Trans. Neural Networks*, vol. 4, no. 1, Jan. 1993, pp. 73–85.

[118] R. –J. Wai and J. –M. Chang, "Intelligent control of induction servo motor drive via wavelet neural network," *Journal of Electric Power Systems Research*, vol. 61, no. 1, Feb. 2002, pp. 67–76.

[119] J. G. Ziegler, N. B. Nichols, and N. Y. Rochester, "Optimum settings for automatic controllers," *Transactions of the A.S.M.E*, vol. 64, November 1942, pp. 759–768.

[120] B. Adkins and R. G. Harley, *The General Theory of Alternating Current Machines: Application to Practical Problems*, London, UK: Chapman and Hall, 1975.

[121] R. Krishnan, *Electric Motor Drives: Modeling, Analysis, and Control*, Upper Saddle River, NJ: Prentice Hall, 2001.

[122] M. A. Rahman, D. M. Vilathgamuwa, M. N. Uddin, and K. –J. Tseng, "Nonlinear control of interior permanent-magnet synchronous motor," *IEEE Transactions on Industry Applications*, vol. 39, no. 2, March–April 2003, pp. 408–416.

[123] Mathworks, *Matlab: Neural Network Tool Box*, 2006, version r2006b.

APPENDIX A

IPMSM Parameters

Number of phases = 3

Number of poles = 4

Rated current = 3 A

Rated frequency = 60 Hz

Rated power = 1 hp

Rated input line to line voltage = 208 V

q-axis inductance L_q = 0.07957 H

d-axis inductance L_d = 0.04244 H

Stator resistance per phase r_s = 1.93 Ω

Inertia constant J_m = 0.003 Kg.m^2

Rotor damping constant B_m = 0.0008 (N-m)/rad./sec.

Permanent magnet flux linkage λ_M = 0.314 volts/rad./sec.

Magnet type = Samarium Cobalt

APPENDIX B

BJT Inverter

A bipolar junction transistor (BJT) is a current controlled device and requires base current to flow current in the collector. The current gain is highly dependent on the junction temperature as the collector current is dependent on the base current. In order to implement the proposed control scheme, a BJT inverter has been built at the Power Device and Systems research laboratory of Memorial University of Newfoundland. The schematic of the BJT inverter module with its snubber circuit is shown in Fig. B. 1. The snubber circuit [95] is used to limit the rate of change of voltage across the inverter legs because of the unpredictable transient behavior of the interior permanent magnet synchronous motor (IPMSM).

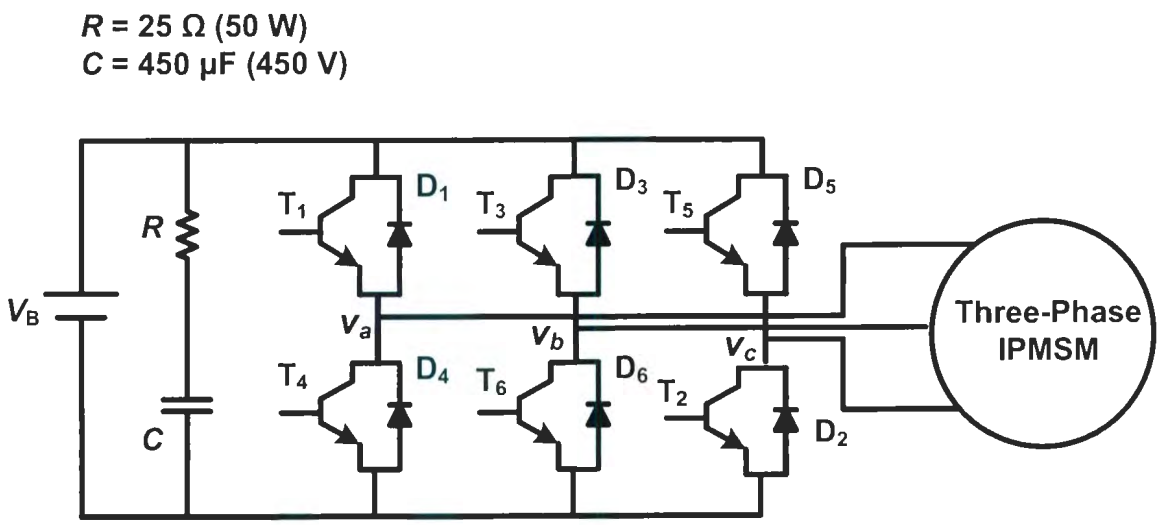

Figure B.1: Basic circuit of a BJT inverter module.

APPENDIX C

Base Drive Circuits

The output pins of the digital I/O subsystem of the DSP controller board ds1102 are used to generate driving pulses for the six transistors of the inverter. The logic signals from the digital I/O subsystem are applied between the base and emitter of the inverter transistors. So, the grounds of the logic signals are not common for the upper transistors (T_1, T_3, and T_5) of the inverter. Therefore, isolation is needed between the logic signals and the transistors. Moreover, the amplitudes of the logic signals from the digital I/O subsystem are equal to 5 V, which is not sufficient for the gate drive of the insulated gate bipolar transistors (IGBT). The base drive circuits provide the isolation and appropriate voltage levels for the inverter switches. The components of base drive circuits for the real time implementation of the proposed control algorithm based IPMSM drive system are shown in Figs. C.1–C.3. The chip SN7407N is used as voltage level shifter, which shifts the voltage level from +5 V to +15 V. The pin diagram of this chip is shown in Fig. C.1. An isolated power supply is built in order to provide +20 V isolated power to the optocoupler and the driver. The schematic of the isolated power supply is shown in Fig. C.2. The optocoupler chip HP2531 is used to provide isolation between the logic circuit and the power circuit of the inverter. The pin diagram of the chips HP2531 and IR2130 of the base drive circuit is shown in Fig. C.3. The driver chip IR2130 is used to provide six driving pulses for the six switches of the inverter.

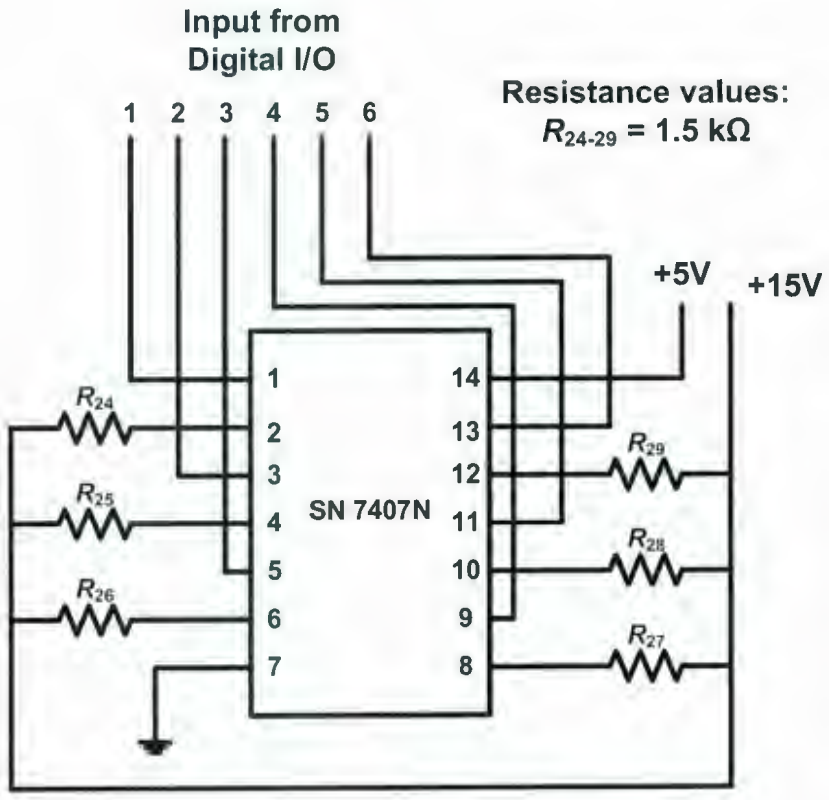

Figure C.1: Pin diagram of the voltage level shifter chip SN7407N.

Capacitor values: C_1 = 2200 µF, C_2 = 10 µF
Resistance values: R_1 = 1.1 kΩ, R_4 = 3.3 kΩ

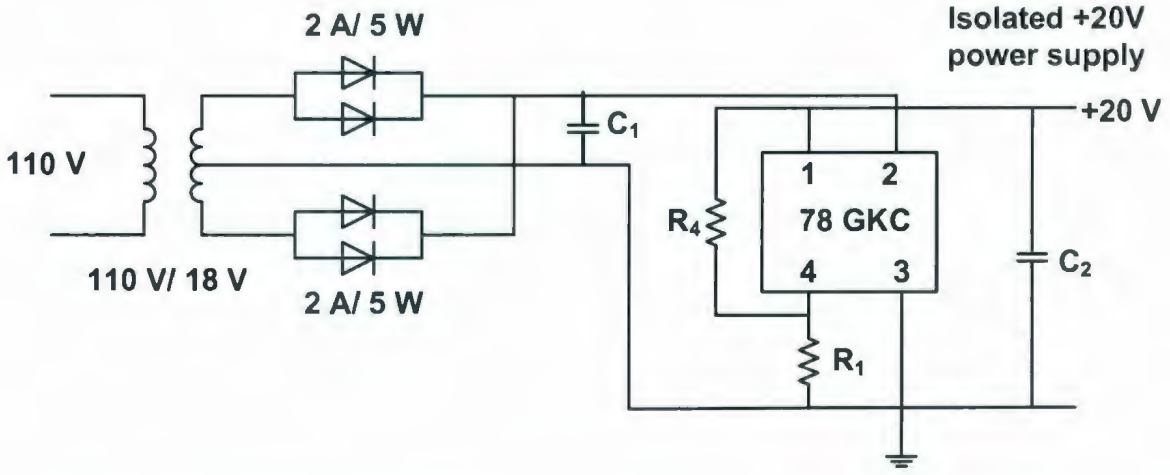

Figure C.2: Schematic of the isolated power supply for the optocoupler and the drive.

Resistance values: $R_{18\text{-}23}$ = 22 Ω, $R_{12\text{-}17}$ = 680 Ω, $R_{5\text{-}10}$ = 3.3 Ω, R_{11} = 3.3 kΩ

Capacitor values: $C_{3\text{-}5}$ = 10 µF, $C_{6\text{-}11}$ = 180 pF, C_{12} = 100 µF, C_{13} = 47 µF

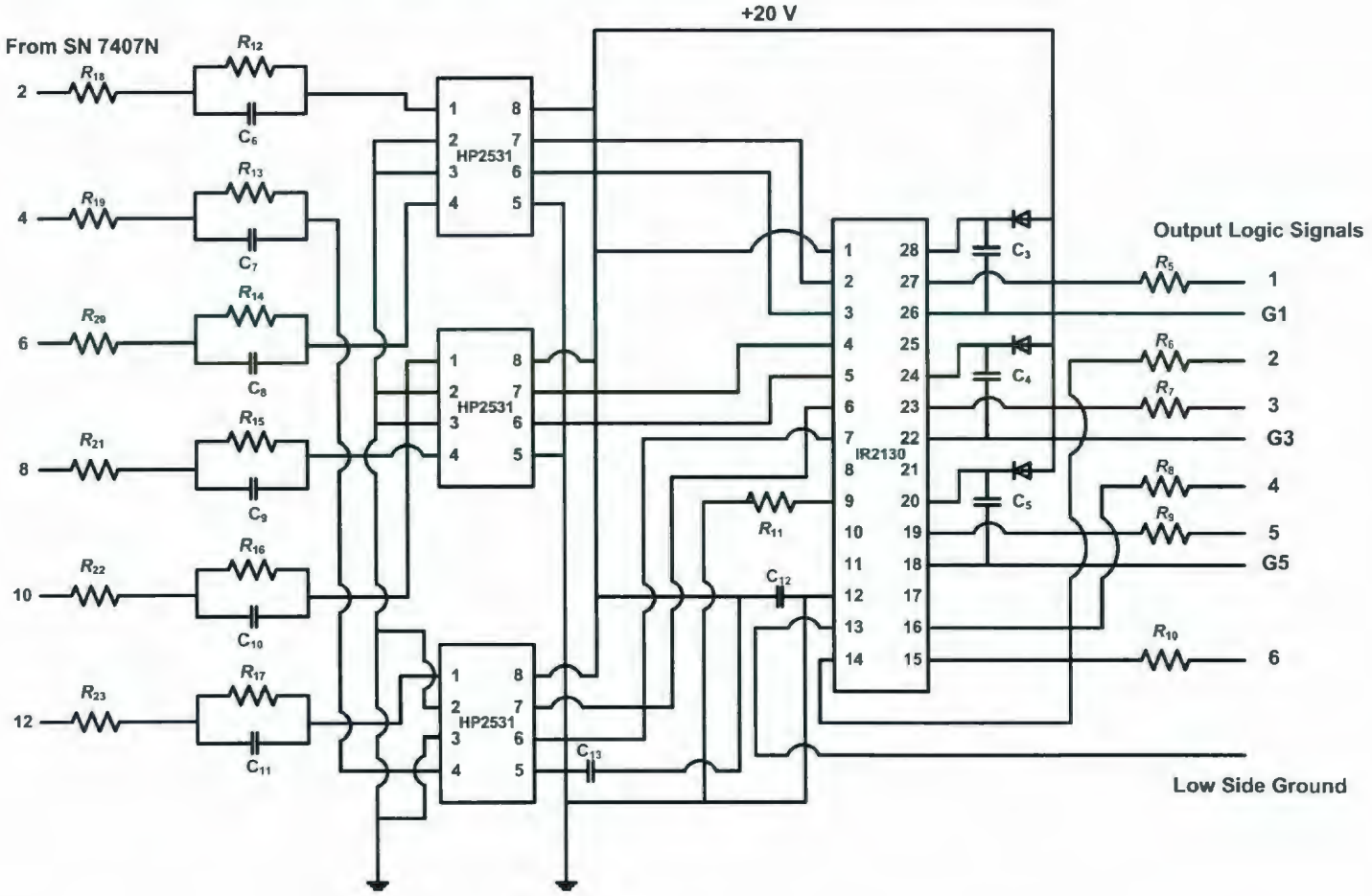

Figure C.3: Pin diagrams of the optocoupler chip HP2531 and the driver chip IR213021.

APPENDIX D

Detailed Derivations of Equation (3.10):

From equation (3.8) of chapter three, we have

$$i_d^r = \frac{\lambda_M}{2(L_q - L_d)} - \sqrt{\frac{\lambda_M^2}{4(L_q - L_d)^2} + (i_q^r)^2} \tag{D.1}$$

Let

$$f(i_q^r) = \sqrt{\frac{\lambda_M^2}{4(L_q - L_d)^2} + (i_q^r)^2} \tag{D.2}$$

The Maclaurin series expansion of equation (D.2) is carried out around $i_q^r = 0$. Using the Maclaurin series expansion, equation (D.2) can be expressed as

$$f(i_q^r) = f(0) + \frac{f'(0)}{1} i_q^r + \frac{f''(0)}{2}(i_q^r)^2 + \frac{f'''(0)}{6}(i_q^r)^3 + \frac{f'''(0)}{24}(i_q^r)^4 + \ldots \tag{D.3}$$

Now,

$$f'(i_q^r) = \frac{i_q^r}{\sqrt{\frac{\lambda_M^2}{4(L_q - L_d)^2} + (i_q^r)^2}} \tag{D.4}$$

$$f''(i_q^r) = \frac{1}{\left[\frac{\lambda_M^2}{4(L_q - L_d)^2} + (i_q^r)^2\right]^{\frac{1}{2}}} - \frac{(i_q^r)^2}{\left[\frac{\lambda_M^2}{4(L_q - L_d)^2} + (i_q^r)^2\right]^{\frac{3}{2}}} \tag{D.5}$$

$$f'''\left(i_q^r\right)=-\frac{3i_q^r}{\left[\frac{\lambda_M^2}{4\left(L_q-L_d\right)^2}+\left(i_q^r\right)^2\right]^{\frac{3}{2}}}+\frac{3\left(i_q^r\right)^3}{\left[\frac{\lambda_M^2}{4\left(L_q-L_d\right)^2}+\left(i_q^r\right)^2\right]^{\frac{5}{2}}} \tag{D. 6}$$

$$f'''''\left(i_q^r\right)=-\frac{3}{\left[\frac{\lambda_M^2}{4\left(L_q-L_d\right)^2}+\left(i_q^r\right)^2\right]^{\frac{3}{2}}}+\frac{18\left(i_q^r\right)^2}{\left[\frac{\lambda_M^2}{4\left(L_q-L_d\right)^2}+\left(i_q^r\right)^2\right]^{\frac{5}{2}}}-\frac{15\left(i_q^r\right)^4}{\left[\frac{\lambda_M^2}{4\left(L_q-L_d\right)^2}+\left(i_q^r\right)^2\right]^{\frac{7}{2}}} \tag{D. 7}$$

Substituting $i_q^r = 0$ into equations (D. 2), (D. 4)–(D. 7), one can get

$$f(0)=\frac{\lambda_M}{2\left(L_q-L_d\right)}=\frac{0.314}{2(0.07957-0.04244)}=4.2284 \tag{D. 8}$$

$$f'(0)=0 \tag{D. 9}$$

$$f''(0)=\frac{2\left(L_q-L_d\right)}{\lambda_M}=\frac{2(0.07957-0.04244)}{0.314}=0.2365 \tag{D. 10}$$

$$f'''(0)=0 \tag{D. 11}$$

$$f'''''(0)=-\frac{3}{\left[\frac{\lambda_M^2}{4\left(L_q-L_d\right)^2}\right]^{\frac{3}{2}}}=-\frac{24(0.07957-0.04244)^3}{(0.314)^3}=-0.0397 \tag{D. 12}$$

Now the equation (D. 3) can be re-written as

$$\begin{aligned} f\left(i_q^r\right) &= 4.2284 + \frac{0.2365}{2}\left(i_q^r\right)^2 - \frac{0.0397}{24}\left(i_q^r\right)^4 + \ldots \\ &= 4.2284 + 0.11825\left(i_q^r\right)^2 - 0.00165\left(i_q^r\right)^4 + \ldots \end{aligned} \tag{D. 13}$$

Substituting equation (D. 13) into equation (D.1) one can get

$$\begin{aligned} i_d^r &= 4.2284 - \left[4.2284 + 0.11825\left(i_q^r\right)^2 - 0.00165\left(i_q^r\right)^4 + \ldots\right] \\ &= -0.11825\left(i_q^r\right)^2 + 0.00165\left(i_q^r\right)^4 - \ldots \end{aligned} \tag{D. 14}$$

Neglecting the higher order terms of equation (D. 14), one can write as

$$i_d^r \cong -0.11825\left(i_q^r\right)^2 + 0.00165\left(i_q^r\right)^4 \tag{D. 15}$$

Detailed Derivations of Equation (3.11):

From equation (3.9) of chapter three, we have

$$\begin{aligned} T_e &= \frac{3P}{2}\left(\frac{\lambda_M i_q^r}{2} + \left(L_q - L_d\right)\sqrt{\frac{\left(\lambda_M i_q^r\right)^2}{4\left(L_q - L_d\right)^2} + \left(i_q^r\right)^4}\right) \\ &= \frac{3P}{2}\left(\frac{\lambda_M i_q^r}{2} + \left(L_q - L_d\right) i_q^r \sqrt{\frac{\lambda_M^2}{4\left(L_q - L_d\right)^2} + \left(i_q^r\right)^2}\right) \end{aligned} \tag{D. 16}$$

Again, using the Maclaurin series expansion around $i_q^r = 0$, one can write

$$\begin{aligned} f\left(i_q^r\right) &= \sqrt{\frac{\lambda_M^2}{4\left(L_q - L_d\right)^2} + \left(i_q^r\right)^2} \\ &= 4.2284 + 0.11825\left(i_q^r\right)^2 - 0.00165\left(i_q^r\right)^4 + \ldots \end{aligned} \tag{D. 17}$$

Substituting equation (D. 17) into equation (D. 16) and using the IPMSM parameters one can get

$$T_e = \frac{3\times 2}{2}\left[\frac{0.314}{2} i_q^r + (0.07957 - .04244) i_q^r \times \left(4.2284 + 0.11825\left(i_q^r\right)^2 - 0.00165\left(i_q^r\right)^4 + \ldots\right)\right] \qquad \text{(D. 18)}$$
$$= 3\left[0.157 i_q^r + 0.157 i_q^r + 0.0044\left(i_q^r\right)^3 - 0.00006125\left(i_q^r\right)^5 + \ldots\right]$$

Neglecting third and higher order terms, the equation (D. 18) can be re-written as

$$T_e \approx 3\times 2\times 0.157 i_q^r \approx 0.942 i_q^r \qquad \text{(D. 19)}$$

So, from equation (D. 19) one can write

$$i_q^r \approx 1.0616 T_e \qquad \text{(D. 20)}$$

Detailed Derivations of Equation (3.17):

From equation (3.12) of chapter three, we have

$$i_d^r = -\frac{\lambda_M}{L_d} + \frac{1}{L_d}\sqrt{\frac{(V_m')^2}{P^2\omega_r^2} - \left(L_q i_q^r\right)^2} = -\frac{\lambda_M}{L_d} + \frac{1}{L_d}\frac{V_m'}{P\omega_r}\sqrt{1 - \left(\frac{P\omega_r L_q i_q^r}{V_m'}\right)^2} \qquad \text{(D. 21)}$$

Let $$f\left(i_q^r\right) = \sqrt{1 - \left(\frac{P\omega_r L_q i_q^r}{V_m'}\right)^2} \qquad \text{(D. 22)}$$

So,

$$f'\left(i_q^r\right)=-\frac{\left(\frac{P\omega_r L_q}{V_m'}\right)^2 i_q^r}{\left[1-\left(\frac{P\omega_r L_q i_q^r}{V_m'}\right)^2\right]^{\frac{1}{2}}} \tag{D. 23}$$

and

$$f''\left(i_q^r\right)=-\frac{\left(\frac{P\omega_r L_q}{V_m'}\right)^2}{\left[1-\left(\frac{P\omega_r L_q i_q^r}{V_m'}\right)^2\right]^{\frac{1}{2}}}-\frac{\left(\frac{P\omega_r L_q}{V_m'}\right)^4\left(i_q^r\right)^2}{\left[1-\left(\frac{P\omega_r L_q i_q^r}{V_m'}\right)^2\right]^{\frac{3}{2}}} \tag{D. 24}$$

Substituting $i_q{}^r = 0$ into equations (D. 22)–(D. 24), one can get

$$f(0)=1 \tag{D. 25}$$

$$f'(0)=0 \tag{D. 26}$$

$$f''(0)=-\left(\frac{P\omega_r L_q}{V_m'}\right)^2 \tag{D. 27}$$

Using the Maclaurin series one can rewrite the equation (3.22) as

$$f\left(i_q^r\right)=1-\frac{\left(\frac{P\omega_r L_q}{V_m'}\right)^2}{2}\left(i_q^r\right)^2+\ldots \tag{D. 28}$$

Neglecting higher order terms and substituting equation (D. 28) into equation (D. 21) one can get

$$
\begin{aligned}
i_d^r &\cong -\frac{\lambda_M}{L_d} + \frac{1}{L_d}\frac{V_m'}{P\omega_r}\left[1-\frac{1}{2}\left(\frac{P\omega_r L_q i_q^r}{V_m'}\right)^2\right] \\
&\cong -\frac{0.314}{0.04244} + \frac{1}{0.04244}\frac{V_m'}{2\omega_r}\left[1-2\left(\frac{\omega_r L_q i_q^r}{V_m'}\right)^2\right] \\
&\cong -7.398 + \frac{1}{0.08488}\frac{V_m'}{\omega_r}\left[1-2\left(\frac{\omega_r L_q i_q^r}{V_m'}\right)^2\right]
\end{aligned}
\tag{D. 29}
$$

From equation (3.16) of chapter 3 we have

$$
V_m = \frac{2}{\pi} V_B \tag{D. 30}
$$

Let $V_B = 300$ volt

So,

$$
\begin{aligned}
V_m &= \frac{2}{\pi} \times 300 \\
&= 190.986
\end{aligned}
\tag{D. 31}
$$

Now

$$
\begin{aligned}
V_m' &= \sqrt{(V_m)^2 - (I_a R)^2} \\
&= \sqrt{(190.986)^2 - (3 \times 1.93)^2} \\
&= 190.9
\end{aligned}
\tag{D. 32}
$$

Substituting the value of V_m' into equation (D. 29) and using the IPMSM parameter, one can get

$$
i_d^r \cong -7.398 + \frac{2249.06}{\omega_r}\left[1 - 0.000000347 \times \left(i_q^r \omega_r\right)^2\right]. \tag{D. 33}
$$